FLORIDA INTERNATIONAL UNIVERSITY

Miami, Florida

EXONUCLEASE DIGESTION ASSAY FOR STREAMLINING APTAMER CHARACTERIZATION, ENGINEERING, AND SENSOR DEVELOPMENT

A dissertation submitted in partial fulfillment of the

requirements for the degree of

DOCTOR OF PHILOSOPHY

In

CHEMISTRY

by

Juan Canoura

2022

To: Dean Michael R. Heithaus
College of Arts, Sciences and Education

This dissertation, written by Juan Canoura, and entitled Exonuclease Digestion Assay for Streamlining Aptamer Characterization, Engineering, and Sensor Development, having been approved in respect to style and intellectual content, is referred to you for judgment.

We have read this dissertation and recommend that it be approved.

_____
Christopher Dares

_____
Kevin O'Shea

_____
Alexander Mebel

_____
Prem Chapagain

_____
Yi Xiao, Major Professor

Date of Defense: June 28, 2022

The dissertation of Juan Canoura is approved.

_____
Dean Michael R. Heithaus
College of Arts, Sciences and Education

_____
Andrés G. Gil
Vice President for Research and Economic Development
and Dean of the University Graduate School

Florida International University, 2022

DEDICATION

I dedicate this thesis to my parents, Juan Canoura and Mercy Canoura and grandmother, Ella Garcia, for their constant support and encouragement.

ACKNOWLEDGMENTS

The work described in this dissertation could not have been accomplished independently. I am forever thankful to all the people I have met and worked with during my study at FIU; they have shaped who I am as a person and a scientist, and I would like to communicate my acknowledgments below.

I want to express my sincere gratitude to my major professor, Dr. Yi Xiao, who has foster my desire to do research and provided invaluable guidance. The incredible time and effort she has invested into my development cannot be understated. As my role model, she has shown me what a good person and scientist should be by example and has helped me develop my curiosity, courage, patience, creativity, and persistence. The memories I have collected working in her lab will always serve as a guiding light. I am successful because of her efforts.

I am deeply grateful to my dissertation committee, Dr. Prem Chapagain, Dr. Christopher Dares, Dr. Kevin O'Shea, and Dr. Alexander Mebel, for their endless support and advice throughout my Ph. D study. Each member of my dissertation committee has provided me with insightful comments and suggestions, which have helped shape my critical thinking and presentation skills.

Moreover, I would like to thank all the current and formal lab members who have directly supported me in my research or have served as excellent role models. Specifically, I would like to thank Dr. Haixiang Yu, Obtin Alkhamis, Yingzhu Liu, Dr. Zongwen Wang, Yingping Luo, Dr. Weijuan Yang, Dr. Pingping Liang, and Dr. Bhargav Guntupalli. They have directly contributed to my dissertation research.

I want to acknowledge the Ronald E. McNair Graduate Fellowship, which funded my stipend from 2016 to 2018. I would also like to acknowledge the National Institute of Justice Graduate Research Fellowship Program, which funded my stipend and research from 2020 to 2021, and the Dissertation Year Fellowship and Provost Degree Completion Tuition Fellowship from the University Graduate School at FIU for their financial support during 2021 and 2022. Finally, I would like to thank the Graduate and Professional Student Committee and the College of Arts, Sciences & Education at Florida International University for providing me with travel funding. This support provided me with excellent opportunities to learn and apply my knowledge which was essential for my professional development.

I would also like to thank Magali Autie, Jackelyn Marcos, Lilia San Miguel, and the Department of Chemistry and Biochemistry staff and faculty members who have helped me throughout my Ph. D study.

Finally, I would like to extend my sincere thanks to my parents, Juan Canoura and Mercy Canoura, and my grandmother Ella Garcia, for their endless support and encouragement over these many years

ABSTRACT OF THE DISSERTATION

EXONUCLEASE DIGESTION ASSAY FOR STREAMLINING APTAMER CHARACTERIZATION, ENGINEERING, AND SENSOR DEVELOPMENT

by

Juan Canoura

Florida International University, 2022

Miami, Florida

Professor Yi Xiao, Major Professor

Aptamers are DNA or RNA oligonucleotide-based bioreceptors isolated in vitro through the Systematic Evolution of Ligands by Exponential Enrichment. Given the ease with which a selection can be customized, aptamers can be evolved to function in nearly any chemical environment, making them tailormade for their final application. However, the post-SELEX characterization of the 100-1000's aptamer candidates remains a significant bottleneck as there are no suitable techniques for high-throughput characterization of each candidate's affinity/specificity. Moreover, the final aptamer must be engineered to possess signal reporting functionality; this is often done via trail-and-error truncation to yield a structure-switching aptamer. This dissertation describes the development of an exonuclease-based fluorescence assay that can simultaneously engineer structure-switching aptamers from their parent aptamers and provide the binding profile of these truncated aptamers. We first demonstrate that a mixture of Exonuclease III (Exo III) and Exonuclease I (Exo I) could detect small-molecule target-binding events in fully folded aptamers yielding a truncated intact oligonucleotide product in the presence of the target, but completely digests unbound aptamers into mononucleotides. We utilized this

phenomenon to construct a highly sensitive enzyme-assisted aptamer-based sensor using SYBR Gold dye to report the presence of the inhibition product as a proxy for target concentration in biological matrixes or molecular beacons for multiplexed detection of small-molecule targets simultaneously in a single reaction volume. We then used a panel of aptamer mutants to demonstrate a qualitative relationship between target-induced enzymatic inhibition and a mutant's binding affinity. This was further confirmed as a qualitative relationship using a testbed of 28 newly isolated aptamers for 655 aptamer-ligand pairs. Characterization of the inhibition products observed during these tests revealed that it possesses structure-switching functionality, and the truncated products can be incorporated into electrochemical aptamer-based (E-AB) sensors. Finally, we applied our assay to generate a truncated THC-binding aptamer, which was then incorporated into an E-AB sensor to detect THC in the plant extract. The work done in this dissertation highlights the strength of the exonuclease-based fluorescence assay for aptamer characterization, engineering, and sensor development.

TABLE OF CONTENTS

CHAPTER PAGE

1: Introduction....1
1.1. Overview....1
1.2. Motivation and goals....3
1.3. Scope of the dissertation....5

2: Background and Literature Review....6
2.1. Importance of small-molecule biosensors....6
2.2. Aptamers as biorecognition elements....7
2.3. Advantages of aptamers over other biorecognition elements....8
2.4. Small-molecule-binding aptamer isolation....10
2.4.1. Target-immobilized SELEX....10
2.4.2. Library-immobilized SELEX....12
2.4.3. Homogeneous SELEX....13
2.5. High-throughput sequencing of enriched pools....15
2.6. Characterization of aptamer candidates....17
2.6.1. Instrument-based approaches....17
2.6.1.1. Isothermal titration calorimetry (ITC)....18
2.6.1.2. Microscale thermophoresis (MST)....18
2.6.1.3. Surface plasmon resonance (SPR) spectroscopy....19
2.6.2. Assay-based approaches....19
2.6.2.1. cDNA-based competition assays....20
2.6.2.2. Target-based approaches....21
2.6.2.3. Bead-based competition assays....21
2.7. Post-engineering of small-molecule-binding aptamers....22
2.8. Small-molecule aptamer-based sensors....24
2.8.1. Structure-switching aptamer-based sensors....24
2.8.2. Split aptamer-based sensors....26
2.8.3. cDNA displacement sensors....28
2.8.4. Aptamer beacon-based sensors....29
2.8.5. Fully-folded aptamer based sensors....30
2.9. Enzyme-based aptamer characterization, engineering, and sensing....33
2.9.1. Exonuclease-based affinity characterization....33
2.9.2. Nuclease-based footprinting and aptamer engineering....33
2.9.3. Nuclease-based sensing....36
2.9.3.1. Nuclease-based signal amplification....36
2.9.3.2. Enzyme-assisted target recycling....37
2.10. Small molecule targets used in this work....39
2.10.1. Dehydroepiandrosterone-3-sulfate (DIS)....39
2.10.2. Cocaine....40
2.10.3. Adenosine and analogs....40

2.10.4. Ochratoxin A 41
2.10.5. Fentanyl and analogs 41
2.10.6. Δ^9-Tetrahydrocannabinol (THC) 42
2.11. Proteins and enzymes used in this work 42
2.11.1 Exo III (*E. coli*) 42
2.11.2 Exo I (*E. coli.*) 43
2.11.3. Immunoglobulin E (IgE) 44
2.11.4. Thrombin 44

3: No Structure-Switching Required: A Generalizable Exonuclease-Mediated Aptamer-Based Assay for Small-Molecule Detection 45
3.1. Introduction 45
3.2. Experimental section 48
3.2.1. Reagents 48
3.2.2. Aptamer digestion experiments 49
3.2.3. SYBR gold fluorescence experiments 50
3.2.4. Multiplex target detection using fluorophore-quencher-modified molecular beacons 51
3.2.5. Isothermal titration calorimetry (ITC) experiments 52
3.3. Results and discussion 52
3.3.1. Structure selectivity of Exo III for target-aptamer complexes 52
3.3.2. Inhibition of Exo III requires formation of the target-aptamer complex 55
3.3.3. Mechanism of Exo III inhibition and development of the dual-exonuclease-mediated assay 57
3.3.4. Label-free detection of DIS using a dual-exonuclease-mediated fluorescence assay 60
3.3.5. Application of the dual-exonuclease-mediated assay to a three-way-junction cocaine aptamer 64
3.3.6. Application of our assay to a hairpin-structured ATP aptamer 66
3.3.7. Multiplex detection of cocaine and ATP using fluorophore-quencher-modified molecular beacons 70
3.4. Conclusion 75

4: Accelerating Post-SELEX Aptamer Engineering Using Exonuclease Digestion 79
4.1. Introduction 79
4.2. Experimental section 82
4.2.1. Reagents 82
4.2.2. Aptamer digestion experiments 84
4.2.3. Analysis of aptamer digestion rates 85
4.2.4. Reverse ITC experiments 86
4.2.5. Isothermal titration calorimetry experiments for ATP-analogue-binding aptamers 87
4.2.6. Polyacrylamide gel electrophoresis (PAGE) analysis of digestion products 89

4.2.7. Circular dichroism (CD) spectroscopy 89
4.2.8. Electrochemical aptamer-based adenosine sensor fabrication 90
4.2.9. Electrochemical measurements 91
4.3. Results and discussion 91
4.3.1. Exonuclease fluorescence assay to characterize affinity and specificity of ochratoxin-binding aptamers 91
4.3.2. Characterizing a cross-reactive ATP-binding aptamer 101
4.3.3. Identification of a new highly ADE-specific aptamer 111
4.3.4. Fabrication of E-AB sensors from ADE-specific aptamers 114
4.3.5. Generality of the exonuclease fluorescence assay for protein-binding aptamers 122
4.4. Conclusion 126

5: Label-Free, High-Throughput, Quantitative Binding Analysis of DNA Aptamers using Exonucleases 131
5.1. Introduction 131
5.2. Experimental section 134
5.2.1. Reagents 134
5.2.2. SELEX procedure 136
5.2.3. High-throughput sequencing 139
5.2.4. Aptamer digestion experiments 140
5.2.5. ITC experiments 141
5.2.6. Strand-displacement fluorescence assay 143
5.2.6.1. Determination of F27-FAM binding affinity 143
5.2.6.2. Determination of aptamer specificity and cross-reactivity 145
5.2.7. Fabrication of E-AB sensors 146
5.2.8. Electrochemical measurements and optimization of E-AB sensor performance 147
5.2.9. Cross-reactivity and binary-mixture measurements using E-AB Sensors constructed with F13-32-MB 147
5.2.10. Detection of fentanyl in 50% saliva using E-AB sensors constructed with F27-38-MB 148
5.2.11. Polyacrylamide gel electrophoresis (PAGE) analysis of digestion products 149
5.2.12. Confirmation of structure-switching functionality of aptamer digestion products using circular dichroism (CD) spectroscopy 149
5.3. Results and discussion 150
5.3.1. Isolation of aptamers against fentanyl and its analogs using SELEX 150
5.3.2. High-throughput sequencing (HTS) of enriched pools 155
5.3.3. Rapid screening of 28 aptamer candidates for their target-binding affinity 158
5.3.4. High-throughput screening of aptamer specificity 182
5.3.5. High-throughput screening of aptamer cross-reactivity to fentanyl analogs 187
5.3.6. Development of E-AB sensors with customized analytical

performance 191
5.4. Conclusion 198

6: Rapid Development of an E-AB sensor for detection of THC 201
6.1. Introduction 201
6.2. Experimental section 204
6.2.1. Reagents 204
6.2.2. Aptamer digestion experiments 205
6.2.3. Polyacrylamide gel electrophoresis (PAGE) analysis of digestion products 205
6.2.4. Confirmation of structure-switching functionality using circular dichroism (CD) spectroscopy 206
6.2.5. Fabrication of electrochemical aptamer-based (E-AB) sensors 206
6.2.6. Electrochemical measurements and optimization of E-AB sensor performance 207
6.2.7. Isothermal titration calorimetry (ITC) 208
6.3. Results and discussion 209
6.3.1. Engineering structure-switching THC-binding aptamers 209
6.3.2. Construction of E-AB sensors using a hydrophobic monolayer 214
6.3.3. THC detection using E-AB sensors backfilled with hydrophilic monolayers 218
6.3.4. Detection of THC spiked into marijuana placebo extract 223
6.4. Conclusion 224

7: Summary and Future Work 225
7.1. Summary 225
7.2. Future work 228

REFERENCES 230

VITA 257

LIST OF TABLES

TABLE PAGE

CHAPTER 3

3-1. Sequences ID and DNA sequences used in Chapter 3 49
3-2. Comparison of various structure-switching aptamer-based assays for detection of cocaine and ATP 78

CHAPTER 4

4-1. All oligonucleotide sequences used in Chapter 4 83
4-2. Aptamers, ligands, and aptamer/ligand concentration used for reverse ITC experiments and determined K_D 87
4-3. ATP-binding aptamers, ligands, and ligand concentration used for ITC and determined K_{D1}, K_{D2}, and $K_{1/2}$ 88

CHAPTER 5

5-1. DNA sequences used in chapter 5 135
5-2. Selection strategy and condition for fentanyl SELEX 137
5-3. Selection strategy and condition for acetyl fentanyl SELEX 138
5-4. Selection strategy and condition for furanyl fentanyl SELEX 139
5-5. Aptamer ID, K_D, and ITC conditions 142
5-6. Aptamer digestion product ID, K_D, and ITC conditions 143

CHAPTER 6

6-1. DNA sequences used in chapter 6 205
6-2. Aptamer ID, dissociation constant (K_D), and ITC experiment conditions 208

LIST OF FIGURES

FIGURE PAGE

CHAPTER 3

3-1. Time course of Exo III digestion of a DIS-binding aptamer (DIS37) in the absence or presence of DIS 53
3-2. Characterization of target-binding affinity of DIS-binding aptamers using ITC 54
3-3. Aptamer mutant DIS-37-M and its binding affinity to DIS 55
3-4. PAGE analysis of exonuclease-treated DIS-37 and DIS-37-M after a 15 minute reaction in the absence or presence of DIS 57
3-5. PAGE analysis of DIS-30 and DIS-34 after 15 minutes of exonuclease digestion in the absence and presence of 250 µM DIS 57
3-6. Exonuclease digestion of DIS-37 and its mutant (DIS-37-M) at increasing concentrations of DIS after 15 min 58
3-7. DIS detection using our label-free, aptamer-based dual-exonuclease-mediated fluorescence assay 59
3-8. Quantification of the digestion product of DIS-37 generated by the exonuclease mixture with 0 – 250 µM DIS via staining with SYBR Gold 61
3-9. Quantification of the digestion product of DIS-37 generated by exonuclease mixture with 0 – 10 µM DIS via staining with SYBR Gold 61
3-10. PAGE analysis of exonuclease digestion products of COC-38 and COC-38-M with and without 250 µM cocaine after 25 min of reaction and performance of the cocaine-detecting dual-exonuclease-mediated fluorescence assay 62
3-11. Schematic of dual-exonuclease-mediated COC-38 digestion in the absence and presence of cocaine 62
3-12. Characterization of target-binding affinity of cocaine-binding aptamers and a mutant using ITC 63
3-13. Target concentration-dependent inhibition of dual-exonuclease-mediated digestion of a cocaine-binding aptamer (COC-38) and its mutant (COC-38-M) after a 25-min reaction 65
3-14. PAGE analysis of exonuclease digestion products of ATP-33 and ATP-33-M with and without 250 µM ATP after 20 min of digestion and performance of the dual exonuclease-mediated fluorescence assay for ATP detection 66
3-15. Schematic of dual-exonuclease-mediated ATP-33 digestion in the absence and presence of ATP 67
3-16. Characterization of target binding affinity of ATP-binding aptamers and a mutant using ITC 67
3-17. Target concentration-dependent inhibition of dual-exonuclease-mediated digestion of an ATP-binding aptamer (ATP-33) and its mutant (ATP-33-M) after a 20 min reaction 68
3-18. Design of molecular beacons for the ATP- and cocaine-binding aptamer digestion products produced by the exonuclease mixture 69

3-19. Scheme of dual-exonuclease-mediated, molecular beacon-based multiplexed detection of cocaine alone, ATP alone, both cocaine and ATP, and neither target ... 70
3-20. Fluorescence spectra of COC-MB and ATP-MB for exonuclease mixture-treated samples with no, either, or both cocaine and ATP at concentrations of 0, 25, or 100 µM ... 72
3-21. Calibration curves of the dual-exonuclease-mediated molecular-beacon-based multiplex assay for the detection of cocaine and ATP ... 74
3-22. Comparison of the performance of the molecular-beacon-based multiplex assay with individual exonucleases versus both ... 74

CHAPTER 4

4-1. Design and characterization of binding properties of OBAwt and six mutant derivatives ... 92
4-2. Fluorescence time-course of the digestion of OBA3 and OBA4 with the mixture of Exo III and Exo I in the absence and presence of 100 µM OTA ... 94
4-3. Characterization of OBA3 digestion kinetics by Exo III and Exo I ... 95
4-4. Evaluation of the binding profile of OTA-binding aptamers using the exonuclease digestion assay ... 96
4-5. Characterization of OBA3 affinity for OTA and OTB using ITC ... 99
4-6. Characterization of OBA5 affinity for OTA and OTB using ITC ... 99
4-7. Characterization of OBA1 affinity for OTA and OTB using ITC ... 100
4-8. Characterization of ATPwt digestion kinetics by Exo III and Exo I ... 100
4-9. Exonuclease-based fluorescence profiling of ATPwt binding to various targets ... 102
4-10. Digestion of ATPwt with Exo III and Exo I in the absence and presence of 100 µM ADE, AMP, ADP, or ATP ... 102
4-11. Characterization of affinity of ATPwt to ATP, ADP, AMP, and ADE using ITC ... 103
4-12. Design and characterization of ATPwt mutants ... 104
4-13. Evaluating the binding profile of various G10 mutant aptamers using the exonuclease digestion assay ... 105
4-14. Evaluating the binding profile of various A13 mutant aptamers using the exonuclease digestion assay ... 106
4-15. Evaluating the binding profile of various A23 mutant aptamers using the exonuclease digestion assay ... 107
4-16. Evaluating the binding profile of various A26 mutant aptamers using the exonuclease digestion assay ... 108
4-17. Characterization of affinity of single-site mutants for ADE using ITC ... 110
4-18. Design and characterization of a double-mutant aptamer ... 111
4-19. Characterization of affinity of G10T-A23G for ADE using ITC ... 112
4-20. PAGE analysis of A23T and G10T-A23G products after 30 min of digestion with Exo III and Exo I in the absence or presence of 250 µM ADE, AMP, ADP, or ATP ... 113
4-21. Sequence and secondary structure of A23T-30, A23T-29, G10T-A23G-30,

and G10T-A23G-29 113
4-22. Characterization of affinity of ADE-specific aptamer mutants using ITC 114
4-23. Characterizing structure-switching functionality of A23T and G10T-A23G digestion products using CD spectroscopy 115
4-24. Characterization of A23T-29 affinity using ITC 117
4-25. Characterization of G10T-A23G-29 affinity using ITC 118
4-26. Surface coverage of E-AB sensors fabricated using G10T-A23G-29-MB, A23T-29-MB, or both 119
4-27. Performance of E-AB sensors fabricated using G10T-A23G-29-MB, A23T-29-MB, or a mixture of both aptamers 119
4-28. Specific detection of ADE in serum using the dual aptamer E-AB sensor 120
4-29. SWV curves in the absence (black) or presence (red) of 100 µM ADE in buffer or 50% serum using dual-aptamer E-AB sensors constructed with A23T-29-MB and G10T-A23G-29-MB 121
4-30. Dual-aptamer E-AB sensor response to 100 µM ADE, AMP, ADP, or ATP or other nucleotide triphosphates in 50% serum 122
4-31. Exonuclease-based fluorescence profiling of thrombin-binding aptamers 123
4-32. Characterization of the thrombin-binding affinity of Tasset, Bock, and Bock-hang using ITC 124
4-33. Exonuclease-based fluorescence profiling of an IgE-binding aptamer 125
4-34. Characterization of ligand-binding affinity of a recently published ADE-binding aptamer (A10-excised) to ADE using ITC at room temperature 125
4-35. Characterization of OBA3 affinity for OTA using the exonuclease digestion assay 126

CHAPTER 5

5-1. The chemical structures of fentanyl and its analogs 151
5-2. Isolation of fentanyl-binding aptamers via library-immobilized SELEX 153
5-3. Isolation of acetyl fentanyl-binding aptamers via library-immobilized SELEX 154
5-4. Isolation of furanyl fentanyl-binding aptamers via library-immobilized SELEX 155
5-5. HTS analysis of enriched pools 157
5-6. Schematic of our exonuclease digestion assay for distinguishing ligand-bound and non-bound aptamers 158
5-7. Fentanyl binding affinity of 11 aptamer candidates 159
5-8. Acetyl fentanyl binding affinity of 10 aptamer candidates 160
5-9. Furanyl fentanyl binding affinity of 12 aptamer candidates 160
5-10. R_{value} for aptamer candidates in the presence of 100 µM of their respective selection targets 160
5-11. Characterization of fentanyl binding affinity of six aptamer candidates using ITC 162
5-12. Characterization of fentanyl- and acetyl fentanyl-binding affinity of six aptamer candidates using ITC 163

5-13. Characterization of acetyl fentanyl binding affinity of six aptamer candidates using ITC 164
5-14. Characterization of acetyl fentanyl- and furanyl fentanyl-binding affinity of six aptamer candidates using ITC 165
5-15. Characterization of furanyl fentanyl binding affinity of six aptamer candidates using ITC 166
5-16. Characterization of furanyl fentanyl binding affinity of aptamer candidate F6 using ITC 167
5-17. Characterization of furanyl fentanyl binding affinity of F27 using ITC 167
5-18. Determination of F27's furanyl fentanyl and acetyl fentanyl binding affinity using a fluorescence strand-displacement assay 168
5-19. Correlation between target-binding-induced exonuclease inhibition and aptamer affinity 168
5-20. Determining enzyme inhibition at low concentrations of fentanyl 170
5-21. Determining enzyme inhibition at low concentrations of acetyl fentanyl 170
5-22. Determining enzyme inhibition at low concentrations of furanyl fentanyl 171
5-23. Identification of the major inhibition product for three aptamer-ligand pairs 172
5-24. Identification of the major inhibition product for three aptamer-ligand pairs 173
5-25. Identification of the major inhibition product for three aptamer-ligand pairs 174
5-26. Identification of the major inhibition product for three aptamer-ligand pairs 175
5-27. Identification of the major inhibition product for three aptamer-ligand pairs 176
5-28. Identification of the major inhibition product for three aptamer-ligand pairs 177
5-29. Characterization of fentanyl binding affinity of six major inhibition products using ITC 178
5-30. Characterization of fentanyl binding affinity of six major inhibition products using ITC 179
5-31. Characterization of fentanyl binding affinity of six major inhibition products using ITC 180
5-32. Characterization of selection target binding affinity of F27-42 using ITC 181
5-33. The equation used for fitting and adjusted R^2 values obtained during the fitting of parent aptamer/major digestion product K_D against the R_{value} at 1.5, 5, 25, and 100 µM selection target concentrations 181
5-34. The chemical structure of 19 interferent molecules employed for the aptamer specificity test, which included controlled substances, adulterants, and cutting agents 182
5-35. Screening the specificity of 11 aptamer candidates using our exonuclease digestion assay 183
5-36. Screening the specificity of six aptamer candidates using our exonuclease digestion assay 183
5-37. Specificity of 11 aptamer candidates. R_{value}s were obtained from time-course digestion of F4, F5, F6, F13, F14, F17, F18, F23, F24, F25, and F27 184
5-38. Specificity of six aptamer candidates. R_{value}s of F8, F9, F15, F16, F26, and F28 were obtained by exonuclease digestion with 100 µM of various interferents or their selection target 185
5-39. Optimization of cDNA-Dab-induced quenching of F4-FAM, F27-FAM, and

F13-FAM 186
5-40. Comparison of aptamer specificity determined using fluorescence-strand displacement assay and exonuclease digestion assay 186
5-41. Screening the cross-reactivity of 11 aptamer candidates using our exonuclease digestion assay 188
5-42. Screening the cross-reactivity of 11 aptamer candidates to fentanyl and its analogs using our exonuclease digestion assay 189
5-43. mparison of aptamer cross-reactivity determined using a fluorescence strand-displacement assay and exonuclease digestion assay 190
5-44. Determination of F27-42-FAM's optimal aptamer/cDNA ratio 191
5-45. Characterization of fentanyl-binding affinity for F27-42 and F13-39 using ITC 193
5-46. Confirmation of structure-switching functionality of major exonuclease digestion products 194
5-47. Analytical performance of E-AB sensor for detection of fentanyl or its analogs 194
5-48. Optimization of analytical performance for E-AB sensors constructed with F27-38-MB 195
5-49. Optimization of analytical performance for E-AB sensors constructed with F13-32-MB 195
5-50. SWV response of E-AB sensor constructed with F13-32-MB to 5 µM fentanyl or its analogs 196
5-51. SWV response of E-AB sensor constructed with F13-32-MB in binary mixtures 197
5-52. Correlation between parent aptamer binding affinity and performance based on abundance in the final pool and enrichment between early and final rounds 198

CHAPTER 6

6-1. Working principle of the exonuclease-assisted truncation strategy 209
6-2. Engineering a TA-47-derived structure-switching aptamer using an exonuclease-assisted truncation strategy 211
6-3. Characterization of TA-39 and TA-35 THC binding affinity using ITC 211
6-4. Engineering high-affinity mutants of TA-35 213
6-5. Characterization of TA-mut1 and TA-mut2 structure-switching functionality and THC binding affinity 214
6-6. Fabrication of an E-AB sensor for THC detection 215
6-7. Detection of THC using a TA-mut1-MB-based E-AB sensor 216
6-8. Specificity of TA-mut1-MB-based E-AB sensors 217
6-9. Detection of THC using TA-39-MB-based E-AB sensors backfilled with hydrophilic monolayers 218
6-10. Performance of different E-AB hydrophilic monolayers in complex matrices 219
6-11. Testing E-AB sensors constructed with MHA monolayers 220
6-12. Determination of THC adsorption onto electrode surfaces modified with

various backfillers..... 221
6-13. Detection of THC using electrodes immobilized with TA-39-MB and backfilled with PEG..... 222
6-14. Detection of THC spiked into marijuana placebo extracts in MeOH in the presence of various surfactants..... 224

LIST OF ABBREVIATIONS

ACRONYMS

<	Less than
>	Greater than
2D	Two dimensional
3D	Three dimensional
a.u.	Arbitrary units
AP	Apurinic/apyrimidinic site
AUC	Area-under-curve
CBSA	Cooperative-binding split aptamer
CD	Circular dichroism
cDNA	Complementary deoxyribonucleic acid
DI	Deionized
DNAzyme	DNA enzyme
E. coli	Escherichia coli
e.g.	Exempli gratia
E-AB	Electrochemical aptamer-based
EATR	Enzyme assisted target recycling
EIS	Electrochemical impedance spectroscopy
et al.	Et alia
Exo M	Exonuclease mixture
FET	Field effect transistor

G1	Group 1
G2	Group 2
G3	Group 3
G4	Group 4
G5	Group 5
G6	Group 6
G7	Group 7
G8	Group 8
GC	Gas chromatography
HTS	High throughput sequencing
ITC	Isothermal titration calorimetry
LC-MS	Liquid chromatography – mass spectrometry
LOD	Limit of Detection
MEME	Multiple Em for Motif Elicitation
NESA	Nicking enzyme signal amplification
NMR	Nuclear magnetic resonance
PAGE	Polyacrylamide gel electrophoresis
PCR	Polymerase chain reaction
RE-SELEX	Restriction enzyme-systematic evolution of ligands by exponential enrichment
RPM	Reads per million
R_{value}	Resistance value
SCE	Saturated calomel electrode

SELEX	Systematic evolution of ligands by exponential enrichment
SPR	Surface plasmon resonance
SWV	Square wave voltammetry
UV	Ultraviolet

CHEMICALS AND MATERIALS

A	Adenine
ADE	Adenosine
ADP	Adenosine diphosphate
AF	Acetyl fentanyl
AMP	Adenosine monophosphate
APAP	Acetaminophen
ATP	Adenosine triphosphate
BSA	Bovine serum albumin
C	Cytosine
CBD	Cannabidiol
CBD-A	Cannabidiolic acid
CBG	Cannabigerol
CBG-A	Cannabigerolic acid
COC	Cocaine
CPZ	Chlorpromazine
CTP	Cytosine triphosphate
Cy5	Diethylthiadicarbocyanine

Cy7	Diethylthiatricarbocyanine
Dab	Dabcyl
DAPI	4′,6-diamidino-2-phenylindole
DIS	Dehydroepiantrosterone-3-sulfate
DMSO	Dimethyl sulfoxide
DNA	Deoxyribonucleic acid
DNase I	Deoxyribonuclease I
DPH	Diphenhydramine
EDC	1-Ethyl-3-(3-dimethylaminopropyl)carbodiimide
EDTA	Ethylenediaminetetraacetic acid
Exo I	Exonuclease I
Exo III	Exonuclease III
FAM	Fluorescein
FF	Furanyl fentanyl
G	Guanosine
GTP	Guanosine triphosphate
HCl	Hydrochloride
HEX	1-Hexanethiol
HIV	Human immunodeficiency virus
IgE	Immunoglobulin E
IgG	Immunoglobulin G
MB	Methylene blue
MCH	6-Mercapto-1-hexanol

MDPV	Methylenedioxypyrovalerone
MeOH	Methanol
(+)-METH	(+)-Methamphetamine
MHA	6-Mercaptohexanoic acid
MTC	3,3′-di(3-sulfopropyl)-4,5,4′,5′-dibenzo-9-methyl-thiacarbocyanine
N	Random nucleotide
NHS	N-Hydroxysuccinimide
(+)-PSE	(+)-Pseudoephedrine
OTA	Ochratoxin A
OTB	Ochratoxin B
P32	Phosphorus-32
PEG	2-[2-[2-[2-mercaptoethoxy]ethoxy]ethoxy
RNA	Ribonucleic acid
SDS	Sodium dodecyl sulfate
T	Thymidine
T5 Exo	T5 exonuclease
TBE	Tris Boric acid EDTA
TCEP	Tris(2-carboxyethyl)phosphine
TdT	Deoxynucleotidyl transferase
THC	Δ^9-Tetrahydrocannabinol
THC-A	Tetrahydrocannabinolic acid
UTP	Uridine triphosphate

α-PVP	alpha-Pyrrolidinopentiophenone

UNIT AND PROPERTIES

%	Percent
°C	Degrees Celsius
µC	Microcoulomb
µcal	Micro calorie
µL	Microliter
µM	Micromolar
bp	Base pair
cm	Centimeter
ε	Extinction coefficient
Hz	Frequency
I	Current
K	Kelvin
$K_{1/2}$	Half-saturation point
kcal	Kilo calorie
K_D	Dissociation constant
K_{D1}	Aptamer and cDNA affinity
K_{D2}	Aptamer-cDNA complex target affinity
K_{ET}	Electron transfer rate
M	Molar
mg	Milligram

min	Minute
mm	Millimeter
mol	Mole
mV	Millivolt
nM	Nanomolar
nm	Nanometer
nmol	Nanomole
nt	Nucleotide
pM	Picomolar
pmol	Picomole
s	Second
$t_{1/2}$	Half-life
U	Activity unit
V	Volts
v/v	Volume/volume
w/v	Weight/volume
$\Delta\varepsilon_{MR}$	Mean residue molar extinction coefficient
ΔG	Gibbs free energy
ΔH	Enthalpy
ΔS	Entropy
λ	Wavelength
Ω	Ohm

CHAPTER 1: Introduction

1.1. Overview

Aptamers are nucleic acid-based biorecognition elements that are isolated *in vitro* via a technique termed Systematic Evolution of Ligands by Exponential Enrichment (SELEX). This process isolates specific nucleic acid sequences from a randomized DNA or RNA pool to yield aptamers that bind to a target of interest, which may be a protein, small molecule, ion, or cell type. There are several advantages of aptamers which highlight their use over conventional protein-based bio-affinity element such as antibodies and enzymes. Since SELEX is an entirely *in vitro* process, there are few limitations in terms of the range of targets that can be used for aptamer generation, including non-immunogenic molecules and even highly toxic small molecules. This also means that the ionic strength, pH, temperature, and solvent composition of the selection process can be precisely controlled to yield an aptamer that performs optimally in a given final application. Additionally, aptamers are highly stable over a range of pH conditions, from mildly acidic to basic, and their function can even be recovered after being exposed to denaturing conditions. This is in stark contrast to antibodies, which can only reliably be applied in physiological conditions and lose their functionality upon denaturation. Finally, once an aptamer sequence is identified, that aptamer can be routinely chemically synthesized with low batch-to-batch variation, and readily modified with different signaling reporters for various applications. These capabilities make aptamers a versatile for applications including medical diagnostics, environmental monitoring, medical therapeutics, and food safety.

The exceptional customizability of the SELEX process allows for the isolation of highly specialized aptamers. However, once the SELEX process has been completed, there

are still several steps that must be taken to facilitate the identification of a high-performance aptamer. A SELEX experiment typically yields hundreds or thousands of aptamer candidates, from which the aptamer with the highest affinity/specificity must be selected. This is problematic, as a sequence's abundance in the final round and degree of enrichment between rounds are not always indicative of its binding properties. As a result, it is necessary to conduct thorough screening of the binding profile of many individual aptamer candidates. In some cases, the final aptamer's affinity or specificity may still be inadequate for its intended sensing application, possibly due to poorly-planned SELEX experiments or selection bias. In this situation, the affinity or specificity of the aptamer can be further improved via mutagenesis or reselection using a biased library based on the isolated aptamer (Doped SELEX). Once the ideal aptamer has been identified, further engineering must often be performed before it can be introduced into a sensor, as newly-selected aptamers seldom possess the intrinsic signal-reporting functionality needed for target detection. In many cases, this requires the introduction of structure-switching functionality, such that the aptamer undergoes a large conformational change upon target binding. These aptamers exist in an unfolded state in the absence of the target, but fold into a double-stranded state in the presence of its target. Introducing such functionality is a lengthy trial-and-error process, typically entailing extensive engineering such as aptamer truncation or splitting the aptamer into thermally-destabilized fragments that reassemble in the presence of target. Finally, the engineered aptamers can be modified with a label, such that the target-induced conformational change is readily transduced into a measurable signal.

1.2. Motivation and goals

The primary goal of this dissertation was to develop a generalizable strategy for expediting the screening, optimization, engineering, and sensor development process for small-molecule-binding aptamers. To achieve this, we first developed an exonuclease-based fluorescence assay that can be used to detect multiple small-molecule targets simultaneously without the need for a binding-induced conformational change (see Chapter 3). This assay is based on previous studies that have shown that exonuclease III (Exo III), a 3'-to-5' double-strand DNA exonuclease, is sensitive to local structural changes induced in the aptamer binding domain by small-molecule target interaction. These changes result in halted digestion 3–4 bases prior to the binding domain, yielding a truncated, target-bound digestion product. In contrast, unbound aptamers are progressively digested by Exo III into a single-stranded product. Based on this finding, we also employed exonuclease I (Exo I), a 3'-to-5' single-strand DNA exonuclease, to fully digest these single-stranded products into mononucleotides while leaving target-bound aptamers intact. These partially digested products can then be detected using SYBR gold, a DNA-binding dye, as a signal reporter. Using this assay, we demonstrated highly sensitive detection of small-molecule targets using various aptamers that bind to dehydroepiandrosterone-3-sulfate, cocaine, and ATP. Importantly, this assay was also compatible with molecular beacon-based signal reporting, allowing for multiplexed detection of cocaine and ATP in a single sample.

This exonuclease-based fluorescence assay can clearly indicate the binding of aptamers to their respective targets without any need for prior sequence engineering, truncation, or labeling, making it an ideal method for rapidly screening aptamer affinity and specificity (see Chapter 4). We first validated this approach using a panel of ochratoxin

A-binding aptamer mutants with known binding affinities, and found that the degree of target-induced inhibition demonstrated a qualitative inverse relationship with the binding affinity measurements obtained using a fluorescence polarization assay. Based on these results, we tested the assay on a panel of newly isolated pool of ATP-binding aptamers including single and double point mutants, and screened these for their specificity against ATP, ADP, AMP, and adenosine. Our exonuclease-based fluorescence assay enabled us to identify two adenosine-specific mutants. Further characterization of the resulting exonuclease digestion products revealed that they possess structure-switching functionality, simplifying the subsequent fabrication of an electrochemical aptamer-based (E-AB) sensor based on these aptamers, which we then used for the detection of adenosine in 50% serum.

We then attempted to extract quantitative information from the digestion time-course of aptamers using this exonuclease-based fluorescence assay (see Chapter 5). We digested a panel of aptamer candidates from three separate SELEX experiment in the presence of various concentrations of their respective targets. The target-binding affinities of the parent aptamers and their respective digestion product were determined using isothermal titration calorimetry and plotted against their degree of enzymatic inhibition. We observed strong correlation between the extent of inhibition and the binding affinity of the truncated, structure-switching digestion product, indicating that this assay is ideal for screening high-affinity structure-switching aptamers from panels of newly-isolated aptamer candidates. This novel capability should expedite the development of optimal structure-switching candidates for aptamer-based sensors.

Finally, we fabricated an E-AB sensor for the detection of Δ^9-tetrahydrocannabinol (THC), the primary psychoactive component of marijuana. We used our exonuclease-based fluorescence assay to generate a structure-switching THC-binding aptamer, which was then directly incorporated into an E-AB sensor (see Chapter 6). Once we had optimized the operating parameters of this sensor with respect to the backfilling molecule and measurement frequency, we were able to detect THC in a spiked marijuana placebo extract.

1.3. Scope of the dissertation

The organization of this dissertation is as follows. Chapter 2 will provide a general literature review of aptamer isolation, characterization, engineering, and sensor development for small-molecule targets, as well as the proteins and small molecules used in the work. Chapter 3 details the development of the exonuclease-based assay and its compatibility with signal-reporting strategies such as fluorescent dye molecules and fluorophore-quencher modified molecular beacons. Chapter 4 demonstrates the generalizability of our exonuclease-based assay by screening the affinity and specificity of aptamer mutants for ochratoxin A, ATP and its analogs, and thrombin. Chapter 5 establishes an accurate and quantitative relationship between the target binding affinity of an aptamer's digestion product and the degree of enzymatic inhibition observed during the digestion. Chapter 6 demonstrates rapid generation of a structure-switching THC-binding aptamer with our exonuclease-based assay, and the subsequent utilization of this aptamer in an E-AB sensor for the detection of THC in plant extract. Finally, Chapter 7 summarizes the dissertation and proposes future research directions.

CHAPTER 2: Background and Literature Review

2.1. Importance of small-molecule biosensors.

The detection of small-molecule analytes such as drugs, cell signaling molecules, antibiotics, pesticides, and mycotoxins is important for applications in clinical diagnostics, drug discovery, environmental monitoring, law enforcement, and food analysis.[1–4] The most widely used instrument-based approaches for small-molecule detection include spectroscopic and spectrometric methods that require sample clean-up via techniques such as solid-phase extraction or chromatographic separation prior to detection.[5] These preparatory steps are often expensive and time-consuming, limiting the throughput that can be achieved with screening workflows. Highly sensitive and specific biosensors that can achieve robust performance in complex sample matrices offer an ideal alternative for the rapid screening and monitoring of small-molecule analytes in various biological samples.[4,6,7] These sensors utilize bioreceptors such as antibodies,[8] enzymes,[9] cells,[10] or aptamers,[11] which are integrated with a transducing element that converts bioreceptor binding events into a measurable (*e.g.* optical,[12] piezoelectric,[13] or electrochemical[14]) signal. One well-known example of a small-molecule biosensor is the glucose meter, which provides rapid, accurate measurements of blood glucose at low cost.[15] This biosensor utilizes the enzyme glucose oxidase, which converts glucose into glucono-delta-lactone and hydrogen peroxide.[16] The peroxide is either directly detected electrochemically, or via the inclusion of other enzymes that enable alternative electrochemical or optical signaling mechanisms.[16] Numerous other biosensors are now commercially available for the detection of other small-molecule targets.[17]

2.2 Aptamers as biorecognition elements.

Until relatively recently, the chemical functionality of nucleic acids was generally thought to be limited to the encoding of genetic information. However, these molecules can fold into complex 3D structures that are also capable of other functions such as catalyzing chemical reactions[18] or binding to cellular metabolites,[19] thereby contributing to a host of biological activities such as controlling gene expression, regulating cellular metabolism, and mediating protein synthesis.[20–22] The emergence of the capacity to manufacture large populations of randomized oligonucleotides via solid-phase synthesis in the late 1990s has given researchers the ability to generate synthetic reagents that exert similar functions through screening protocols that facilitate the *in vitro* evolution of nucleic acid molecules with non-biological functions. A technique known as Systematic Evolution of Ligands by EXponential enrichment (SELEX) has proven especially powerful in this context, enabling the isolation of synthetic nucleic acid-based 'aptamers' that can bind to a specific molecular target.[23,24] In one early demonstration of this approach, Szostak *et al.*[23] isolated RNA molecules that bind to anionic organic dyes using a random DNA library containing 10^{15} individual sequences. Each library molecule consisted of a 100-nucleotide random region flanked by primer binding sites and featuring a T7 RNA polymerase promoter. Prior to each selection round, the DNA library was transcribed to produce a random RNA library which was subjected to affinity chromatography for selection. The affinity column consisted of an organic dye covalently linked to agarose beads; RNA molecules with affinity for these dyes were retained on the column, whereas those with no affinity remained free in solution. Unbound RNA molecules were then washed away, while the bound RNA molecules were collected for subsequent reverse transcription and PCR

amplification, generating a new library for the next round of selection. The selection was repeated for 5–6 cycles, after which the pool was cloned and subjected to Sanger sequencing,[25] yielding RNA aptamers with micromolar binding affinity for selected organic dyes including Cibacron Blue 3GA, Reactive Red 120, Reactive Yellow 86, Reactive Brown 10, Reactive Green 19, and Reactive Blue 4.

Subsequent iterations of SELEX have introduced several changes to the selection procedure. Aptamers are typically isolated from random libraries of DNA, RNA, or synthetic nucleic acid molecules composed of a random nucleotide domain (typically 30–70 nt) flanked by PCR primer-binding sites. The library molecules can also be biased towards specific structures such as G-quadruplexes,[26] hairpin loops,[27] or three-way junctions[28] to expedite selection or impart additional functionalities onto the final aptamer. During the subsequent screening process, the amount of target available for binding can be reduced to create selection pressure for higher-affinity aptamers, or interfering molecules can be added to remove nonspecific aptamers.[29] The separation efficiency during the partitioning step has been shown to be critical to the isolation of high-quality aptamers. High-efficiency separation methods such as microfluidic separation[30,31] yield aptamers quickly (3–4 rounds) relative to low-efficiency separation methods such as nitrocellulose filtration (10–15 rounds).[24] Finally, the binders are PCR amplified to generate a new population of library molecules for the next round of selection. The selection process is repeated until the pool is enriched with target-binding aptamers, after which the pool is sequenced using sequencing techniques such as Sanger or high-throughput sequencing.

2.3. Advantages of aptamers over other biorecognition elements.

Aptamer isolation process is performed entirely *in vitro*, conferring several advantages to aptamers relative to conventional biorecognition elements such as antibodies.[32,33] For example, the ionic strength, pH, temperature, and solvent composition during the screening process can be precisely controlled to match the aptamer's final application. As such, aptamers can be isolated to function in physiological conditions for *in vivo* applications, or under non-physiological buffers and temperatures for *in vitro* diagnostics. In contrast, since antibodies are generated *in vivo*, their performance in different non-physiological conditions can be unpredictable and this may lead to loss of function.[32,33] Moreover, aptamers—particularly DNA aptamers—are chemically robust, remaining stable under mildly acidic or highly basic conditions, and their function can be recovered even after being exposed to highly denaturing environments (*e.g.*, chaotropic agents, high temperature, etc.). In contrast, the target-binding affinity of antibodies is nearly always lost after they have been denatured.[32,33] Additionally, aptamers can be chemically synthesized via solid-phase synthesis with a high degree of purity, resulting in little to no batch-to-batch variation, whereas antibodies collected from different batches of serum or hybridomas may have entirely different binding properties.[32,33] Moreover, the chemical synthesis process allows for the attachment of reporter molecules such as fluorescein and biotin at precise locations in the aptamer sequence.[32,33] Finally, the aptamer selection process can be controlled to favor aptamers with desired target affinity or specificity, whereas no such control is possible with *in vivo*-generated antibodies.[34]

2.4. Small-molecule-binding aptamer isolation.

The success of aptamer isolation is tied to the partitioning efficiency of target-bound library molecules from unbound library molecules. This step is particularly difficult for small-molecule-binding aptamers, as the formation of the target-aptamer complex results in very little change in the physicochemical properties of the target-bound library molecule relative to unbound library molecules.[35,36] As a result, most small-molecule aptamer isolation efforts rely on surface immobilization of the target[23] or library[28,37] to achieve physical separation of target-bound aptamers from unbound library molecules. These isolation strategies are referred to as target-immobilized and library-immobilized SELEX, respectively.

2.4.1. Target-immobilized SELEX.

The first examples of small-molecule-binding aptamer isolation were achieved with target-immobilized SELEX. This method requires the target to be covalently coupled to a solid support. Generally, this is done by using an activated solid support that possesses a good leaving group or other highly-reactive electrophile, which are susceptible to nucleophilic attack by the small-molecule target. Examples of activated solid supports employed during SELEX include N-hydroxysuccinimide-,[38] tosyl-,[39] epoxy-,[40] and dihydrazine-activated[41] magnetic beads or agarose beads/resins.[42] Coupling can also be done by combining the electrophilic group of a small-molecule target with a solid support containing a nucleophilic group—most commonly, a primary amine.

During target-immobilized SELEX, the library pool is first incubated with the unmodified solid support. Unbound library molecules remain free in solution whereas non-specific bead-binding library strands will generally bind to the solid support.[43] The

unbound library can then be collected with the aid of gravity flow, centrifugation, or magnetic separation.[43] This is a critical step in target-immobilized SELEX as it prevents the enrichment of bead-binding aptamers that can otherwise quickly come to dominate the pool and prevent identification of a target-specific aptamer.[43] The collected library molecules are then incubated with the target-modified support and subjected to several buffer washing steps to remove unbound or weakly-bound library molecules, after which the target-bound library molecules are eluted from the support via heat,[44] EDTA, oligonucleotide denaturants,[45] or any combination thereof[46] for subsequent PCR amplification. The specificity of the final aptamer can also be enhanced by including counter-selection steps. This is often done by including washing steps with buffer containing selected interferent molecules, a procedure known as counter-SELEX.[29]

Despite its widespread use, target-immobilized SELEX still faces many challenges. To begin with, immobilization of the target requires the formation of a covalent bond, which may require assistance from experienced chemists if the target is not compatible with well-established coupling chemistry.[47] For example, EDC–NHS coupling is frequently employed for small molecules that contain a primary amine or carboxylic acid functional group, where these form an amide bond with the solid support's carboxylic acid or primary amine functional group, respectively. However, this coupling strategy would not be ideal for small molecules which lack the necessary functional group, such as cannabinoids[48] or steroids.[49] Such scenarios may necessitate the design of custom coupling strategies or the synthesis of target analogs with desirable functional groups. The use of small-molecule functional groups also presents additional issues. For example, the exploitation of a small molecule's functional group for coupling removes a potential

interaction site for the aptamer.[50] Additionally, the coupling chemistry may create a novel functional group on the molecule that influences library binding such that the final selected aptamer exhibits weaker affinity for the free target in solution.[51]

2.4.2. Library-immobilized SELEX.

Library-immobilized SELEX provides an ideal alternative to target-immobilized SELEX, particularly for small-molecules with a limited number of functional groups.[52] During library-immobilized SELEX, a biotinylated complementary DNA strand (cDNA), is immobilized onto a streptavidin-modified solid support (typically magnetic beads or agarose beads/resin) via the high-affinity interaction between streptavidin and biotin (K_D = ~10^{-15} M).[53] These library molecules typically contain a constant region that forms a 15-bp duplex with the cDNA, effectively immobilizing them to the support via non-covalent interactions. Once the library has been immobilized onto the beads, they are washed with buffer to remove nonspecific library strands. Following the addition of the target, library strands that bind to the target with sufficient affinity displace the cDNA and elute from the support into solution, allowing for easy collection via magnetic separation, centrifugation, or gravity flow.[52]

Li *et al.*[54] were the first to demonstrate library-immobilized SELEX, using a library whose cDNA-binding region was incorporated between two 20-nt randomized domains. After 18 rounds of selection, they were able to enrich ATP- and GTP-binding aptamers. Importantly, they observed several sequences enriched with mutations or deletions at the cDNA-binding site; these most likely arose from polymerase error during PCR amplification. This is problematic, as it is likely to result in reduced cDNA-binding affinity, effectively reducing the energetic barrier[55] that target binding must overcome to elute a

sequence from the support, and thus undermining the overall stringency of selection. Stojanovic *et al.*[28] later improved on this work by directly incorporating the cDNA binding-domain into the PCR primer site. This simple design significantly reduces the opportunity for mutations to occur in the cDNA binding domain, as these sequences are chemically rather than enzymatically synthesized. This strategy has since been used to isolate aptamers with low nanomolar affinity for several small molecules with various physiochemical properties (*e.g.*, anionic,[56] cationic,[57] hydrophilic,[27] or hydrophobic[58] targets). Library-immobilized SELEX still faces two major challenges. First, since the immobilization of the library is noncovalent, nonspecific library sequences may also be collected upon addition of the target, resulting in co-enrichment of both target-specific and non-specific library strands during every round. This requires several washing steps to overcome, raising the risk of loss of high-quality aptamers—especially during early rounds of SELEX, when copy numbers are low. Additionally, the initial binding environment is confined to the solid surface, which may have different physiochemical conditions relative to the bulk solution or create steric hindrance that may be unfavorable for aptamer binding, resulting in the loss of potentially high-quality aptamers.

2.4.3. Homogeneous SELEX.

The ideal selection strategy allows for the target and library to interact freely in solution without restraints imposed by physical supports. These selection strategies are termed homogeneous SELEX, and there are only a few examples of such platforms for the isolation of small-molecule-binding aptamers. The first reported homogeneous SELEX technique was based on capillary electrophoresis separation, which utilizes the difference in mobility between unbound and target-bound library molecules under an external electric

field for partitioning. This technique was first pioneered by Bowser *et al.*, with a focus on protein targets such as human immunoglobulin E[59] and HIV-1 reverse transcriptase.[60] Capillary electrophoresis SELEX is ideal for protein targets, where binding causes a large shift in mobility. However, this technique has limited utility for small-molecule targets, where the mobility of target-aptamer complexes is very similar to that of unbound library molecules, resulting in poor separation efficiency. To date, the only small-molecule target for which this technique has been successfully employed is N-methyl mesoporphyrin, for which an aptamer was obtained after three rounds of selection.[61]

Graphene oxide-based SELEX has demonstrated great potential as a homogeneous SELEX platform for small-molecule targets.[62,63] This technique achieves partitioning of binders from nonbinders in solution via the preferential binding of graphene oxide to single-stranded DNA over folded DNA structures.[64] Strands that bind to the target will fold into a duplexed structure that resists adsorption onto the graphene oxide surface, such that unbound single-stranded library molecules can rapidly be collected and removed via centrifugation. This technique has been used to obtain DNA aptamers against several pesticides and toxins within 5–10 rounds of selection.[65,66] However, it does not allow for the use of structured libraries, requiring laborious post-SELEX optimization to generate structure-switching aptamers for use in biosensing platforms. Moreover, the incorporation of counter-SELEX only makes the technique partially homogeneous.[62,63,65,66] During counter SELEX, the library is allowed to interact with interferent molecules free in solution. Specific library molecules remain in a single-stranded state and are capture by the graphene oxide while non-specific library strands are removed by centrifugation and removal of the supernatant. As a result, target-binding library strands are immobilized on

graphene oxide and eluted by affinity-based desorption with the target, a process which mimics heterogenous SELX platforms. Given the importance of aptamer specificity for detection of the target in complex matrices which contain the interferent molecule, the target-binding portion of this selection platform will generally mimic a heterogenous selection platform rather than a homogeneous one.

Recently, a homogenous SELEX platform which employs restriction endonucleases, termed RE-SELEX,[67] has been reported. The library design for RE-SELEX mimics that of library-immobilized SELEX, but with the addition of an EcoRI restriction site in the cDNA-binding domain.[68] Digestion by EcoRI results in loss of the forward primer binding site, preventing exponential amplification during PCR. However, library molecules that bind to the target with sufficient affinity to displace the cDNA will disrupt the recognition site, preventing digestion by EcoRI. These intact library strands can be exponentially amplified during PCR and should outnumber the undigested library after sufficient rounds of amplification. This difference in PCR amplification efficiency forms the basis of partitioning between binders and non-binders and does not require any physical separation steps. Thus far this technique has been used to isolate an aptamer against kanamycin—albeit with questionable success, as the binding domain of the aptamer was determined to include the forward primer-binding site along with four nucleotides of the randomized domain.[67]

2.5. High-throughput sequencing of enriched pools.

The aptamer isolation process yields a library pool enriched with sequences that bind to the target. Bacterial cloning, wherein aptamer sequences are incorporated into vectors that are infected into *E. coli*, combined with Sanger sequencing of individually-

picked clones is the classical aptamer identification method.[25] Due to the limited throughput of Sanger sequencing, only 30–100 clones are typically selected. This requires the final pool to be highly enriched, as otherwise no dominating sequence may be observed. Today, high-throughput sequencing (HTS) technologies allow for the simultaneous analysis of millions to billions of candidate aptamer sequences.[69] Due to the high number of reads and multiplexing capability, HTS can feasibly be done for each round of selection, allowing for the monitoring of dynamic sequence changes between rounds. The first demonstration of the utility of HTS for aptamer sequencing was by *Soh et al.*[69] in 2010, during selection of an aptamer for the platelet-derived growth factor BB protein. Three rounds of microfluidic device-assisted selection were performed, and each enriched pool was subjected to HTS. More than 10^7 sequences were obtained for each pool, enabling determination of the population growth, or 'enrichment-fold', of each sequence between rounds. The three most abundant aptamers in the final pool were compared to the top three sequences based on enrichment-fold, and it was discovered that the aptamers with highest affinity and specificity all came from the high enrichment-fold category. The ability to identify aptamers using enrichment-fold requires the use of HTS, as Sanger sequencing is limited to only 50–100 sequences. Other groups have attempted to employ enrichment-fold as a predictor of an aptamer candidate's success but with mixed results. A hallmark study by *Glökler et al.*[70] revealed that this may be linked to the number of rounds of selection performed, where the performance of aptamers from rapid selections (3–4 rounds) is closely tied to enrichment-fold, whereas this relationships is minimal for aptamers identified from lengthier selections (>5 rounds). This is presumably due to the increased cycles of PCR performed in lengthier selection processes; this introduces PCR

amplification bias based on the polymerase enzyme's preferences with regard to nucleotide composition and secondary structure.[71–73] To date, no single factor has been identified that can consistently successfully predict an aptamer candidate's performance independent of the total of selection rounds performed.

2.6. Characterization of aptamer candidates.

Thorough characterization of the selected aptamer candidates is a critical aspect of aptamer development. Even carefully designed selections can yield candidates with little-to-no target-binding affinity. This is primarily due to three reasons. First, differences in the experimental conditions used during the intended application of the aptamer relative to those used in the selection process may result in loss of binding.[74,75] For example, aptamers isolated using target-immobilized beads may experience complete loss of binding for the free target.[51] Second, aptamer representation in the final pool does not solely depend on an aptamer's affinity, but also its PCR amplification efficiency.[71,72] Thus, the sequence's final population or degree of enrichment does not necessarily reflect its binding performance. Finally, the primer-binding regions of the library molecules are often truncated after selection, and in certain cases these may be necessary for stabilizing the aptamer structure.[76] More recently, several groups have developed more sophisticated characterization methodologies using specialized instrumentation, competition-based assays, or target-based properties.

2.6.1. Instrument-based approaches.

These methods directly measure the thermodynamic or kinetic properties of aptamer-ligand interactions. Although they are incredibly accurate and provide extensive information, they are generally limited by their cost and sample throughput.

2.6.1.1. Isothermal titration calorimetry (ITC).

ITC allows for the determination of thermodynamic properties of small-molecule-binding aptamers that cannot be easily measured by other means.[77,78] During a typical ITC experiment, the ligand is repeatedly injected into a sample cell containing the aptamer until all binding sites are saturated. Each injection results in a release in heat, which is the concatenation of aptamer-ligand binding events, dilution of the ligand, and stirring of the cell. This heat is then subtracted from the heat generated by the same titration into a cell that does not contain the aptamer. A binding curve is then constructed using the heat measured after each titration, and this allows for the determination of the aptamer's dissociation constant (K_D), stoichiometry, and enthalpy (ΔH) of binding. From these measurements, the Gibbs free energy (ΔG) and entropy (ΔS) can then be extrapolated.[79] A major advantage of ITC is that there is no need for aptamer labeling. Moreover, the technique is compatible with various measurement temperatures (4–80 °C) and buffer compositions (*e.g.*, pH, salts, organic co-solvents). However, ITC experiments require high aptamer and target concentrations, which may be a limitation in terms of cost or solubility.

2.6.1.2. Microscale thermophoresis (MST).

MST relies on measuring the change in an aptamer's thermophoretic properties.[80] Thermophoresis describes the movement of molecules through a temperature gradient, a property that depends on its size, charge, and hydration shell.[81,82] Upon binding to a small-molecule target, one of these properties is expected to change, resulting in altered thermophoretic movement in unbound versus bound aptamers. To perform this assay, either the aptamer or the target must be fluorescent or labeled so that their movement can be monitored. After allowing the aptamer and its target to reach binding equilibrium, the

solution is loaded into a capillary tube and the fluorescence in a small area of the tube is continuously monitored. An infrared laser is then used to heat the monitored area, causing the fluorescence in the heated area to diffuse away, resulting in a reduction of fluorescence that is proportional to the formation of the aptamer–target complex. The concentration of the fluorescent molecule is kept constant, while the partner molecule is varied over a large concentration range. A binding-isotherm can be fitted based on the fluorescence change after heating versus the concentration of unlabeled aptamer or target to determine K_D.[83] Although this technique provides limited information, it is the only instrument that can directly measure aptamer binding affinity in complex biological matrices such as whole blood.[84]

2.6.1.3. Surface plasmon resonance (SPR) spectroscopy.

SPR spectroscopy has become the gold standard technique for the characterization of protein–aptamer interactions.[85] This technique monitors the change in refractive index caused by ligand-binding events occurring on a gold sensor surface in real time. It can provide information on an aptamer's kinetic and thermodynamic properties, but is hindered by the need to immobilize the aptamer[86] or target[87] onto the gold surface. Immobilization of the aptamer can hinder its target binding, resulting in a different affinity then would be observed in solution. Moreover, there are few examples of SPR spectroscopy being applied to small-molecule-binding aptamers, as the change in refractive index produced by small-molecule binding events is far smaller than for proteins.

2.6.2. Assay-based approaches.

The high cost and general low throughput of the instrument-based approaches described above makes thorough characterization of large numbers of aptamer candidates

nearly impossible. As such, these specialized techniques are typically reserved for the top aptamer identified in a given pool of candidates. This is typically achieved using various assays, which can generally be categorized as cDNA-based competition assays, target property-based assays, and bead-based competition assays.

2.6.2.1. cDNA-based competition assays.

cDNA-based competition assays offer a reliable and accurate method to measure the affinity and specificity of small-molecule binding aptamers. This method relies on target-induced displacement of a cDNA stand that is initially hybridized to a constant region adjacent to the target-binding domain of the aptamer.[27] The K_D for the target is calculated by determining the affinity between the aptamer and cDNA (K_{D1}), followed by the affinity of the target for the aptamer–cDNA complex (K_{D2}). The K_D is equal to the ratio of K_{D1}/K_{D2}.[88] The thermodynamic basis of this method was first established by Easley and Hu,[88] using microchip electrophoresis to assess aptamer–cDNA binding and was later adapted by Stojanovic *et al.* using a fluorescence-based approach.[27] Their widely-used approach employs a quencher-modified cDNA and fluorophore-modified aptamer. Hybridization of these two strands brings the fluorophore and quencher into close proximity, resulting in reduced fluorescence; this fluorescence can then be recovered upon target-induced displacement of the cDNA.[27,56,57] The cDNA-based competition assay is simple, rapid, and accurate, and can be used to screen the cross-reactivity of an aptamer towards numerous targets. However, this method may involve some trial-and-error to identify a suitable cDNA length that can be efficiently displaced by target binding.[55] Additionally, certain ligands have been found to affect the optical properties of the fluorophore or quencher, requiring carefully designed control experiments.[89]

2.6.2.2. Target-based approaches.

Aptamer binding can result in a change in the optical properties of certain small-molecule targets. This means that a binding isotherm can be generated by recording the changes in absorbance,[90] fluorescence,[91,92] or fluorescence polarization[93] of the small molecule as a function of the aptamer concentration. This method is easily applied to DNA-binding dyes with strong optical properties in the visible light range,[94,95] but is much more challenging for small molecules that lack absorbance or fluorescence signatures in the visible light range.

2.6.2.3. Bead-based competition assays.

Bead-based assays utilize physical separation to quantify the fraction of bound aptamers over a range of target concentrations.[23] The target is immobilized onto a solid support (typically magnetic beads or agarose beads/resins) via an appropriately chosen coupling reaction.[96,97] This method is most often employed for aptamers isolated via target-immobilized SELEX, with a coupling method that mimics what was used during selection. Next, fluorescent- or P^{32}- labeled aptamers are incubated with various concentrations of the target-immobilized beads. Unbound aptamers are removed by washing with buffer, after which the bead-bound aptamers are collected by applying mildly denaturing conditions (*e.g.* heat, urea, EDTA, or a combination thereof) and the collected aptamers are quantified. Alternative approaches have also employed PCR prior to measurement to improve the detection limit of the assay. The amount of target immobilized onto the beads can be quantified via UV absorption, and the half saturation point ($K_{1/2}$) can be measured by constructing a calibration curve of target concentration versus collected aptamer signal. Importantly, the $K_{1/2}$ of the assay can provide information about each aptamer's relative

affinity for the target. However, the relative affinities obtained from this assay do not necessarily reflect the binding affinity of the aptamer for free target. Additionally, it can be challenging to screen aptamer specificity against interferent molecules that may not be compatible with the same immobilization chemistry, which thus requires competition between the free interferent molecule and bead-immobilized target.[48,98]

2.7. Post-engineering of small-molecule-binding aptamers.

Occasionally, SELEX fails to yield aptamers with suitable affinity and specificity for an intended application, and this can be attributed to a variety of reasons. First, since starting oligonucleotide libraries encompass anywhere from 10^{18} to 10^{40} possible unique sequences (for libraries containing 30–70 random nucleotides), it is unrealistic to include every possible sequence in a SELEX experiment, which inevitably excludes high-quality aptamer candidates.[73] Second, given that most sequences are initially present as just a single copy in the starting library, oligonucleotides with desirable binding properties can spontaneously be lost during washing steps in the early rounds of SELEX. Finally, the best aptamer candidates can be outcompeted by weaker sequences if they have low PCR amplification efficiency due to their sequence and/or structure.[99–101]

Several strategies have been developed to improve the binding affinity or specificity of aptamers isolated by SELEX. These methods focus on exploring the surrounding sequence space of the isolated aptamer to identify mutants with enhanced binding properties. These mutants are typically identified by reselection using an aptamer sequence-doped library (termed 'doped-SELEX')[102] or by mass synthesis and screening of several aptamer mutants.[103] During doped-SELEX, a sequence with known binding affinity to the desired target is used as a template for a new doped library. The first example of

doped selection was done by Szostak *et al.*[102] using a mutagenized library based on the Rev-responsive element of the HIV genome. Each base from the random domain in a given library molecule had a 65% chance of being the wild-type base, 30% chance of being another base, and 5% chance of being deleted. This pool contained the original sequence as well as single, double, triple, and higher-order mutants that may have improved binding affinity or specificity. This mutagenized library was used to isolate a Rev protein-binding aptamer mutant. The final mutant possessed two mutations relative to the wild-type sequence, and demonstrated 2.4-fold greater binding to the Rev protein. Famulok *et al.*[40] later employed a doped-SELEX approach with a similar pool design to modify the specificity of an L-citrulline-binding aptamer so that it bound to L-arginine. The final aptamer possessed micromolar affinity for L-arginine with no binding-affinity for L-citrulline. There are few examples to date of successful doped selections for small molecules, and the extent of improvement in binding performance is typically modest.[98,104,105] This is primarily attributable to the fact that each mutant is not being represented equally: doped libraries are greatly biased towards the parent sequence, with the abundance of each mutant diminishing as more mutations are incorporated into the sequence.[106]

Mass synthesis and individual testing of aptamer mutants provides a less biased and more accurate approach for identifying the best mutant. However, the lack of high-throughput screening techniques for aptamer characterization limits this procedure to only a handful of aptamer mutant. As such, the mutants must be intelligently designed to eliminate oligonucleotides that lack binding affinity. This is often done with guidance from genetic algorithms,[107] computationally-predicted secondary structures,[108,109] or 3D

structures[110,111] in order to selectively mutate nucleotides located either in the target-binding domain[109,112] or surrounding scaffold regions.[103,108,110] With the aid of 2D-nuclear magnetic resonance (NMR) experiments, Liu *et al.*[110] were able to improve the binding affinity of an ochratoxin A-binding aptamer by 50-fold via strategically-designed base mutations and insertions. This method eliminates the population bias associated with doped-SELEX but is ultimately reliant on the use of data to guide mutagenesis. In the absence of an 3D aptamer structure, it may be necessary to screen hundreds or thousands of mutants to achieve significant improvements in affinity or specificity, creating high costs in terms of time and money.

2.8. Small-molecule aptamer-based sensors.

Many signal transduction strategies have been developed that enable aptamer-based sensors to generate optical, electrochemical, or electrical readouts in response to target binding.

2.8.1. Structure-switching aptamer-based sensors.

To achieve aptamer-based sensing, the aptamer-target binding event must generate a measurable signal. Many sensors rely on aptamers with structure-switching functionality that undergo a large conformational change upon binding to the target, and thereby produce a change in absorbance, fluorescence, or electrochemical signal.[113] This functionality can be introduced by truncating the primary stem of the aptamer, such that it exists in an unfolded state at room temperature but refolds into its native state in the presence of its target, forming a target-aptamer complex.[114] Each end of the aptamer can be modified with a signal reporter that produces an optical[114,115] or electrochemical signal[116,117] upon undergoing a target-induced conformational change. The first example[114] of such a small-

molecule biosensor employed a cocaine-binding aptamer that had been modified with fluorescein and dabcyl at its 5'- and 3'-ends, respectively. In the absence of the target, the aptamer was unfolded, producing a strong fluorescent signal. Cocaine-binding stabilized the aptamer, bringing its ends into close proximity and resulting in concentration-dependent quenching of the fluorophore. This simple sensing strategy has been successfully applied to a variety of other small-molecule aptamers as well.[118,119]

Electrochemical aptamer-based (E-AB) sensors are another standard format for aptamer-based sensors.[116] These sensors are capable of real-time, interferent-free detection of small-molecule targets in complex matrices.[117,120] These sensors utilize structure-switching aptamers modified with a thiol group at one end and a methylene blue redox tag at the other. The thiol group allows the aptamer to be immobilized onto a gold electrode surface via thiol-gold chemistry, whereas the redox tag produces a measurable current dependent on its distance from the electrode surface. Plaxco *et al.*[117] were the first to demonstrate detection of cocaine in bulk powders using an E-AB sensor constructed from a structure-switching aptamer. In the absence of target, the unfolded aptamer orients the redox reporter away from the electrode surface, resulting in low background current. However, in the presence of cocaine, the aptamer folds into a duplexed state, bringing the redox reporter close to the surface and producing a large increase in measured current. This sensor platform has since been used to detect a variety of small molecules with various physiochemical properties in biological samples.[121–123]

Despite their conceptual simplicity, the engineering of a structure-switching aptamer can be challenging. Most SELEX experiments use unstructured libraries, yielding aptamers with unpredictable binding domains that seldom possess structure-switching

functionality.[54] Thus, additional engineering steps are required to introduce such functionality into the aptamer. First, the binding domain of the aptamer is identified, after which the primary stem is systematically truncated to identify a minimal aptamer sequence that can undergo a large target-induced conformational change.[124,125] This trial-and-error process is labor-intensive and costly, and often results in aptamers with significantly reduced affinity relative to their parent aptamers.[124]

2.8.2. Split aptamer-based sensors.

Splitting aptamers into fragments is an alternative to conventional structure-switching aptamers.[126] By cutting single-stranded loops in an aptamer's structure, one can obtain two[127] or three[128] fragments that are thermodynamically unstable on their own at room temperature, but which reassemble in the presence of the target to form a stabilized target-bound complex. Reporting of target-binding events can be achieved by labeling aptamer fragments with small-molecule reporters[127,128] or enzyme fragments[129] that generate an electronic,[130] fluorescent,[127] or colorimetric[128] signal upon assembly. Successful splitting requires prior knowledge of the binding domain and is most feasible with aptamers that have predictable secondary structures with well-defined stems, such as three-way-junction structured aptamers.[131] Split aptamers can still be generated from parent molecules with greater structural complexity, such as G-quadruplexes[98] and triplexes,[132] although this generally requires more trial-and-error testing.

One general advantage that split aptamers have over traditional structure-switching aptamers is incredibly low background signal. This has been showcased by Zuo *et al.*,[133] who utilized split aptamers for the detection of small-molecule targets in blood and crude cell lysates. They modified one fragment with a thiol group to facilitate immobilization

onto a gold electrode surface and modified the second fragment with a methylene blue redox tag. The presence of the target promoted the assembly of the aptamer fragments on the surface of the gold electrode, bringing methylene blue close to the surface and resulting in a large increase in measured current. The minimal self-assembly of the fragments in the absence of the target yielded negligible background current, resulting in large signal gains in the presence of target, even in complex matrices. The authors were able to detect cocaine and ATP in blood and crude cell lysates, respectively, albeit with moderate detection limits of 1 μM. This limited sensitivity is a consequence of the large disruption in target-binding affinity—typically 10–100-fold[127,134,135]—that aptamers experience when split. To overcome this issue, Yu *et al.*[136] has developed cooperative-binding split aptamers (CBSA), in which incorporate two sequential target-binding domains into a split aptamer which are separated by a short nucleotide stem. The initial target-binding event assembles one binding pocket as well as the connecting stem, and this in turn stabilizes the second binding domain, facilitating subsequent binding of a second target with greater binding affinity. This 'positive cooperativity'[137] effect is responsible for improving the target responsiveness of CBSAs at low target concentrations relative to traditional split aptamers. Yu *et al.*[136] constructed a cocaine sensor by modifying one of the CBSA strands with a fluorophore and quencher at its ends. Due to the flexibility of the single-stranded fragment, the fluorophore and quencher remain in relatively close proximity, quenching its fluorescence. The addition of target facilitates the assembly of the full CBSA, physically separating the fluorophore and quencher and producing a fluorescence signal. This CBSA format was able to detect 50 nM cocaine in 10% saliva, which is far more sensitive than conventional split-aptamer-based sensors. To date, CBSAs have been constructed from

cocaine-,[136,138–140] 3,4-methylenedioxypyrovalerone (MDPV)-,[140] and dehydroepiandrosterone-3-sulfate (DIS)[138]-binding aptamers, all of which possess three-way-junction structures. However, there remains a need for strategies to engineer CBSAs from aptamers with more complex secondary structures.

2.8.3. cDNA displacement sensors.

Strand displacement-based sensors provide an alternative approach for generating large target-induced conformational changes without the need for engineering structure-switching or split aptamers.[141] These strategies utilize a short cDNA strand, which is complementary to and forms a stable duplex with the aptamer in the absence of the target. In the presence of the target, the aptamer undergoes a conformational change that displaces the cDNA, and this can be transduced into a measurable signal by modifying the aptamer and cDNA with reporters. The earliest example of such a sensor was described by Nutiu *et al.*,[142] who utilized an ATP-binding aptamer hybridized to two different cDNAs. The first cDNA was labeled with a fluorophore, and did not overlap with the aptamer's target-binding domain. As a result, target-binding events should not displace this cDNA. The second cDNA was modified with a quencher and overlapped with the aptamer domain, allowing for displacement in the presence of the target. In the absence of ATP, both cDNAs were hybridized to the aptamer, bringing the fluorophore and quencher into close proximity and resulting in a low fluorescence signal. Upon binding to ATP, the aptamer displaces the quencher-modified strand, resulting in a target-dependent fluorescence increase. Although this assay does not require aptamer engineering, the cDNA length, incorporation of mismatches, and choice of hybridized nucleotides in the aptamer domain are all critical to the assay's performance and require careful optimization.[105] This was demonstrated by

Munzar *et al*.,[55] who studied the binding dynamics of strand-displacement assays using hundreds of cDNAs of varying lengths, hybridization locations, and mismatched bases, which were immobilized as separate features on a DNA microarray. The array was then incubated with fluorophore-modified aptamer, enabling simultaneous monitoring of the hybridization and subsequent target-induced displacement of each cDNA. Based on this assay, the optimal cDNA length as well as critical nucleotides for initial target-binding could be identified. Alternatively, isolating aptamers via library-immobilized SELEX bypasses the need for trial-and-error testing or massive screening, as the final aptamer has already been evolved to readily displace the cDNA employed during selection.[28,37]

2.8.4. Aptamer beacon-based sensors.

Displacement-based sensors typically require long cDNA sequences to achieve stable hybridization and maintain a low background signal, and this can make optimization challenging given the length of the overlapping region in the original aptamer. Tang *et al.*[143] greatly reduced the length of the cDNA required by using a molecular beacon-style design that exploits intramolecular displacement, in which the cDNA competitor is physically coupled to the aptamer via a PEG linker. This 'aptamer-switch probe' construct consists of three sections: a fluorophore-modified aptamer domain, a quencher-modified cDNA domain, and the linker connecting the two. In the absence of target, the short cDNA hybridizes with a small section of the aptamer, quenching the aptamer's fluorescence signal. Target binding causes the aptamer to undergo a large conformational change, displacing the short cDNA and recovering the fluorescence. Tang *et al.*[143] constructed an aptamer-switch probe using the ATP-binding aptamer that achieved a measurable detection limit of 10 μM. Although they did not observe improved sensitivity compared to traditional

strand displacement-based sensors,[142] aptamer-switch probes can achieve maximal signal within seconds as opposed to hours. Moreover, additional sensing functionality can be incorporated by modifying the PEG linker. For example, Thompson *et al.*[144] replaced the PEG linker with a pH-responsive cytosine-rich i-motif.[145] At pH < 6.5, the linker domain adopts a structure that imposes steric hindrance on the cDNA domain, facilitating displacement by the target. However, at pH >7, the i-motif instead adopts a hairpin structure that stabilizes the cDNA domain, requiring a ~100-fold greater concentration of target to achieve the same degree of strand displacement relative to low pH.

2.8.5. Fully-folded aptamer based sensors.

The sensitivity of structure-switching, split aptamer, and strand-displacement sensors ultimately suffer from impaired aptamer binding affinity due to destabilization of the aptamer's structure[103,124] or competition with high-affinity cDNAs[142] (with nM K_D). Dye-displacement assays[146] offer an appealing alternative for two reasons. First, they do not require truncation or splitting, and instead utilize aptamers in their native, high-affinity state.[108] Second, they rely on small-molecule dyes that compete with the target at the aptamer's binding domain. These dyes bind with significantly reduced affinity (μM K_D) relative to cDNAs,[147] allowing for facile displacement by the target. Aptamer binding events are then reported by a change in the absorbance or fluorescence properties of the dye as a consequence of the change in its physiochemical environment.[148,149] These assays are highly effective, as they are label-free, simple, sensitive, and have rapid turnaround times, but they are generally hindered by the limited compatibility between dyes and different aptamer structures. Stojanovic and Landry[146] described the first aptamer-based dye-displacement assay, using a cocaine-binding aptamer and the cyanine dye

diethylthiotricarbocyanine iodide (Cy7). In aqueous solution, Cy7 exists mainly as a dimer with peak absorbance at 670 nm. However, the authors showed that Cy7 preferentially binds to the binding domain of a three-way-junction structured cocaine-binding aptamer in its monomeric form, which has peak absorbance at 760 nm. Bound Cy7 monomers could be displaced by cocaine, resulting in a decrease in the monomer peak that yielded a measurable detection limit of 0.5 μM cocaine. However, Cy7 was only identified as a suitable dye after screening 35 dyes for their compatibility with dye-displacement sensors. Another study by the Stojanovic[149] group tested the applicability of the dye thiazole orange with various DNA and RNA aptamers for construction of a dye-displacement sensor, and found that only eight of the 19 tested aptamers were compatible with this dye. These results suggest that not every dye can be used for dye-displacement-based sensors, and that a given dye may not be compatible with all aptamers. Importantly, the ratio of dye to aptamer was not explored in these studies. Recent work by Alkhamis *et al.*[147] has demonstrated that the DNA-to-dye ratio is critical to the potential performance of a dye-displacement assay. Specifically, they demonstrated that different aptamers have varying affinity for the dyes Cy7 and 3,3'-di(3-sulfopropyl)-4,5,4',5'-dibenzo-9-methyl-thiacarbocyanine (MTC).[150] As such, optimization of the DNA-to-dye ratio was required to reach an appropriate equilibrium of complexed dye that could be displaced upon target binding. Of the 12 aptamer/dye pairs tested, three had low displacement efficiency (~30%); however, all sensors were able to achieve reproducible detection of their respective targets. These results demonstrate that dye displacement assays may be generalizable after empirical optimization of the sensor.

Aptamer-immobilized field effect transistors (FETs) offer an alternative approach to the construction of fully-folded aptamer sensors. FETs are composed of an electron source and electron drain separated by a semiconductor layer. These sensors are incredibly sensitive to local conductivity changes imposed by charged small molecules that approach the semiconductor surface.[151] However, FETs face two major challenges. First, high ionic strength solutions limit the sensing distance to < 1 nm at physiological conditions.[152] Second, the approach of small molecules that have little or no charge has little effect on the semiconductor and thus produces minimal sensor response.[153] To overcome these obstacles, Nakatsuka *et al.*[57] immobilized aptamers onto a semiconductor surface. Given the high anionic charge of the aptamer backbone and its proximity to the surface, the FET becomes highly sensitive to minor conformational changes in the aptamer. Upon constructing FET sensors with immobilized dopamine and serotonin aptamers, they were able to achieve detection of 10 fM concentrations of their respective target in artificial cerebrospinal fluid.[57] This is particularly impressive given that these detection limits are ~1,000,000-fold lower than the binding affinities of the receptors (30–150 nM). Similar sensors constructed using a glucose aptamer also achieved impressive detection limits of 10 μM concentrations in diluted mouse blood, which is 1,000-fold below the aptamer's K_D.[57] Although structure-switching functionality did not need to be engineered into these aptamers, the sensor response was strongly affected by the distance of the aptamer binding domain from the surface, and required minor truncation of the aptamer stem to achieve a robust target response.[57] Moreover, the generality of this approach still needs to be demonstrated for other aptamer-ligand pairs.[154,155]

2.9. Enzyme-based aptamer characterization, engineering, and sensing.

2.9.1. Exonuclease-based affinity characterization.

The increased availability and affordability of HTS has opened new possibilities for aptamer selection. HTS allows selection to be completed in far fewer rounds, yielding thousands of possible aptamer candidates—and this in turn introduces new challenges in terms of characterizing the affinity and specificity of so many aptamer candidates. Alkhamis *et al.*[89] developed a high-throughput label-free exonuclease-based assay for profiling aptamer binding properties. This strategy relies on the discovery that aptamer digestion by T5 exonuclease (T5 Exo), a 5'-to-3' single- and double-stranded DNA exonuclease with single-stranded endonuclease and 5'-flap endonuclease activities,[156–158] is inhibited by small-molecule binding, where the degree of inhibition is proportional to the aptamer's affinity for the small-molecule ligand.[89] They determined that T5 Exo digests unbound aptamers into a single-stranded product, which can then be digested by exonuclease I (Exo I) into mononucleotides.[159] In contrast, the T5-truncated, target-bound aptamer inhibits further digestion by both exonucleases, and these intact oligonucleotides can then be quantified using the DNA-binding dye, SYBR Gold. Using this assay, Alkhamis *et al.*[89] profiled the affinity and specificity of ATP-,[98] MDPV-,[160] and several mephedrone-binding aptamers [89] with various secondary structures.

2.9.2. Nuclease-based footprinting and aptamer engineering.

Exonucleases are enzymes that digest nucleic acids from either the 3'-end (such as Exonuclease III)[161] or 5'-end (such as T7 exonuclease)[162] in a double- or single-stranded specific manner, whereas endonucleases digest internal nucleic acid regions in a sequence-dependent (such as EcoRI)[68] or -independent (such as deoxyribonuclease I)[163] manner.

These enzymes are further subcategorized as deoxyribonucleases and ribonucleases, which have activity on DNA and RNA, respectively. A pioneering study by Galas and Schmitz[164] revealed that protein-bound DNA nucleotides are protected from cleavage by deoxyribonuclease I (DNase I)[163], an enzyme that induces phosphodiester bond cleavage at random positions on DNA duplexes. By optimizing the DNAse I concentration, they were able to control the digestion of 5'-P^{32} labeled DNA molecules so that each DNA molecule is cut only once. In the absence of DNA-binding protein, polyacrylamide gel electrophoresis analysis of the digested sample revealed truncated fragments spanning the entirety of the molecule. In contrast, protein binding to the duplex protects interacting nucleotides from cleavage by DNase I, resulting in an absence of digested fragments in the region containing the protein-binding sequence.[164] Since then, several studies have revealed that this same phenomenon also holds true for minor-groove-binding small molecules such as actinomycin, chromomycin, and distamycin.[165]

A similar mechanism has been observed with exonuclease III (Exo III). Exo III induces phosphodiester bond cleavage at the 3'-end of double-stranded DNA, progressively releasing mononucleotides until the duplex is completely digested or only single-stranded DNA remains. However, in the presence of a minor-groove-binding adduct, Exo III digestion is inhibited 3–4 bases prior to the binding site, resulting in a clearly truncated strand that can be visualized using polyacrylamide gel electrophoresis.[166,167] Since Exo III digestion occurs in a single direction rather than randomly across the duplex, this Exo III assay does not require optimization of the enzyme concentration to generate single-nucleotide cleavage fragments, making its application

much simpler. This assay has been demonstrated for footprinting the binding of saframycin A, saframycin S, saframycin MX1, DAPI, Hoechst 33258, and distamycin A.[168,169]

Exo III-based footprinting has since been extended to non-minor-groove-binding small molecules. Wang *et al.*[170] recently discovered that Exo III-mediated digestion of small-molecule-binding aptamers is inhibited in the vicinity of the target-binding domain. Specifically, they found that digestion of a three-way-junction structured cocaine-binding aptamer and stem-loop-structured ATP-binding aptamer yields a truncated product 3–4 bases prior to the binding domain. The structural properties of the inhibition product were probed using Exo I, which catalyzes the consecutive cleavage of mononucleotides from the 3'-end of single-stranded DNA. They observed that the chemically-synthesized cocaine and ATP aptamer inhibition products were completely digested by Exo I, indicating that the unbound aptamer exists in predominantly single-stranded state.[170] However, digestion of these same aptamer byproducts was greatly inhibited in the presence of their respective targets, indicating that it has folded into a double-stranded target-bound state. These results suggest that the inhibition products produced by Exo III possesses structure-switching functionality which is a critical component of several aptamer-based sensor platforms such as E-AB sensors and fluorophore-quencher assays.[170] Indeed, these enzyme-truncated inhibition products are directly compatible with both of these assay formats. This single-step truncation strategy based on Exo III thus provides an ideal alternative to the traditional trial-and-error process of incorporating structure-switching functionality into recently isolated aptamers.

2.9.3. Nuclease-based sensing.

2.9.3.1. Nuclease-based signal amplification.

Traditional aptamer-based sensor platforms rely on a single receptor producing a single signal upon target binding. These methods are straightforward, but generally not sensitive enough for real-world detection applications in which targets may be present at ultra-low concentrations.[113] To remedy this issue, several groups have attempted to combine nucleases and polymerases to achieve ultra-sensitive detection of small-molecule targets.[171] Specifically, a nuclease is employed to generate a nicked or intact oligonucleotide with a free 3'-end, which is then extended by a polymerase to generate a multitude of signaling strands from each single target-binding event.[171] One such strategy developed by Shlyahovsky *et al.*,[172] termed nicking enzyme signal amplification (NESA), uses the nicking endonuclease Nt.BbvC I[173] in combination with the Klenow polymerase[174] fragment for amplification. Specifically, they modified the 5'-end of a cocaine-binding aptamer to contain a partial Nt.BbvC I recognition site, which acts as a template for polymerase extension of the aptamer's 3' end when the sequence is fully folded. The cocaine aptamer was then hybridized to a cDNA that blocks this 3' extension in the absence of target. But when the aptamer binds to cocaine, the cDNA is displaced, creating a duplexed 3'-end that can then be extended by the polymerase to complete the Nt.BbC I recognition site. Nt.BbvC I cleavage results in a new 3'-end which can again be used for polymerase extension, displacing the nicked strand, and resulting in a continuous cycle of isothermal polymerase extension and strand displacement. The nicked strands are then measured using sequence-specific molecular beacons. This assay achieved a detection limit of 5 μM cocaine,[172] and the use of strand displacement as a NESA initiator may have been

a severe limiting factor, as the binding of the cDNA to the aptamer is significantly stronger (nM K_D) than that of cocaine to the aptamer (μM K_D)[103]. Additional downstream signal amplification can improve the sensitivity of these strand-displacement-mediated NESA assays. For example, Wang *et al.*[175] improved on the previously described sensor by modifying the released signaling DNA sequence into a Mg^{2+}-dependent DNAzyme, which catalyzed the cleavage of linear beacon probes to produce a fluorescence signal. The addition of this downstream amplification strategy resulted in an impressive 50-fold reduction in the detection limit to 0.1 μM, albeit at the cost of increased assay time (12 hours).[175]

Leung *et al.*[176] developed an alternative nuclease-based signal amplification strategy using Exo I to distinguish target-binding events for structure-switching aptamers, along with deoxynucleotidyl transferase (TdT)[177] to amplify the resulting intact oligonucleotides. During this assay, unbound aptamers exist in a single-stranded state and are rapidly digested by Exo I, whereas target-bound aptamers fold into double-stranded state that resists digestion and remains intact. The 3'-ends of these target-bound aptamers are then extended by TdT, which adds deoxyguanosine and deoxyadenosine to the 3'-end of the intact oligonucleotide in a template-independent manner. The final amplified sequence possesses several G-quadruplexes, which are specifically detected using an Ir(III) complex-based dye, resulting a detection limit of 0.5 μM for cocaine, which is 10-fold lower than a similar Exo I assay that does not utilize TdT amplification.[178]

2.9.3.2. Enzyme-assisted target recycling.

An alternative approach to enhancing the sensitivity of aptamer-based assays relies on 'recycling' the target to increase the number of binding events generated by a single

target.[179] In such enzyme-assisted target recycling (EATR) assays,[180] target-bound aptamers are specifically digested by a nuclease, degrading the aptamer and releasing the target back into solution. The target then binds to another aptamer and facilitates its digestion by the nuclease. This process allows more target-binding events to occur, effectively amplifying the signal generated by each small-molecule analyte.[181,182] To facilitate detection, aptamers are often modified with an optical or redox label that emits a signal after it has been released from the aptamer via nuclease digestion. One such assay was developed by Lu *et al.*[181], who utilized DNase I to selective digest target-bound structure-switching aptamers while leaving unbound single-stranded aptamers intact. They used graphene sheets that strongly adsorb these single-stranded aptamers through π-stacking interactions with the nucleobases,[183] thereby protecting them from digestion. Target-bound aptamers fold into a double-stranded state that resists adsorption by the graphene sheets, allowing for DNase I digestion. This releases the target, allowing subsequent target-binding events to occur. To achieve target detection, aptamers were modified with fluorescein, a dye that is quenched by graphene but fluoresces strongly when free in solution.[181] Using cocaine- and ATP-binding aptamers as an example, the authors achieved a detection limit of 0.1 and 0.2 μM for ATP and cocaine, respectively, which is 100-fold lower than a 1:1 binding strategy that does not use DNase I. Several other EATR variants have been described that use alternative enzymes such as Exo III[182] and T7[184] exonuclease. Although these achieved amplified detection via target recycling, the use of exonucleases is problematic because target-bound aptamers often adopt complex tertiary structures such as G-quadruplexes, which have been shown to inhibit exonucleases.[178] Moreover, small-molecule binding to DNA has also been shown to inhibit nuclease

digestion.[170,185] Endonucleolytic EATR strategies could offer an ideal alternative in this regard. Yu et al.[138] demonstrated one such approach, in which they inserted an abasic site between the binding domains of a dehydroepiandrosterone-3-sulfate (DIS)-binding CBSA construct. Specifically, they modified the short fragment of the CBSA at its ends with a fluorophore and quencher, and with an abasic site at its center. In the absence of DIS, the flexibility of the short fragment causes the fluorophore to come into close proximity with the quencher, resulting in reduced fluorescence. In the presence of DIS, CBSA assembly creates a double-stranded abasic site that Exo III can recognize and cleave. The cleavage of the short fragment results in dissociation of the CBSA, releasing the target to undergo subsequent rounds of CBSA assembly and digestion, each of which liberates a fluorophore molecule from the quencher, resulting in recovery of fluorescence. This assay achieved 100-fold improved sensitivity compared to a similar assay without Exo III.[138]

2.10. Small molecule targets used in this work

2.10.1. Dehydroepiandrosterone-3-sulfate (DIS).

DIS is the major metabolite of dehydroepiandrosterone and an intermediate in the biosynthesis of other androgen and estrogen steroids.[186] DIS is nearly exclusively produced and excreted by the adrenal gland and has no hormonal function.[186] The concentration of DIS in blood is highly correlated with sexual maturity, peaking between ages 20–30, and its levels in urine reflect the health of the adrenal gland.[187] This concentration ranges from ~0.1–3 μM[188,189] in healthy adults with increases or decreases in excretion indicative of malignancy in adrenal tumors[190] or hypertension,[191] respectively.

2.10.2. Cocaine.

Cocaine is a schedule II-controlled substance obtained from the leaves of the *Erythroxylum coca* and *Erythroxylum novogranatense* species.[192] Although this drug has limited medical use, the illicit production, trafficking, and abuse of cocaine poses a serious threat to public health and safety.[193] Cocaine is the third most abused drug (as of 2020)[194] and is highly addictive. Long-term use is associated with several health risks including increased risk of stroke, seizures, and heart attack, as well as inflammation of the heart muscle and neurological problems.[193,195] On-site testing of seized cocaine powder currently relies on the cobalt (II) thiocyanate test,[196,197] which produces a bright blue color in the presence of cocaine. Further confirmatory testing is then done using gas chromatography (GC)- or liquid chromatography-mass spectrometry (LC-MS) techniques.[198]

2.10.3. Adenosine and its analogs.

Adenosine and its analogs are important organic compounds that are cofactors for numerous enzymes.[199,200] Adenosine is composed of an adenine base and ribose sugar, with ATP, ADP, and AMP possessing an additional tri-, di-, and mono-5'-phosphate tail, respectively.[201,202] ATP, ADP, and AMP are heavily involved in cellular metabolism; ATP is the energy currency of the cell, and ADP and AMP are the key metabolic byproducts and regulators of its synthesis and consumption.[201,202] Adenosine mainly behaves as a neurotransmitter, and regulates myocardial and coronary circulatory functions.[203–205] Adenosine is normally present at nanomolar concentrations, and spikes to 1–50 μM are indicative of cardiac problems such as ischemia.[206–208]

2.10.4. Ochratoxin A.

Ochratoxin A is a mycotoxin produced by several fungi species including *Aspergillus ochraceus* and *Penicillium verrucosum*.[209] It is a common contaminant found in food products worldwide, including cereals, coffee beans, dry vine fruits, and wine.[210–212] Effects of ochratoxin A poisoning include nephrotoxicity and carcinogenicity for humans and livestock.[213] The economic impact of ochratoxin A is particularly evident in contaminated poultry feed, which results in reduced weight gain, poor feed conversion, reduced egg production, and poor eggshell quality.[214,215]

2.10.5. Fentanyl and its analogs.

Fentanyl and its analogs are potent narcotic analgesics which activate the μ-opioid receptors, with widespread medical use for the treatment of pain.[216,217] Fentanyl belongs to a family of synthetic opioids based on a phenyl-4-piperidinyl-acetamide backbone, and possesses multiple sites that allow for the addition or substitution of various chemical functional groups to produce novel compounds with similar or greater analgesic effects.[216,217] As of 2020, fentanyl and its analogs are the fourth most abused illicit substance and the greatest cause of drug-related overdose deaths.[194] These opioids can be encounter as powders or pills, and law enforcement institutions have reported the presence of at least 56 fentanyl analogs in seized substances.[218–221] This number is only expected to rise, as the fentanyl core-structure is postulated to accommodate an estimated total of 1,400 modifications while still retaining its analgesic effects.[222–224] Presumptive testing for fentanyl and its analogs currently relies on several color spot tests whose aggregated results indicate the presence of fentanyl or its analogs.[225,226] Lateral-flow immunoassays, which utilize antibodies as biorecognition elements, are a quick and highly specific alternative

that allows for the visual detection of fentanyl with the naked eye after five minutes.[227–229] However, immunoassays typically have limited or no cross-reactivity for many of the fentanyl analogues.[227–229]

2.10.6. Δ^9-Tetrahydrocannabinol (THC).

Marijuana is a plant from the Cannabis family and is the second most widely abused illicit drug in the United States.[193,194] Marijuana's psychoactive effects originate from the compound THC.[230,231] With the passage of the Hemp Farming Act of 2018,[232] cannabis plants have been differentiated into two categories: hemp (legal) and marijuana (illegal). Hemp is a non-psychoactive subtype of cannabis that is valued for its fibers and seeds, which have been turned into a variety of commercial and industrial products.[233–235] Hemp may possess up to 0.3% THC by dry weight and remain legal for commercial use. In contrast, cannabis containing > 0.3% THC is characterized as marijuana, and remains illegal under federal law.[232] Hemp and marijuana are morphologically identical and require chemical analysis of the THC content for identification.[236] Current THC screening utilizes the Duquenois-Levine test, which employs a chemical reaction with THC that produces a colored product.[237,238] However, this test cannot provide quantitative information on the amount of THC present, and is thus unsuitable for distinguishing marijuana from hemp, which requires more costly confirmatory testing.[236]

2.11. Proteins and enzymes used in this work.

2.11.1. Exo III (*E. coli.*).

Exo III is an exonuclease from *Escherichia coli.* that catalyzes the accretive hydrolysis of phosphodiester bonds from the 3'-hydroxy termini of double-stranded DNA as well as RNA/DNA hybrid duplexes.[161] The primary cofactor for Exo III is Mg^{2+}; it has

also been reported that Mn^{2+} can provide greater activity as a cofactor, albeit at the cost of poorer specificity.[239] Exo III recognizes blunt or recessed 3'-termini as well as nicks in duplex DNA.[240,241] Although Exo III is not active on single-stranded DNA, it retains low activity for 3'-overhangs of 1–4 nt.[242] Exo III also possesses 3'-phosphatase activity, and apurinic/apyrimidinic (AP)-endonuclease activities have been reported as well.[240,241] Exo III's biological purpose is to participate in the base excision repair pathway for *E. coli,* allowing for the repair of oxidizing or ionizing radiation-induced DNA damage.[243] Its wide assortment of catalytic activities and robust performance at room temperature and across various buffer conditions has made Exo III one of the most widely-used exonucleases for a variety of sensors.[171,244]

2.11.2. Exo I (*E. coli.*).

Exo I is an exonuclease from *E. coli* that catalyzes the hydrolysis of phosphodiester bonds from the 3'-hydroxy termini of single-stranded DNA.[159] This enzyme digests ~250–300 nt per binding event, making it highly processive.[245–247] When it encounters a double-stranded region, the enzyme dissociates from the substrate, preventing further digestion.[245,246] Exo I also interacts with the single-stranded DNA-binding protein, which enhances its activity by loading single-stranded DNA into the Exo I binding domain and unwinding DNA secondary structures.[248] Exo I's biological purpose is to digest the 3'-overhangs generated during the DNA mismatch repair process.[243] Similar to Exo III, Exo I maintains its activity at room temperature making it ideal for enzyme-assisted aptamer-based assays performed at room temperature.[249]

2.11.3. Immunoglobulin E (IgE).

IgEs are primary component of the body's immune response to parasites and allergens.[250,251] IgE have been demonstrated to elicit physiologic response including local inflammation, itching, mucus production, and bronchial constriction.[250,252] For certain individuals, overproduction of IgE can result in IgE-mediated diseases including allergies, atopic dermatitis, and allergic asthma.[252]

2.11.4. Thrombin.

Thrombin is a serine protease involved in the clotting process.[253,254] Thrombin is produced by proteolytic cleavage of prothrombin, and subsequently converts water-soluble fibrinogen into strands of fibrin that, together with platelets, form clots at wound sites.[253,254] Given its role in both the contact activation pathway and tissue factor pathway of coagulation, several thrombin/prothrombin inhibitors such as heparin and warfarin have been developed to reduce or halt coagulation.[255,256]

CHAPTER 3: No Structure-Switching Required: A Generalizable Exonuclease-Mediated Aptamer-Based Assay for Small-Molecule Detection

3.1. Introduction.

Aptamers are nucleic acid-based affinity reagents, isolated via in vitro systematic evolution of ligands by exponential enrichment (SELEX).[23,24] They have gained considerable attention as excellent biorecognition elements, with diverse applications in areas such as drug screening,[114] environmental monitoring,[257] molecular and cell imaging,[95,258,259] and medical diagnostics.[260,261] This is in part because aptamers can be isolated for essentially any target, including metal ions, small molecules, proteins, or whole cells.[32,33] Aptamers have desirable properties such as high chemical stability and long shelf life and can be chemically synthesized in an inexpensive and reproducible manner.[32,33] These advantages make aptamers ideal for use in biosensors. Aptamer-based assays have been developed for the detection of a multitude of targets, particularly small molecules.[35,262] Most aptamer-based assays are based on structure-switching aptamers which undergo large conformational changes to report the presence of the target.[114,127,142] Upon binding to the sensing aptamer, the target induces a specific folding event that produces a colorimetric,[263] fluorescent,[114,127] or electrochemical readout.[116] However, most SELEX methods use unstructured libraries and therefore yield aptamers that have unpredictable binding domains and no structure-switching functionality.[50,142] Thus, additional engineering steps are typically required to introduce structure-switching functionality into such aptamers.[114,127,142] Specifically, truncation must first be performed to identify the target-binding domain of the aptamer and then to destabilize it so that the aptamer can undergo a large target-induced conformational change. To report this change, the truncated aptamer

must be chemically modified with a signal-reporting element such as a fluorophore,[114] electroactive tag,[116] enzyme,[129] or quantum dot.[264] This sensing strategy is labor intensive and costly, and destabilization of the aptamer greatly reduces its target-binding affinity.[103,124] Strand displacement strategies offer an alternative for small-molecule detection, in which the target-binding domain of an aptamer is identified and then partially blocked via hybridization to a complementary DNA (cDNA) strand. Detection relies on target-induced displacement of the cDNA and quantification of either the displaced cDNA[265] or the target-aptamer complex.[142] Since aptamers generally have higher affinity for the cDNA strand than the small-molecule target, strand-displacement methods are hindered by competition between the cDNA and the target for binding to the aptamer, which reduces target-binding affinity and undermines sensor performance.[266,267]

To overcome the limitations described above, we developed a generalizable aptamer-based assay based on target-induced exonuclease inhibition to detect small-molecule targets without the need for binding-induced conformational changes. Previous studies have shown that exonuclease III (Exo III), a 3′-to-5′ double-strand DNA exonuclease,[161] is sensitive to local structural changes in double-stranded DNA induced by small-molecule binding and that such binding can halt digestion a few bases before the binding site.[166,167,169] We recently found that this phenomenon also holds true for small-molecule binding aptamers and exploited this finding to introduce structure-switching functionality into fully folded aptamers.[170]

Here, we develop an assay that utilizes high-affinity, prefolded aptamers and two exonucleases, Exo III and exonuclease I (Exo I), to detect small molecules. Favorably, this assay does not require any sequence engineering, truncation, or labeling. As proof of

concept, we performed Exo III digestion of a dehydroisoandrosterone-3-sulfate (DIS)-binding 37-nt aptamer,[28] DIS-37, which has a three-way-junction-structured binding domain and a duplexed, blunt-ended 3′ terminus. Exo III catalyzed the 3′-to-5′ digestion of the double-stranded stem of DIS-37, removing three nucleotides to form a 34-nt product regardless of the presence or absence of DIS. Further digestion of the target-bound 34-nt product was halted in the presence of DIS, but in the absence of DIS, the 34-nt product was further digested to produce a single-stranded 30-nt product that was resistant to Exo III digestion. We found that Exo I, a 3′-to-5′ single-strand exonuclease,[159] was able to degrade this 30-nt single-stranded, nontarget-bound digestion product into mononucleotides but was incapable of digesting the 34-nt double-stranded digestion product of the target-bound aptamer. We therefore used a mixture of Exo III and Exo I to develop a fluorescence assay to detect DIS using SYBR Gold, a DNA-binding dye,[268] as a signal reporter. Our assay proved to be very sensitive and had low background, achieving a detection limit of 500 nM DIS in 50% urine within 15 min. We further demonstrated the generality of this fluorescence assay with a three-way-junction-structured cocaine-binding aptamer and a hairpin-structured ATP-binding aptamer. We observed that minimal signal was generated in the absence of target due to the fact that both exonucleases completely digested the nontarget-bound aptamers. In contrast, a large signal was produced in the presence of target as exonuclease digestion of target-bound aptamers was strongly inhibited. Notably, our assay is highly robust as it maintains excellent performance in a variety of buffer conditions and biological sample matrices. Finally, we demonstrated our assay's potential for single-pot, multiplex small-molecule detection by exploiting the fact that the digestion product of each aptamer−target pair has a unique sequence that can be specifically recognized by an

antisense DNA probe. As a demonstration, we used fluorophore− quencher-modified molecular beacons to quantify the digestion products produced by the exonuclease mixture to simultaneously detect ATP and cocaine. Due to the high target specificity of the aptamers and high sequence specificity of the molecular beacons, we were able to simultaneously quantify both targets in microliter-volume samples without any cross talk in 25 min. We believe our assay should be broadly generalizable and can be combined with different DNA signal reporting strategies for multiplexed small-molecule detection in applications such as medical diagnostics, drug screening, food safety, environmental monitoring, and biodefense.

3.2. Experimental section.

3.2.1. Reagents.

Exonuclease III and exonuclease I (both from E. coli) were purchased from New England Biolabs. Adenosine-5′-triphosphate (ATP) disodium salt trihydrate was purchased from MP Biomedical. Formamide was purchased from Fisher Scientific. SYBR Gold was purchased from Invitrogen. Cocaine hydrochloride, dehydroisoandrosterone-3-sulfate, and all other chemicals were purchased from Sigma-Aldrich unless otherwise specified. All oligonucleotides were ordered from Integrated DNA Technologies and purified with HPLC. COC-MB was purchased from LGC Biosearch Technologies with HPLC purification. Oligonucleotides were dissolved in PCR-quality water, and the concentrations were measured using a spectrophotometer (NanoDrop 2000, Thermo Fisher Scientific). All sequences employed in this work are listed in **Table 3-1**.

Table 3-1. Sequences ID and DNA sequences used in Chapter 3.

Sequence ID	Sequence (5'–3')
DIS-37	TCGGGACGTGGATTTTCCGCATACGAAGTTGTCCCGA
DIS-34	TCGGGACGTGGATTTTCCGCATACGAAGTTGTCC
DIS-33	TCGGGACGTGGATTTTCCGCATACGAAGTTGTC
DIS-30	TCGGGACGTGGATTTTCCGCATACGAAGTT
DIS-37-M	TCGGGACGTGGATTTTCCGCCTACGAAGTCGTCCCGA
ATP-33	CGCACCTGGGGGAGTATTGCGGAGGAAGGTGCG
ATP-30	CGCACCTGGGGGAGTATTGCGGAGGAAGGT
ATP-25	CGCACCTGGGGGAGTATTGCGGAGG
ATP-33-M	CGCACCTGGGGAAGTATTGCGGTGGAAGGTGCG
COC-38	GGGTGACAAGGAAAATCCTTCAATGAAGTGGGTCACCC
COC-35	GGGTGACAAGGAAAATCCTTCAATGAAGTGGGTCA
COC-33	GGGTGACAAGGAAAATCCTTCAATGAAGTGGGT
COC-38-M	GGGTGACAAGGAAAATCCTTCGATGAAGTGGGTCACCC
COC-MB	/56-FAM/GCGAGCACCCACTTCATTGAAGGATTTTCCTTGTCACCCGCTCGC/BHQ-1/
ATP-MB	/5Cy5/GCGAGCCTTCCTCCGCAATACTCCCCCAGGTGCGGCTCGC/3IAbRQSp/

(a, /56-FAM/represents FAM; b, /5Cy5/represents Cy5; c, /BHQ-1/represents Blackhole Quencher 1; d, /3IAbRQSp/represents Iowa Black RQ)

3.2.2. Aptamer Digestion Experiments.

Aptamer digestion experiments were performed using the following procedure unless otherwise specified. A 1 μL amount of 50 μM aptamer or mutant aptamer was added into 44 μL of reaction buffer containing various concentrations of the appropriate target in a 200 μL PCR tube. The buffer composition varied for each aptamer−target pair, with final concentrations for each reaction as follows: DIS (20 mM Tris, 25 mM $MgCl_2$, 1% DMSO, 0.1 mg/mL BSA, pH 7.4), cocaine (10 mM Tris, 100 mM NaCl, 1 mM $MgCl_2$, 0.1 mg/mL BSA, pH 7.4), and ATP (10 mM Tris, 10 mM $MgCl_2$, 0.1 mg/mL BSA, pH 7.4). Reaction mixtures were placed in a thermal cycler (C1000 Touch, Bio-Rad) and incubated at 23 °C for 60 min, after which 5 μL of the enzyme(s) was added to each reaction mixture. For DIS, the enzyme concentrations used were 0.13 U/μL Exo III, 1.5 U/μL Exo I, or a mixture of 0.13 U/μL Exo III + 1.5 U/μL Exo I. For cocaine, the enzyme concentrations used were 0.4 U/μL Exo III, 0.9 U/μL Exo I, or a mixture of 0.4 U/μL Exo III + 0.9 U/μL Exo I. For

ATP, the enzyme concentrations used were 0.5 U/μL Exo III, 1.4 U/μL Exo I, or a mixture of 0.5 U/μL Exo III + 1.4 U/μL Exo I. For all experiments, 5 μL of sample was collected at various time points and mixed with 10 μL of formamide loading buffer (75% formamide, 10% glycerol, 0.125% SDS, 10 mM EDTA, and 0.15% (w/v) xylene cyanol) to quench the reaction. Digestion products were analyzed by denaturing polyacrylamide gel electrophoresis (PAGE). Specifically, 3 μL of each collected sample was loaded into the wells of a 15% denaturing PAGE gel. Separation was carried out at 20 V/cm for 3 h in 0.5× TBE running buffer. The gel was stained with 1× SYBR Gold for 25 min and imaged using a ChemiDoc MP Image system (BioRad).

3.2.3. SYBR Gold Fluorescence Experiments.

The dual-exonuclease mediated assay was performed using various concentrations of DIS (0, 0.5, 1, 2.5, 5, 10, 15, 25, 33, 50, 75, 100, and 250 μM), cocaine (0, 0.1, 0.25, 0.5, 1, 2.5, 5, 10, 20, 35, 50, 75, 125, 200, 500, and 1000 μM), and ATP (0, 0.25, 0.5, 1, 2.5, 5, 10, 15, 25, 50, 100, and 250 μM). After digestion, 50 μL of digestion products was mixed with 50 μL of 2× SYBR Gold diluted in 10 mM Tris buffer (pH 7.4) containing 100 mM EDTA and 25% formamide (v/v). On the basis of the estimated extinction coefficient of SYBR Gold as reported in the literature (ε_{494} = 50,000 $M^{-1}cm^{-1}$),[269,270] the concentration of 1× SYBR Gold is equivalent to 1.21 μM. An 80 μL amount of the mixture was loaded into the wells of a 96-well plate. Fluorescence emission spectra were recorded from 510 to 850 nm using a Tecan microplate reader (Infinite M1000 PRO, Switzerland) with a 495 nm excitation wavelength. The fluorescence intensity recorded at 545 nm was used to calculate signal gain using the equation (F − F0)/F0, where F and F0 represent fluorescence intensity in the presence and absence of target, respectively. Calibration curves were

constructed by plotting signal gains against target concentrations. Each experiment was performed in triplicate, and error bars represent the standard deviation of three measurements.

3.2.4. Multiplex Target Detection Using Fluorophore-Quencher-Modified Molecular Beacons.

A 1 μL amount of 25 μM COC-38 and 1 μL of 25 μM ATP-33 were added into 43 μL of reaction buffer (10 mM Tris, 100 mM NaCl, 1 mM $MgCl_2$, and 0.1 mg/mL BSA, pH 7.4) containing various concentrations of either cocaine, ATP, or both in a 200 μL PCR tube. Reaction mixtures were placed in a thermal cycler and incubated at 23 °C for 60 min, after which 5 μL of Exo III (0.5 U/μL) only, Exo I (1.5 U/μL) only, or exonuclease mixture (0.5 U/μL Exo III + 1.5 U/μL Exo I) was added into each sample. After a 20 min reaction, 40 μL of stop solution (10 mM Tris, 12.5 mM EDTA, and 500 mM NaCl, pH 7.4) was added to quench the enzymatic reaction. Then 10 μL of molecular beacon mixture (final concentration 200 nM COC-MB + 200 nM ATP-MB) prepared in hybridization buffer (10 mM Tris buffer, 500 mM NaCl, and 1 mM $MgCl_2$, pH 7.4) was introduced to quantify the digested aptamer(s). An 80 μL amount of the mixture was immediately loaded into the wells of a 96-well plate. Fluorescence emission spectra were recorded with a 495 nm excitation wavelength for FAM and with a 645 nm excitation wavelength for Cy5 using a Tecan microplate reader (excitations were performed separately). Calibration curves were generated using varying concentrations of either ATP (0, 2.5, 5, 10, 25, 50, 75, 100, 250, 350 μM) or cocaine (0, 15, 20, 25, 50, 75, 100, 250, 500, 1000 μM).

3.2.5. Isothermal Titration Calorimetry (ITC) Experiments.

All ITC experiments were performed in reaction buffer with a MicroCal ITC200 instrument (Malvern). The sample cell contained 20 μM aptamer, with 500 μM DIS, 500 μM cocaine, or 800 μM ATP loaded in the syringe. Each experiment consisted of 19 successive 2 μL injections after a 0.4 μL purge injection with a spacing of 180 s to a final ligand to aptamer molar ratio of 5.5:1 for the cocaine-binding aptamers and DIS-binding aptamers and 8.8:1 for the ATP-binding aptamers. All experiments were performed at 23 °C. The raw data were first corrected based on the dilution heat of each target and then analyzed with the MicroCal analysis kit integrated into Origin 7 software with a single-site binding model for DIS and cocaine or a two-site sequential binding model for ATP.

3.3. Results and Discussion.

3.3.1. Structure Selectivity of Exo III for Target-Aptamer Complexes.

Prior work has shown that the 3′-to-5′ exonuclease activity of Exo III on double-stranded DNA can be stalled by covalent[166,167] and noncovalent[169] DNA-binding small molecules. For example, benzo-α-pyrene and benzo-c-phenanthrene react with the primary amine group of deoxyadenosine and deoxyguanosine bases, forming covalent DNA adducts within the helical minor groove[166,167] that halt Exo III digestion 3−4 bases prior to the binding site. Similar behavior was observed with noncovalent DNA-binding small molecules, such as 4′,6-diamidino-2-phenylindole, Hoechst 33258, and distamycin A, which inhibit Exo III digestion 3−6 bases prior to the binding site.[169] We therefore predicted that Exo III activity could be similarly affected by aptamer−target interactions.

As proof of concept, we performed Exo III digestion using a previously reported DIS-binding aptamer (DIS-37).[28] DIS-37 exists in a fully folded state even in the absence

of DIS, due to the seven Watson−Crick base pairs (bp) in stem 1 (**Figure 3-1A**). DIS binds within the aptamer's prefolded three-way-junction-structured target-binding domain without inducing a large conformational change in the aptamer. We performed a time course of DIS-37 Exo III digestion in the presence and absence of DIS and characterized the digestion products using denaturing PAGE, with concentrations calculated relative to a customized DNA ladder loaded in the gel. Regardless of the presence or absence of DIS, Exo III rapidly removed the first three nucleotides from the 3′ end of DIS-37. In the absence of DIS, Exo III continued digestion, forming three intermediate products (33-, 32-, and 31-nt) and eventually resulting in a 30-nt major product (**Figure 3-1B**). In the presence of DIS, further Exo III digestion was greatly inhibited, resulting in accumulation of 33- and 34-nt major products (**Fig. 3-1B & C**). These results demonstrate that Exo III digestion of DIS-37 is strongly inhibited upon the addition of target.

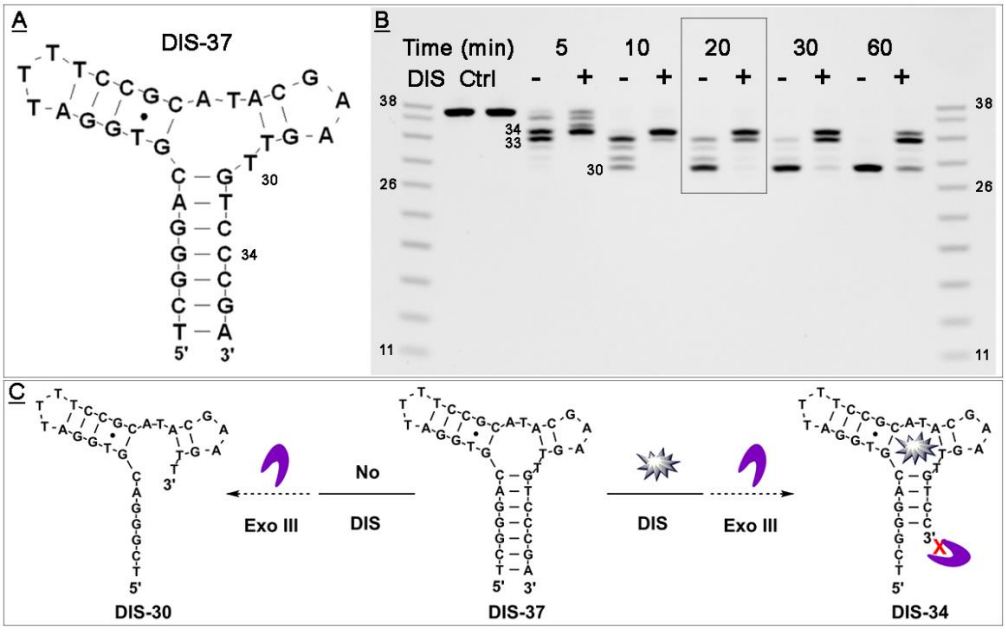

Figure 3-1. Time course of Exo III digestion of a DIS-binding aptamer (DIS-37) in the absence or presence of DIS. (**A**) Oligonucleotide structure of DIS-37. (**B**) PAGE analysis of DIS-37 digestion products over 60 min with or without 250 μM DIS. (**C**) Schematic of Exo III-mediated digestion of nontarget-bound (left) and target-bound (right) DIS-37.

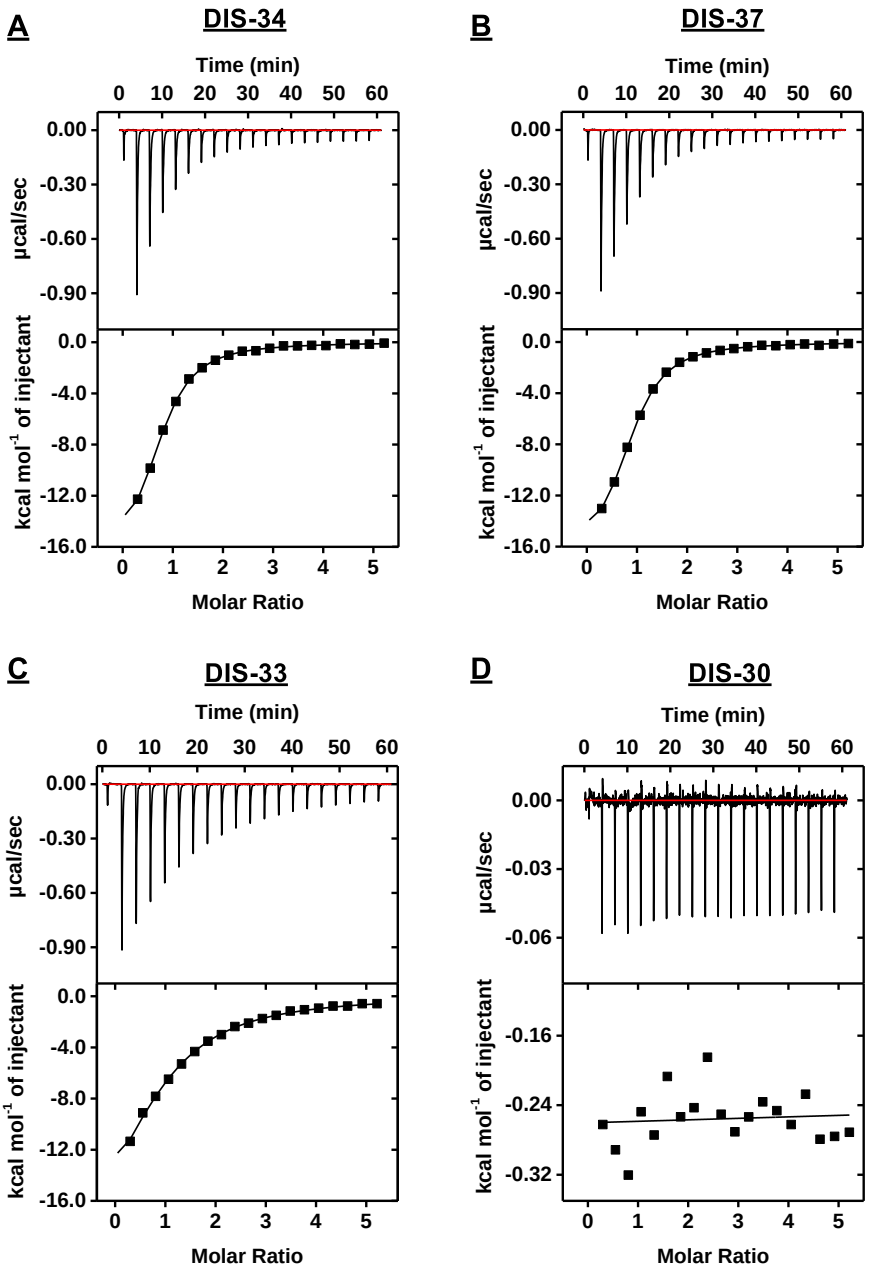

Figure 3-2. Characterization of target-binding affinity of DIS-binding aptamers using ITC. Top panels present raw data showing the heat generated from each titration of DIS for (**A**) DIS-34, (**B**) DIS-37, (**C**) DIS-33, and (**D**) DIS-30. Bottom panels show the integrated heat of each titration after correcting for dilution heat of the titrant.

We then synthesized the 30-, 33-, and 34-nt major products (DIS-30, DIS-33, DIS-34) and used isothermal titration calorimetry (ITC)[77] to investigate their binding affinity

for DIS (**Figure 3-2**). We obtained an equilibrium dissociation constant (K_D) of 4.0 ± 0.2 μM for DIS-34 (**Figure 3-2A**), which is very similar to the K_D of DIS-37 (3.4 ± 0.2 μM, **Figure 3-2B**). A 4-fold decrease in binding affinity was observed for DIS-33 (K_D = 16.0 ± 1.0 μM, **Figure 3-2C**) due to its reduced thermostability. These results suggest that the major products generated in the presence of DIS remain bound to the target. In contrast, DIS-30 resists Exo III digestion but retains no binding affinity for DIS (**Figure 3-2D**), indicating this product presumably exists in a single-stranded state.[159]

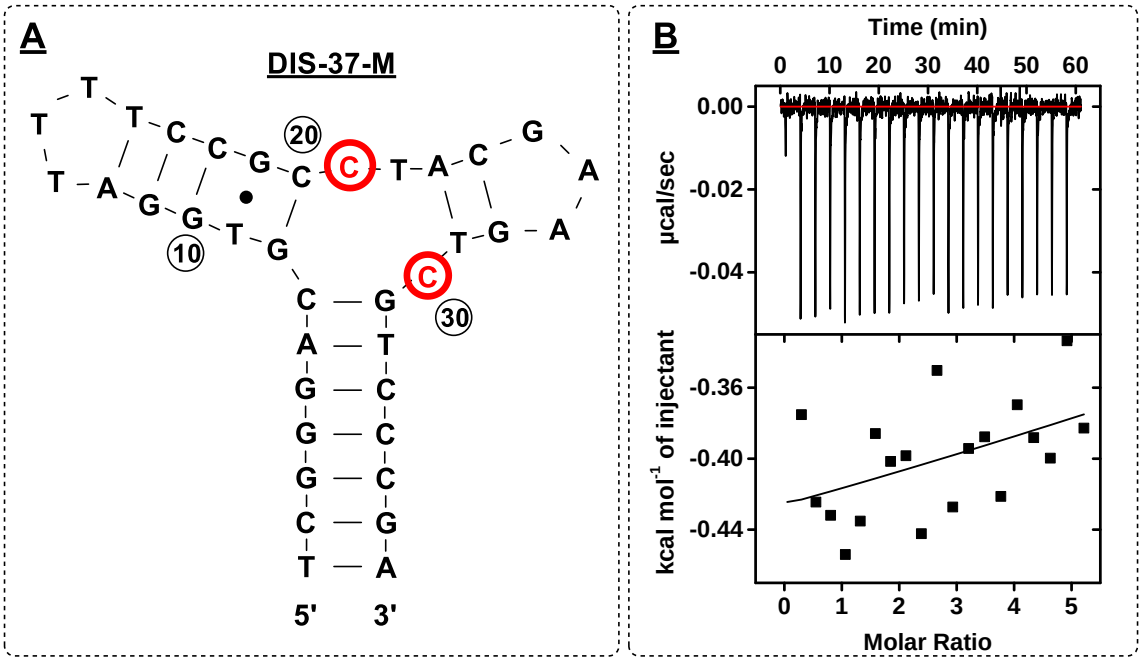

Figure 3-3. Aptamer mutant DIS-37-M and its binding affinity to DIS. (**A**) Oligonucleotide structure of DIS-37-M. Mutated nucleotides are marked in red. (**B**) Characterization of DIS binding affinity of DIS-37-M using ITC. Top panel presents raw data showing the heat generated from each titration of DIS for DIS-37-M. Bottom panel shows integrated heat of each titration after correcting for dilution heat of the titrant.

3.3.2. Inhibition of Exo III Requires Formation of the Target-Aptamer Complex.

To confirm that Exo III digestion of DIS-37 is modulated specifically by target binding, we designed a mutant aptamer with no binding affinity for DIS (**Figure 3-3A**).

This mutant (DIS-37-M) was designed by changing two nucleotides within the target-binding domain; specifically, the adenine at position 21 and the thymine at position 30 were both changed to cytosine (**Figure 3-3A**). We expected that DIS-37-M would retain a three-way junction structure but with impaired target-binding affinity. In order to verify that the aptamer is fully folded, we made use of Exo I, which is able to digest single-stranded but not double-stranded DNA.[159] We incubated both DIS-37 and DIS-37-M with Exo I and found that it was unable to digest either aptamer regardless of the presence or absence of DIS (**Figure 3-4**). This indicated that stem 1 was fully folded in both aptamers. We then used ITC to confirm that DIS-37-M possesses greatly reduced binding affinity for DIS (K_D > 1000 μM, **Figure 3-3B**). To evaluate whether the target itself inhibits Exo III activity, we performed Exo III digestion with DIS-37-M. We found that Exo III digestion of the mutant yielded the same major products (32-, 31-, and 30-nt) regardless of the presence or absence of DIS (**Figure 3-4A**). Given that DIS-37-M cannot form the aptamer−target complex, these results clearly indicate that DIS itself does not impair the function of Exo III. We performed the same experiment with DIS-37 and found that DIS binding inhibited Exo III digestion, whereas the aptamer alone was readily digested by the enzyme (**Figure 3-4B**). These results demonstrated that the formation of the target−aptamer complex is directly responsible for inhibiting Exo III digestion.

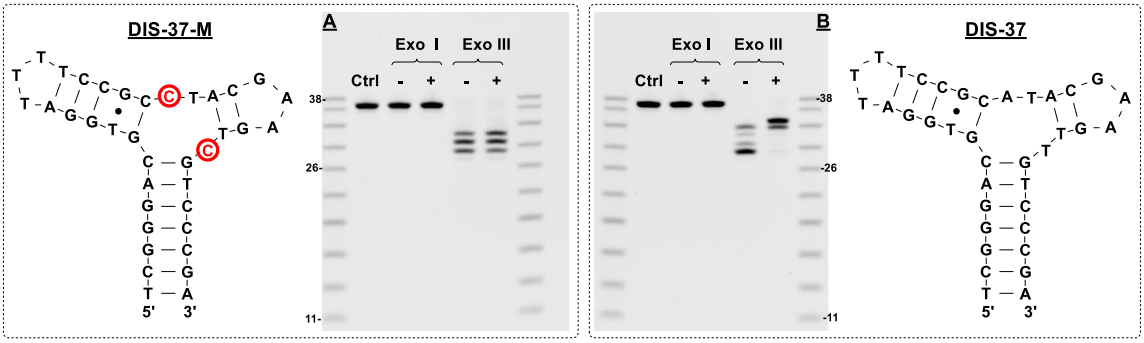

Figure 3-4. PAGE analysis of exonuclease-treated DIS-37 and DIS-37-M after a 15-minute reaction in the absence or presence of DIS. Oligonucleotide structure of (**A**) DIS-37 and (**B**) DIS-37-M and PAGE analysis of their digestion products generated by Exo I or Exo III. Mutated nucleotides marked in red.

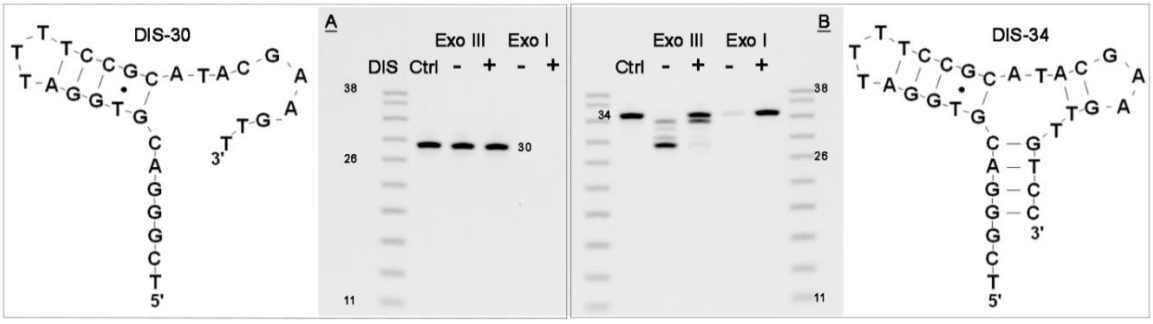

Figure 3-5. PAGE analysis of DIS-30 and DIS-34 after 15 minutes of exonuclease digestion in the absence and presence of 250 μM DIS. Oligonucleotide structure and PAGE analysis of exonuclease digestion products of (**A**) DIS-30 and (**B**) DIS-34.

3.3.3. Mechanism of Exo III Inhibition and Development of the Dual-Exonuclease-Mediated Assay.

We experimentally observed that Exo III digestion of DIS-37 occurred via a two-phase process. First, Exo III rapidly catalyzed the digestion of the double-stranded 3′ end of DIS-37, removing three nucleotides to form a 34-nt product regardless of the presence or absence of DIS. In the absence of target, Exo III continued to digest the 34-nt product into 33-, 32-, and 31-nt products at a progressively slower rate, eventually resulting in a 30-nt major product. In the presence of target, the 34-nt product greatly inhibited Exo III digestion. To understand the mechanism of inhibition, we digested DIS-30 and DIS-34

with either Exo III or Exo I. Regardless of the presence or absence of target, DIS-30 was not digested by Exo III but was completely digested by Exo I (**Figure 3-5A**). This confirms that the 30-nt product primarily exists in a single-stranded state, even in the presence of 250 μM DIS. Both Exo III and Exo I could digest DIS-34 in the absence of target (**Figure 3-5B**), indicating that nontarget-bound DIS-34 is in equilibrium between single- and double-stranded states. In contrast, Exo III digestion of DIS-34 was greatly inhibited in the presence of DIS due to formation of the target−aptamer complex. Similarly, target-bound DIS-34 was not digested by Exo I, indicating that the aptamer was predominantly in a double-stranded state when bound to DIS (**Figure 3-5B**).

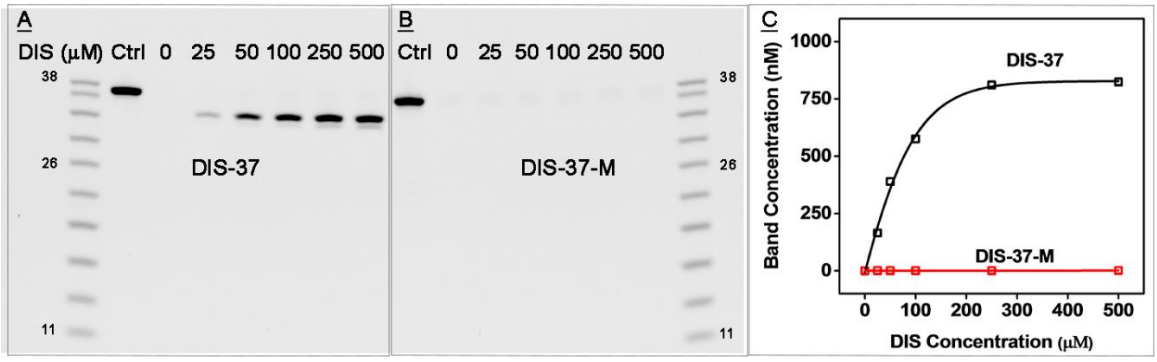

Figure 3-6. Exonuclease digestion of (**A**) DIS-37 and (**B**) its mutant (DIS-37-M) at increasing concentrations of DIS after 15 min. Aptamers were digested with a mixture of Exo III and Exo I, and PAGE analysis was used to characterize the digestion products. (**C**) Calibration curves of the calculated concentration of all digestion products of DIS-37 and DIS-37-M (based on DNA ladder intensity) versus DIS concentration.

On the basis of these results, we developed a dual-exonuclease-mediated assay that utilizes synergistic digestion by Exo III and Exo I to quantify DIS concentrations. We predicted that nontarget-bound DIS-37 would first be digested by Exo III to form several products that are in equilibrium between single- and double-stranded states, which can be completely digested by Exo I. In contrast, in the presence of DIS, Exo III will remove only

three nucleotides from DIS-37, with the resulting target-bound 34-nt product remaining resistant to digestion by both exonucleases. PAGE analysis of this digestion experiment confirmed that DIS-37 was completely digested in the absence of target. In the presence of target, we observed a 34-nt major product, and the concentration of this product increased with increasing concentrations of DIS until reaching saturation at 250 μM (**Figure 3-6A & C**). In order to determine whether higher concentrations of DIS might inhibit either exonucleases' activity, we digested the mutant aptamer, DIS-37-M, with the exonuclease mixture. The mutant was completely digested at DIS concentrations of up to 500 μM (**Figure 3-6B & C**), confirming that DIS itself inhibits neither Exo III nor Exo I.

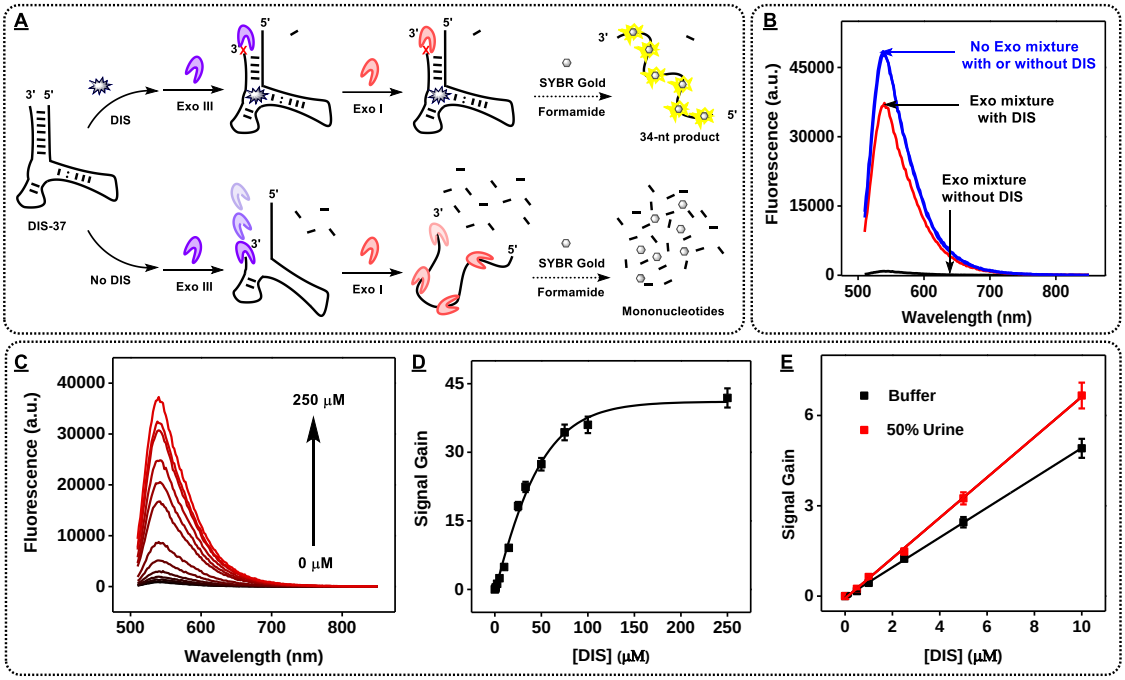

Figure 3-7. DIS detection using our label-free, aptamer-based dual-exonuclease-mediated fluorescence assay. (**A**) Scheme of the DIS-detecting assay using SYBR Gold as a signal reporter. (**B**) Fluorescence spectra of SYBR Gold for exonuclease-mixture-treated (red and black lines) and untreated (blue line) DIS-37 in the presence or absence of 250 μM DIS. (**C**) Fluorescence spectra of the samples generated at various DIS concentrations. (**D**) Calibration curve derived from the fluorescence spectra. (**E**) Linear range of the assay in buffer as well as 50% urine.

3.3.4. Label-Free Detection of DIS Using a Dual-Exonuclease-Mediated Fluorescence Assay.

We subsequently adapted our dual-exonuclease-inhibition approach into a label-free fluorescence-based assay for the sensitive detection of DIS. Digestion of DIS-37 yielded intact oligonucleotide products in the presence of DIS, whereas the aptamer was completely degraded into mononucleotides in the absence of DIS (**Figure 3-7A**). Therefore, we selected SYBR Gold as a signal reporter since it fluorescently stains only oligonucleotides but not mononucleotides.[268] Following a 15 min digestion of DIS-37 by the exonuclease mixture, we added a solution containing EDTA and formamide to deactivate the exonucleases and denature all major products into single-stranded structures. After adding 1× SYBR Gold, we observed a 40-fold signal gain for a sample containing 250 μM DIS relative to the target-free sample, with only minimal background in the absence of DIS (**Figure 3-7B**). As a control, we monitored target-binding induced fluorescence changes of DIS-37 without exonuclease treatment and observed virtually no difference in fluorescence intensity upon the addition of 250 μM DIS (**Figure 3-7B**). We further measured the sensitivity of our assay by generating a fluorescence calibration curve using different concentrations of DIS (**Figure 3-7C**). The fluorescence signal gain increased as the DIS concentration increased (**Figure 3-7D**) with a linear range from 0 to 10 μM and a measurable detection limit[271] of 500 nM (**Figure 3-7E**). Importantly, our dual-exonuclease-mediated assay demonstrated robust performance in biological matrices, and we obtained a similar linear range and detection limit for DIS in 50% urine samples (**Figure 3-7E**).

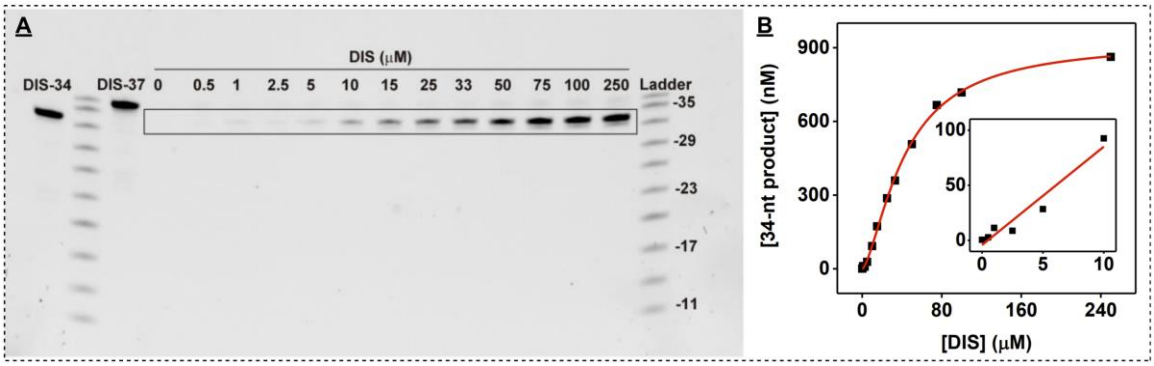

Figure 3-8. Quantification of the digestion product of DIS-37 generated by the exonuclease mixture with 0 – 250 μM DIS via staining with SYBR Gold. (**A**) PAGE analysis of retained inhibition product with varying concentrations of DIS, with major products denoted by the box. (**B**) Calculated inhibition product based on a DIS-34 standard loaded in the gel. Inset shows 34-nt digestion product generated at low concentrations of DIS.

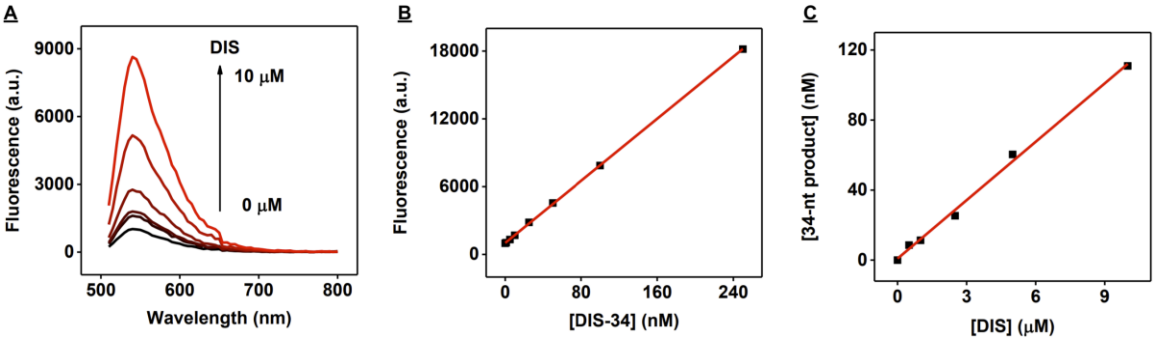

Figure 3-9. Quantification of the digestion product of DIS-37 generated by the exonuclease mixture with 0 – 10 μM DIS via staining with SYBR Gold. (**A**) Fluorescence spectra of SYBR Gold in the presence of varying concentrations of DIS. (**B**) Fluorescence of SYBR Gold in the presence of varying concentrations of synthesized DIS-34. (**C**) Quantification of the 34-nt inhibition product generated in the presence of low concentrations of DIS.

The quantity of 34-nt digestion product generated at different DIS concentrations was then characterized using denaturing PAGE, with concentrations calculated relative to a DIS-34 standard loaded in the gel (**Figure 3-8**). We found that 173, 287, 359, 507, 667, 718, and 863 nM 34-nt product were generated in the presence of 15, 25, 33, 50, 75, 100, and 250 μM DIS, respectively. It was difficult to accurately determine the concentration of

34-nt product formed at low concentrations of DIS (0.5−10 μM). Therefore, we used 1× SYBR Gold to create a calibration curve using DIS34 (**Figure 3-9**). On the basis of this curve, we obtained concentrations of 8.6, 11, 25, 60, and 111 nM of the 34-nt product in the presence of 0.5, 1, 2.5, 5, and 10 μM DIS, respectively.

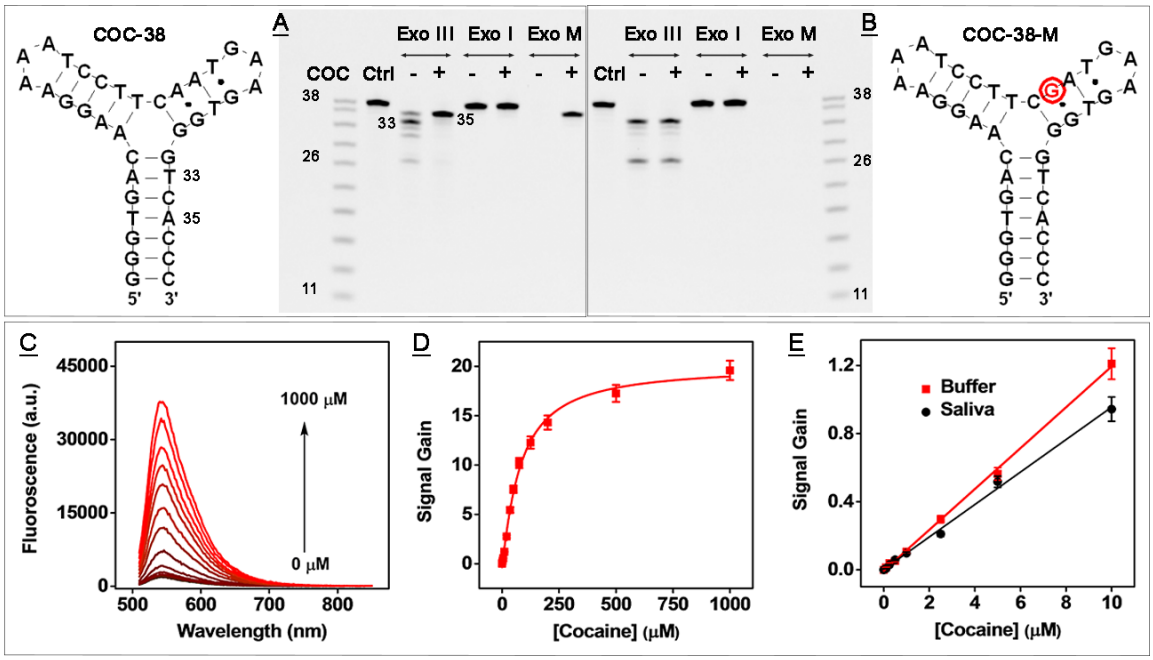

Figure 3-10. PAGE analysis of exonuclease digestion products of COC-38 and COC-38-M with and without 250 μM cocaine after 25 min of reaction and performance of the cocaine-detecting dual-exonuclease-mediated fluorescence assay. Oligonucleotide structure of (**A**) COC-38 and (**B**) COC38-M and PAGE analysis of their digestion products generated by Exo III, Exo I, or a mixture of both. Mutated nucleotides are marked in red. (**C**) Fluorescence spectra of the samples generated at various cocaine concentrations. (**D**) Calibration curve derived from the fluorescence spectra. (**E**) Linear range of the assay in buffer as well as 10% saliva.

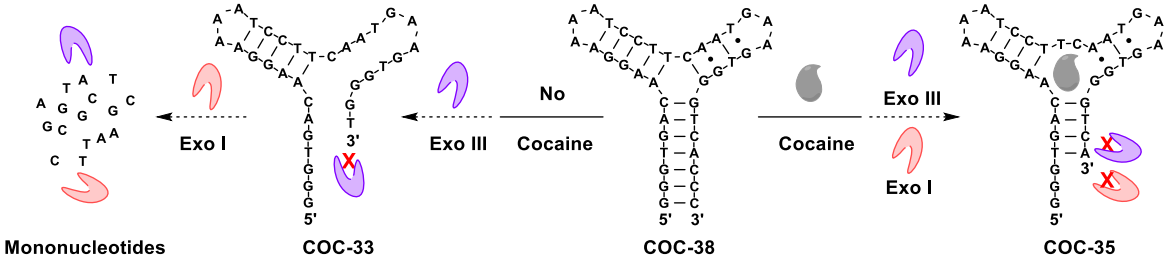

Figure 3-11. Schematic of dual-exonuclease-mediated COC-38 digestion in the absence (left) and presence (right) of cocaine.

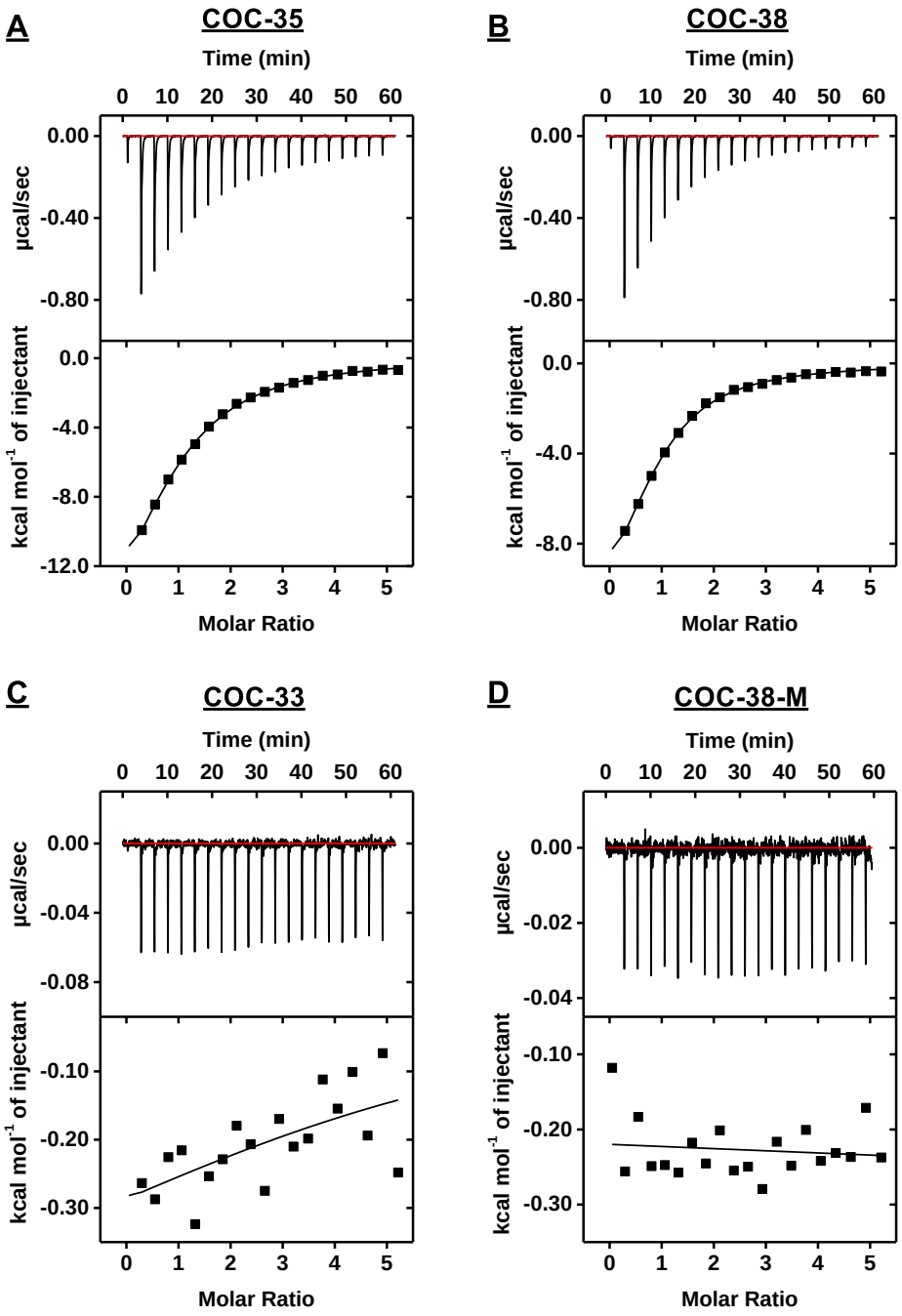

Figure 3-12. Characterization of target-binding affinity of cocaine-binding aptamers and a mutant using ITC. Top panels present raw data showing the heat generated from each titration of cocaine for (**A**) COC-35, (**B**) COC-38, (**C**) COC-33 and (**D**) COC-38-M. Bottom panels show the integrated heat of each titration after correcting for dilution heat of the titrant.

3.3.5. Application of the Dual-Exonuclease-Mediated Assay to a Three-Way Junction Cocaine Aptamer.

We next demonstrated the generality of our assay with a cocaine-binding aptamer (COC-38), which is prefolded and contains a three-way-junction-structured binding domain like DIS-37. COC-38 contains a 7-base-pair blunt-ended stem and is a preferred substrate for Exo III. We incubated COC-38 with Exo I, Exo III, or the exonuclease mixture in the absence and presence of cocaine and characterized the digestion products using PAGE (**Figure 3-10A**). Exo I alone did not digest this prefolded aptamer regardless of the presence or absence of cocaine (**Figure 3-10A**, Exo I). However, Exo III showed a target dependent digestion profile (**Figure 3-10A**, Exo III). Specifically, we observed a 33-nt major product in the absence of target, which we believe is single stranded due to the destabilization of the stems. In the presence of cocaine, only three nucleotides were removed from COC-38 to form a 35-nt product, and further Exo III digestion was strongly inhibited (**Figure 3-11**). As with DIS-34, this 35-nt product is presumably capable of retaining the target and thus remains folded. ITC experiments confirmed that this 35-nt product binds to cocaine (COC-35, $K_D = 16.9 \pm 0.7$ μM) (**Figure 3-12A**) with a similar affinity to COC-38 ($K_D = 11.2 \pm 0.6$ μM) (**Figure 3-12B**), whereas the 33-nt product (COC-33) has no affinity for cocaine (**Figure 3-12C**). Similar to DIS-37, nontarget-bound COC-38 was completely digested by the exonuclease mixture, but both enzymes were strongly inhibited by the target-bound 35-nt product (**Figure 3-10A**, Exo M). To confirm that enzymatic inhibition was specifically associated with formation of the target-aptamer complex, we performed exonuclease digestion with a COC-38 mutant (COC-38-M) containing a single adenine-to-guanine mutation at position 22 (**Figure 3-10B**) that eliminates its binding affinity for cocaine (**Figure 3-12D**).[136] COC-38-M was resistant to

Exo I digestion, indicating that it retains the same prefolded structure as COC-38. (**Figure 3-10B**, Exo I). The Exo III digestion profiles of COC-38-M were identical regardless of the presence or absence of cocaine (**Figure 3-10B**, Exo III), and the mutant was completely digested by the exonuclease mixture with and without cocaine (**Figure 3-10B**, Exo M). Taken together, these results show that target binding is crucial for exonuclease inhibition. We also found that the concentration of the major 35-nt product of COC-38 increased with increasing concentrations of cocaine when the exonuclease mixture was used, while up to 800 μM cocaine did not inhibit exonuclease digestion of COC-38-M (**Figure 3-13**). When we replicated our dual-exonuclease-mediated fluorescence assay for the detection of cocaine (**Figure 3-10C & D**), we obtained a linear range from 0 to 10 μM with a measurable detection limit of 100 nM in both buffer and 10% saliva (**Figure 3-10E**).

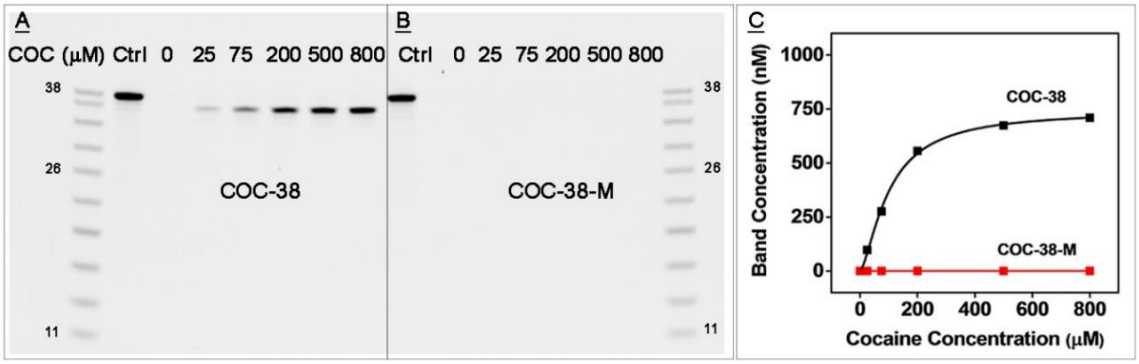

Figure 3-13. Target concentration-dependent inhibition of dual-exonuclease-mediated digestion of a cocaine-binding aptamer (COC-38) and its mutant (COC-38-M) after a 25-min reaction. PAGE analysis of digestion products at increasing concentrations of cocaine for (**A**) COC-38 and (**B**) COC-38-M. (**C**) Calibration curve of the calculated concentration of digestion product versus cocaine concentration for COC-38 (black) and COC-38-M (red). The intensity of the DNA ladder was used to calculate product concentrations.

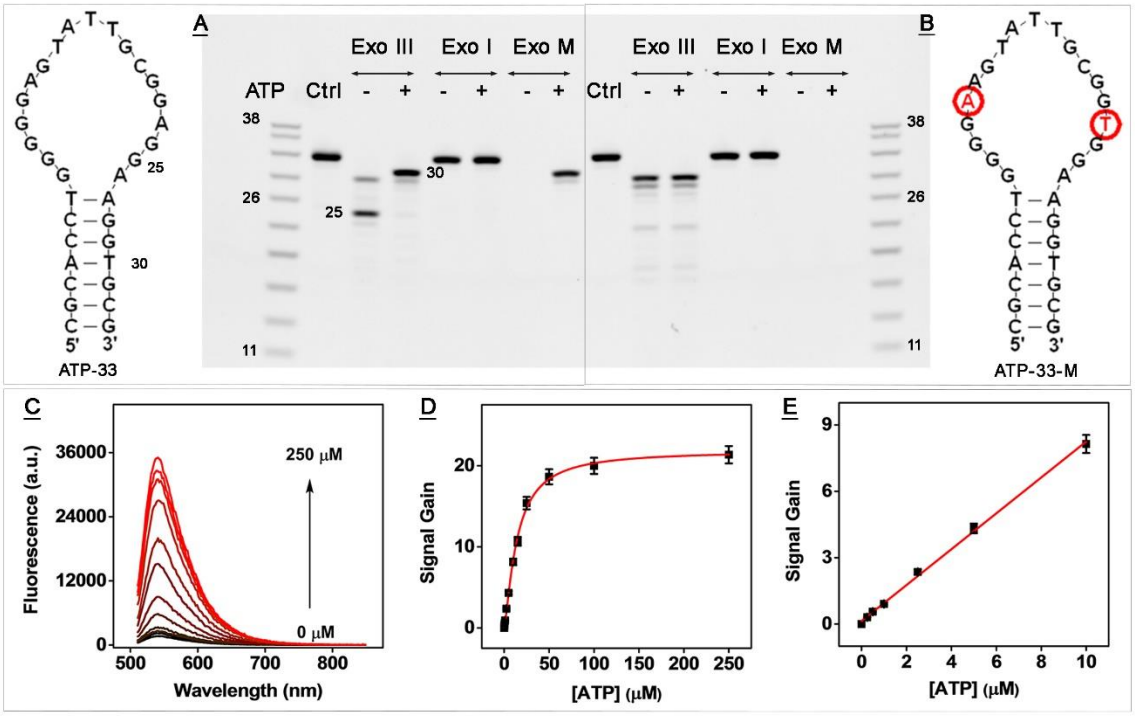

Figure 3-14. PAGE analysis of exonuclease digestion products of ATP-33 and ATP-33-M with and without 250 μM ATP after 20 min of digestion and performance of the dual-exonuclease-mediated fluorescence assay for ATP detection. Oligonucleotide structure of (**A**) ATP-33 and (**B**) ATP-33-M and PAGE analysis of their digestion products generated by Exo III, Exo I, or a mixture of both. Mutated nucleotides are marked in red. (**C**) Fluorescence spectra of the samples generated at various ATP concentrations. (**D**) Calibration curve derived from the fluorescence spectra. (**E**) Linear range of the assay in buffer.

3.3.6. Application of Our Assay to a Hairpin-Structured ATP Aptamer.

We further demonstrated the generality of the dual-exonuclease-mediated assay using an ATP-binding aptamer (ATP-33) of which the exact structure of its target-binding domain has not been conclusively determined. ATP-33 is prefolded and forms a hairpin structure with a 7-bp blunt ended stem that is resistant to Exo I digestion (**Figure 3-14A**, Exo I). Despite its structural difference relative to both DIS-37 and COC-38, ATP-33 also exhibited a target binding-dependent Exo III digestion profile. Exo III digestion produced

a single-stranded 25-nt major product in the absence of ATP and a 30- nt product in the presence of ATP (**Figure 3-15**) (**Figure 3-14A**, Exo III).

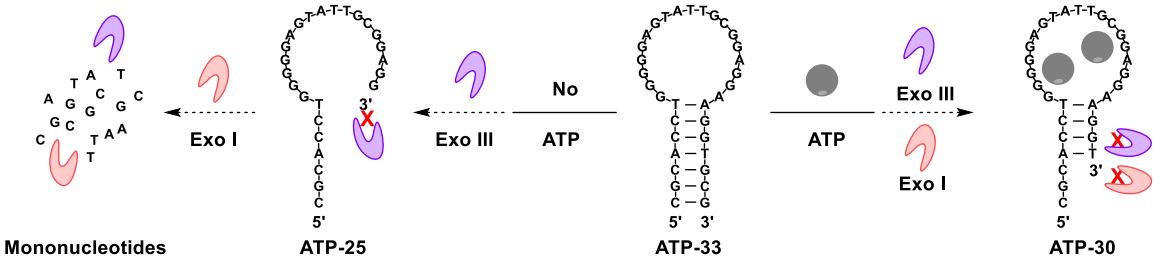

Figure 3-15. Schematic of dual-exonuclease-mediated ATP-33 digestion in the absence (left) and presence (right) of ATP.

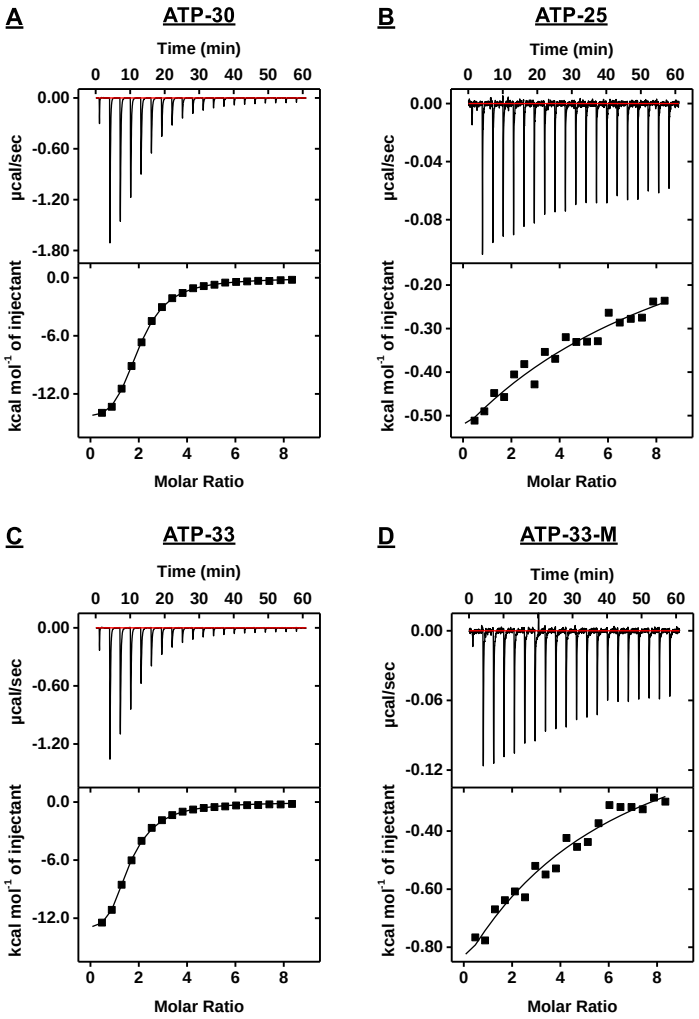

Figure 3-16. Characterization of target binding affinity of ATP-binding aptamers and a mutant using ITC. Top panels present raw data showing the heat generated from each

titration of ATP for (**A**) ATP-30, (**B**) ATP-25, (**C**) ATP-33 and (**D**) ATP-33-M. Bottom panels show the integrated heat of each titration after correcting for dilution heat of the titrant.

We measured the ATP-binding affinity of the 25-nt (ATP-25) and 30-nt (ATP-30) major products as well as the parent aptamer using ITC. Given that the ATP-binding aptamer binds to two ATP molecules, we assessed the binding affinity of ATP-33 and ATP-30 in terms of the target concentration required to reach half-saturation ($K_{1/2}$).[272] We found that the binding affinity of ATP-30 ($K_{1/2}$ = 2.8 ± 0.1 μM, **Figure 3-16A**) was much higher than that of ATP-25 (K_D = 595 ± 86 μM, **Figure 3-16B**) (K_D is used for ATP-25 as it only binds a single target).[109] As with the other two aptamers, the major product of Exo III digestion from target-bound ATP-33 essentially retained the affinity of the undigested aptamer ($K_{1/2}$ = 2.8 ± 0.1 μM, **Figure 3-16C**). We also observed a target-dependent digestion profile with the exonuclease mixture (**Figure 3-14A**, Exo M).

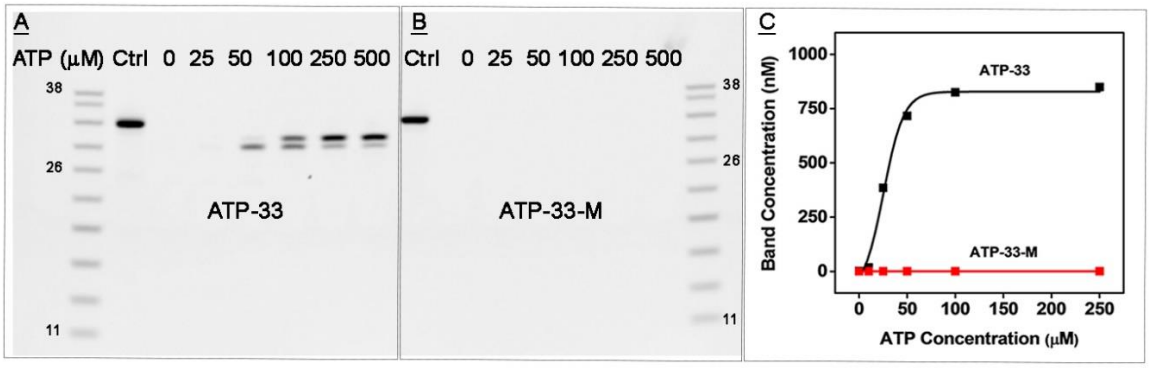

Figure 3-17. Target concentration-dependent inhibition of dual-exonuclease-mediated digestion of an ATP-binding aptamer (ATP-33) and its mutant (ATP-33-M) after a 20 min reaction. PAGE analysis of digestion products at increasing concentrations of ATP for (**A**) ATP-33 and (**B**) ATP-33-M. (**C**) Calibration curve of the calculated concentration of all digestion products versus ATP concentration for ATP-33 (black) and ATP-33-M (red). The intensity of the DNA ladder was used to calculate product concentrations.

To confirm that enzymatic inhibition is specifically due to ATP binding, we engineered an ATP-33 mutant (ATP-33-M) by changing guanine to adenine at position 12

and adenine to thymine at position 23 (**Figure 3-14B**). ATP-33-M possesses no binding affinity to ATP (**Figure 3-16D**) but maintains the same secondary structure as ATP-33, as confirmed by inhibition of Exo I digestion (**Figure 3-14B**, Exo I). As expected, the Exo III and exonuclease mixture digestion profiles of ATP-33-M were identical regardless of the presence or absence of ATP (**Figure 3-14B**, Exo III and Exo M). We performed digestion of ATP-33 and ATP-33-M with the exonuclease mixture at various concentrations of ATP and observed that the concentration of the major 30-nt product of ATP-33 increased with increasing concentrations of target (**Figure 3-17A & C**). Moreover, we found that ATP itself did not inhibit exonuclease activity, even in the presence of 250 μM ATP (**Figure 3-17B & C**). Finally, we carried out our dual-exonuclease-mediated fluorescence assay using ATP-33 and achieved a linear range from 0 to 10 μM, with a detection limit of 250 nM (**Figure 3-14C–E**). These results clearly demonstrated that our exonuclease assay is broadly applicable to diverse aptamers with different secondary structures.

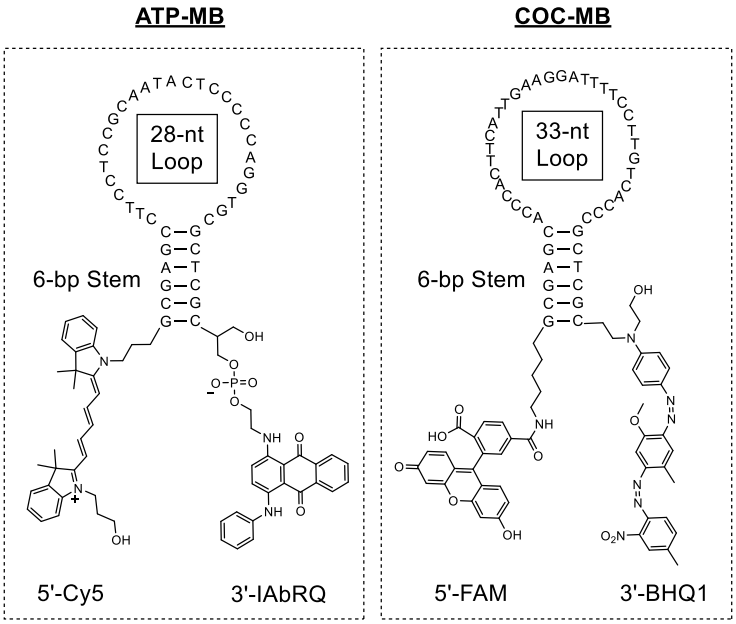

Figure 3-18. Design of molecular beacons for the ATP- and cocaine-binding aptamer digestion products produced by the exonuclease mixture.

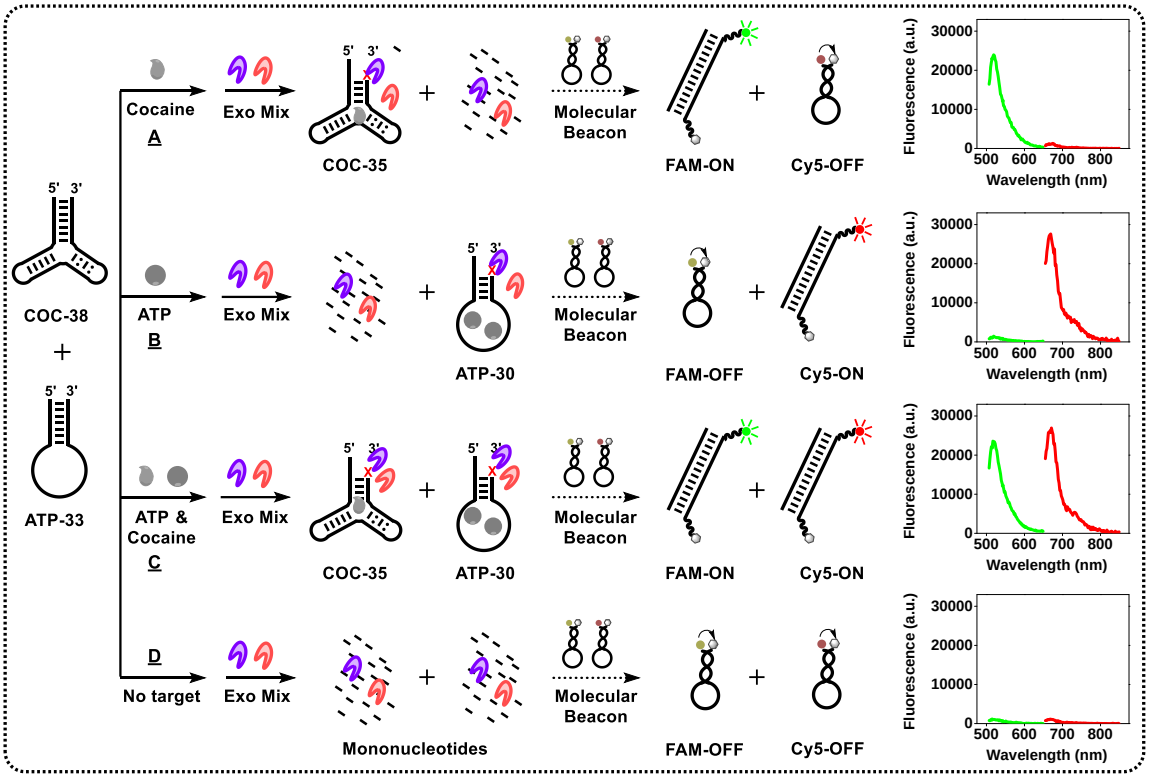

Figure 3-19. Scheme of dual-exonuclease-mediated, molecular beacon-based multiplexed detection of (**A**) cocaine alone, (**B**) ATP alone, (**C**) both cocaine and ATP, and (**D**) neither target. Fluorescence spectra of FAM (green) and Cy5 (red) generated in the presence or absence of 100 μM cocaine and/or ATP.

3.3.7. Multiplex Detection of Cocaine and ATP Using Fluorophore-Quencher-Modified Molecular Beacons.

Multiplex detection is a valuable tool for medical diagnostics, drug screening, and food safety as it enables detection of a multitude of analytes with only a single low-volume sample.[273–275] Our dual-exonuclease-mediated assay can be easily expanded for simultaneous detection of multiple small-molecule analytes. The nucleotide sequences of each aptamer digestion product are known and unique for each aptamer–target pair. These aptamer digestion products can therefore serve as proxies for each individual target and can be quantified using molecular beacons that are designed to specifically hybridize with

an individual digested aptamer strand. The resulting signal can be used to accurately determine the concentration of the target. As a demonstration, we employed our dual-exonuclease-mediated assay with two fluorophore− quencher-modified molecular beacons to simultaneously detect ATP and cocaine. The design of our molecular beacons is very simple, as they share the same 6-bp stem but with different complementary loop regions. The molecular beacon for ATP (ATP-MB) contains a 28-nt loop that is complementary to the 30-nt product and is modified with a 5′-Cy5 and 3′-Iowa Black RQ quencher, while the molecular beacon for cocaine (COC-MB) contains a 33-nt loop that is complementary to the 35-nt product and is modified with a 5′-FAM and 3′-Black Hole Quencher 1 (**Figure 3-18**). To perform the multiplex assay, we digested an aptamer mixture of COC-38 and ATP-33 with both Exo III and Exo I in the presence or absence of cocaine and/or ATP, after which we added a mixture of molecular beacons to achieve target detection (**Figure 3-19**). In the presence of cocaine or ATP, the exonucleases generate specific aptamer digestion products (35-nt from COC-38 or 30-nt product from ATP-33, respectively) that hybridize with their corresponding molecular beacon, separating the fluorophore from the quencher and generating a single target-related fluorescence signal (**Figure 3-19A & B**). When both targets are present, two specific exonuclease digestion products are generated and both COC-MB and ATP-MB hybridize with their respective digestion product, resulting in two fluorescence signals (**Figure 3-19C**). In contrast, both exonucleases completely digest all aptamers in the absence of target, and no fluorescence signal is generated as the beacons remain in a closed and therefore quenched state (**Figure 3-19D**).

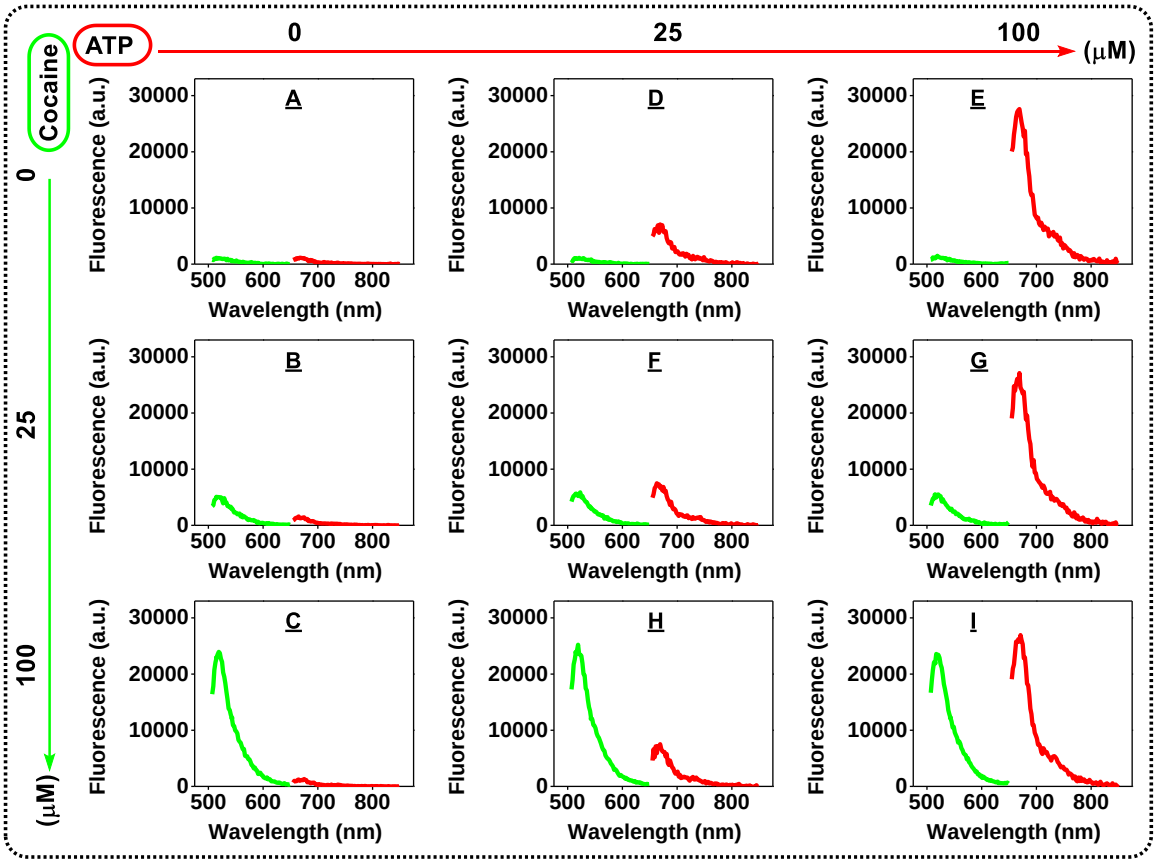

Figure 3-20. Fluorescence spectra of COC-MB (green, emission peak at 520 nm) and ATP-MB (red, emission peak at 668 nm) for exonuclease mixture-treated samples with no, either, or both cocaine and ATP at concentrations of 0, 25, or 100 μM.

We confirmed that our dual-exonuclease-mediated assay performs effectively for multiplex detection of ATP and cocaine (**Figure 3-20**). After 20 min of digesting COC-38 and ATP-33 in the presence of various concentrations of cocaine and ATP (0, 25, or 100 μM), we added EDTA to stop digestion and then added a mixture of beacons (Final concentration: 200 nM COC-MB + 200 nM ATP-MB) to determine target concentrations through quantification of the aptamer digestion products. In the absence of target, minimal fluorescence signal was observed (**Figure 3-20A**). In the presence of 25 or 100 μM cocaine alone, we observed a concentration dependent fluorescence signal at 520 nm (COC-MB;

FAM) but minimal signal at 668 nm (ATP-MB; Cy5) (**Figure 3-20B & C**). Likewise, when ATP alone was present, we observed a concentration-dependent fluorescence signal at 668 nm, with minimal signal detectable at 520 nm (**Figure 3-20D & E**). In the presence of a mixture of both targets at various concentrations, we observed distinct concentration-dependent fluorescence signals at both 520 and 668 nm that corresponded to the presence of cocaine and ATP, respectively (**Figure 3-20F–I**). Notably, the presence of one target did not affect the fluorescence intensity of the other, as the signals generated in the presence of cocaine and ATP were identical regardless of whether the targets were present in a mixture or alone. There was no cross-talk between the molecular beacons since each fluorophore was individually excited at their respective excitation wavelength. At 495 nm, only FAM emits at 520 nm, and we collected the spectra up to 650 nm. Cy5 may become weakly excited at 495 nm, but the emitted light (with a peak at 668 nm) does not overlap with the spectrum of FAM. Conversely, with excitation at 645 nm, only Cy5 emits at 668 nm, as FAM cannot be excited at this wavelength. These results demonstrated the capability of our dual-exonuclease mediated assay to rapidly achieve simultaneous detection of multiple small-molecule targets in a single sample. We then generated calibration curves for our multiplex assay and obtained a linear range from 0 to 100 μM with a measurable detection limit of 15 μM for cocaine (**Figure 3-21A**) and a linear range from 0 to 75 μM with a measurable detection limit of 5 μM for ATP (**Figure 3-21B**).

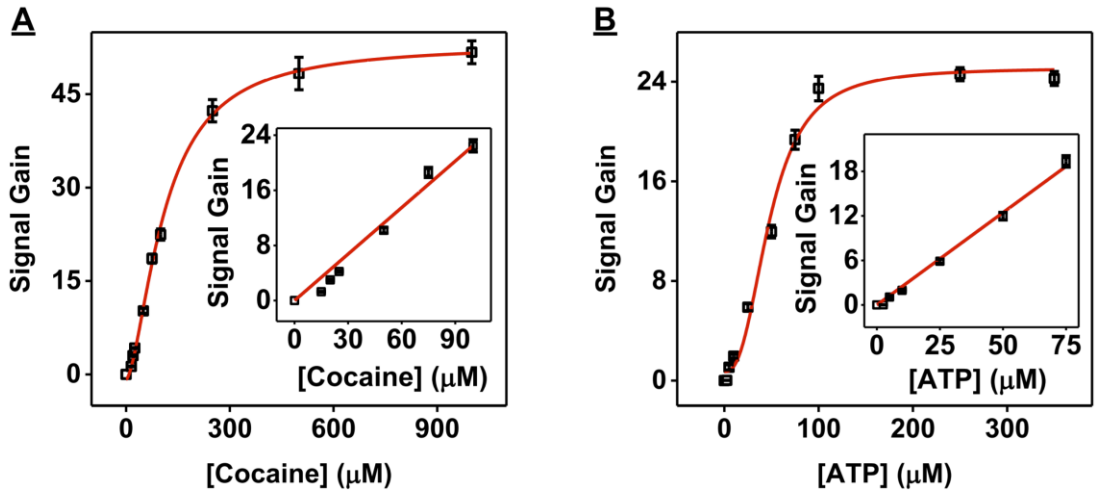

Figure 3-21. Calibration curves of the dual-exonuclease-mediated molecular-beacon-based multiplex assay for the detection of (**A**) cocaine and (**B**) ATP. Inset presents linear range at low concentrations of target. [cocaine] = 0, 15, 20, 25, 50, 75, 100, 250, 500, 1000 μM. [ATP] = 0, 2.5, 5, 10, 25, 50, 75, 100, 250, 350 μM. Each experiment was performed in triplicate and error bars represent the standard deviation of three measurements.

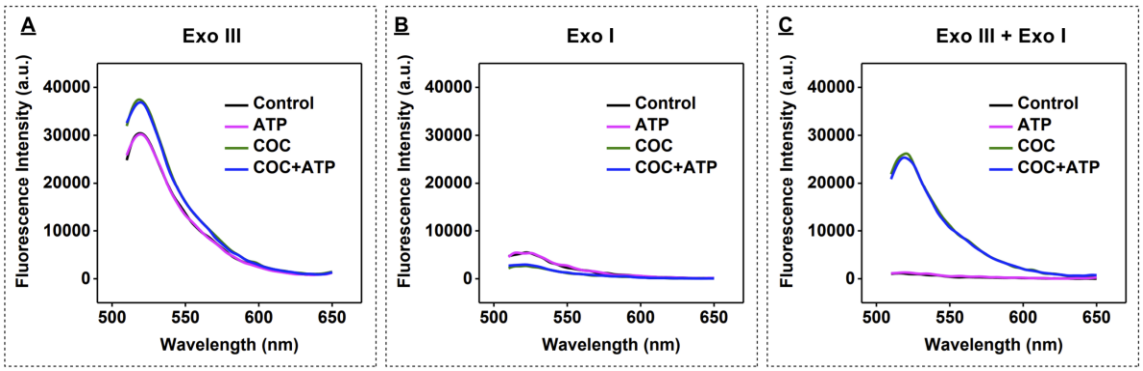

Figure 3-22. Comparison of the performance of the molecular-beacon-based multiplex assay with individual exonucleases versus both. Fluorescence spectra of COC-MB (FAM excitation wavelength = 495 nm) in the presence or absence of 100 μM cocaine, ATP, or both using both COC-38 and ATP -33 with (**A**) Exo III alone, (**B**) Exo I alone, or (**C**) both exonucleases.

To determine the effectiveness of using the exonuclease mixture relative to each enzyme alone, we performed a series of control experiments with cocaine as the target. Specifically, we performed Exo III, Exo I, and dual-exonuclease digestion of a mixture of

COC-38 and ATP-33 with no, either, or both cocaine and ATP at a concentration 100 μM each and then added COC-MB (**Figure 3-22**). Using Exo III alone, we observed a large background signal in the absence of cocaine and a very small signal gain in the presence of cocaine (**Figure 3-22A**). This large background arises from the leftover single-stranded digestion products of nontarget-bound aptamers hybridizing with COC-MB to produce a nonspecific signal. Performing the assay with Exo I alone yielded a low fluorescence signal regardless of the presence or absence of target. This was expected since Exo I cannot digest the duplexed stems of fully folded aptamers, and the molecular beacon can only hybridize with a small fraction of such undigested aptamers in the absence of target. The addition of cocaine stabilizes the folded aptamers, which makes it more difficult to open the molecular beacon, yielding slightly reduced fluorescence (**Figure 3-22B**). When a mixture of Exo III and Exo I was employed, we observed an extremely low background in the absence of the cocaine due to complete digestion of the aptamers, while a clear and large target-related signal gain was obtained in the presence of target (**Figure 3-22C**). These results clearly demonstrate the necessity of using the exonuclease mixture.

3.4. Conclusion.

The binding of small molecules to DNA has been shown to inhibit exonuclease activity.[166,167,169,170] In this work, we found that the binding of small-molecule targets to their respective aptamers can also inhibit exonuclease digestion, and to the best of our knowledge, this is the first work to take advantage of this fact to develop a small-molecule detection assay based on the quantification of aptamer digestion products. We first developed a simple dual-exonuclease-mediated assay that can be generally implemented with unmodified, prefolded aptamers for small-molecule detection. In the absence of target,

Exo III digests the aptamer to produce a single-stranded product, which is then completely digested by Exo I. Aptamer-target binding inhibits Exo III digestion four nucleotides prior to the binding site, leaving behind a double-stranded, target-bound product that remains invulnerable to Exo I digestion. We then used SYBR Gold, a DNA-binding dye that stains DNA in a sequence-independent manner, to quantify the remaining intact aptamer fragments, which reflect the concentration of target present in the sample. This assay allows for rapid, label-free, simple, and sensitive detection of small-molecule targets. We finally demonstrated the generality of our dual-exonuclease-mediated approach and fluorescence assay using aptamers with various secondary structures, including three-way junction and hairpin structures. Importantly, our assay also demonstrated excellent performance in complex biological samples such as saliva and urine.

Our method provides many advantages over existing aptamer-based assays. First, no sequence engineering or aptamer truncation is required, and prefolded aptamers are used instead. Second, target detection is achieved via the quantification of aptamer digestion products instead of target-displaced cDNA, which is preferable given that the use of cDNA usually reduces assay sensitivity.[266,267] Moreover, our assay showed much higher sensitivity compared with previously reported nuclease-assisted aptamer-based assays (**Table 3-2**). For example, we achieved a 50-fold lower limit of detection for cocaine than an Exo I-based assay reported by Lou, which used structure-switching aptamers for target detection.[178] This can be attributed to two factors. First, we employed a prefolded aptamer which has a higher target-binding affinity than the structure-switching aptamer used by Lou. Second, their assay suffered from high background because Exo I could not completely digest all nontarget-bound aptamers. In our assay, the synergistic activity of

Exo III and Exo I completely removed all nontarget-bound aptamers, resulting in minimal background and a robust signal-to-noise ratio.

Since each aptamer−target pair generates a digestion product possessing a unique sequence, we were able to achieve multiplex small-molecule detection within 25 min in a single sample. This was done by quantifying the digestion product of each aptamer−target pair with a complementary fluorophore− quencher-modified molecular beacon. We demonstrated one-pot detection of ATP and cocaine, where each target could be individually or simultaneously detected via the corresponding molecular beacon(s). We observed no cross talk between either aptamer-molecular beacon pair in binary target mixtures, allowing for rapid and robust simultaneous detection. On the basis of these successful results, we believe our assay can be applied for various applications where simultaneous detection of small-molecule targets is key, such as medical diagnostics, drug screening, food safety, environmental monitoring, and biodefense.[273−275] Importantly, since the detection of small-molecule targets in our assay is achieved via quantification of DNA, one can readily envision adopting different DNA signal-amplification strategies such as enzyme-assisted target recycling[179,276] and rolling circle amplification[277,278] to achieve subnanomolar small-molecule detection. Although our assay in its current format is not well suited for on-site detection given the requirement of multiple steps and a fluorimeter, we believe that these limitations can be overcome with the use of a multichannel microfluidic device combined with a colorimetric signal reporter (e.g., gold nanoparticles).

Table 3-2. Comparison of various structure-switching aptamer-based assays for detection of cocaine or ATP.

Sensing element	Detection strategy	Target	Measurable LOD (μM)	Detection time	ref
Structure-switching aptamer	Exonuclease digestion	Cocaine	5	30 min	[178]
Aptamer & cDNA	Strand displacement Nick/polymerase/DNAzyme amplification	Cocaine	0.1	8 h	[175]
Aptamer & cDNA	Strand displacement Nick/polymerase amplification	Cocaine	5	70 min	[172]
Structure-switching aptamer	Exonuclease digestion/ Transferase amplification	Cocaine	0.5	120 min	[176]
Structure-switching aptamer	DNAzyme amplification	ATP	1	60 min	[279]
Aptamer & cDNA	Strand displacement Lipase amplification	Cocaine	5	60 min	[280]
Aptamer & cDNA	Target-induced Quencher-modified cDNA displacement	ATP	50	5 min	[142]
Aptamer & cDNA	Target-induced gold-nanoparticle-modified cDNA displacement	Cocaine	10	5 min	[263]
Structure-switching aptamer	Electrochemical aptamer-based sensing	Cocaine	10	<1 min	[281]
Structure-switching aptamer	Target-induced stem formation	Cocaine	10	<1 min	[114]
Split aptamer	Target-induced split aptamer assembly	Cocaine	12.5	60 min	[127]
Split aptamer	Target-induced split aptamer assembly	ATP	20	60 min	[127]
Split aptamer	Target-induced split aptamer assembly	Cocaine	1	<1 min	[133]
Split aptamer	Target-induced split aptamer assembly	ATP	1	< 1 min	[133]
Structure-switching aptamers	Target-induced disassembly of fluorophore-quencher modified aptamer beacon	ATP	1	< 1 min	[143]
Pre-folded aptamer	Exonuclease digestion	Cocaine	0.1	25 min	This work
Pre-folded aptamer	Exonuclease digestion	ATP	0.25	20 min	This work

CHAPTER 4: Accelerating Post-SELEX Aptamer Engineering Using Exonuclease Digestion

4.1. Introduction.

Systematic evolution of ligands by exponential enrichment (SELEX) is used to isolate nucleic-acid-based bioaffinity elements known as aptamers from random oligonucleotide libraries.[23,24] This multistep process involves iterative rounds of partitioning target-binding oligonucleotides from nonbinding sequences and amplification of the binders via polymerase chain reaction (PCR).[37] Aptamers offer a number of advantages as molecular sensing reagents relative to antibodies, including greater thermostability, lower cost, excellent reproducibility of manufacturing, and the ease with which they can be engineered or chemically modified.[32,33] However, SELEX sometimes fails to yield aptamers with suitable affinity and specificity for an intended application. This can occur for a variety of reasons. First, since starting oligonucleotide libraries can typically encompass anywhere from 10^{18} to 10^{40} possible unique sequences (for libraries containing 30−70 random nucleotides), it is unrealistic to screen every possible sequence in a SELEX experiment, and this will inevitably exclude high quality aptamer candidates.[35,282] Second, due to the low copy number of each sequence in the starting library, oligonucleotides with desirable binding properties can easily be lost during the early rounds of SELEX.[73,283] Finally, these aptamers can be eliminated if they have low PCR amplification efficiency due to their sequence and/or structure.[71,100,101]

Several strategies can be employed to derive higher performance aptamers upon the completion of SELEX. In doped-SELEX, selection is performed on a partially randomized library based on a parent aptamer sequence obtained from a prior SELEX effort.[40,102]

Doped-SELEX allows for the exploration of the sequence space close to the original aptamer, encompassing sequences that may have been entirely excluded or lost during earlier rounds.[284] However, this method is greatly biased toward the original parent sequence. Based on calculations by Knight and Yarus, the copy number of individual unique sequences decreases exponentially with increasing numbers of mutations from the original sequence.[106] As a result, sequences containing multiple mutations have a high likelihood of being excluded from the doped-SELEX pool. Although doped-SELEX has proven successful in a few instances, the extent of improvement is generally limited, and the success rate varies depending on the target and aptamer.[284] An alternative approach is to design and synthesize a panel of aptamer mutants, and then individually test their binding properties to find the best sequence. Nucleotides may be altered in either the target-binding domain[109,112] or surrounding scaffold regions,[103,108,110] with guidance from genetic algorithms,[107] computationally predicted secondary structures,[103,108] or three-dimensional structures based on nuclear magnetic resonance (NMR) data.[110,111] This method overcomes the competition problem associated with doped-SELEX because mutants are screened individually using instrument-based approaches or microarrays. Techniques such as surface plasmon resonance (SPR) spectroscopy,[285] isothermal titration calorimetry (ITC),[77] and microscale thermophoresis[80] can provide accurate assessments of the binding parameters of the mutants. However, these experiments are costly and labor-intensive and also have low throughput as only a single aptamer−target pair can be tested at a time. Novel nano calorimeters have been reported that allow for simultaneous high-throughput binding affinity determination.[286,287] However, these instruments are not yet commercially available, and it is difficult to fabricate these devices without sufficient resources and

expertise. Microarray-based techniques enable high-throughput characterization of large pools of aptamer mutants[288] but require targets that are either inherently fluorescent or labeled with a fluorophore.[288–290] This is feasible for protein targets[288,289] but is generally impractical for the screening of small-molecule binding aptamers because such labeling could alter binding affinity.

We demonstrate here an efficient and cost-effective exonuclease-based fluorescence assay for accurate, rapid, and label-free screening of the binding affinity and specificity of a panel of DNA aptamers. This assay is based on our previous finding that a mixture of exonuclease III (Exo III), a 3′-to-5′ double-strand DNA exonuclease, and exonuclease I (Exo I), a 3′-to-5′ single-strand DNA exonuclease, digests unbound aptamers into mononucleotides, but such digestion is inhibited for target-bound aptamers.[291,292] We first digested an ochratoxin binding DNA aptamer and its six mutants[110] with a mixture of Exo III and Exo I and demonstrated that the kinetics of aptamer digestion are correlated with the aptamer's relative target-binding strength. We then exploited this finding to sensitively screen the affinity and specificity of engineered aptamer mutants to identify and confirm high-performance mutants. To demonstrate the generality of this assay, we then used this method to improve the specificity of a previously described DNA aptamer that binds indiscriminately to ATP and its analogues.[292] Specifically, we designed 13 aptamer mutants from this aptamer and performed our exonuclease-based assay with 59 aptamer−ligand pairs. We identified mutations at various positions surrounding the binding domain that greatly affect affinity and specificity and obtained two new structure-switching aptamers that retain the parent aptamer's affinity for adenosine (ADE) but not for its phosphorylated analogues. We used these two aptamers to fabricate an electrochemical

aptamer-based (E-AB) sensor that could sensitively detect ADE with a measurable limit of detection of 1 μM and minimal response to adenosine analogues in 50% serum. We finally demonstrated the generality of our method to sensitively profile the binding affinities of protein-binding aptamers. Our exonuclease-based screening strategy is a facile single-step fluorescence assay and therefore could be easily adapted into a high-throughput format using liquid-handling systems. Such a screening platform could greatly simplify and accelerate the identification of small-molecule-binding aptamers with desirable binding properties for various applications.

4.2. Experimental section.

4.2.1. Reagents.

Exonuclease III (Escherichia coli) (Exo III) (100 U/μL) and exonuclease I (E. coli) (Exo I) (20 U/μL) were purchased from New England Biolabs. Human α-thrombin and human factor X were purchased from Haematologic Technologies. Human plasma immunoglobulin G and human myeloma plasma λ immunoglobulin E were purchased from Athens Research and Technology. Deionized (DI) water with resistivity of 18 MΩ·cm was obtained from a Millipore water dispensing system. SYBR Gold was purchased from Invitrogen. Formamide, 0.5 M EDTA solution, glycerol, and sodium dodecyl sulfate (SDS) were purchased from Fisher Scientific. Ochratoxin A and B were purchased from Cayman Chemicals and dissolved in 100% DMSO to a final concentration of 4 mM. Adenosine-5′-triphosphate (ATP) disodium salt trihydrate was purchased from MP Biomedical. Adenosine-5′-diphosphate (ADP) sodium salt, adenosine-5′-monophosphate (AMP) sodium salt, and adenosine (ADE) were purchased from Sigma-Aldrich. ATP, ADP, AMP, and ADE stock solutions were prepared by dissolving in DI water to a final concentration

of 2.5 mM followed by the addition of Tris base and NaCl to reach a molar equivalent of $2Na^+ \cdot 2Tris \cdot 1ATP$/ analogue. HCl was added as needed to neutralize the pH of the solution. A blank solution was created by dissolving Tris base and NaCl in DI water to a final concentration of 5 mM and neutralizing the solution with HCl. All other chemicals were purchased from Sigma-Aldrich. Unmodified oligonucleotides were purchased from Integrated DNA Technologies with standard desalting purification; they were dissolved in PCR-quality water, and their concentrations were measured using a NanoDrop 2000 (Thermo Fisher Scientific) spectrophotometer. Thiolated methylene blue (MB)-modified aptamers were purchased from LGC Biosearch Technologies with dual-HPLC purification and dissolved in TE Buffer (10 mM Tris− HCl + 1 mM EDTA, pH 8.0). All DNA sequences are listed in **Table 4-1**. Nunc 384-well black plates were purchased from Thermo Fisher Scientific.

Table 4-1. All oligonucleotide sequences used in chapter 4.

Sequence ID	Sequence (5'–3')
OBAwt	GGG GTG AAA CGG GTC CCG
OBA1	CGG GGT GAA ACG GGT CCC G
OBA2	GGG GCG AAG CGG GTC CCG
OBA3	CGG GGC GAA GCG GGT CCC G
OBA4	GGG GTG AAA CGG TCC CG
OBA5	CCG GGG CGA AGC GGG TCC CGG
OBA6	GCG GGG CGA AGC GGG TCC CGC
ATPwt	CGC ACC TGG GGG AGT ATT GCG GAG GAA GGT GCG
G10A	CGC ACC TGG AGG AGT ATT GCG GAG GAA GGT GCG
G10T	CGC ACC TGG TGG AGT ATT GCG GAG GAA GGT GCG
G10C	CGC ACC TGG CGG AGT ATT GCG GAG GAA GGT GCG
A13T	CGC ACC TGG GGG TGT ATT GCG GAG GAA GGT GCG
A13G	CGC ACC TGG GGG GGT ATT GCG GAG GAA GGT GCG
A13C	CGC ACC TGG GGG CGT ATT GCG GAG GAA GGT GCG

A23T	CGC ACC TGG GGG AGT ATT GCG GTG GAA GGT GCG
A23T-30	CGC ACC TGG GGG AGT ATT GCG GTG GAA GGT
A23T-29	CGC ACC TGG GGG AGT ATT GCG GTG GAA GG
A23G	CGC ACC TGG GGG AGT ATT GCG GGG GAA GGT GCG
A23C	CGC ACC TGG GGG AGT ATT GCG GCG GAA GGT GCG
A26T	CGC ACC TGG GGG AGT ATT GCG GAG GTA GGT GCG
A26G	CGC ACC TGG GGG AGT ATT GCG GAG GGA GGT GCG
A26C	CGC ACC TGG GGG AGT ATT GCG GAG GCA GGT GCG
G10T-A23G	CGC ACC TGG TGG AGT ATT GCG GGG GAA GGT GCG
G10T-A23G-30	CGC ACC TGG TGG AGT ATT GCG GGG GAA GGT
G10T-A23G-29	CGC ACC TGG TGG AGT ATT GCG GGG GAA GG
G10T-A23G-29-MB	/Thiol-C6/-CCT GGT GGA GTA TTG CGG GGG AAG G-/MB/
A23T-29-MB	/Thiol-C6/-CGC TCC TGG GGG AGT ATT GCG GTG GAAG GTTT-/MB/
A10-excised	GTA TTG CGG AGG AAG GTT TTT AAC CTT CGG GG
Tasset	AGT CCG TGG TAG GGC AGG TTG GGG TGA CT
Bock	GGT TGG TGT GGT TGG
Bock-hang	TAA GTT CAT CTC CCC GGT TGG TGT GGT TGG
IgE Aptamer	GGG GCA CGT TTA TCC GTC CCT CCT AGT GGC GTG CCC C

a. Mutated nucleotides are colored red and underlined
b. /Thiol-C6/ represents a 5’ modified thiol group with a six-carbon spacer
c. /MB/ represents a 3’ modified methylene blue redox reporter

4.2.2. Aptamer Digestion Experiments.

Unless otherwise specified, all digestion experiments were performed using the following procedure at 25 °C in 50 µL reaction volumes. Enzyme reaction buffer consisted of 8.1 mM Na_2HPO_4, 1.9 mM KH_2PO_4, 10 mM $MgCl_2$, 0.1 mg/mL bovine serum albumin (BSA), 2.5% DMSO, pH 7.4, for ochratoxin-binding aptamers, 10 mM Tris−HCl, 20 mM NaCl, 1.5 mM $MgCl_2$, 0.1 mg/mL BSA, pH 7.4, for ATP-analogue-binding aptamers, or 10 mM Tris−HCl, 137 mM NaCl, 2.7 mM KCl, 1 mM $MgCl_2$, 0.1 mg/ mL BSA, pH 7.4, for thrombin- and immunoglobulin E-binding aptamers. Aptamers were dissolved in their respective buffer (final concentration 1 µM for ochratoxin- and ATP-analogue-binding

aptamers and 0.5 μM for thrombin- and immunoglobulin E-binding aptamers), heated to 95 °C for 10 min, and then immediately cooled on ice, followed by the addition of salts and BSA. Next, various concentrations of ligand or blank solution were added to the reaction mixture, and the mixture was incubated in a thermal cycler (C1000 Touch, Bio-Rad) at 25 °C for 60 min, after which 5 μL of enzymes (final concentrations: 0.025 U/μL Exo III and 0.05 U/μL Exo I) were added to each reaction mixture. An amount of 5 μL of sample was collected at various time-points and loaded directly into the wells of a Nunc 384-well black plate containing 10, 15, and 20 μL of quench solution (final concentration: 10 mM Tris−HCl, 12.5% formamide, 10 mM EDTA, 1× SYBR Gold) used for ochratoxin-, thrombin- and immunoglobulin E-, and ATP-analogue-binding aptamers, respectively. Fluorescence intensity at 545 nm was recorded using a Tecan Infinite M1000 PRO microplate reader with excitation at 495 nm. All error bars represent the standard error of fitting with the first-order rate equation.

4.2.3. Analysis of Aptamer Digestion Rates.

Data analysis was performed using the Origin 2019 software. The time-dependent fluorescence plots obtained from the aptamer digestion experiments were fit using first-order reaction kinetics described by **eq 4-1**:

$$F_t = F_0 2^{-t/t_{1/2}} + C$$

where t is the time of digestion in minutes, F_t is the fluorescence intensity at time t, F_0 is the maximum fluorescence intensity of the inhibition product, C is a constant to correct for background fluorescence, and $t_{1/2}$ is the half-life of the reaction in minutes. The first time-point was excluded from fitting unless otherwise specified. During fitting, bounds were placed on F_0 and C; these values could vary between 75−100% and 0−10% of the

fluorescence intensity of the undigested aptamer, respectively. Error bars represent the standard error of fitting. The three parameters used to determine target-binding-induced inhibition of enzyme digestion are the $t_{1/2}$ ratio, first-order rate reduction, and resistance value. The $t_{1/2}$ ratio was obtained by dividing the $t_{1/2}$ obtained in the presence of ligand by the $t_{1/2}$ obtained from the blank sample. On the basis of the fitted parameter of $t_{1/2}$, the first-order reaction rates (k) can also be obtained by dividing −ln(2) by $t_{1/2}$. Rate reduction was calculated by the expression $1 - (k_{ligand}/k_{blank})$. Finally, resistance values were calculated as previously described.[89] The area under the curve (AUC) of the fluorescence digestion plots was determined using Origin 2019 software, and the resistance value was calculated using the expression $(AUC_{ligand}/ AUC_{blank}) - 1$.

4.2.4. Reverse ITC Experiments.

Reverse ITC experiments were performed with a MicroCal ITC200 instrument (Malvern) at 23 °C. For ochratoxin-binding aptamer titrations, the following buffer was used: 8.1 mM Na_2HPO_4, 1.9 mM KH_2PO_4, 10 mM $MgCl_2$, and 2.5% DMSO, pH 7.4. For thrombin-binding aptamer titrations, the following buffer was used: 10 mM Tris−HCl, 137 mM NaCl, 2.7 mM KCl, and 1 mM $MgCl_2$, pH 7.4. For each experiment, 60 μL of aptamer solution was heated at 95 °C for 10 min in its respective buffer and cooled on ice, after which salts were added and then DMSO was added as appropriate. For ochratoxin-binding aptamer titrations, the cell was loaded with 300 μL of 15 μM ochratoxin A or ochratoxin B in reaction buffer, and the syringe was loaded with 250 or 500 μM ochratoxin-binding aptamer, respectively. For thrombin-binding aptamer titrations, 5 or 7.5 μM thrombin in buffer was loaded in the cell and 50 or 75 μM thrombin-binding aptamer was loaded in the syringe, respectively. Concentrations of aptamer and ligands used are listed in **Table 4-2**.

Each titration consisted of an initial purge injection of 0.4 μL and 19 successive injections of 2 μL aptamer, with a spacing of 180 s between injections. The raw data was first corrected for the dilution heat of the aptamer, and then analyzed with the MicroCal analysis kit integrated into the Origin 7 and fitted using a single-site model to obtain K_D.

Table 4-2. Aptamers, ligands, and aptamer/ligand concentration used for reverse ITC experiments and determined K_D.

Aptamer	Ligand	[Ligand] (μM)	[Aptamer] (μM)	K_D (μM)
OBA1	OTA	15	250	5.5 ± 0.2
OBA1	OTB	15	500	74.1 ± 9.5
OBA3	OTA	15	250	1.8 ± 0.1
OBA3	OTB	15	500	25.5 ± 1.2
OBA5	OTA	15	250	3.4 ± 0.1
OBA5	OTB	15	500	59.9 ± 6.9
Tasset	Thrombin	5	50	0.0136 ± 0.0031
Bock	Thrombin	5	50	0.0231 ± 0.0054
Bock-hang	Thrombin	7.5	75	0.097 ± 0.019

4.2.5. Isothermal Titration Calorimetry Experiments for ATP-Analogue-Binding Aptamers.

ITC experiments for the ATP-binding aptamer and its mutants were performed with a MicroCal ITC200 instrument at 23 °C in reaction buffer of 10 mM Tris−HCl, 20 mM NaCl, and 1.5 mM $MgCl_2$, pH 7.4. For each experiment, 300 μL of a 20 μM ATP-analogue-binding aptamer solution was heated at 95 °C for 10 min in Tris buffer and cooled down on ice, after which salt was added. The syringe was then loaded with ADE, AMP, ADP, or ATP in reaction buffer. Concentrations of aptamer and ligands are listed in **Table 4-3**. Each titration consisted of an initial purge injection of 0.4 μL and either 38 successive injections

of 1 μL of ligand or 19 successive injections of 2 μL of ligand, with a spacing of 120−180 s between injections. For titrations of AMP, ADP, or ATP to A23T-29 and G10T−A23G-29, a total of three successive titrations were performed to saturate the aptamer with ligand. The raw data was first corrected for the dilution heat of the ligand, and then analyzed with the MicroCal analysis kit integrated into the Origin 7 software and fitted with a two-site sequential binding model to yield K_{D1} and K_{D2}.

Table 4-3. ATP-binding aptamers, ligands, and ligand concentration used for ITC and determined K_{D1}, K_{D2}, and $K_{1/2}$.

Aptamer	Ligand	[Ligand] (μM)	Injection volume (μL)	K_{D1} (μM)	K_{D2} (μM)	$K_{1/2}$ (μM)
ATPwt	ADE	800	1	1.3 ± 0.1	13.7 ± 0.3	4.2 ± 0.1
ATPwt	AMP	800	1	6.4 ± 0.1	30.9 ± 0.4	14.1 ± 0.2
ATPwt	ADP	800	1	2.1 ± 0.1	19.1 ± 0.3	6.3 ± 0.1
ATPwt	ATP	800	1	4.4 ± 0.1	23.9 ± 0.4	10.2 ± 0.2
A23T	ADE	1,800	1	7.0 ± 0.5	29.1 ± 0.6	14.3 ± 0.5
A23T-30	ADE	1,800	1	13.1 ± 0.5	26.6 ± 0.6	18.6 ± 1.7
A23T-29	ADE	1,800	1	35.3 ± 1.0	39.8 ± 0.6	37.4 ± 6.2
A23T-29	AMP	1,200	2	NA	NA	NA
A23T-29	ADP	1,200	2	169.5 ± 3.4	480.8 ± 9.7	285.4 ± 5.7
A23T-29	ATP	1,200	2	327.8 ± 17.2	505.0 ± 28.1	406.3 ± 21.8
G10T-A23G	ADE	1,200	1	7.3 ± 0.2	32.4 ± 0.5	15.3 ± 0.2
G10T-A23G-30	ADE	1,200	1	8.8 ± 0.2	37.1 ± 0.6	18.1 ± 0.4
G10T-A23G-29	ADE	1,200	1	9.2 ± 0.2	37.4 ± 0.6	18.5 ± 0.4
G10T-A23G-29	AMP	1,200	2	352.1 ± 12.4	131.4 ± 4.3	214.7 ± 7.2
G10T-A23G-29	ADP	1,200	2	167.9 ± 3.0	142.6 ± 2.4	162.9 ± 2.8
G10T-A23G-29	ATP	1,200	2	50.2 ± 1.4	591.7 ± 13.6	171.9 ± 4.3
A23G	ADE	1,500	1	6.7 ± 0.4	28.3 ± 0.9	13.8 ± 0.6
A23C	ADE	1,500	1	1.5 ± 0.1	17.1 ± 0.5	5.0 ± 0.3
A26T	ADE	1,000	1	8.6 ± 0.6	1297 ± 153	105.6 ± 9.5
A26G	ADE	1,000	1	5.5 ± 0.6	3246 ± 1897	133.6 ± 33.0
A10-excised	ADE	1,000	2	311.5 ± 11.3	NA	NA

4.2.6. Polyacrylamide Gel Electrophoresis (PAGE) Analysis of Digestion Products.

Digestion products were analyzed by denaturing PAGE by combining 5 µL of sample with 10 µL of formamide loading buffer (75% formamide, 10% glycerol, 0.125% SDS, 10 mM EDTA, and 0.15% (w/v) xylene cyanol), and then loading 6 µL of each sample into the wells of a 15% denaturing PAGE gel. Separation was carried out at 6 V/cm for 30 mins followed by 25 V/cm for 3 h in 0.5 × TBE. The gel was stained with 1× SYBR Gold solution for 25 mins and imaged using a ChemiDoc MP Image system (Bio-Rad).

4.2.7. Circular Dichroism (CD) Spectroscopy.

All CD experiments were performed at room temperature in 10 mM Tris-HCl, 20 mM NaCl, and 1.5 mM $MgCl_2$ (pH 7.4) using a Jasco J-815 circular dichroism spectropolarimeter. Prior to each experiment, 1.5 µM aptamer (final concentration) was heated to 95 °C for 10 mins in Tris buffer and then immediately cooled on ice. Afterwards, salt was added. Blank solution or ADE was then added to aptamer solution to a final concentration of 25, or 50 µM. 300 µL of sample was transferred into a 1 cm quartz cuvette (Hellma Analytics) for measurements. The following parameters were used: 210 to 310 nm scan range, 50 nm/min scan speed, 5 mdeg sensitivity, 4 s response time, 1 nm bandwidth, and 5 accumulation scans total. Reference spectra of reaction buffer without aptamer were taken with 0, 25, or 50µM ADE. Reference spectra were subtracted from CD spectra collected in the presence of aptamer with ADE. To correct for differences in nucleotide length, the CD signal was converted to the mean residue molar extinction coefficient ($\Delta\varepsilon_{MR}$).[293]

4.2.8. Electrochemical Aptamer-Based Adenosine Sensor Fabrication.

Gold disk electrodes (CH Instruments) (2 mm in diameter) were polished with 1 μm diamond slurry (Buehler) followed by 0.05 μm alumina suspension. To remove bound particulates, electrodes were sonicated in 70% ethanol solution for 5 min, and then in DI for another 5 min. Electrochemical cleaning was performed using a previously published protocol.[294] The charge consumed during reduction of surface gold oxide in 0.05 M H_2SO_4 was used to calculate the surface area of each electrode, using the previously reported value of 390 ± 10 μC/cm^2.[295] The roughness factor of the electrodes was calculated based on the ratio between the electrochemically measured area and the geometric surface area and ranged from 1.0 to 1.05. Sensor fabrication involved a multistep process. First, 2 μL of 200 μM thiolated MB-modified aptamer (A23T-29-MB or G10T−A23G-29-MB) was mixed with 8 μL of 100 mM tris(2-carboxyethyl)phosphine (TCEP) at room temperature for 2 h to reduce disulfide bonds. The aptamer solution was then diluted with 1×PBS buffer (10 mM phosphate buffer, 1 M NaCl, 1 mM $MgCl_2$, pH 7.2) to a final DNA concentration of 50 nM for A23T-29-MB or G10T−A23G-29-MB alone or 25 nM of each aptamer for the dual-aptamer electrode. Freshly cleaned gold electrodes were dried under a nitrogen stream, and then incubated in 250 μL of thiolated MB-modified aptamer solution overnight at room temperature. The electrodes were then backfilled with 1 mM 6-mercapto-1-hexanol for 2 h at room temperature. After sensor fabrication, the electrode surface coverage was determined as previously reported.[296] The electrodes were stored in 10 mM Tris buffer (pH 7.4) for at least 1 h prior to use.

4.2.9. Electrochemical Measurements.

Electrochemical measurements were taken using a CHI 760 bipotentiostat (CH Instruments). Prior to measurement, the electrodes were incubated in 10% SDS for 15 mins followed by a 20s DI water rinse, after which the electrode was stored in 10 mM Tris-HCl, 20 mM NaCl, and 1.5 mM $MgCl_2$ (pH 7.4) reaction buffer. All measurements were performed at room temperature using a three-electrode system, including an aptamer-modified gold working electrode, a platinum wire counter electrode, and an Ag/AgCl (3M KCl) reference electrode (CH Instruments) in a 2 mL electrochemical cell. Square-wave voltammetry was used for sensor measurements, and voltammograms were collected from -0.1 to -0.4 V (vs Ag/AgCl) using a frequency of 200 Hz with an amplitude of 25 mV. Calibration curves were collected by challenging the E-AB sensors with varying concentrations of ligand dissolved in reaction buffer or 50% fetal bovine serum diluted in reaction buffer. The sensor was equilibrated for 1 min at each target concentration prior to measurements. Signal gain (SG) was calculated using **eq. 4-2**:

$$SG = [(I - I_0)/I_0)] \times 100$$

here I_0 and I are the peak currents obtained in the absence and presence of target, respectively. Cross-reactivity of the sensor to AMP, ADP, ATP, GTP, CTP and UTP was calculated relative to the signal gain produced by 100 µM ADE.

4.3. Results and Discussion.

4.3.1. Exonuclease Fluorescence Assay to Characterize Affinity and Specificity of Ochratoxin-Binding Aptamers.

We recently developed a sensitive and label-free aptamer-based assay for small-molecule detection using Exo III and Exo I.[292] Specifically, we determined that a mixture

of Exo III and Exo I digests aptamers into mononucleotides (**Figure 4-1A**, left), whereas the digestion of target-bound aptamers is stalled several bases prior to the binding domain (**Figure 4-1A**, right). We quantified the concentration of these partially digested aptamers at a single time-point using SYBR Gold (**Figure 4-1A**) and used this measurement to determine target concentration. On the basis of these findings, we hypothesized that these exonucleases could be used to rapidly profile aptamer-binding affinity and specificity and that the kinetics of aptamer digestion could potentially be used to accurately determine relative ligand-binding affinity.

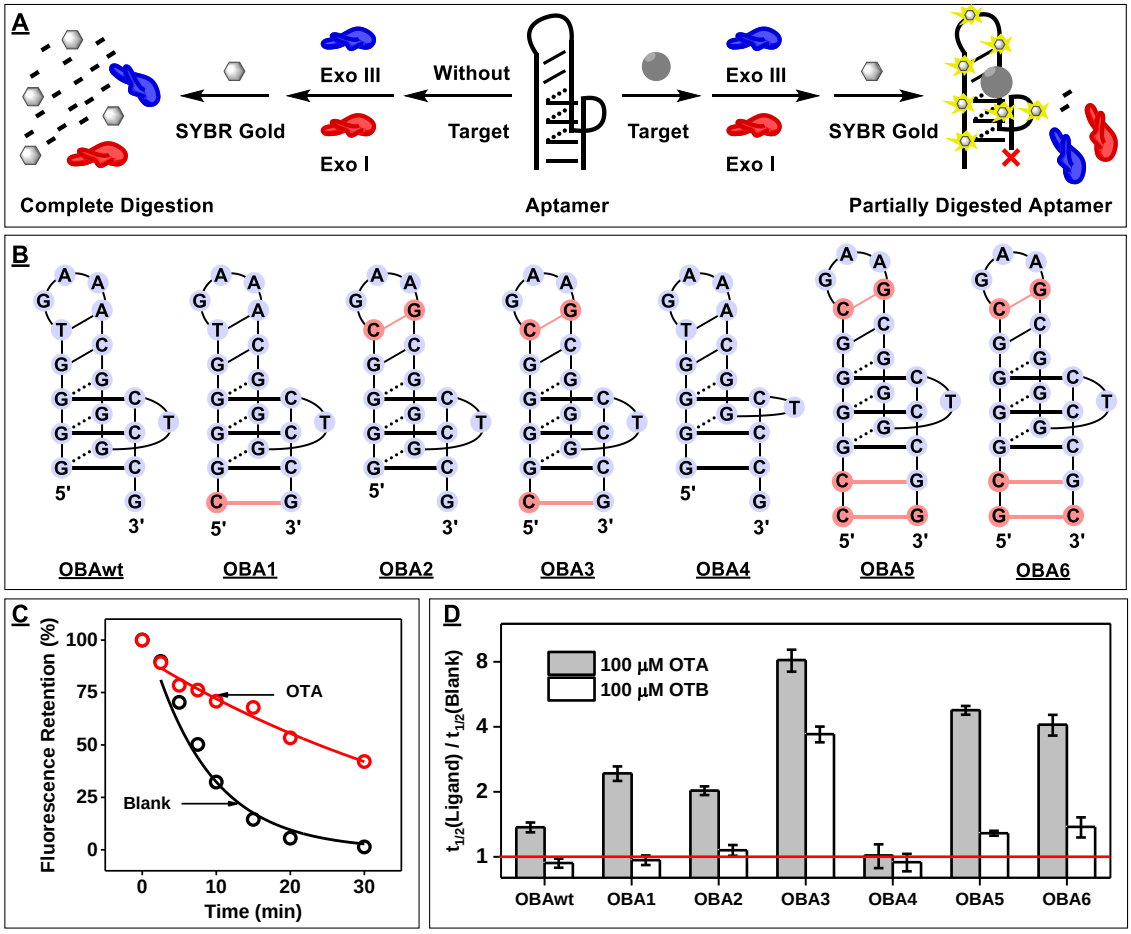

Figure 4-1. Design and characterization of binding properties of OBAwt and six mutant derivatives. (**A**) Secondary structure of ligand-bound aptamers, with mutated nucleotides relative to the OBAwt parent sequence highlighted in red. (**B**) Schematic of the

exonuclease digestion assay based on Exo III and Exo I. (**C**) Time-course plot of OBA3 digestion by Exo III and Exo I in the absence and presence of 25 μM ochratoxin A (OTA). (**D**) Half-life ($t_{1/2}$) ratio of the digestion reaction was used to determine the relative binding affinity of OBAwt and its six mutants to 100 μM OTA or OTB. The red line indicates a $t_{1/2}$ ratio of 1, which means there was no inhibition of aptamer digestion.

To demonstrate this, we performed a series of exonuclease digestion experiments with a well-studied ochratoxin A (OTA) aptamer, OBAwt, and a variety of derivatives of this sequence (**Figure 4-1B**). Xu et al. reported that the binding domain of OBAwt is composed of a G−G−C DNA triplex with a short hairpin and a GAA loop.[110] They subsequently engineered five mutants via base mutations and insertions that stabilize either the DNA triplex (OBA1), the short hairpin (OBA2), or both structures (OBA3, OBA5, and OBA6) and characterized their binding affinities. To demonstrate the importance of the DNA triplex, they also generated one additional mutant (OBA4) by deletion of a guanine within the triplex, resulting in complete loss of affinity. These sequences and DNA triplex structure have not been previously tested using the exonuclease mixture. We first digested the 19-nt OBA3 sequence, which tightly binds OTA with a dissociation constant (K_D) of 1.4 μM.[110,297] The digestion process was monitored by collecting aliquots of the reaction mixture at different time-points, followed by quenching with EDTA and fluorescence-based quantification of the remaining oligonucleotides with SYBR Gold. In the absence of the target, OBA3 was completely digested into mononucleotides and the fluorescence intensity rapidly decreased exponentially within 30 min (**Figure 4-1C**, blank). However, digestion of OBA3 was inhibited and the decrease of fluorescence intensity was greatly reduced in the presence of 25 μM OTA (**Figure 4-1C**, OTA), and a further increase in inhibition was observed when the concentration of OTA was raised to 100 μM (**Figure 4-**

2A). This suggests that aptamer binding to OTA inhibits enzymatic digestion in a concentration-dependent manner.

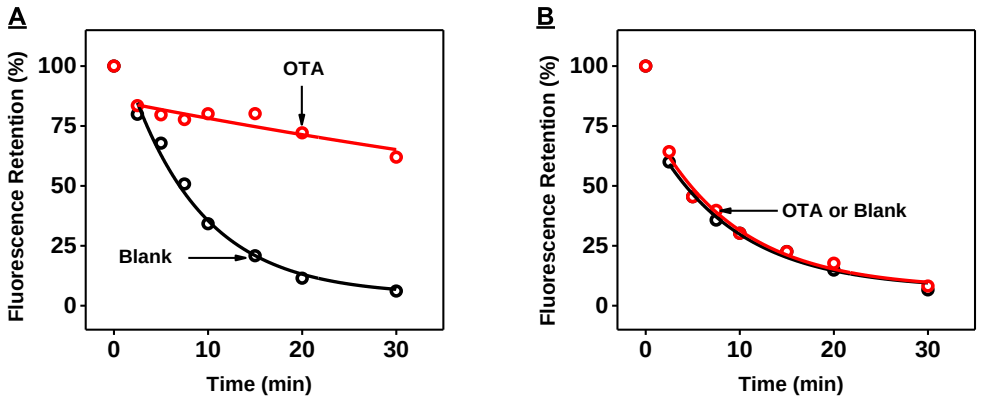

Figure 4-2. Fluorescence time-course of the digestion of (**A**) OBA3 and (**B**) OBA4 with the mixture of Exo III and Exo I in the absence (black) and presence of 100 µM OTA (red).

To confirm that enzyme inhibition is a result of aptamer–target binding, we performed this same digestion with OBA4, which was reported to have no affinity for OTA.[110] We observed no inhibition of digestion of OBA4 in the presence of OTA (**Figure 4-2B**), which demonstrates that OTA itself does not inhibit enzymatic activity in the case where the aptamer does not bind to the ligand. We observed that the enzymatic digestion of OBA3 occurred exponentially, possibly indicating first-order reaction kinetics. To confirm this, we digested various concentrations of OBA3 (0.25–2 µM) with or without 25 µM OTA. Both in the absence and presence of OTA, the natural logarithm of fluorescence plotted against time at each aptamer concentration followed a linear trend (**Figure 4-3**), which indicates that digestion obeys first-order reaction kinetics under the experimental conditions we employed.[298] To determine the half-life ($t_{1/2}$) of digestions, we fit each time-course plot using a first-order exponential decay equation (see section 4.2.3). Notably, the $t_{1/2}$ of aptamer digestion in the presence of 25 µM OTA was approximately 4.8-fold higher

relative to that in the absence of OTA, showing that OTA strongly binds to the aptamer and the binding inhibits aptamer digestion by the enzyme mixture (**Figure 4-1C**).

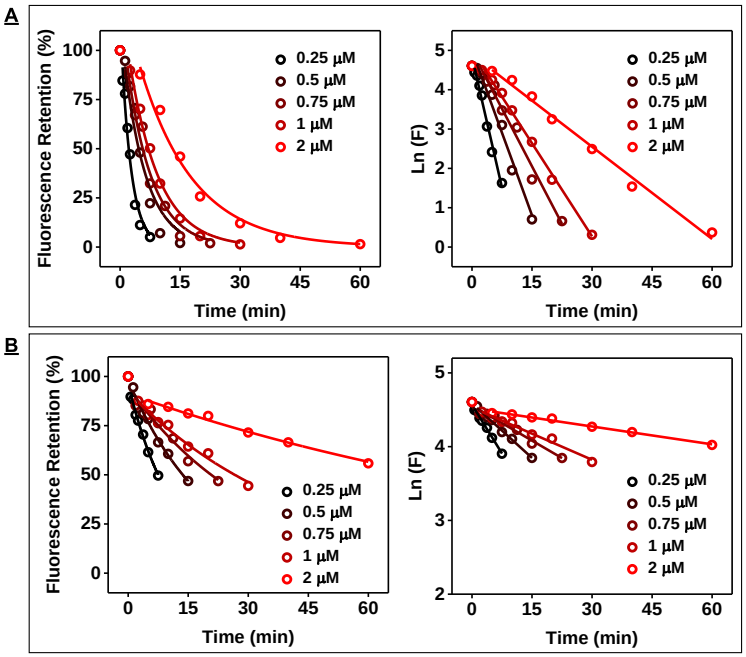

Figure 4-3. Characterization of OBA3 digestion kinetics by Exo III and Exo I. Fluorescence time-course of the digestion (left) of 0.25, 0.5, 0.75, 1, or 2 µM OBA3 (indicated by black to red color gradient) and natural log plot (right) of fluorescence retention in the (**A**) absence and (**B**) presence of 25 µM OTA.

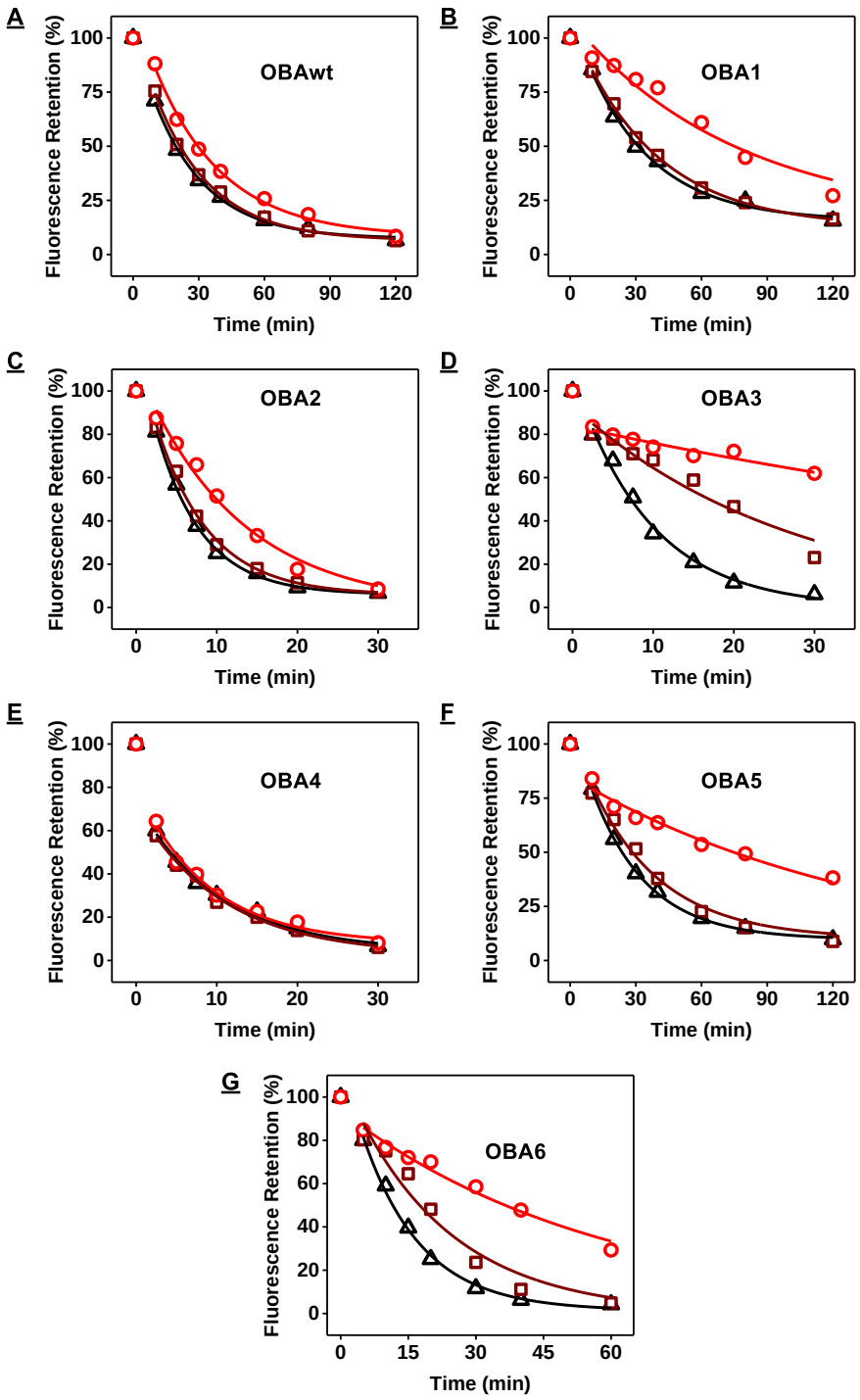

Figure 4-4. Evaluation of the binding profile of OTA-binding aptamers using the exonuclease digestion assay. Digestion of (**A**) OBAwt, (**B**) OBA1, (**C**) OBA2, (**D**) OBA3, (**E**) OBA4, (**F**) OBA5, and (**G**) OBA6 with the mixture of Exo III and Exo I in the absence (black triangles) or presence of 100 µM OTA (red circles) or 100 µM ochratoxin B (OTB) (burgundy squares).

Having established a correlation between the kinetics of an aptamer's digestion and its target-binding affinity, we utilized our exonuclease digestion assay to investigate the effects of mutations, insertions, and deletions on aptamer−ligand binding performance. We first digested OBAwt and its six mutants, OBA1−6, in the absence and presence of 100 μM OTA to determine their target-binding affinity. We observed a large variation in the $t_{1/2}$ of the digestion reactions for each aptamer in the absence of OTA. For example, OBA2, OBA3, and OBA4 had $t_{1/2}$ values between 4 and 8 min, whereas OBAwt, OBA1, OBA5, and OBA6 had $t_{1/2}$ values between 15 and 33 min (**Figure 4-4**). These different digestion rates are most likely due to the aptamers having different tertiary structures as a result of their respective mutations, insertions, or deletions. We used the ratio of $t_{1/2}$ in the presence versus the absence of target as a metric to determine the extent of binding-induced inhibition of enzyme digestion for other ligands. A larger $t_{1/2}$ ratio indicates stronger enzymatic inhibition and presumably greater ligand-binding affinity, while a $t_{1/2}$ ratio equal to 1 indicates no binding-related enzyme inhibition. Our experimental results demonstrated that OBA4 had no binding to OTA, with a $t_{1/2}$ ratio of 1, while OBAwt, OBA1, OBA2, OBA3, OBA5, and OBA6 produced $t_{1/2}$ ratios of 1.4, 2.4, 2.0, 8.3, 4.7, and 4.1, respectively (**Figure 4-1D**). These results indicate that OBA3 has the highest OTA affinity, while the other mutants have lower affinity (OBA5 > OBA6 > OBA1 > OBA2 > OBAwt > OBA4). These results closely correspond to the affinities measured by Xu et al. using a fluorescence polarization technique, and we also obtained similar results using ITC. For example, the K_D values of OBA3, OBA5, and OBA1 for OTA were 1.8 ± 0.1 (**Figure 4-5)**, 3.4 ± 0.1 (**Figure 4-6)**, and 5.5 ± 0.2 μM (**Figure 4-7)**, respectively. This confirms that our assay

can accurately profile the relative target-binding affinity of aptamer mutants regardless of differences in their sequence, length, or structure.

We further tested the specificity of these six mutants and OBAwt against 100 μM ochratoxin B (OTB), which differs from OTA by a single chlorine atom on the coumarin ring. In the presence of OTB, OBAwt, OBA1, OBA2, and OBA4 had $t_{1/2}$ ratios of nearly 1 (**Figure 4-1D**), indicating little or no affinity for OTB. However, OBA5 and OBA6 demonstrated moderate enzyme inhibition, with $t_{1/2}$ ratios of 1.3 and 1.4, which indicated weak binding to OTB. Digestion of OBA3 was strongly inhibited by OTB, with a $t_{1/2}$ ratio of 3.7, demonstrating tight binding (**Figure 4-1D**). These results again correlated well with our ITC results which determined the K_D values for OTB of 25.5 ± 1.2 (**Figure 4-5)**, 59.9 ± 6.9 (**Figure 4-6)**, and 74.1 ± 9.5 μM (**Figure 4-7)** for OBA3, OBA5, and OBA1, respectively. Overall, our digestion results show that, although OBA1 and OBA2 have low affinity for OTA, they are capable of distinguishing OTA from OTB with high specificity. And while OBA3 has greater affinity for OTA, its specificity is poorer relative to OBA1 and OBA2. Thus, $t_{1/2}$ ratio can be used to discriminate high-affinity binding from weaker-binding ligands and to report the relative binding affinity of an aptamer to various ligands.

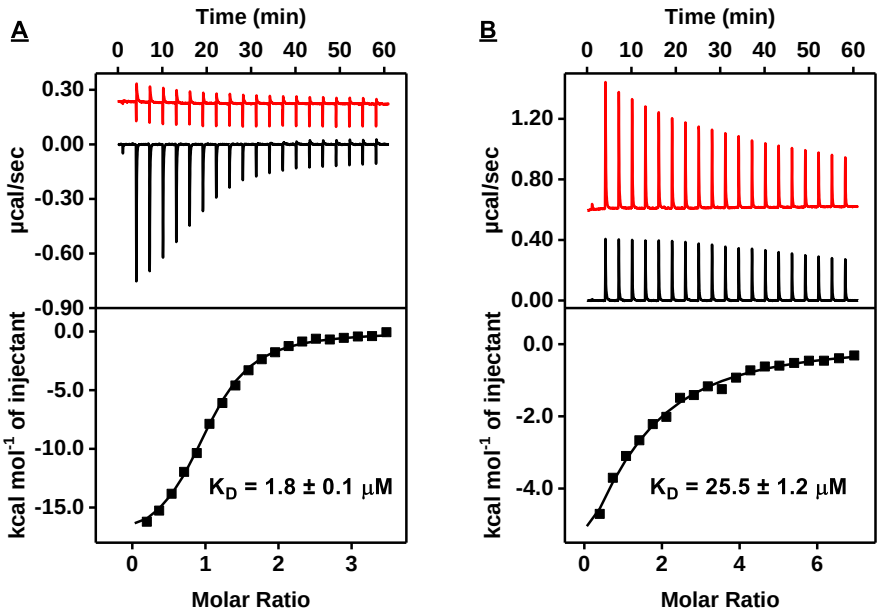

Figure 4-5. Characterization of OBA3 affinity for OTA and OTB using ITC. Top panels display the heat generated from each titration of OBA3 to (**A**) buffer (red) or OTA (black) and (**B**) buffer (red) or OTB (black). Bottom panels show the integrated heat of each titration after correcting for the heat of dilution of the titrant.

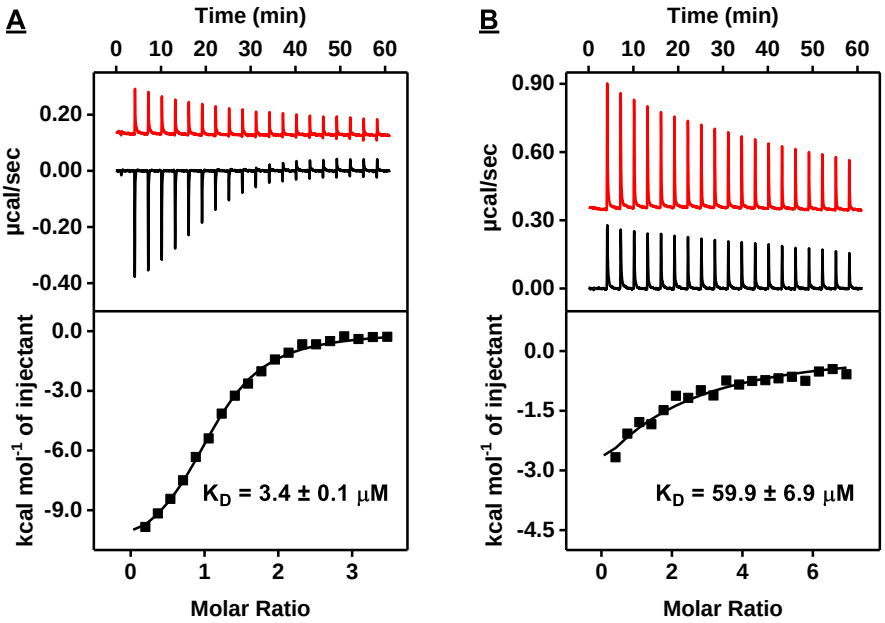

Figure 4-6. Characterization of OBA5 affinity for OTA and OTB using ITC. Top panels display the heat generated from each titration of OBA5 to (**A**) buffer (red) or OTA (black) and (**B**) buffer (red) or OTB (black). Bottom panels show the integrated heat of each titration after correcting for the heat of dilution of the titrant.

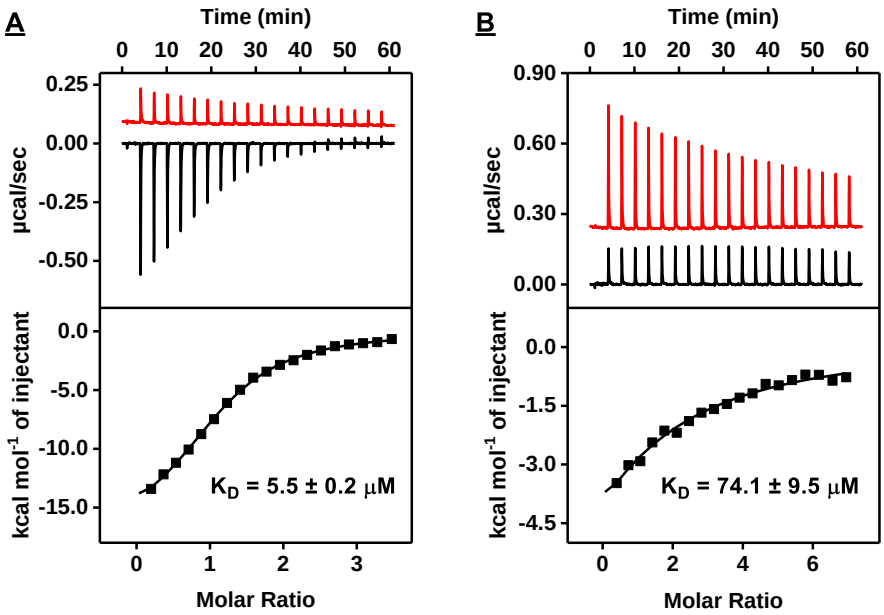

Figure 4-7. Characterization of OBA1 affinity for OTA and OTB using ITC. Top panels display the heat generated from each titration of OBA1 to (**A**) buffer (red) or OTA (black) and (**B**) buffer (red) or OTB (black). Bottom panels show the integrated heat of each titration after correcting for the heat of dilution of the titrant.

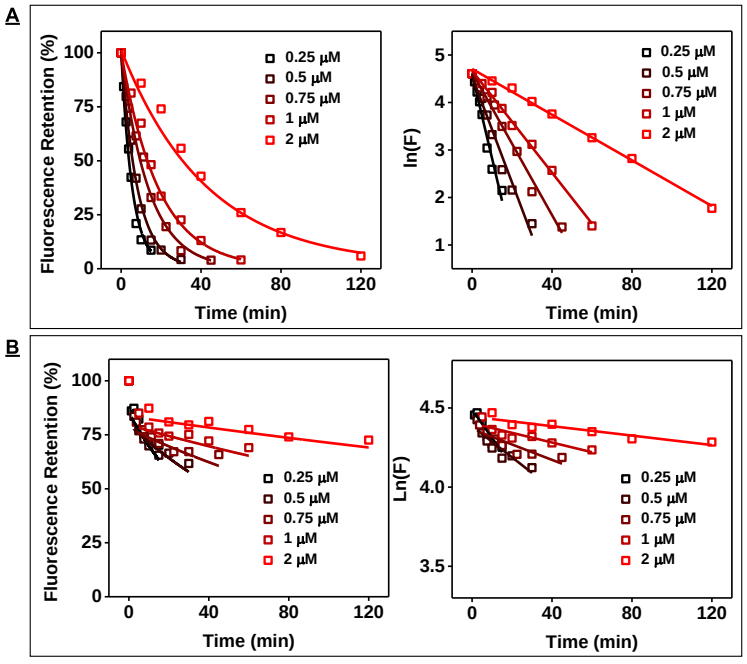

Figure 4-8. Characterization of ATPwt digestion kinetics by Exo III and Exo I. Time-course digestion (left) of 0.25, 0.5, 0.75, 1, or 2 µM ATPwt (indicated by the black to red color gradient) and natural log plot (right) of digestion progress (**A**) in the absence and (**B**) presence of 250 µM ATP.

4.3.2. Characterizing a Cross-Reactive ATP-Binding Aptamer.

To demonstrate the generality of our exonuclease fluorescence assay, we next studied a well-characterized 33-nt ATP-binding DNA aptamer (ATPwt).[98,292] This aptamer also binds to adensoine-5′-diphosphate (ADP), adenosine-5′-monophosphate (AMP), and ADE but not to uridine-5′-triphosphate (UTP), guanosine-5′-triphosphate (GTP), or cytosine-5′-triphosphate (CTP).[83,98] In order to determine whether our assay could accurately profile the binding spectrum of ATPwt, we first confirmed that the digestion of this aptamer follows first-order kinetics by digesting various concentrations of ATPwt (0.25−2 μM) with or without 250 μM ATP (**Figure 4-8**). We then digested ATPwt in the absence and presence of 250 μM ATP or its analogues. The $t_{1/2}$ ratio of digestion in the presence of UTP, GTP, and CTP was approximately 1, which corresponds to previous reports showing that ATPwt does not bind to these molecules.[83,98] However, digestion of ATPwt was greatly reduced in the presence of ATP, ADP, AMP, and ADE (**Figure 4-9A**), with $t_{1/2}$ ratios of 13.8, 14.0, 11.2, and 14.9, respectively (**Figure 4-9B**), confirming that binding to these ligands strongly inhibits exonuclease digestion. These $t_{1/2}$ ratios were essentially indistinguishable, which is most likely due to the saturating target concentration (250 μM) used in this experiment. When the same experiment was performed with 100 μM ligand, we observed significant differences, with a $t_{1/2}$ ratio of 4.0, 6.4, 2.4, and 13.8 for ATP, ADP, AMP, and ADE, respectively (**Figure 4-9B and Figure 4-10**). This indicated the following binding preference: ADE > ADP > ATP > AMP. We confirmed this by ITC, obtaining a $K_{1/2}$ (concentration of ligand required to reach half saturation) of 4.2 ± 0.1, 6.3 ± 0.1, 10.2 ± 0.2, and 14.1 ± 0.2 μM for ADE, ADP, ATP and AMP, respectively (**Figure**

4-11). Again, $t_{1/2}$ ratio is clearly a reliable indicator of the relative binding affinities of an aptamer to various ligands, including those with similar affinities.

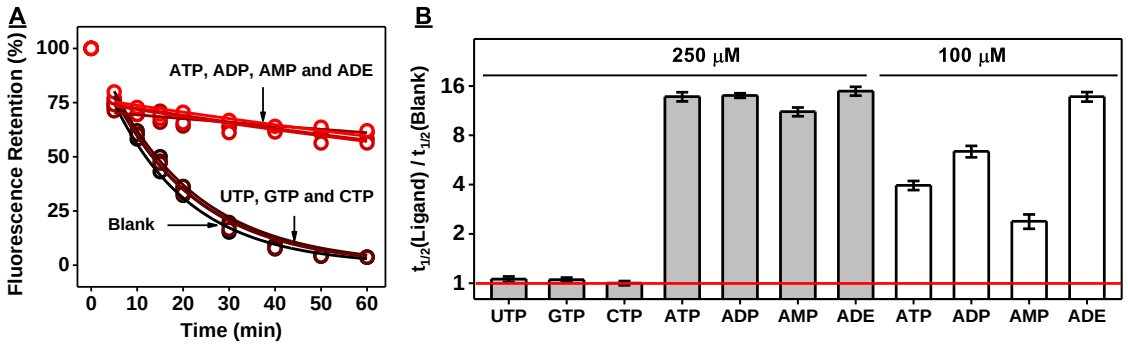

Figure 4-9. Exonuclease-based fluorescence profiling of ATPwt binding to various targets. (**A**) Time-course plot of ATPwt digestion by Exo III and Exo I in the absence and presence of various ribonucleotides at a concentration of 250 μM. (**B**) $t_{1/2}$ ratio was used to determine the relative binding affinity to each ligand at 100 and 250 μM. The red line indicates a $t_{1/2}$ ratio of 1, which reflects no inhibition of aptamer digestion.

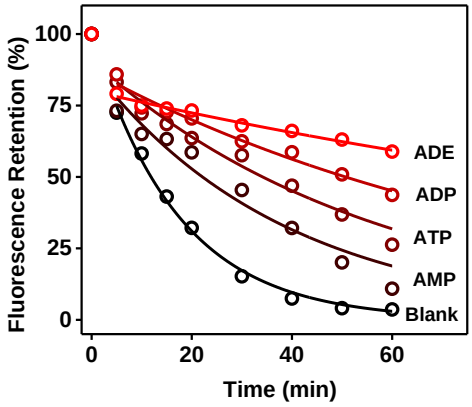

Figure 4-10. Digestion of ATPwt with Exo III and Exo I in the absence and presence of 100 μM ADE, AMP, ADP, or ATP.

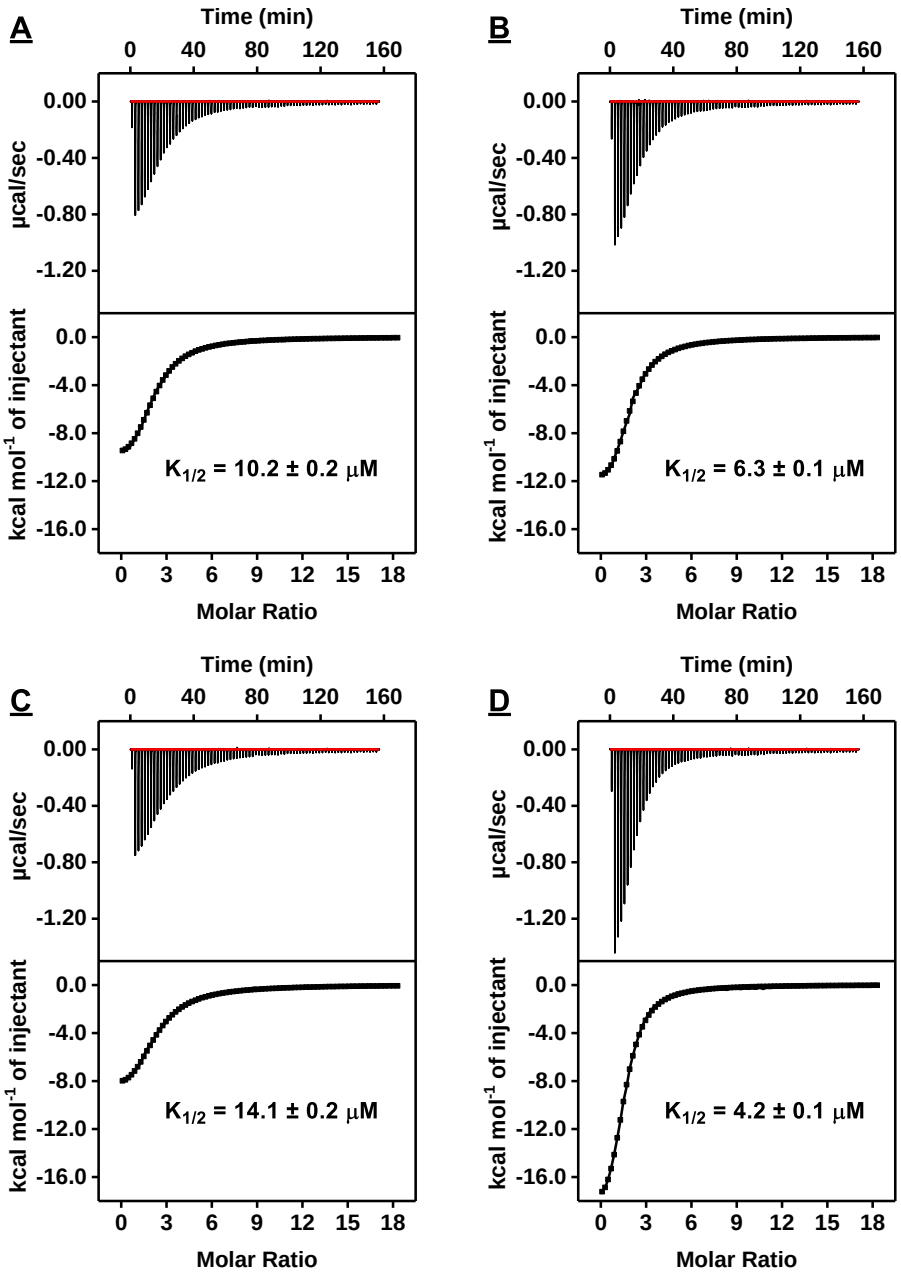

Figure 4-11. Characterization of affinity of ATPwt to ATP, ADP, AMP, and ADE using ITC. Top panels display the heat generated from each titration of (**A**) ATP, (**B**) ADP, (**C**) AMP, and (**D**) ADE to ATPwt. Bottom panels show the integrated heat of each titration after correcting for the heat of dilution of the titrant.

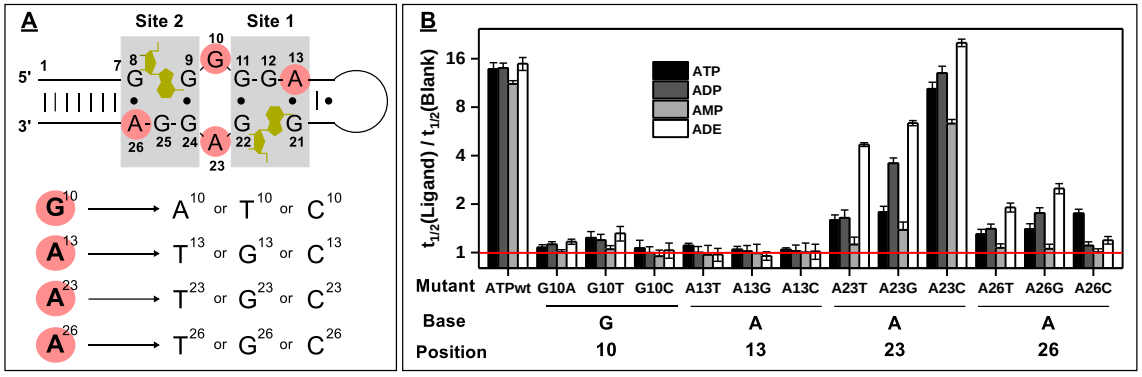

Figure 4-12. Design and characterization of ATPwt mutants. (**A**) Secondary structure of ligand-bound ATPwt, with mutated nucleotides highlighted in red. The ligand is highlighted in gold and nucleotide positions are marked. Twelve different point-mutants were generated by changing G^{10}, A^{13}, A^{23}, A^{26} to either of the three alternative nucleobases. (**B**) $t_{1/2}$ ratio (with $\log_2$ scale) for each mutant in the presence of ATP, ADP, AMP, or ADE. The red line indicates a $t_{1/2}$ ratio of 1, reflecting no binding-induced inhibition of enzyme digestion.

Having demonstrated accurate and sensitive profiling of aptamer−ligand binding, we next tested whether this method could be used to screen for new aptamer candidates with improved binding properties from a panel of mutants. ATPwt has limited analytical utility in that it binds to ADE, AMP, ADP, and ATP, which typically coexist at similar concentrations in biological media,[202] and we therefore set out to identify a more specific aptamer that selectively binds only to one of these molecules. On the basis of its NMR[299] structure, ATPwt possesses two binding domains within the minor groove of a DNA helix composed of G·G and A·G mismatches (**Figure 4-12A**). In the first binding site, G12 forms hydrogen bonds with the adenine base of the ligand. G11 and G21 base stack with G12 to stabilize this binding domain, and further base-stacking occurs between the adenine of the ligand and G22. In the second binding site, the adenine of the ligand hydrogen bonds with G25, which is supported by base-stacking with G8 and G24. Similar stacking is also observed between the ligand and G9. These G's are clearly crucial for ligand binding, and

there is a high likelihood that mutations at these positions would greatly reduce the affinity of the aptamer. However, mutating the nucleotides at the periphery of these binding sites could yield aptamer sequences with improved binding affinity and/or specificity. We therefore mutated nucleotides G10, A13, A23, and A26 adjacent to the binding domain of ATPwt, generating a set of 12 point mutants in which we substituted each nucleotide with the three alternate nucleobases (**Figure 4-12A and Table 4-1**).

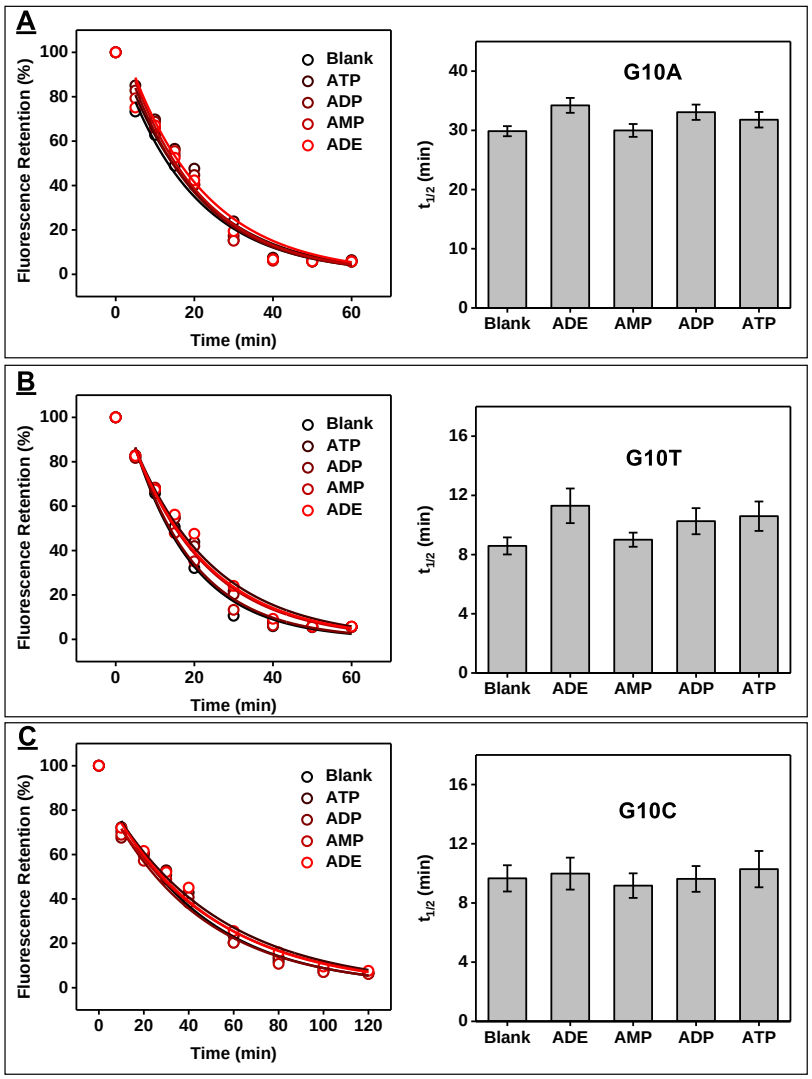

Figure 4-13. Evaluating the binding profile of various G10 mutant aptamers using the exonuclease digestion assay. Fluorescence time-course for the digestion (left) and

calculated $t_{1/2}$ (right) of (**A**) G10A, (**B**) G10T, and (**C**) G10C in the absence or presence of 250 µM ATP, ADP, AMP, or ADE.

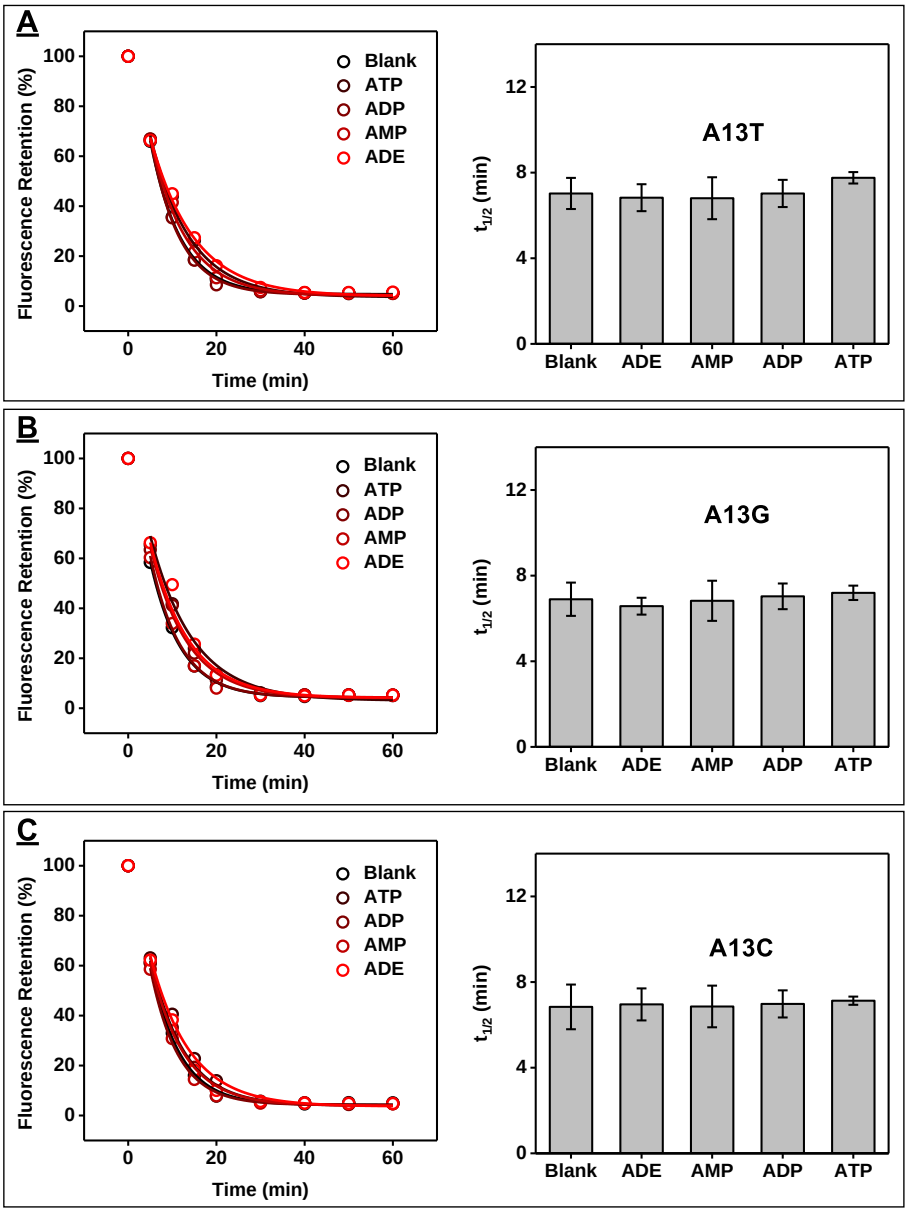

Figure 4-14. Evaluating the binding profile of various A13 mutant aptamers using the exonuclease digestion assay. Fluorescence time-course for the digestion (left) and calculated $t_{1/2}$ (right) of (**A**) A13T, (**B**) A13G, and (**C**) A13C in the absence or presence of 250 µM ATP, ADP, AMP, or ADE.

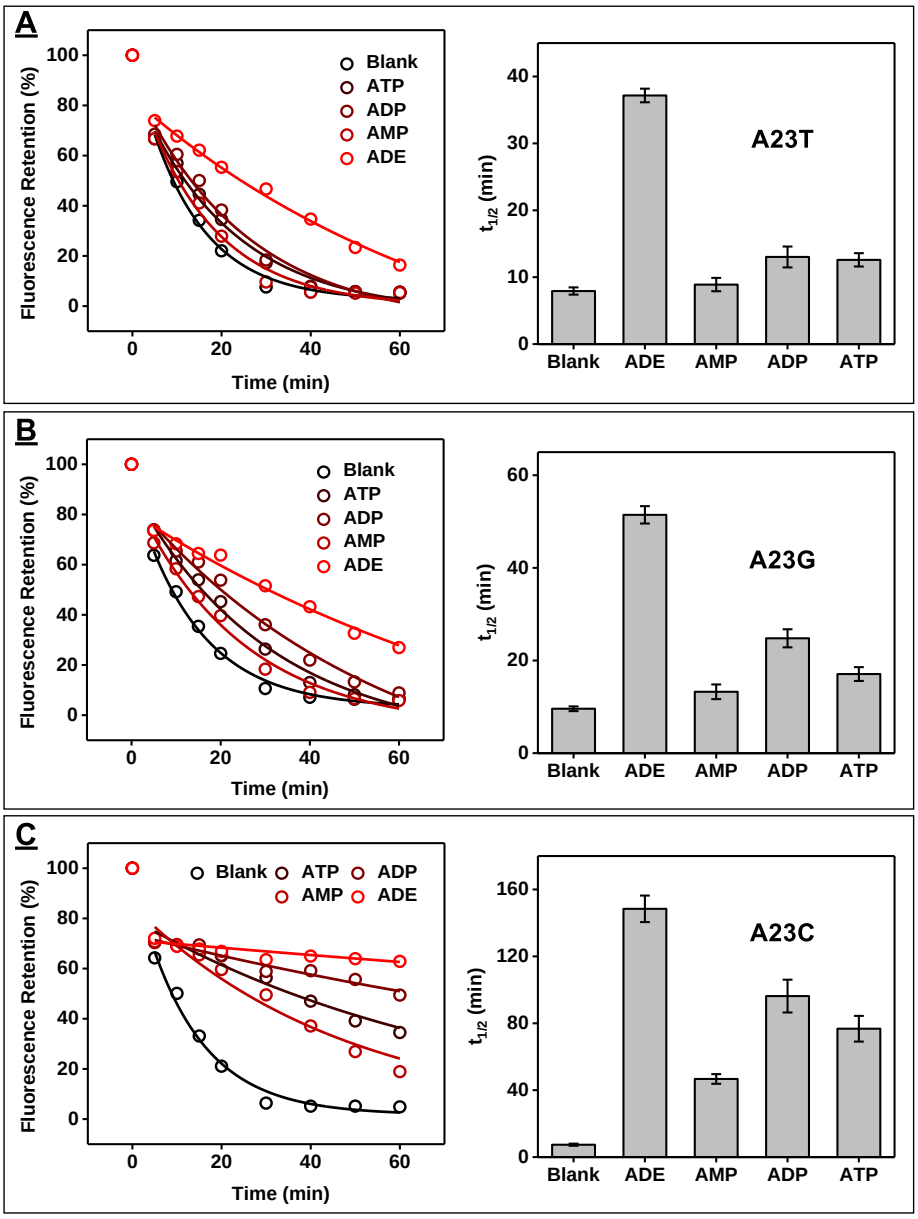

Figure 4-15. Evaluating the binding profile of various A23 mutant aptamers using the exonuclease digestion assay. Fluorescence time-course for the digestion (left) and calculated $t_{1/2}$ (right) of (**A**) A23T, (**B**) A23G, and (**C**) A23C in the absence or presence of 250 µM ATP, ADP, AMP, or ADE.

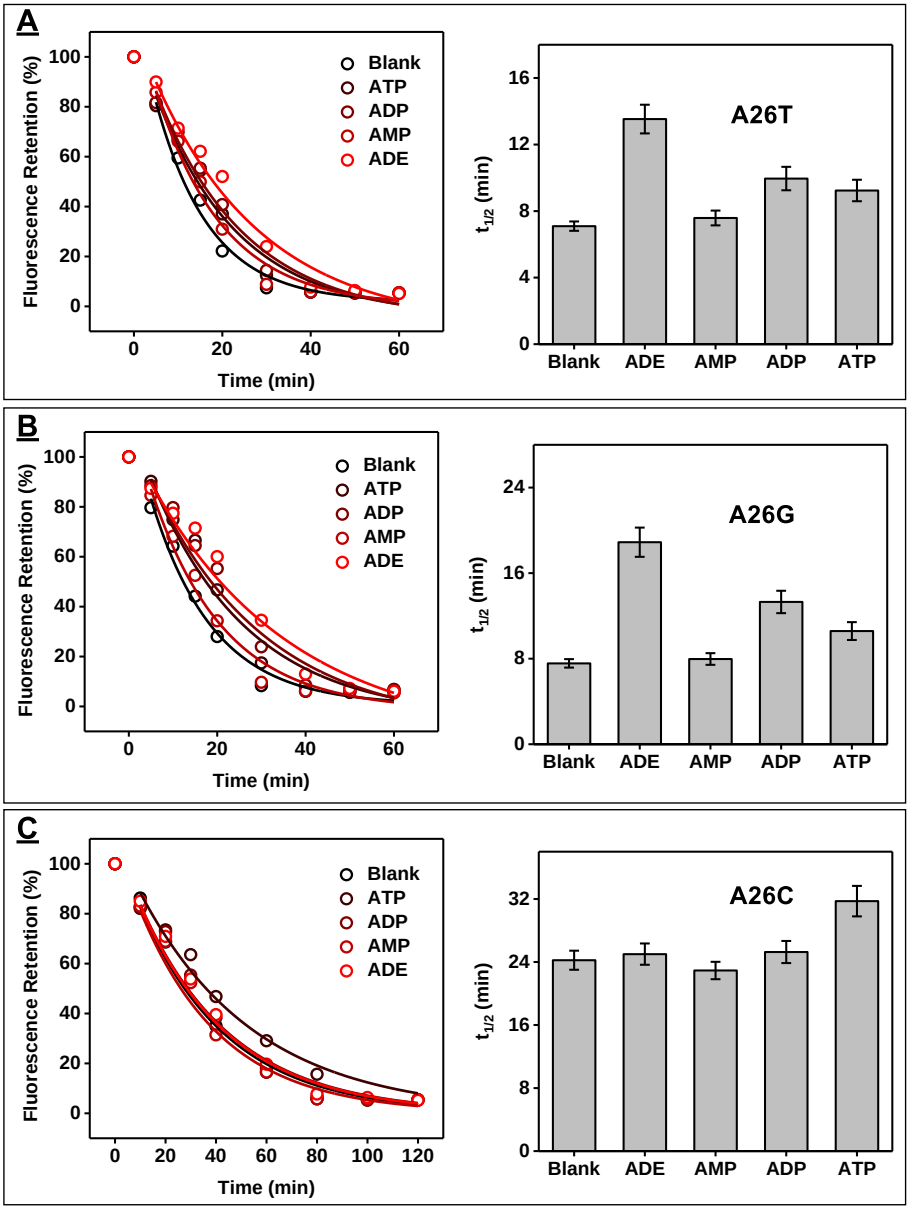

Figure 4-16. Evaluating the binding profile of various A26 mutant aptamers using the exonuclease digestion assay. Fluorescence time-course for the digestion (left) and calculated $t_{1/2}$ (right) of (**A**) A26T, (**B**) A26G, and (**C**) A26C in the absence or presence of 250 µM ATP, ADP, AMP, or ADE.

We then investigated the affinity and specificity of these mutants for ATP, ADP, AMP, and ADE using our exonuclease fluorescence assay. We digested each mutant as well as ATPwt in the absence of ligand and found that each had a different rate of digestion

(**Figures 4-13 – 4-16**). G10T, A13T, A13G, A13C, A23T, A23C, A26T, and A26G were digested slightly faster ($t_{1/2}$ = 6−8 min) than ATPwt ($t_{1/2}$ = 10 min). Two mutants (G10C and A23G) had the same $t_{1/2}$ as ATPwt, while the remaining two (G10A and A26C) had much slower digestion rates ($t_{1/2}$ = 25−35 min). We believe that these disparities can be attributed to differences in the tertiary structures of the aptamers. All of the mutants were then digested in the presence of 250 μM of each ligand, and we observed different digestion rates and levels of enzymatic inhibition (**Figures 4-13 – 4-16**). Our results demonstrated that G10 and A13 mutants had no meaningful affinity for any of the analogues, with $t_{1/2}$ ratios of ∼1 (**Figure 4-12B**). A26 mutants demonstrated low levels of enzymatic inhibition for all tested ligands, with $t_{1/2}$ ratios ranging from 1 to 2.4, indicating greatly reduced affinity relative to ATPwt, with $t_{1/2}$ ratios of 11.2−14.9. Notably, we also observed that mutations at this site altered aptamer specificity: A26T and A26G showed a minor preference for ADE over the other analogues, while A26C had slightly better specificity for ATP (**Figure 4-12B**). A23 mutants displayed the highest levels of enzymatic inhibition among all mutants, with a notable preference for ADE. Notably, A23T had the highest ligand specificity, with a $t_{1/2}$ ratio of 4.6 for ADE versus A23G ≈ A23T > A26G ≈ A26T. We confirmed an identical relative affinity profile for this set of mutants via ITC (**Figure 4-17**).

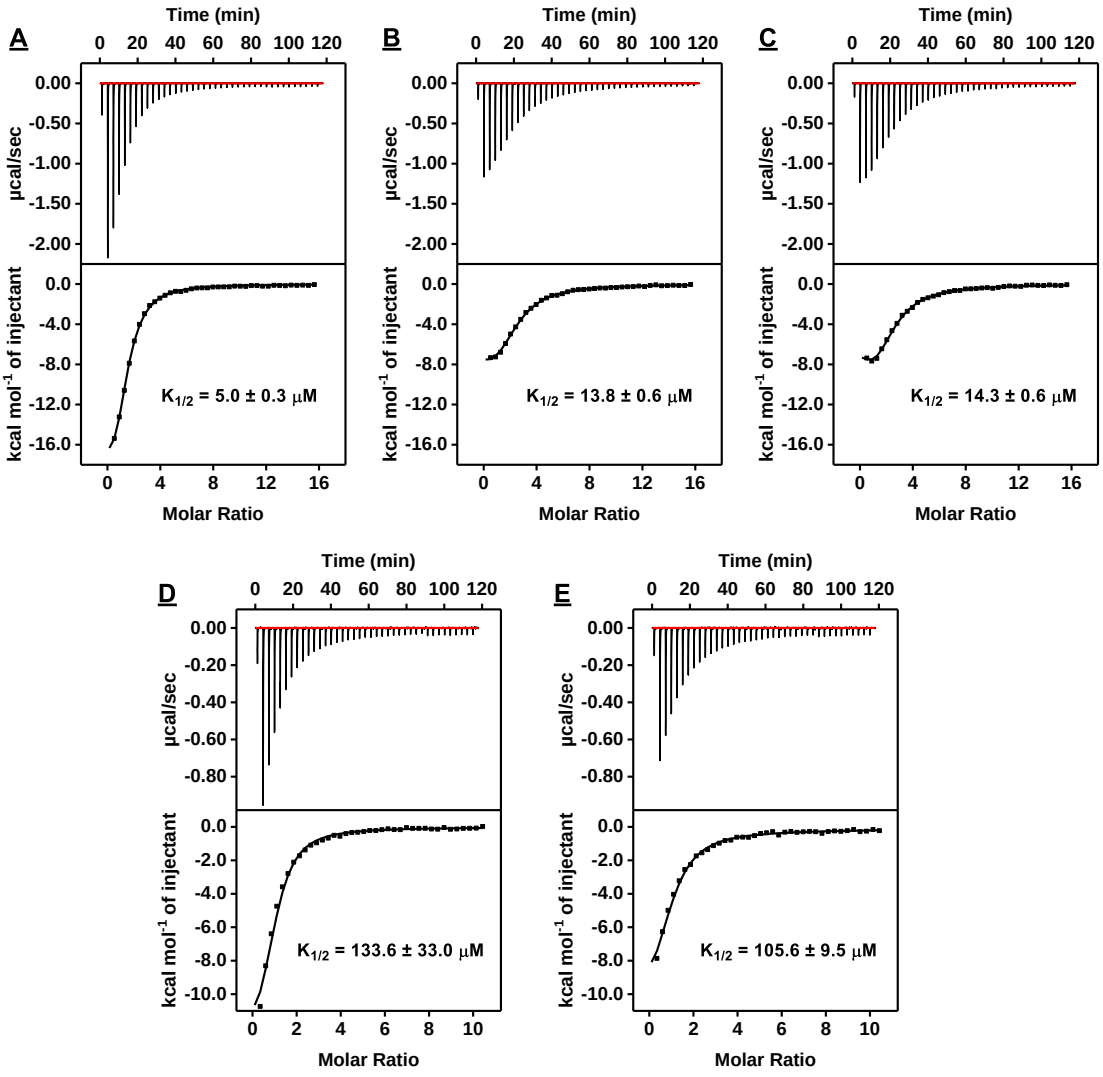

Figure 4-17. Characterization of affinity of single-site mutants for ADE using ITC. Top panels display the heat generated from each titration of ADE to (**A**) A23C, (**B**) A23G, (**C**) A23T, (**D**) A26G, and (**E**) A26T. Bottom panels show the integrated heat of each titration after correcting for the heat of dilution of the titrant.

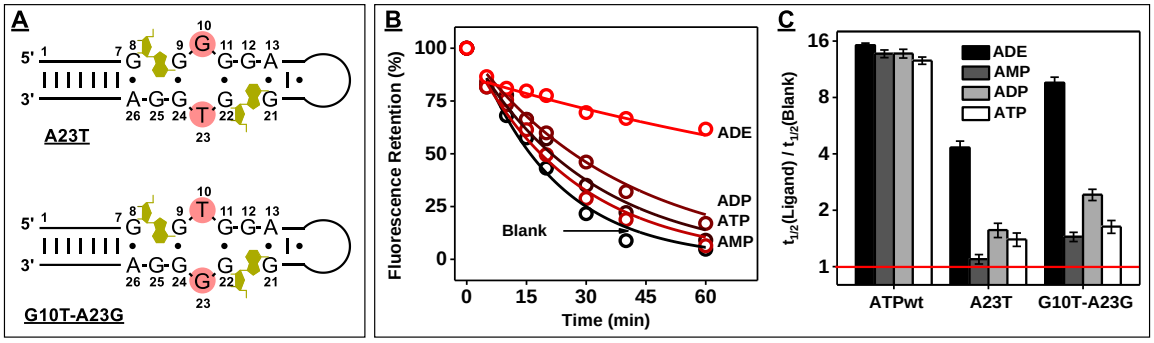

Figure 4-18. Design and characterization of a double-mutant aptamer. (**A**) Inversion of nucleotides G10 and T23 in construct A23T results in a double-mutant G10T-A23G. (**B**) Fluorescence time-course plot of G10T-A23G digestion by Exo III and Exo I in the absence and presence of 250 μM ADE, AMP, ADP, and ATP. (**C**) $t_{1/2}$ ratio (with $\log_2$ scale) for ATPwt, A23T, and G10T-A23G in the presence versus the absence of 250 μM of each ligand. The red line indicates a $t_{1/2}$ ratio of 1, reflecting no inhibition of aptamer digestion. Error bars represent the standard error of fitting.

4.3.3. Identification of a New Highly ADE-Specific Aptamer.

On the basis of our point mutation experiments, G10 is essential for target binding, while T23 greatly enhances specificity toward ADE. According to the reported three-dimensional structure of ATPwt, nucleotides G10 and T23 basestack with binding sites 1 and 2, respectively.[299] Previous work has also reported that interchanging the nucleotides at these two positions in ATPwt does not impair aptamer affinity.[98] To confirm that this held true for A23T, we designed a double mutant (G10T−A23G) in which we swapped the G at position 10 with the T at position 23 (**Figure 4-18A**). Digestion of G10T−A23G in the absence and presence of 250 μM ATP or its analogues demonstrated greater inhibition than A23T in the presence of ADE (**Figure 4-18B**), with a $t_{1/2}$ ratio of 9.5 (**Figure 4-18C**). This double mutant also exhibited excellent specificity against other ligands, with a $t_{1/2}$ ratio of 1.6, 2.4, and 1.4 for ATP, ADP and AMP, respectively (**Figure 4-18C**). Using ITC,

we determined that G10T−A23G tightly binds to ADE, with a $K_{1/2}$ of 15.3 ± 0.2 μM (**Figure 4-19**).

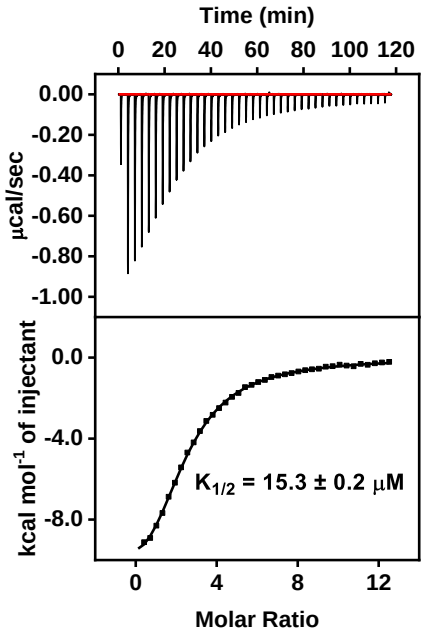

Figure 4-19. Characterization of affinity of G10T-A23G for ADE using ITC. Top panel displays the heat generated from each titration of ADE to G10T-A23G. Bottom panel shows the integrated heat of each titration after correcting for the heat of dilution of the titrant.

A23T and G10T−A23G possess similar target affinities but have different $t_{1/2}$ ratios. To determine the reason for the greater ADE-induced enzymatic inhibition of G10T−A23G relative to A23T we identified the digestion products using polyacrylamide gel electrophoresis (PAGE). We observed that exonuclease digestion halted 3 or 4 nt from the 3′ end of both aptamers, resulting in two major products of 30 nt and 29 nt (**Figure 4-20**, parts A and B). We synthesized these digestion products of A23T (A23T-30 and A23T-29) and G10T−A23G (G10T−A23G-30 and G10T−A23G-29) (**Figure 4-21**) and determined their affinity for ADE using ITC (**Figure 4-22**). A23T-30 ($K_{1/2}$ = 18.6 ± 1.7 μM), G10T−A23G-30 ($K_{1/2}$ = 18.1 ± 0.4 μM), and G10T−A23G-29 ($K_{1/2}$ = 18.5 ± 0.4 μM) had

similar ADE affinities to their parent aptamers. However, A23T-29 had nearly 3-fold poorer affinity for this ligand ($K_{1/2}$ = 37.4 ± 6.2 μM). Thus, the observed $t_{1/2}$ ratios are not only linked to the binding affinity of the parent aptamer but the truncated products as well. This accounts for the lower enzymatic inhibition and smaller $t_{1/2}$ ratio value displayed by A23T relative to G10T−A23G.

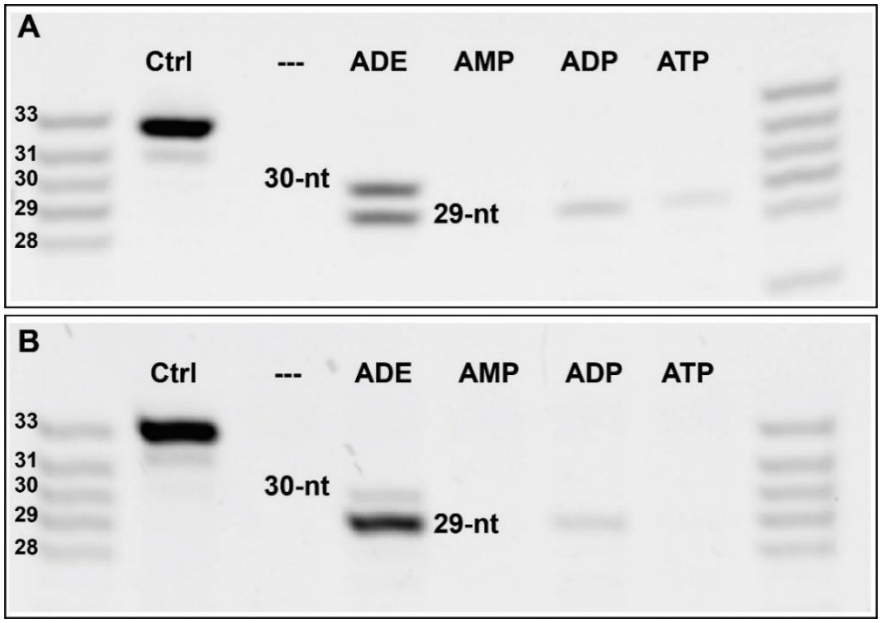

Figure 4-20. PAGE analysis of (**A**) A23T and (**B**) G10T-A23G products after 30 min of digestion with Exo III and Exo I in the absence or presence of 250 μM ADE, AMP, ADP, or ATP.

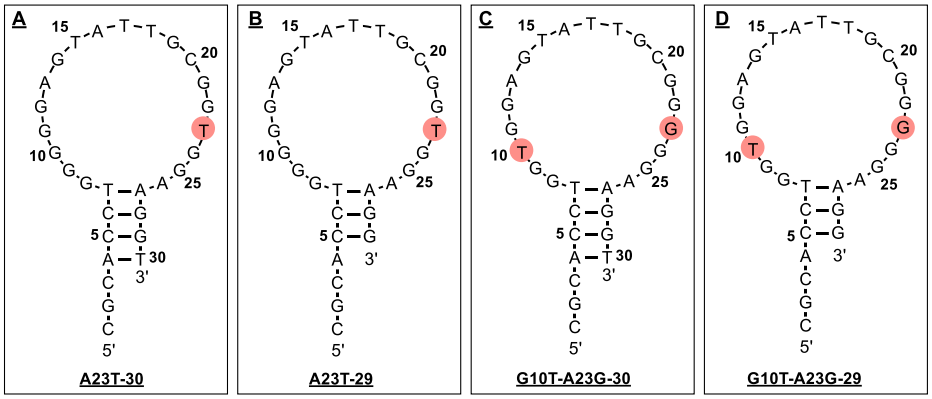

Figure 4-21. Sequence and secondary structure of (**A**) A23T-30, (**B**) A23T-29, (**C**) G10T-A23G-30, and (**D**) G10T-A23G-29. Mutated nucleotides are marked in red.

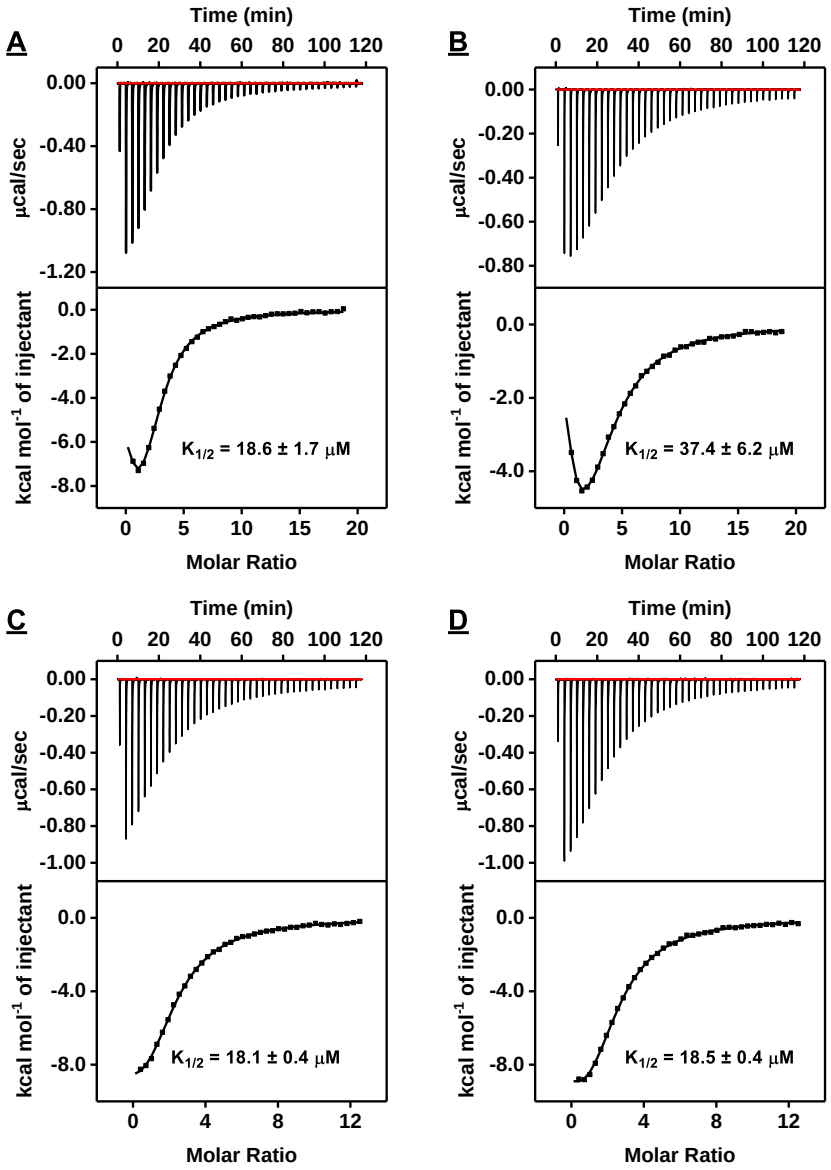

Figure 4-22. Characterization of affinity of ADE-specific aptamer mutants using ITC. Top panels display the heat generated from each titration of ADE to (**A**) A23T-30, (**B**) A23T-29, (**C**) G10T-A23G-30, and (**D**) G10T-A23G-29. Bottom panels show the integrated heat of each titration after correcting for the heat of dilution of the titrant.

4.3.4. Fabrication of E-AB Sensors from ADE-Specific Aptamers.

ADE is a ubiquitous extracellular signaling molecule that has diagnostic value for cardiovascular diseases including cerebral ischemia, tissue ischemia, and cardiac ischemia.[203–205] Basal ADE levels in the cerebrospinal fluid and circulatory system are in

the nanomolar range but increase to 1−50 μM during ischemic episodes, with large variations.[206–208] We anticipated that our engineered aptamers A23T and G10T−A23G could be useful for the clinical detection of ADE in serum due to their high specificity.

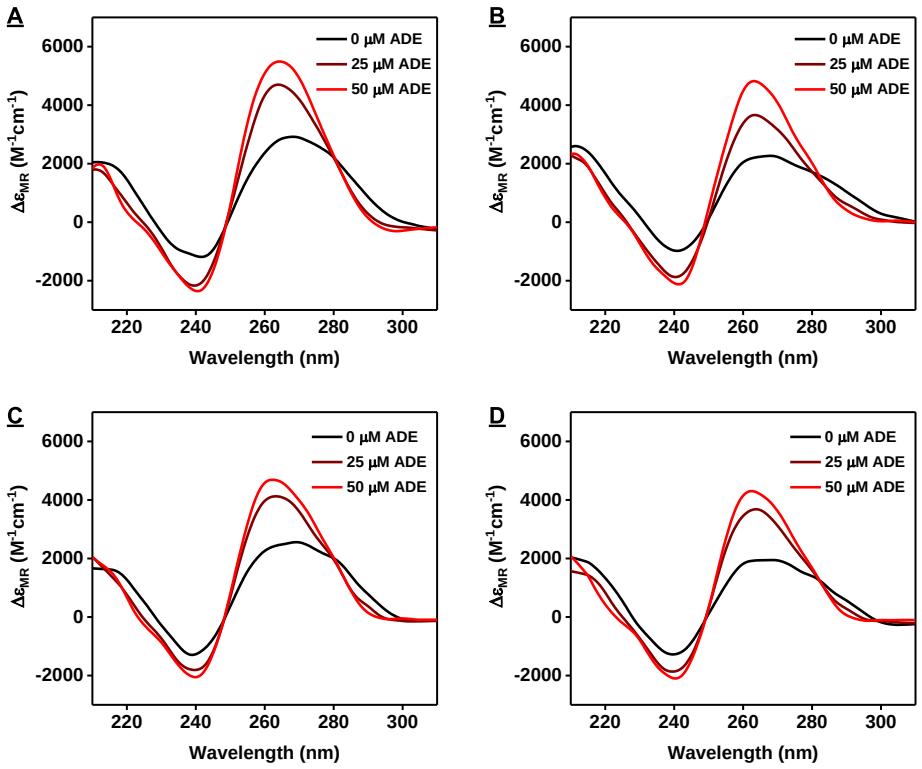

Figure 4-23. Characterizing structure-switching functionality of A23T and G10T-A23G digestion products using CD spectroscopy. CD spectra of (**A**) A23T-30, (**B**) A23T-29, (**C**) G10T-A23G-30, and (**D**) G10T-A23G-29 in the absence or presence of various concentrations of ADE.

E-AB sensors represent an excellent platform for the sensitive and specific detection of small-molecule analytes in complex samples such as serum[117] and whole blood.[120] These consist of thiolated aptamers that are tagged with electroactive molecules (e.g., methylene blue, MB) and immobilized onto gold electrodes. Aptamer−ligand binding induces a conformational change that repositions the MB tag, resulting in a target-concentration-dependent change in current. We have previously determined that exonuclease-truncated aptamers have structure-switching functionality[170,291] and thus

determined that it should be feasible to directly incorporate the exonuclease-truncated ADE-specific aptamers into an E-AB sensor. We first assessed the structure-switching functionality of A23T-30, A23T-29, G10T−A23G-30, and G10T−A23G-29 based on circular dichroism (CD), a well-established method for studying conformational changes in aptamers.[300] In the absence of target, we observed a negative peak at 245 nm and a broad positive peak ranging from 255 to 300 nm, with a maximum at 265 nm (**Figure 4-23**), indicating an unfolded single-stranded DNA structure.[300] Upon addition of ADE, all aptamers produced similar spectra but with target-concentration dependent increases in the intensity of all peaks (**Figure 4-23**). The observed increases in the intensities of the 245 and 265 nm peaks indicate a target-induced transition from a single-stranded structure to a folded structure with anti−anti stacking of guanine bases.[301] This is consistent with the previously described NMR structure of the ligand-bound ATPwt aptamer.[299] Since A23T-29 and G10T−A23G-29 displayed the largest target-induced conformational changes, we used these aptamers to fabricate the E-AB sensors. We further confirmed that these aptamers retain high specificity for ADE via ITC. A23T-29 exhibited binding affinities of 37.4 ± 6.2, >1000, 285.4 ± 5.7, and 406.3 ± 21.8 μM for ADE, AMP, ADP, and ATP, respectively (**Figure 4-24**). Similarly, G10T− A23G-29 exhibited binding affinities of 18.5 ± 0.4, 214.7 ± 7.2, 162.9 ± 2.8, and 171.9 ± 4.3 μM for ADE, AMP, ADP, and ATP, respectively (**Figure 4-25**).

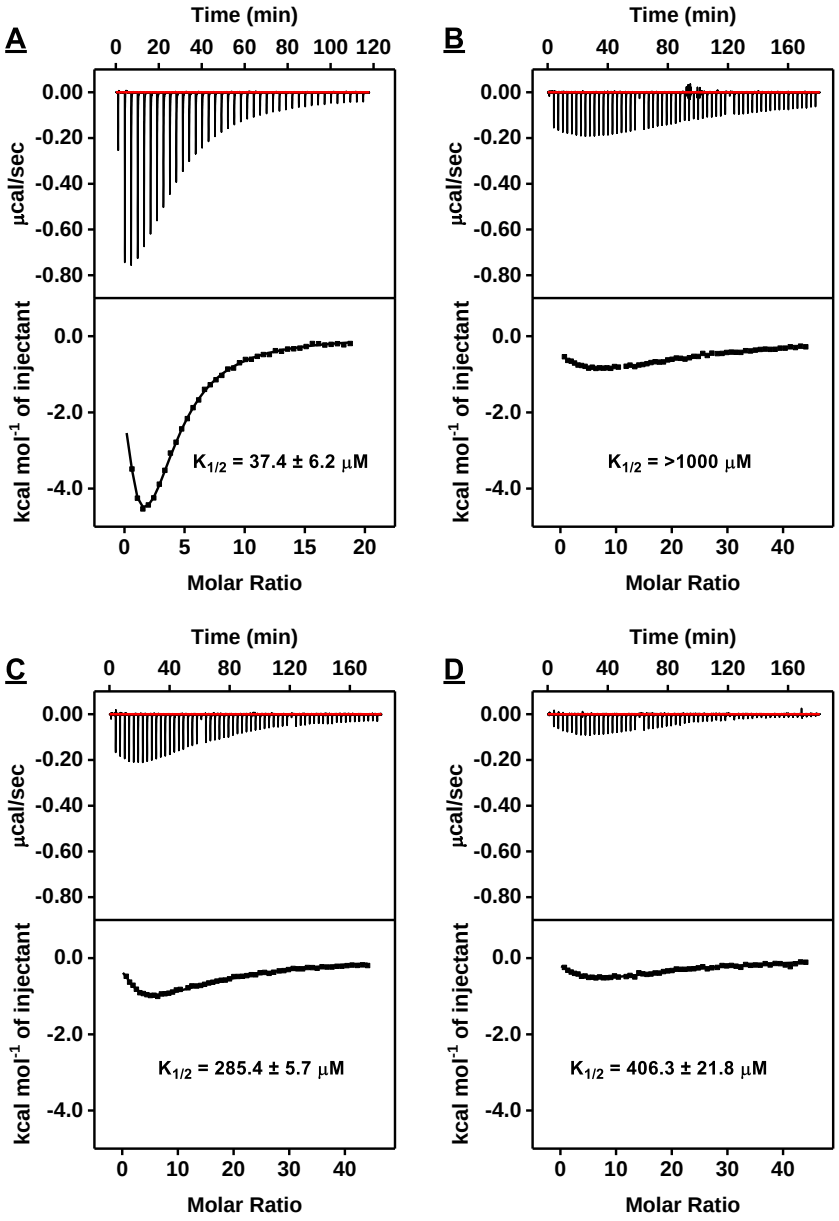

Figure 4-24. Characterization of A23T-29 affinity using ITC. Top panels display the heat generated from each titration of (**A**) ADE, (**B**) AMP, (**C**) ADP, and (**D**) ATP to A23T-29. Bottom panels show the integrated heat of each titration after correcting for the heat of dilution of the titrant.

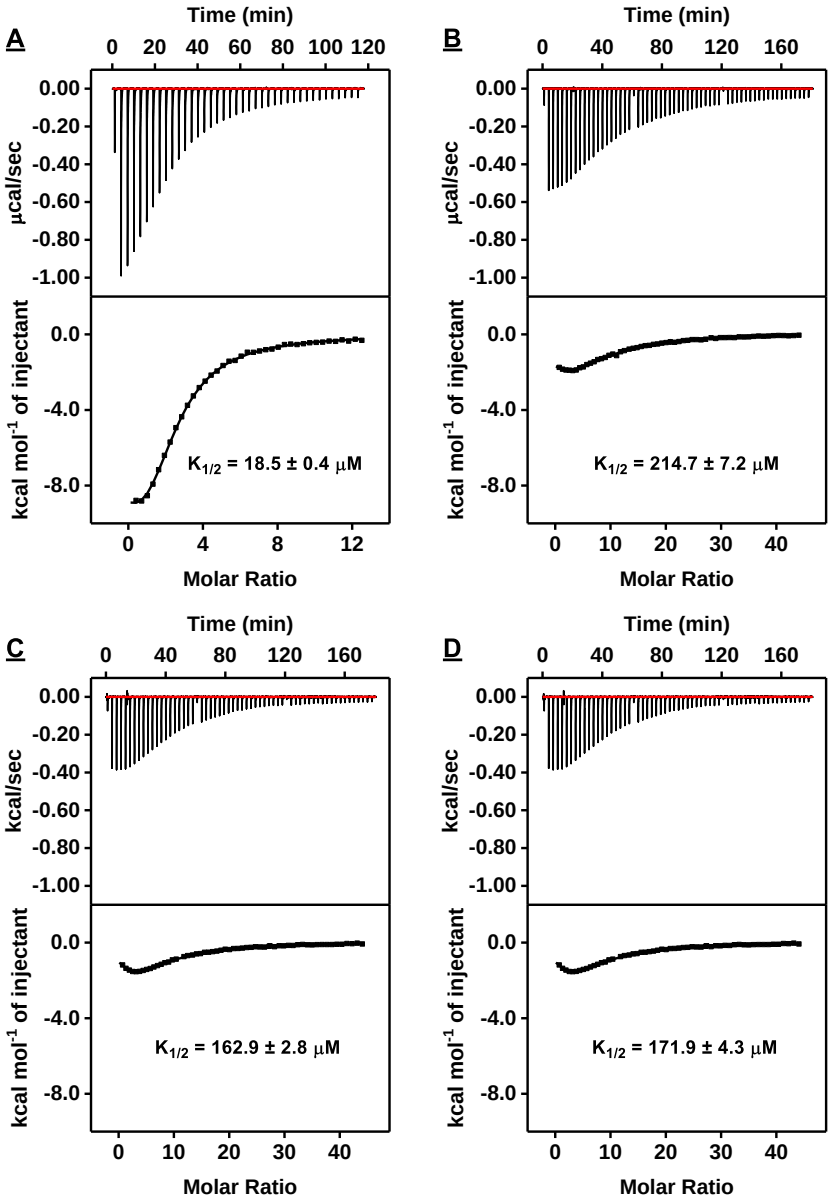

Figure 4-25. Characterization of G10T-A23G-29 affinity using ITC. Top panels display the heat generated from each titration of (**A**) ADE, (**B**) AMP, (**C**) ADP, and (**D**) ATP to G10T-A23G-29. Bottom panels show the integrated heat of each titration after correcting for the heat of dilution of the titrant.

We then synthesized 5′-thiolated/3′-MB-modified versions of G10T−A23G-29 and A23T-29 (G10T−A23G-29-MB and A23T-29-MB) and immobilized 50 nM of each aptamer onto individual gold disk electrodes to fabricate single-aptamer E-AB sensors.

Using a previously reported method,[296] we determined that both sensors had similar surface coverages of 4.6 ± 0.3 and 4.2 ± 0.3 pmol/cm^2, respectively (**Figure 4-26**). We used both sensors to perform ADE detection (**Figure 4-27A**). The G10T-A23G-29-MB sensor produced a linear range from 1 to 25 μM with a limit of detection of 1 μM, whereas the A23T-29-MB sensor had a linear range from 25 to 500 μM with a limit of detection of 25 μM (**Figure 4-27B**). The lower sensitivity of the A23T-29-MB sensor can be attributed to the lower ADE affinity of this aptamer relative to G10T-A23G-29.

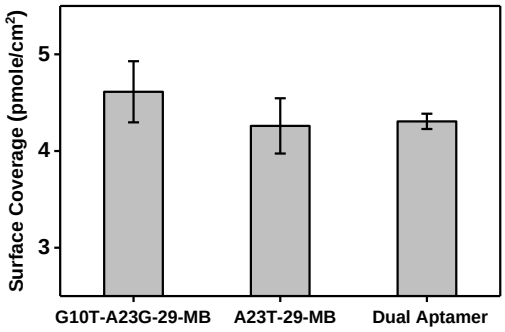

Figure 4-26. Surface coverage of E-AB sensors fabricated using G10T-A23G-29-MB, A23T-29-MB, or both. The average DNA length was used when calculating the surface coverage of sensors fabricated using both aptamers. Error bars represent the standard deviation of the measurements of three different electrodes.

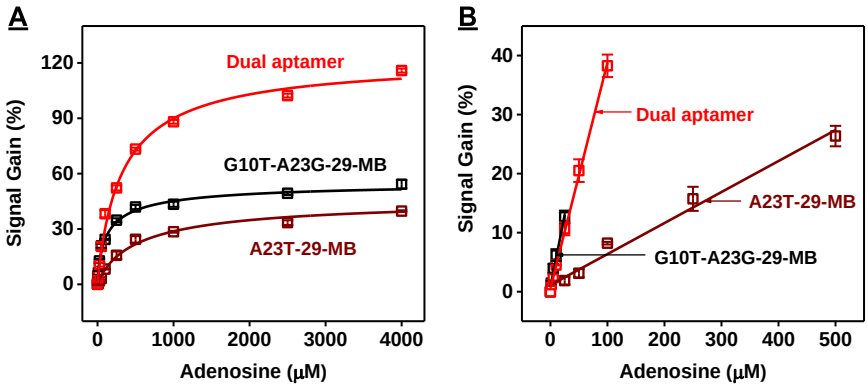

Figure 4-27. Performance of E-AB sensors fabricated using G10T-A23G-29-MB, A23T-29-MB, or a mixture of both aptamers. (**A**) Calibration curve and (**B**) linear range of the three sensors for the detection of various concentrations of ADE in buffer. Error bars represent the average standard deviation of three electrodes.

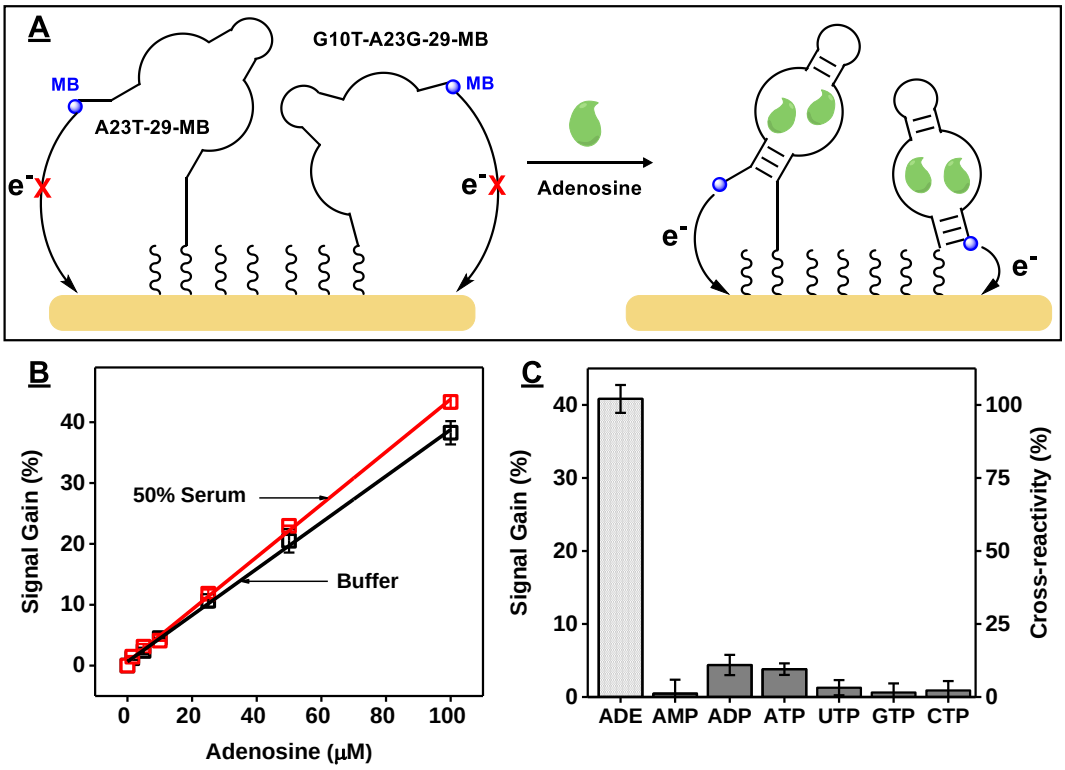

Figure 4-28. Specific detection of ADE in serum using the dual aptamer E-AB sensor. (**A**) Schematic of the dual-aptamer-modified E-AB sensor. (**B**) Linear range of the sensor in buffer and 50% fetal bovine serum. (**C**) Signal gain and cross-reactivity (relative to ADE) of the sensor to 100 μM ADE, AMP, ADP, ATP, UTP, GTP, and CTP in 50% serum. Error bars represent the average standard deviation of three electrodes.

Clinically useful detection requires a sensor that responds to ADE across a large range of concentrations (1−50 μM),[206–208] and we were unable to achieve this using our single-aptamer E-AB sensors. It has been reported that the linear range of an aptamer-based sensor can be expanded by using a mixture of different aptamers with varying target-binding affinities.[302–304] We therefore fabricated a dual-aptamer E-AB sensor using a 1:1 ratio of A23T-29-MB and G10T-A23G-29-MB (**Figure 4-28A**). This dual-aptamer modified electrode had similar surface coverage (4.3 ± 0.3 pmol/cm^2) to the single-aptamer E-AB sensors fabricated with each individual aptamer (**Figure 4-26**). Importantly, the dual-aptamer sensor produced a broader linear range from 1 to 100 μM ADE (**Figure 4-**

28B), which was probably facilitated by the relatively low ADE affinity of A23T-29-MB. Importantly, this dual-aptamer sensor still retained a limit of detection of 1 μM, presumably due to the high affinity of G10T−A23G-29-MB (**Figure 4-27B**). Finally, we used our dual-aptamer E-AB sensor to perform detection in 50% fetal bovine serum and evaluated the sensor's specificity against ADE as well as AMP, ADP, ATP, UTP, GTP, and CTP. The dual-aptamer sensor produced ~30% lower current in 50% serum (**Figure 4-29**), regardless of the absence or presence of ADE, presumably due to protein fouling of the electrode surface.[305] However, the linear range and limit of detection remained the same in 50% serum as in buffer (**Figure 4-28B and Figure 4-27B**), demonstrating the sensor's excellent performance in biological samples. We further determined that the dual-aptamer E-AB sensor had less than 10% cross-reactivity to the various nucleotide analogues in 50% serum relative to ADE at a concentration of 100 μM (**Figure 4-28C and Figure 4-30**), reflecting the high specificity of the aptamers we used.

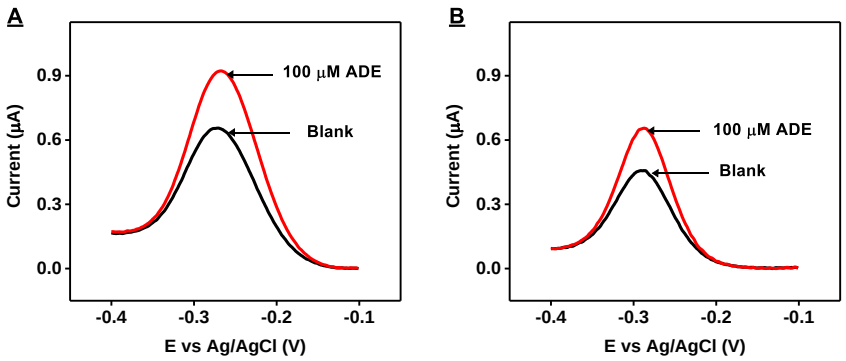

Figure 4-29. SWV curves in the absence (black) or presence (red) of 100 μM ADE in (**A**) buffer or (**B**) 50% serum using dual-aptamer E-AB sensors constructed with A23T-29-MB and G10T-A23G-29-MB.

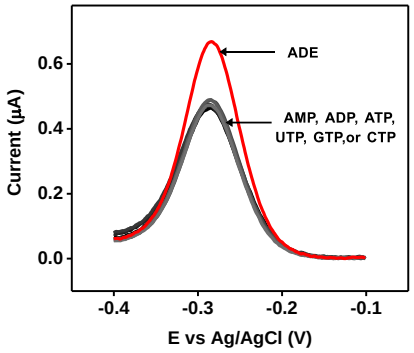

Figure 4-30. Dual-aptamer E-AB sensor response to 100 μM ADE, AMP, ADP, or ATP or other nucleotide triphosphates in 50% serum.

4.3.5. Generality of the Exonuclease Fluorescence Assay for Protein-Binding Aptamers.

We finally used our exonuclease fluorescence assay to determine the binding characteristics of three different G-quadruplex aptamers that bind to human α-thrombin: Tasset,[306] Bock,[307] and Bock-hang[116] in Tris-buffered saline. We digested 500 nM aptamer in the absence and presence of 500 nM thrombin or human factor X, which was reported to have no binding affinity to these aptamers.[308] For all three aptamers, relative fluorescence intensities decreased in the absence of target at an exponential rate down to 2−5% within 30 min, indicating complete digestion into mononucleotides (**Figure 4-31A−C**). The aptamers were likewise completely digested in the presence of factor X ($t_{1/2}$ ratios: ∼1), confirming that they did not have any affinity for this protein. In the presence of thrombin, the digestion of all three aptamers was greatly inhibited, with $t_{1/2}$ ratios of 14.0, 10.4, and 3.6 for Tasset, Bock, and Bock-hang, respectively (**Figure 4-31D**). These results suggested that the thrombin affinity of these aptamers follows the order of Tasset > Bock > Bock-hang. We confirmed this by measuring the thrombin-binding affinity of these

aptamers using ITC in Tris-buffered saline at 23 °C, observing K_D's of 13.6 ± 3.1, 23.1 ± 5.4, and 97 ± 19 nM for Tasset, Bock, and Bock-hang, respectively (**Figure 4-32**).

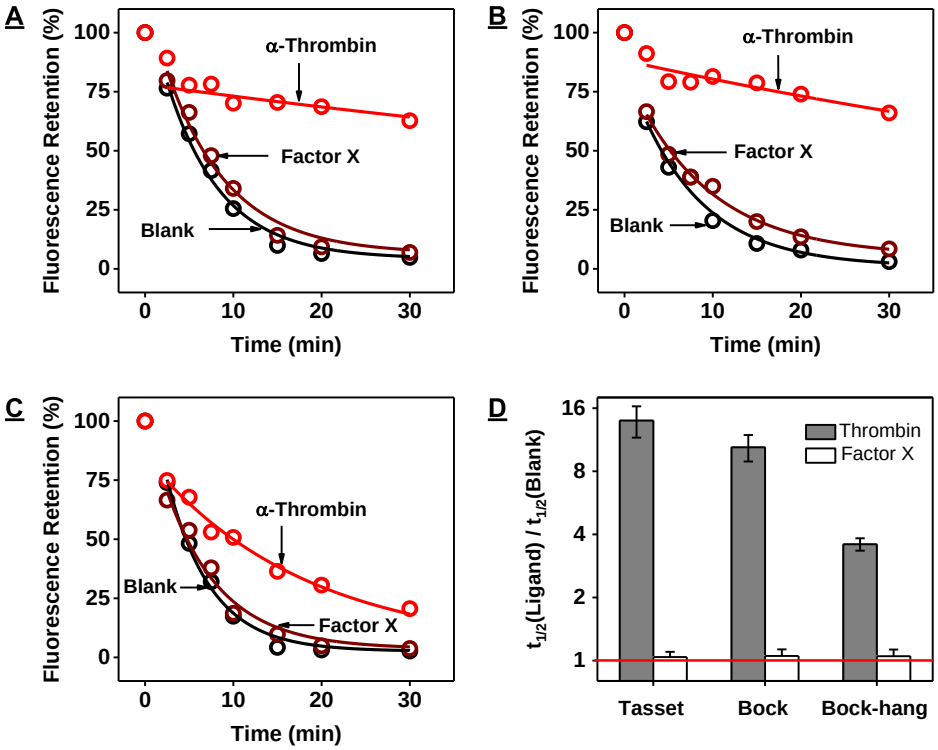

Figure 4-31. Exonuclease-based fluorescence profiling of thrombin-binding aptamers. Time-course plot of digestion of 500 nM (**A**) Tasset, (**B**) Bock and (**C**) Bock-hang by Exo III and Exo I in the absence (black) and presence of 500 nM human α-thrombin (red) or human Factor X (brown). (**D**) Half-life ($t_{1/2}$) ratio of the digestion reaction was used to determine relative aptamer binding affinity to α-thrombin and Factor X. The y-axis is $\log_2$ scaled. The red line indicates a $t_{1/2}$ ratio of 1, which means there was no inhibition of aptamer digestion.

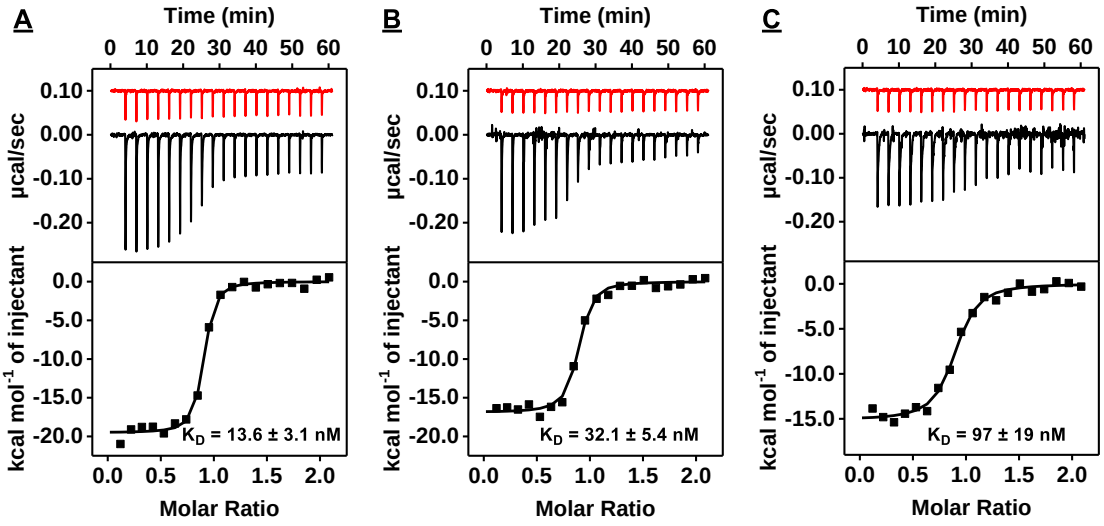

Figure 4-32. Characterization of the thrombin-binding affinity of Tasset, Bock, and Bock-hang using ITC. Top panels display the heat generated from each titration of (**A**) Tasset, (**B**) Bock and (**C**) Bock-hang to buffer (red) or thrombin (black). Bottom panels show the integrated heat of each titration after correcting for the heat of dilution of the titrant.

We then performed our exonuclease fluorescence assay to characterize a stem−loop-structured DNA aptamer that has nanomolar affinity for IgE but at least 1000-fold lower affinity for IgG.[309] We digested the aptamer in the absence and presence of these proteins in Tris-buffered saline. This aptamer was completely digested in the absence of target and in the presence of 500 nM human IgG, confirming that the aptamer does not strongly bind this protein. However, digestion was greatly inhibited in the presence of 500 nM human IgE, with a $t_{1/2}$ ratio of 5.4 (**Figure 4-33**), demonstrating that the aptamer binds IgE. Thus, our method is generalizable for protein-binding aptamers regardless of their binding affinity, secondary structure, or the size of the target protein.

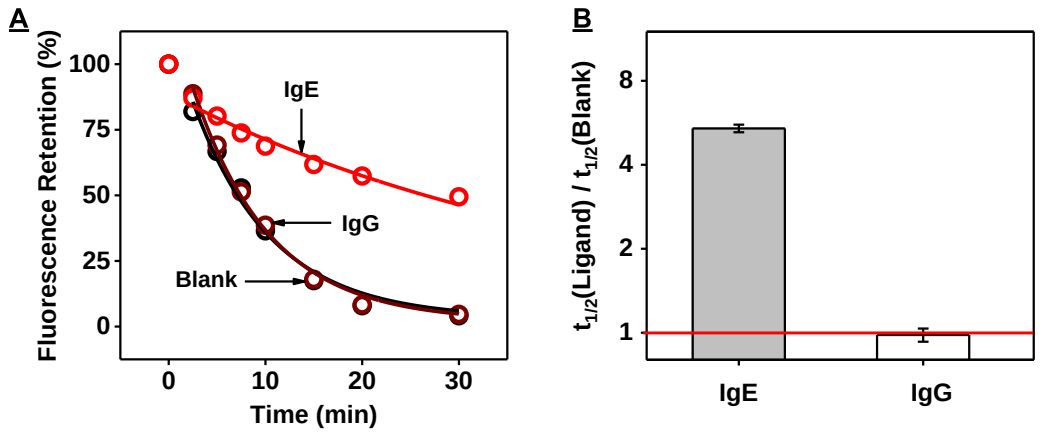

Figure 4-33. Exonuclease-based fluorescence profiling of an IgE-binding aptamer. (**A**) Time-course plot of aptamer digestion by Exo III and Exo I in the absence (black) and presence of 500 nM human IgE (red) or IgG (brown). (**B**) $t_{1/2}$ ratios calculated from plot A. The y-axis is $\log_2$ scaled. The red line indicates a $t_{1/2}$ ratio of 1, which means there was no inhibition of aptamer digestion.

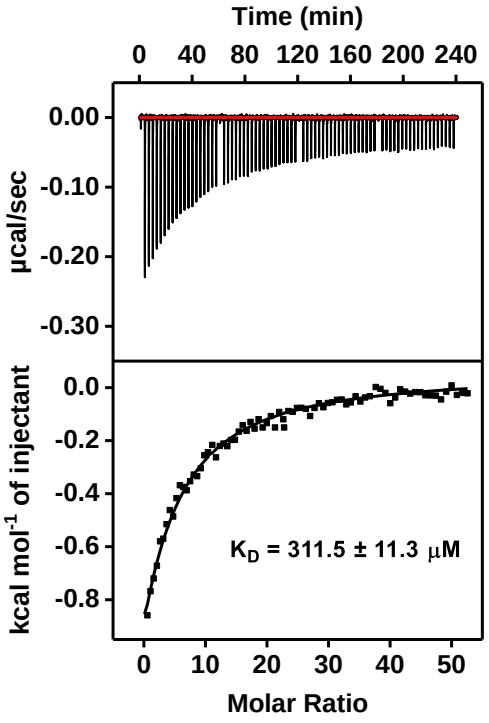

Figure 4-34. Characterization of ligand-binding affinity of a recently published ADE-binding aptamer (A10-excised) to ADE using ITC at room temperature. Top panel displays the heat generated from each titration of ADE to the aptamer. Bottom panel shows the integrated heat of each titration after correcting for the heat of dilution of the titrant. Buffer: 10 mM Tris-HCl, pH 7.4, 20 mM NaCl and 1.5 mM $MgCl_2$.

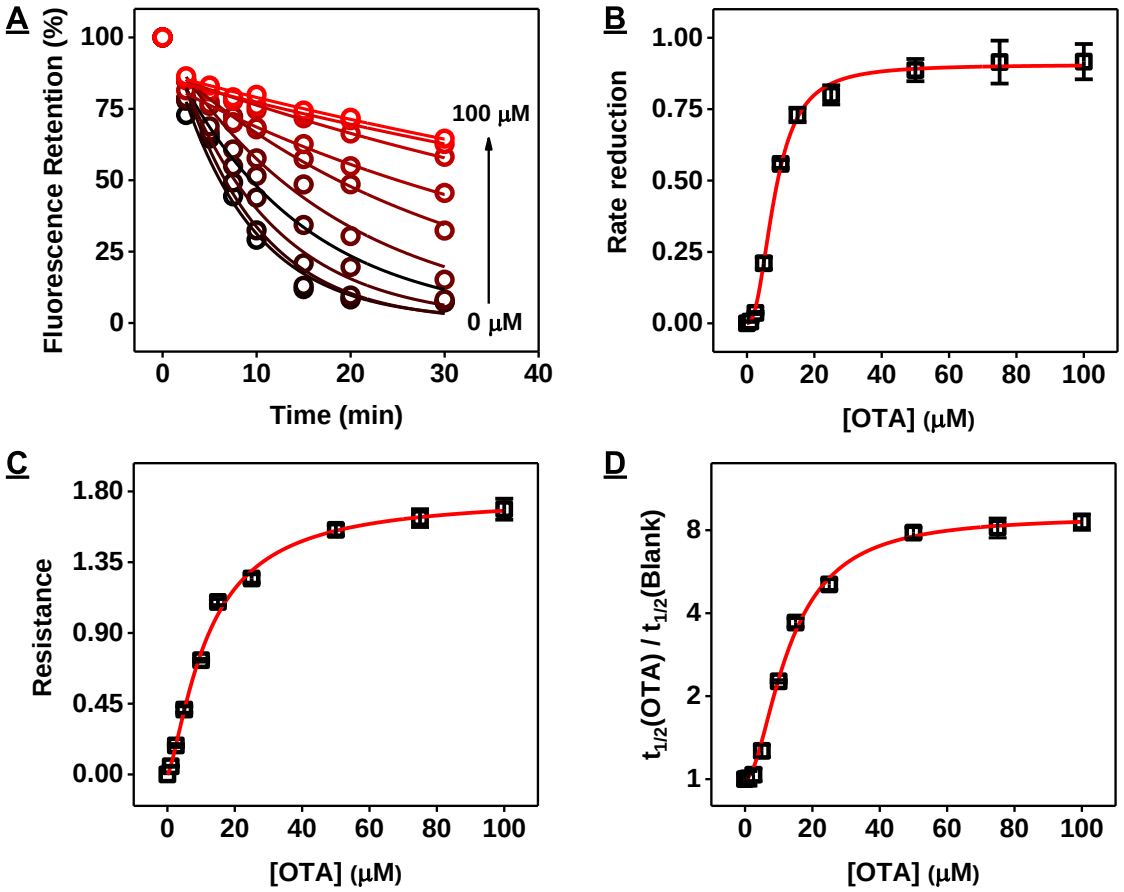

Figure 4-35. Characterization of OBA3 affinity for OTA using the exonuclease digestion assay. (**A**) Fluorescence time-course of the digestion of 1 µM OBA3 in the absence and presence of 0, 2.5, 5, 10, 15, 25, 50, 75 and 100 µM OTA (indicated by black to red color gradient). Data analysis performed by plotting (**B**) reduction in first-order reaction rate of aptamer digestion ($1 - k_{OTA}/k_{blank}$); (**C**) the aptamer's resistance to digestion based on the area under the curve (AUC) of fluorescence digestion plots ($(AUC_{OTA}/AUC_{blank}) - 1$); and (**D**) $t_{1/2}$ ratio at each ligand concentration.

4.4. Conclusion.

Aptamers offer a variety of advantages relative to antibodies that make them desirable biorecognition elements for a variety of applications. The SELEX procedure efficiently partitions and amplifies target-binding sequences from large random oligonucleotide libraries but often yields aptamers with suboptimal binding properties due

to the limited sequence capacity of the library employed for selection and the biases from PCR amplification. Post-SELEX mutagenesis can facilitate identification of new high-performance aptamers, but current characterization strategies are limited by low throughput and the need for specialized instrumentation (e.g., SPR or ITC) or require the use of aptamers or targets that are intrinsically fluorescent or fluorescently labeled (e.g., for microarray assays), which is unfeasible for small-molecule-binding aptamers.

We have developed a novel exonuclease-based fluorescence assay for characterizing the binding properties of small-molecule-binding aptamers in a high-throughput, label-free manner. We determined that there is a strong correlation between relative aptamer−ligand binding affinity and the kinetics of aptamer digestion by the exonucleases Exo III and Exo I. By profiling previously reported aptamers and mutants that bind to ochratoxin A, we determined that the ratio of exonuclease digestion half-lives ($t_{1/2}$) in the presence versus the absence of target could be used to compare aptamer affinity in an unbiased fashion and the aptamer with a longer $t_{1/2}$ ratio has a higher binding affinity compared to those that yielded shorter $t_{1/2}$ ratios. After examining the affinity and specificity of 14 aptamer−ligand pairs, we were able to identify those with the highest affinity for OTA (OBA3) and the greatest capability to distinguish OTA from OTB (OBA1 and OBA2). Importantly, the results of our exonuclease assay closely matched those in a previous report as well as results from the gold-standard method, ITC.

We then characterized a DNA aptamer isolated by Huizenga and Szostak that binds to ATP, ADP, AMP, and ADE with similar binding affinities and improved its binding characteristics by designing and testing 13 mutants. We screened 59 aptamer−ligand pairs and identified two new aptamers with high specificity for ADE relative to its

phosphorylated analogues while still retaining the high affinity of the parent aptamer sequence. Again, the results of our exonuclease-based fluorescence assay correlated well with ITC but offer a more high-throughput and cost-effective alternative. Notably, the Liu group[310] recently engineered a new derivative of the ADE-binding DNA aptamer (A10-excised) that also specifically binds to ADE, but this has 20-fold lower ADE affinity compared to our aptamers under the same buffer conditions (**Figure 4-34**). Our assay can also generate structure-switching aptamers during the screening process, which can be directly incorporated into folding-based sensing platforms. As a demonstration, we employed two ADE-specific, structure-switching aptamers identified from our screen to construct a dual-aptamer E-AB sensor that achieved sensitive and specific detection of ADE with a measurable limit of detection of 1 μM and no cross-reactivity to ATP, ADP, or AMP in 50% serum.

Finally, we assessed the generality of our assay by determining the binding properties of protein-binding aptamers. We digested three G-quadruplex-structured DNA aptamers which bind to human α-thrombin and once again observed a clear correlation between aptamer−ligand binding affinity and $t_{1/2}$ ratio. We also performed our assay with a stem−loop-structured IgE-binding aptamer and determined that the aptamer binds to IgE but not IgG, which is consistent with previously reported findings. These examples demonstrate that our assay is not only applicable for small-molecule-binding aptamers but also for protein-binding aptamers regardless of their binding affinity, secondary structure, or the size of the target protein.

On the basis of the systems we have studied, we provide a guide to interpreting $t_{1/2}$ ratio values as well as using other methods of analyzing the kinetic data. The $t_{1/2}$ ratio

values are not necessarily directly proportional to the K_D of the aptamer, but the $t_{1/2}$ ratio can be used as a relative measure of affinity. Generally, lower $t_{1/2}$ ratios imply weaker binding and vice versa. As described above, the $t_{1/2}$ ratio is dependent on the affinity of both the parent and truncated products. Thus, for a single aptamer, $t_{1/2}$ ratios can be used to compare the relative affinity of the aptamer to a set of ligands. Similarly, $t_{1/2}$ ratios can also be used to evaluate the relative affinity of a set of aptamer mutants derived from a common parent aptamer for the same ligand. We have also identified two other parameters to assess exonuclease digestion assay data: first-order reaction rates of digestion and aptamer resistance to digestion. To demonstrate these different methods of analysis, we digested 1 μM OBA3 with Exo III and Exo I in the presence of 0−100 μM OTA (**Figure 4-35A**). We respectively plotted the reduction in first-order reaction rate of aptamer digestion (**Figure 4-35B**), aptamer resistance to digestion (calculated as resistance value)(**Figure 4-35C**), and $t_{1/2}$ ratio (**Figure 4-35D**) at each ligand concentration. We found that the first-order reaction rate was the most sensitive parameter to ligand concentration, followed by aptamer resistance. However, the $t_{1/2}$ ratio demonstrated a linear relationship across a broader range of target concentrations. We believe that all three parameters are interchangeable and can be used to accurately perform data analysis.

Together, these results indicate that our exonuclease fluorescence assay can be used to determine the binding profiles of aptamers regardless of their sequence, structure, binding affinity, or the properties of the ligand being tested. Although we studied aptamer mutants designed with the guidance from their known tertiary structures, we believe that our method can be generally applied to other small-molecule-binding aptamers without any need for prior knowledge of the target-binding site or overall structure. We recommend

two methods to design mutants. First, for in silico maturation techniques, genetic algorithms create mutants via a combination of crossing over different aptamer sequences and point mutations, and these are then tested in vitro. The outcome of these experiments is used by the algorithm to generate a new batch of mutants, and the process is iterated several times until an aptamer with the desired binding characteristics is found.[107] Second, for aptamers found through high-throughput sequencing, the sequencing data can be analyzed using clustering algorithms such as aptaMOTIF[311] and MEME[312] to identify consensus sequences and variable motifs or nucleotides. This information can be used to design mutants. Although it is difficult to estimate the likelihood of finding a better aptamer from a collection of mutants, this probability can be greatly increased by testing more mutants and higher-order mutants (i.e., double or triple mutants). Since our assay only requires a single mix-and-read step, it can readily be performed using multichannel pipettes and 384-microwell plates to screen hundreds of aptamer−ligand combinations simultaneously within <2 h or even adapted into a high-throughput screening format using an automated liquid handling system. As such, we believe our approach should allow for the greatly accelerated characterization of aptamers for a variety of applications.

CHAPTER 5: Label-Free, High-Throughput, Quantitative Binding Analysis of DNA Aptamers using Exonucleases

5.1. Introduction.

Aptamers are short DNA or RNA oligonucleotides that are isolated *in vitro* on the basis of their ability to recognize a target with high affinity and specificity.[23,24] These oligonucleotides are often employed as biorecognition elements in aptamer-based sensors.[113,262,313] Aptamers have several advantages over other existing recognition elements such as antibodies, including low cost, standardized chemical synthesis and modification protocols, high chemical stability, and long shelf-life.[32,33] Aptamers are isolated through a multi-round process termed systematic evolution of ligands by exponential enrichment (SELEX), which typically yields oligonucleotide pool containing 10^3–10^5 unique sequences. The final SELEX pool and pools from earlier rounds are subjected to high-throughput sequencing, and promising aptamers candidates are then chosen based on their relative abundance in the final pool and/or their enrichment-fold between rounds.[69] However, selection based on these these parameters can be confounded by several biases that appear during selection, such as polymerase amplification bias.[71,72] Therefore, determining the best aptamer sequence for a given application requires a detailed characterization of the binding properties of each candidate.

The characterization of aptamer binding affinity is often done using specialized instrumentation, such as isothermal titration calorimetry (ITC),[77] microscale thermophoresis,[80] and surface plasmon resonance,[285] which can directly measure thermodynamic constants of binding. However, these techniques cannot handle large aptamer candidate pools because of their inherently low throughput. A variety of other

aptamer assays can be performed for initial screening that provide accurate information on aptamer binding profiles in a high-throughput fashion, albeit with less thermodynamic information. The strand-displacement fluorescence assay is one such example that has been used to characterize affinity and specificity for several small-molecule-binding aptamers. This assay employs aptamers modified with a fluorophore tag and a complementary cDNA (cDNA) modified with a quencher.[27,56,57] The hybridization of the cDNA and aptamer brings the quencher near the fluorophore, reducing fluorescence. However, aptamer binding displaces the cDNA, resulting in fluorescence recovery. The change in fluorescence intensity over several target concentrations can be used as a proxy to describe the aptamer-binding strength.[27,56,57] Although this assay has high-throughput capabilities, it is ultimately limited by the high cost of aptamer labeling. Alternatively, the Soh group[314] has incorporated aptamer candidates into DNA microarrays for high-throughput affinity screening. They performed four rounds of SELEX against human angiopoietin-2, and then synthesized the top 235 aptamer candidates from each pool onto a microarray and incubated the array with various concentrations of the fluorophore-labeled protein target. The resulting fluorescence calibration curves allowed them to determine each candidate's binding affinity. However, this assay would be challenging for small-molecule targets, as labeling such targets can significantly impair their aptamer-binding affinity.

We have recently developed a label-free exonuclease-based fluorescence assay that utilizes Exonuclease III (Exo III) and Exonuclease I (Exo I) to assess the affinities and specificities of many aptamer mutants in parallel.[315] In this assay, Exo III and Exo I respectively digest the double-stranded and single-stranded portions of unbound aptamers until only mononucleotides remain. In contrast, the digestion of target-bound aptamers is

inhibited a few bases away from the target-binding domain, yielding a target-bound inhibition product that resists further digestion.[291,292,315] We observed a qualitative relationship between an aptamer's target-binding affinity and its rate of digestion.[315] Here in, we performed a more thorough investigation to establish a quantitative relationship between exonuclease digestion rate and aptamer affinity. Specifically, we performed SELEX experiments with the small-molecule drugs fentanyl, acetyl fentanyl, and furanyl fentanyl. We characterized the binding properties of 28 aptamer candidates using our exonuclease assay, and correlated these results with gold-standard techniques such as ITC and the strand-displacement fluorescence assay. We observed that the degree of an aptamer's exonuclease inhibition is primarily related to the binding affinity (measured as the dissociation constant, K_D) of that aptamer's major digestion product. We were also able to measure the cross-reactivity of several aptamer candidates against 19 interferent molecules and 14 fentanyl analogs. The resulting exonuclease digestion products also possessed structure-switching functionality,[291,315] allowing for rapid incorporation into various aptamer-based sensor formats. We identified optimal aptamer candidates using this assay to develop two electrochemical aptamer-based (E-AB) sensors.[116] The first E-AB sensor was used for sensitive detection of fentanyl in 50% human saliva. The second was used for presumptive testing of fentanyl and its analogs in seized substances. Given our assay's generalizability for aptamers with various sequences and secondary structures, we believe it should expedite the characterization of ideal structure-switching aptamer candidates in a high-throughput and label-free manner for a variety of sensor applications.

5.2. Experimental section.

5.2.1. Reagents.

Exo I (E. coli) (20 U/μL) and Exo III (E. coli) (100 U/μL) were purchased from New England Biolabs. Fentanyl, acetyl fentanyl, furanyl fentanyl, acryl fentanyl, butyryl fentanyl, valeryl fentanyl, cyclopropyl fentanyl, methoxyacetyl fentanyl, p-fluoro isobutyryl fentanyl, o-methyl furanyl fentanyl, and alpha-methyl thiofentanyl were purchased from Cayman Chemicals. Cis-3-methyl fentanyl, p-methoxy furanyl fentanyl, p-fluoro fentanyl, and p-methoxy butyryl fentanyl were provided by the United States Drug Enforcement Administration's Southwest Laboratory. Fentanyl and its analogs were formulated as hydrochloride (HCl) salts. Lorazepam, morphine sulfate, codeine phosphate, and heroin HCl were purchased from Cayman Chemicals. Papaverine HCl, noscapine HCl, and lidocaine HCl were obtained from Acros Organic, Tokyo Chemical Industry, and Alfa Aesar, respectively. Acetaminophen, benzocaine, caffeine, chlorpromazine HCl, cocaine HCl, diphenhydramine HCl, lactose, mannitol, (+)-methamphetamine, procaine HCl, (+)-pseudoephedrine, and quinine hemisulfate monohydrate were purchased from Sigma Aldrich. Formamide was purchased from Thermo Fisher Scientific, and SYBR Gold was purchased from Invitrogen. All other reagents were purchased from Sigma Aldrich unless otherwise noted. ExoSAP-IT Express PCR Purification Kit, streptavidin-modified agarose beads, and Nunc 384-well black plates were purchased from Thermo Fisher Scientific. 800 μL micro-gravity columns were purchased from Bio-Rad, and 3 kDa cut-off spin filters were purchased from Millipore Sigma. GoTaq Hot Start Colorless Master Mix was purchased from Promega. Unmodified oligonucleotides were purchased with standard desalting purification from Integrated DNA Technologies. The random DNA library and

fluorophore- or quencher-modified DNA were purchased from Integrated DNA technologies with HPLC purification. All oligonucleotides were dissolved in PCR-quality water, and their concentrations were measured using a NanoDrop 2000 spectrophotometer. 5'-thiolated and 3'-methylene blue-modified aptamers were purchased with dual HPLC purification from LGC Biosearch Technologies and dissolved in 1×TE Buffer (10 mM Tris-HCl with 1 mM EDTA, pH 8.0). The DNA sequences employed in this work are shown in **Table 5-1**. Deionized (DI) water with conductivity of 18.2 MΩ×cm was obtained from a Milli-Q EQ 7000 ultrapure water filtration system.

Table 5-1. DNA sequences used in chapter 5.

Sequences ID	Sequence (5'–3')
Random library	CGAGCATAGGCAGAACTTACGAC(N30)GTCGTAAGAGCGAGTCATTC
Bio-cDNA	TTTTTGTCGTAAGTTCTGCCATTTT-/3BioTEG/
Forward primer	CGAGCATAGGCAGAACTTAC
Biotinylated-reverse primer	/3BioTEG/-GAATGACTCGCTCTTACGAC
Reverse primer	GAATGACTCGCTCTTACGAC
F1	CTTACGACACGAGGTGTTTGGACTAAGTTCGGTTTCGGGTCGTAAG
F2	CTTACGACGACTGCGTGTGGCCGGTGTGAGGGAGGGTTGTCGTAAG
F3	CTTACGACAGCGGGTGTATGTACTAAGTCCGGTTCGGTGTCGTAAG
F4	CTTACGACACTGGCAGGAGGGTCGGGTGTGGGAACGTGGTCGTAAG
F5	CTTACGACCAGGCCTACGGAAGCAGCGTCAGCGGGGGGGTCGTAAG
F6	CTTACGACTAGTGGAGTAGGGTCGGGTAGTGGGCCTCAGTCGTAAG
F7	CTTACGACCACCATGGGAATCGGGTGGCTTGGAGGTGCGTCGTAAG
F8	CTTACGACGAGCATCGGTTTTTTCGGTGATGTCTGGGAGTCGTAAG
F9	CTTACGACGGAGGTTGGGAAGGAGGGGGAGGCCGGAGAGTCGTAAG
F10	CTTACGACGGCAGGTGTTTGCACTAAGTCCGGTATGTCGTCGTAAG
F11	CTTACGACCGGTGTGCTCGGGGAAGGGGGGCCCTAGGTGTCGTAAG
F12	CTTACGACATCTGCGTGTGGCCGGTGTGAGGGAGGGATGTCGTAAG
F13	CTTACGACCATGGGTGTTTGCACTAAGTCCGGTTCTTGGTCGTAAG
F14	CTTACGACCGGTGTGCTCGGGGAAGGGGGCCCTAGGTGGTCGTAAG
F15	CTTACGACACCGGGATCCAGATGGGTAGTTTGATGTGTGTCGTAAG
F16	CTTACGACCGGCGGAAGGCTGGAGGGGTTGGGGGAGGTGTCGTAAG
F17	CTTACGACCGGTGGGGAGGCCGGAGTTGGGAACGGGGGGTCGTAAG
F18	CTTACGACCGGGATCCTTTGGGACAACCTGGTGGGCATGTCGTAAG
F19	CTTACGACGGGGTACCCGGACAGTGATGTTTGGTGTTCGTCGTAAG
F20	CTTACGACGAAGCAACGGGGTTTCGGAGGGCAGGTGTCGTCGTAAG
F21	CTTACGACCGGACATGTGATCGGGCAGCTGGGAGTCGGGTCGTAAG
F22	CTTACGACGTCGAGGGGTACCCTTTGGCGTTCGTCGAGGTCGTAAG
F23	CTTACGACCAGGCTACGTGGGGGAGGGTGGGAAGACGGGTCGTAAG

F24	CTTACGACACAGGGTGTGTTGTGCTCAGTGGTGTATGTGTCGTAAG
F25	CTTACGACAGGGGTACCCGCGTATAACGTGGCGTTCGTGTCGTAAG
F26	CTTACGACGGGGTGGGGGCGGCTTCCCATGGGAGGGGTGTCGTAAG
F27	CTTACGACGAGCGCGTGTGGCCGGCGTGAGGGAGGTGAGTCGTAAG
F28	CTTACGACGGGTGGGGAGGCCCTCTAGTTGGGAACGGTGTCGTAAG
F4-FAM	/FAM/TGGCAGAACTTACGACACTGGCAGGAGGGTCGGGTGTGGGAACGTGG TCGTAAG
F13-FAM	/FAM/TGGCAGAACTTACGACCATGGGTGTTTGCACTAAGTCCGGTTCTTGGT CGTAAG
F27-FAM	/FAM/TGGCAGAACTTACGACGAGCGCGTGTGGCCGGCGTGAGGGAGGTGA GTCGTAAG
F27-42-FAM	/FAM/TGGCAGAACTTACGACGAGCGCGTGTGGCCGGCGTGAGGGAGGTGA GTCG
cDNA-Dab	GTCGTAAGTTCTGCC/Dab/
F13-39	CTTACGACCATGGGTGTTTGCACTAAGTCCGGTTCTTGG
F27-42	CTTACGACGAGCGCGTGTGGCCGGCGTGAGGGAGGTGAGTCG
F13-32-MB	/ThiolC6/CCATGGGTGTTTGCACTAAGTCCGGTTCTTGG/MB/
F27-38-MB	/ThiolC6/CGACGAGCGCGTGTGGCCGGCGTGAGGGAGGTGAGTCG/MB/

N30 represents 30 random nucleotides; /3BioTEG/ represents biotin tag; /FAM/ represents fluorescein tag; /Dab/ represents dabcyl quencher tag; /ThiolC6/ represents thiol group with six-carbon spacer; /MB/ represents methylene blue redox tag

5.2.2. SELEX procedure.

Isolation of aptamers against fentanyl, acetyl fentanyl, and furanyl fentanyl was carried out using the previously reported library-immobilized SELEX protocol with some modifications.[28,37] The selection buffer employed was 10 mM Tris-HCl (pH 7.4), 20 mM NaCl, 0.5 mM $MgCl_2$, with 1% (v/v) methanol. The initial random library pool consisted of ~6×10^{14} (1 nmol) oligonucleotides. Each library strand contains a randomized 30-nt loop flanked by two PCR primer-binding sites with an 8-nt stem-forming constant region. The general SELEX procedure comprised library immobilization, washing, target elution, library amplification, and single-strand generation, as described previously.[28,37] Selection strategies and conditions for fentanyl, acetyl fentanyl, and furanyl fentanyl SELEX experiments can be found in **Tables 5-2, 5-3, and 5-4**, respectively.

Table 5-2. Selection strategy and condition for fentanyl SELEX.

Round	Pool (pmol)	Wash steps	Counter SELEX								Wash steps
1	1000	10	NA								NA
2	350	10	Cocaine ×3 (100 µM)					Heroin ×3 (100 µM)			30
3	350	30	G1 ×3 (100 µM)					G2 ×3 (100 µM)			30
4	300	30	G1 ×3 (100 µM)					G2 ×3 (100 µM)			30
5	300	30	G1 ×3 (100 µM)					G2 ×3 (100 µM)			30
6	300	30	G1 ×3 (250 µM)					G2 ×3 (250 µM)			30
7	300	30	G1 ×3 250 µM	G2 ×3 250 µM	G3 ×3 100 µM	G4 ×3 100 µM	G5 ×3 100 µM	G6 ×3 100 µM	G7 ×3 100 µM	G8 ×3 100 µM	30
8	200	30	G1 ×3 250 µM	G2 ×3 250 µM	G3 ×3 250 µM	G4 ×3 250 µM	G5 ×3 250 µM	G6 ×3 250 µM	G7 ×3 250 µM	G8 ×3 250 µM	30
9	200	30	G1 ×3 500 µM	G2 ×3 500 µM	G3 ×3 500 µM	G4 ×3 500 µM	G5 ×3 500 µM	G6 ×3 250 µM	G7 ×3 250 µM	G8 ×3 250 µM	30
10	200	30	G1 ×3 500 µM	G2 ×3 500 µM	G3 ×3 500 µM	G4 ×3 500 µM	G5 ×3 500 µM	G6 ×3 250 µM	G7 ×3 250 µM	G8 ×3 250 µM	30
11	200	30	G1 ×3 500 µM	G2 ×3 500 µM	G3 ×3 500 µM	G4 ×3 500 µM	G5 ×3 500 µM	G6 ×3 250 µM	G7 ×3 250 µM	G8 ×3 250 µM	30

Counter-target groups were as follows:

G1 (cocaine, procaine, and lidocaine)
G2 (heroin and quinine)
G3 (acetaminophen, benzocaine, diphenhydramine, (+)-pseudoephedrine, and (+)-methamphetamine)
G4 (codeine, morphine, and chlorpromazine)
G5 (lactose, mannitol, and caffeine)
G6 (lorazepam)
G7 (papaverine)
G8 (noscapine)

Listed concentrations are for each chemical present in the group. Each wash consisted of 250 µL 1× SELEX buffer. Between each counter-target, three washes with 1× SELEX buffer were performed. Washing for each counter target or target group was performed three times.

Table 5-3. Selection strategy and condition for acetyl fentanyl SELEX.

Round	Pool (pmol)	Wash steps	Counter SELEX								Wash steps	Target (μM)
1	1000	10	NA								NA	500
2	350	10	Cocaine ×3 (100 μM)				Heroin ×3 (100 μM)				30	500
3	350	30	G1 ×3 (100 μM)				G2 ×3 (100 μM)				30	250
4	300	30	G1 ×3 (100 μM)				G2 ×3 (100 μM)				30	250
5	300	30	G1 ×3 100 μM		G2 ×3 100 μM		G6 ×3 250 μM		G7 ×3 250 μM	G8 ×3 250 μM	30	250
6	300	30	G1 ×3 250 μM		G2 ×3 250 μM		G6 ×3 250 μM		G7 ×3 250 μM	G8 ×3 250 μM	30	250
7	300	30	G1 ×3 250 μM	G2 ×3 250 μM	G3 ×3 250 μM	G4 ×3 100 μM	G5 ×3 100 μM	G6 ×5 250 μM	G7 ×5 250 μM	G8 ×5 250 μM	30	200
8	200	30	G1 ×3 250 μM	G2 ×3 250 μM	G3 ×3 250 μM	G4 ×3 250 μM	G5 ×3 250 μM	G6 ×10 250 μM	G7 ×10 250 μM	G8 ×10 250 μM	30	100
9	200	30	G1 ×3 500 μM	G2 ×3 500 μM	G3 ×3 500 μM	G4 ×3 500 μM	G5 ×3 500 μM	G6 ×10 250 μM	G7 ×10 250 μM	G8 ×10 250 μM	30	75
10	200	30	G1 ×3 500 μM	G2 ×3 500 μM	G3 ×3 500 μM	G4 ×3 500 μM	G5 ×3 500 μM	G6 ×10 250 μM	G7 ×10 250 μM	G8 ×10 250 μM	30	50

Counter-target groups were as follows:

G1 (cocaine, procaine, and lidocaine)
G2 (heroin and quinine)
G3 (acetaminophen, benzocaine, diphenhydramine, (+)-pseudoephedrine, and (+)-methamphetamine)
G4 (codeine, morphine, and chlorpromazine)
G5 (lactose, mannitol, and caffeine)
G6 (lorazepam)
G7 (papaverine)
G8 (noscapine)

Listed concentrations are for each chemical present in the group. Each wash consisted of 250 μL 1× SELEX buffer. Between each counter-target, three washes with 1× SELEX buffer were performed. Washing for each counter target or target group was performed three times.

Table 5-4. Selection strategy and condition for furanyl fentanyl SELEX.

Round	Pool (pmol)	Wash steps	Counter SELEX								Wash steps	Target (μM)
1	1000	10	NA								NA	500
2	350	10	Cocaine ×3 (100 μM)				Heroin ×3 (100 μM)				30	500
3	350	30	G1 ×3 100 μM	G2 ×3 100 μM	G6 ×3 250 μM	G7 ×3 250 μM	G8 ×3 250 μM				30	250
4	300	30	G1 ×3 100 μM	G2 ×3 100 μM	G6 ×3 250 μM	G7 ×3 250 μM	G8 ×3 250 μM				30	250
5	300	30	G1 ×3 100 μM	G2 ×3 100 μM	G6 ×5 250 μM	G7 ×5 250 μM	G8 ×5 250 μM				30	250
6	300	30	G1 ×3 250 μM	G2 ×3 250 μM	G6 ×5 250 μM	G7 ×5 250 μM	G8 ×5 250 μM				30	250
7	300	30	G1 ×3 250 μM	G2 ×3 250 μM	G3 ×3 100 μM	G4 ×3 100 μM	G5 ×3 100 μM	G6 ×5 250 μM	G7 ×5 250 μM	G8 ×5 250 μM	30	200
8	200	30	G1 ×3 250 μM	G2 ×3 250 μM	G3 ×3 250 μM	G4 ×3 250 μM	G5 ×3 250 μM	G6 ×10 250 μM	G7 ×10 250 μM	G8 ×10 250 μM	30	100
9	200	30	G1 ×3 500 μM	G2 ×3 500 μM	G3 ×3 500 μM	G4 ×3 500 μM	G5 ×3 500 μM	G6 ×10 250 μM	G7 ×10 250 μM	G8 ×10 250 μM	30	50
10	200	30	G1 ×3 500 μM	G2 ×3 500 μM	G3 ×3 500 μM	G4 ×3 500 μM	G5 ×3 500 μM	G6 ×10 250 μM	G7 ×10 250 μM	G8 ×10 250 μM	30	25

Counter-target groups were as follows:

G1 (cocaine, procaine, and lidocaine)
G2 (heroin and quinine)
G3 (acetaminophen, benzocaine, diphenhydramine, (+)-pseudoephedrine, and (+)-methamphetamine)
G4 (codeine, morphine, and chlorpromazine)
G5 (lactose, mannitol, and caffeine)
G6 (lorazepam)
G7 (papaverine)
G8 (noscapine)

Listed concentrations are for each chemical present in the group. Each wash consisted of 250 μL 1× SELEX buffer. Between each counter-target, three washes with 1× SELEX buffer were performed. Washing for each counter target or target group was performed three times.

5.2.3. High-throughput sequencing.

Round 9 and 11 fentanyl pools, round 8 and 10 acetyl fentanyl pools, and round 7 and 10 furanyl fentanyl pools were submitted for high-throughput sequencing (HTS) at FIU's DNA Core Facility with an Ion Personal Genome Machine System with an Ion 318 v2 chip (Thermo Fisher Scientific). Before sequencing, each library pool (final

concentration: 10 nM) was mixed with GoTaq Hot Start Colorless Master Mix, forward primer (final concentration: 1 μM), and reverse primer (final concentration: 1 μM) and diluted with PCR-quality water to a final volume of 50 μL. Nine PCR cycles were performed using the following conditions: 2 min at 95 °C; 9 cycles of 95 °C for 15 s, 58 °C for 30 s, and 72 °C for 45 s; and finally, 5 min at 72 °C. 40 μL of each PCR product was added to 16 μL of ExoSAP-IT reagent and kept on ice. The mixture was then incubated at 37 °C for 15 min to degrade the remaining primers and dNTPs, followed by incubation at 80 °C for 15 min to inactivate the ExoSAP-IT reagent, after which the samples were submitted for sequencing. Primer sequences were trimmed by cutadapt,[316] and further analysis of sequence population and enrichment between rounds was done using FASTAptamer.[317]

5.2.4. Aptamer digestion experiments.

Screening of aptamer candidates was performed using an exonuclease fluorescence assay, as previously reported.[315] Briefly, a 1 μL solution of aptamer (final concentration 1 μM) was added to 5 μL Tris–HCl (pH 7.4), heated to 95 °C for 10 min and immediately cooled on ice, and then diluted to a volume of 35 μL with salts, methanol, and BSA (final concentration: 10 mM Tris–HCl, 20 mM NaCl, 0.5 mM $MgCl_2$, 1% (v/v) MeOH, 0.1 mg/mL BSA, pH 7.4). Next, 5 μL of buffer, fentanyl, fentanyl analog, or interferent solution (final concentration varied depending on the experiment) was added to the reaction mixture and incubated in a thermal cycler (C1000 Touch, Bio-Rad) at 25 °C for 60 min. Finally, 5 μL of exonuclease mixture (final concentrations: 0.025 U/μL Exo III and 0.05 U/μL Exo I) was added to each reaction. To monitor the digestion progress, 5 μL of the samples were collected at various time-points and added to the wells of a Nunc 384-well

black plate containing 25 µL of quench solution (final concentrations: 10 mM Tris-HCl (pH 7.4), 12.5% formamide, 10 mM EDTA, 1× SYBR Gold). The fluorescence intensity of SYBR gold ($\lambda_{ex}/\lambda_{em}$ = 495/537 nm)[268] was recorded using a Tecan Infinite M1000 PRO microplate reader and plotted as a function of time. The area under the curve (AUC) of the aptamer fluorescence time-course plot was calculated in the absence and presence of the target. Resistance value (R_{value}), a target-binding induced enzyme inhibition metric, was calculated as $R_{value} = (AUC_{target}/AUC_{blank})-1$.[89]

5.2.5. ITC experiments.

All ITC experiments were performed in selection buffer with a MicroCal ITC200 instrument (Malvern) at 23 °C. For each experiment, 300 µL of parent aptamer or major digestion product (final concentrations varying depending on experiments) in Tris–HCl buffer (pH 7.4, without salts) was heated at 95 °C for 10 min and immediately cooled on ice. Salts and methanol were subsequently added to match selection buffer conditions before loading into the sample cell. The syringe was loaded with fentanyl, acetyl fentanyl, furanyl fentanyl, or quinine in selection buffer. The concentrations used are listed in **Tables 5-5 and 5-6**. Typically, each titration consisted of an initial purge injection of 0.4 µL and 19 successive injections of 2 µL with a spacing of 180 sec between each injection but was changed as necessary for specific sequences (F2, F5-40, F7-40, F12, F16, F27, F2-38, F12-38, F16-43, and F22-42). The raw data were first corrected for the dilution heat of the ligand and then analyzed with the MicroCal analysis kit integrated into Origin 7 software and fitted with a single-site binding model.

Table 5-5. Aptamer ID, K_D, and ITC conditions.

Aptamer ID	Ligand type	[Ligand] (μM)	[Aptamer] (μM)	K_D (nM)
F1	Fentanyl	200	20	510 ± 13
F2	Fentanyl	150	15	93 ± 5
F3	Fentanyl	200	20	709 ± 37
F4	Fentanyl	200	20	923 ± 41
F5	Fentanyl	150	20	316 ± 17
F6	Fentanyl	100	10	42 ± 4
F7	Fentanyl	100	10	43 ± 5
F8	Fentanyl	100	10	350 ± 22
F9	Fentanyl	100	10	72 ± 9
F21	Fentanyl	150	20	310 ± 10
F28	Fentanyl	100	10	43 ± 4
F10	Acetyl fentanyl	200	20	546 ± 25
F11	Acetyl fentanyl	1000	40	27,200 ± 650
F12	Acetyl fentanyl	65	7.5	60 ± 7
F13	Acetyl fentanyl	200	20	251 ± 15
F14	Acetyl fentanyl	200	20	68 ± 4
F15	Acetyl fentanyl	100	10	156 ± 10
F16	Acetyl fentanyl	50	10	67 ± 18
F17	Acetyl fentanyl	100	10	98 ± 7
F18	Acetyl fentanyl	100	10	29 ± 3
F19	Furanyl fentanyl	250	20	NA
F20	Furanyl fentanyl	100	10	207 ± 14
F21	Furanyl fentanyl	150	15	193 ± 18
F22	Furanyl fentanyl	100	10	240 ± 22
F23	Furanyl fentanyl	100	10	51 ± 3
F24	Furanyl fentanyl	100	10	63 ± 11
F25	Furanyl fentanyl	100	10	171 ± 11
F26	Furanyl fentanyl	150	10	59 ± 7
F27	Furanyl fentanyl	100	10	4 ± 1
F28	Furanyl fentanyl	60	7.5	62 ± 9
F2	Furanyl fentanyl	100	10	53 ± 12
F6	Furanyl fentanyl	100	10	63 ± 7

Table 5-6. Aptamer digestion product ID, K_D, and ITC conditions.

Aptamer ID	Target type	[Ligand] (μM)	[Aptamer] (μM)	Product K_D (nM)	Parent K_D (nM)	K_D of Product/Parent
F1-40	Fentanyl	1000	50	3,730 ± 110	510 ± 13	7.3
F2-38	Fentanyl	1400	80	40,600 ± 5627	93 ± 5	436.6
F3-37	Fentanyl	1000	40	64,900 ± 2100	709 ± 37	91.5
F5-40	Fentanyl	150 × 2	20	2,808 ± 377	316 ± 17	8.9
F7-40	Fentanyl	1000	40	15,800 ± 1300	43 ± 5	367.4
F8-42	Fentanyl	100	10	165 ± 16	350 ± 22	0.5
F13-39	Fentanyl	320	20	5550 ± 285	NA	NA
F21-35	Fentanyl	1000	40	NA	310 ± 10	NA
F27-42	Fentanyl	200	30	203 ± 28	NA	NA
F10-37	Acetyl fentanyl	1500	100	91,700 ± 3700	546 ± 25	167.9
F12-38	Acetyl fentanyl	600	60	12,722 ± 195	60 ± 7	212.0
F13-39	Acetyl fentanyl	100	10	2,659 ± 37	251 ± 15	10.6
F16-43	Acetyl fentanyl	100	20	35 ± 7	67 ± 18	0.5
F18-43	Acetyl fentanyl	100	10	17 ± 4	29 ± 3	0.6
F27-42	Acetyl fentanyl	200	30	122 ± 10	12.4 ± 1[a]	9.8
F20-40	Furanyl fentanyl	400	40	6,450 ± 449	207 ± 14	31.2
F21-35	Furanyl fentanyl	400	40	NA	193 ± 18	NA
F22-42	Furanyl fentanyl	400	40	4,761 ± 412	240 ± 22	19.8
F23-40	Furanyl fentanyl	100	10	523 ± 67	51 ± 3	10.3
F27-42	Furanyl fentanyl	200	30	130 ± 18	7.5 ± 0.4[a]	17.3
F2-38	Furanyl fentanyl	300 × 5	60	5,747 ± 293	53 ± 12	108.4

NA[a]: Aptamer affinity was determined using a strand-displacement assay.

5.2.6. Strand-displacement fluorescence assay.

5.2.6.1. Determination of F27-FAM binding affinity.

The strand-displacement fluorescence assay was performed using a previously reported protocol. The K_D between target and aptamer is equal to the ratio of K_{D1} (cDNA-aptamer affinity) and K_{D2} (target affinity for the aptamer-cDNA complex). To determine K_{D1}, fluorescein-modified F27 (F27-FAM) was hybridized with a 15-nt dabcyl-modified cDNA (cDNA-Dab). Specifically, 72 μL of F27-FAM dissolved in 1× selection buffer (final concentration: 50 nM) was mixed with 8 μL of various concentrations of cDNA-Dab

(final concentrations: 0, 7, 15, 31, 62, 125, 250, 500, or 1,000 nM) in 1× selection buffer. The mixture was heated to 90 °C for 10 min and then cooled gradually to room temperature over 20 min to promote annealing. Afterward, 70 µL of each solution was loaded into the wells of a Nunc 384-well black plate, and the fluorescence intensity was immediately recorded using a Tecan microplate reader ($\lambda_{ex}/\lambda_{em}$ = 495/520 nm). K_{D1} was determined by fitting the curve using a Langmuir binding isotherm and calculating the free cDNA concentration at 50% quenching efficiency, resulting in a K_{D1} of 15.2 ± 1 nM. To determine K_{D2}, a 72 µL solution of aptamer-cDNA complex (final concentrations: 50 nM F27-FAM and 125 nM cDNA-Dab) dissolved in 1× selection buffer was heated to 90 °C for 10 min and cooled to room temperature over 20 min to promote perfect hybridization between both strands. Then 8 µL of acetyl fentanyl or furanyl fentanyl at various concentrations in 1× selection buffer (final concentrations: 0, 5, 10, 20, 39, 78, 156, 312.5, 625, 1,250, 2,500, and 5,000 nM) was added to the aptamer/cDNA complexes. The mixture was incubated at room temperature for 1 hour to allow the system to reach equilibrium, after which 70 µL of each solution was loaded into the wells of a Nunc 384-well black plate with the fluorescence intensity ($\lambda_{ex}/\lambda_{em}$ = 495/520 nm) being immediately recorded. K_{D2} was calculated by fitting the fluorescence recovery to a Langmuir binding isotherm and dividing the free cDNA by the free target concentration at the half-saturation point of the cDNA displacement curve. A K_{D2} value of 1.23 and 2.02 were obtained for acetyl fentanyl and furanyl fentanyl, respectively. Based on K_{D1} and K_{D2}, F27 yielded a K_D of 12.4 ± 1 and 7.5 ± 0.4 nM for acetyl fentanyl and furanyl fentanyl, respectively.

5.2.6.2. Determination of aptamer specificity and cross-reactivity.

First, the concentration of cDNA-Dab necessary to achieve ~75% quenching efficiency was determined. 72 µL of fluorescein-modified F4 (F4-FAM), fluorescein-modified F13 (F13-FAM), F27-FAM or fluorescein-modified F27-4 (F27-42-FAM) (final concentrations: 50 nM) dissolved in 1× selection buffer. For F4-FAM, F13-FAM, and F27-FAM, the solution was mixed with 8 µL of various concentrations of cDNA-Dab in 1× selection buffer (final concentrations: 0, 7, 15, 31, 62, 125, 250, 500, or 1,000 nM). For F27-42-FAM, a cDNA containing a single G–T mismatch (cDNA-GT-Dab) was used instead (final concentrations: 0, 16, 31, 62.5, 125, 250, 500, 1,000, 2,000, or 4,000 nM). The mixture was heated to 90 °C for 10 min and slowly cooled down to room temperature over 20 min to promote the annealing of both strands. Afterward, 70 µL of each solution was loaded into the wells of a Nunc 384-well black plate, and the fluorescence intensity was immediately recorded using a Tecan microplate reader ($\lambda_{ex}/\lambda_{em}$ = 495/520 nm). An optimized aptamer/cDNA ratios for each aptamer was determined for specificity and/or cross-reactivity testing (50 nM F4-FAM/100 nM cDNA-Dab, 50 nM F13-FAM/250 nM cDNA-Dab, 50 nM F27-FAM/250 nM cDNA-Dab, or 50 nM F27-42-FAM/250 nM cDNA-GT-Dab). The specificity of F4-FAM, F13-FAM, and F27-FAM was determined against the 19 counter-targets employed during selection. The cross-reactivity of F13-FAM, F27-FAM, and F27-42-FAM was determined against fentanyl and its 14 analogs. Specifically, 72 µL of aptamer/cDNA mixture in 1.1× selection buffer was heated and then cooled to promote annealing. The target and interferent molecules were prepared in DI water containing 10% methanol to enhance drug solubility. Then 72 µL aptamer/cDNA mixture was added to an 8 µL solution of selection target or analog (final concentration:

100 µM) or interferent (final concentration: 100 µM) and incubated for 1 hour at room temperature to allow the system to reach equilibrium. 70 µL of each sample was then loaded into the wells of a Nunc 384-well black plate, and the fluorescence intensity ($\lambda_{ex}/\lambda_{em}$ = 495/520 nm) was immediately recorded. For F4-FAM, F13-FAM, F27-FAM, or F27-42-FAM, cross-reactivity was calculated based on the signal produced by fentanyl, acetyl fentanyl, furanyl fentanyl, or furanyl fentanyl, respectively.

5.2.7. Fabrication of E-AB sensors.

Aptamer-modified gold electrodes were prepared using a target-assisted immobilization strategy.[318] Polishing and cleaning of the electrodes were performed using a previously reported protocol.[294] Methylene blue-modified thiolated aptamers (F13-32-MB or F27-38-MB) were mixed with 100 mM Tris(2-carboxyethyl)phosphine hydrochloride in deionized water for 2 hours to reduce the disulfide bonds between aptamers. The freshly reduced aptamers were further diluted to various concentrations (final concentrations: 50, 100, or 150 nM for F13-32-MB or 10, 25, 50, or 100 nM for F27-38-MB) in selection buffer containing 50 µM acetyl fentanyl or fentanyl, respectively. Cleaned electrodes were incubated in the aptamer solution for 13 hours at room temperature in the dark. After aptamer immobilization, the electrode was rinsed with deionized water and then backfilled with 1 mM 6-mercapto-1-hexanol prepared in 1× selection buffer containing 50 µM acetyl fentanyl or fentanyl for F13-32-MB or F27-38-MB, respectively, for 2 hours at room temperature. Finally, the electrodes were rinsed with DI water and stored in 10 mM Tris–HCl (pH 7.4) for 1 hour before measurements.

5.2.8. Electrochemical measurements and optimization of E-AB sensor performance.

All electrochemical measurements were performed using a CHI760D electrochemical workstation with a three-electrode system containing an Ag/AgCl reference electrode (3M KCl) (CHI), a platinum wire counter electrode (CHI), and an aptamer-modified gold working electrode. To optimize surface coverage, E-AB sensors were constructed using 50, 100, or 150 nM F13-32-MB or 10, 25, or 50 nM F27-38-MB. Peak currents produced by 5, 15, and 50 μM target were obtained for each modified electrode with square-wave voltammetry (SWV) measurement frequency of 200 Hz. The signal gain was calculated using the equation $(I - I_0)/I_0 \times 100\%$, where I and I_0 are the peak current in the presence and absence of the target, respectively. The best sensing performance was achieved with electrodes modified with 100 nM F13-32-MB or 10 nM F27-38-MB, corresponding to a surface coverage of 3.33 ± 0.4 and 2.17 ± 0.1 pmol/cm^2, respectively, based on the method reported by Tarlov et al.[296] Next, we optimized the frequency of SWV measurements in the range of 50–400 Hz by measuring the signal gain at 50 μM target. The optimal frequency was 200 and 400 Hz for E-AB sensors constructed with F13-32-MB and F27-38-MB, respectively. All data represent the average of measurements taken with three independent working electrodes.

5.2.9. Cross-reactivity and binary-mixture measurements using E-AB sensors constructed with F13-32-MB.

E-AB sensors were fabricated as previously described using 100 nM F13-32-MB. Each electrode was placed in 1 mL selection buffer alone or containing fentanyl or one of its analogs (final concentration: 5 μM). After 1 minute of incubation at room temperature, the peak SWV current was recorded three times, and the average current was used to

calculate signal gain. Sensor cross-reactivity was calculated relative to the signal gain produced by 5 μM fentanyl. For detection of fentanyl in binary mixtures, a similar detection procedure was done, except the electrodes were placed in 1 mL selection buffer containing either 5 μM fentanyl or 5 μM fentanyl mixed with 500 μM cocaine, lactose, mannitol, quinine, lidocaine, heroin, benzocaine, (+)-methamphetamine, diphenhydramine, (+)-pseudoephedrine, acetaminophen, codeine, chlorpromazine, morphine, caffeine, or procaine, or 200 μM papaverine, noscapine, or lorazepam. Cross-reactivity was calculated relative to the signal gain produced by 5 μM fentanyl only. All data represent the average of measurements taken with three working electrodes.

5.2.10. Detection of fentanyl in 50% saliva using E-AB sensors constructed with F27-38-MB.

To perform detection of fentanyl in saliva, we first prepared pooled human saliva based on a published protocol. Drug-spiked 50% saliva samples were prepared by mixing 500 μL of 2× selection buffer with or without fentanyl with 500 μL of human saliva. Before detection, sensors constructed with 10 nM F27-38-MB were first incubated in a 6 M guanidinium HCl solution for 10 min to unfold the aptamers and release any remaining fentanyl from the target-assisted immobilization step. The treated electrodes were then incubated in fentanyl-spiked 50% saliva samples for 1 min, and the peak SWV current was recorded three times. The signal gain was calculated using the average peak current. All data represent the average of measurements taken with three independent working electrodes.

5.2.11. Polyacrylamide gel electrophoresis (PAGE) analysis of digestion products.

Aptamer digestion products were analyzed using denaturing PAGE by collecting 5 µL of samples at various time intervals and mixing it with 10 µL of formamide loading buffer (75% formamide, 10% glycerol, 0.125% SDS, 10 mM EDTA, and 0.15% (w/v) xylene cyanol). 6 µL of each sample was loaded into a 15% denaturing PAGE gel. Separation was carried out at 6 V/cm for 30 mins followed by 25 V/cm for 4 hr in 0.5× TBE running buffer. The gel was stained with 1× SYBR Gold for 25 min and imaged using a ChemiDoc MP Image system (Bio-Rad). The major digestion product of each aptamer was determined using a DNA ladder customized for each sequence.

5.2.12. Confirmation of structure-switching functionality of aptamer digestion products using circular dichroism (CD) spectroscopy.

CD experiments were performed at room temperature using a Jasco J-815 CD spectropolarimeter. F13-39 or F27-42 (1.5 µM final concentration) was prepared in Tris–HCl buffer, heated to 95 °C for 10 mins, and immediately cooled on ice for 5 min, after which salts and methanol were added (Final concentration: 10 mM Tris–HCl, pH 7.4, 20 mM NaCl, 0.5 mM $MgCl_2$, 1% MeOH). Then DI water or target (final concentration: 10 µM) was added to the solution to a total volume of 300 µL. The solution was transferred to a 1 cm quartz cuvette (Hellma Analytics) and measured using the following parameters: scan range of 210 to 310 nm, scan speed of 50 nm/min, sensitivity of 5 mdeg, response time of 4 s, bandwidth of 1 nm, and accumulation of 5 scans. Reference spectra of selection buffer were taken with and without target. To produce the final reported spectra, they were subtracted from the CD spectra collected with aptamer in the absence or presence of their respective target.

5.3. Results and Discussion.

We have recently developed a label-free exonuclease fluorescence assay for characterizing the binding profile of several aptamer mutants.[315] Our previous screening results using ochratoxin A- and ATP-binding DNA aptamers showed a qualitative relationship between the degree of enzymatic inhibition and the aptamer's target-binding affinity.[315] However, we could not find a quantitative relationship as the dataset was too small. We now used a testbed of 28 aptamer candidates isolated from three separate SELEX experiments against fentanyl, acetyl fentanyl, and furanyl fentanyl. Each aptamer candidate's exonuclease results were compared against either ITC or the strand-displacement fluorescence assay to validate the relationship between enzyme inhibition and K_D.

5.3.1. Isolation of aptamers against fentanyl and its analogs using SELEX.

Fentanyl and its analogs are a family of potent narcotic analgesics. As of 2020,[194] fentanyl and its analogs were the fourth most abused illicit substance and the top cause of drug-related overdose deaths in the USA. These molecules act on the μ-opioid receptors, providing potent pain relief with several-fold greater potency than morphine.[216,217] Fentanyl and its analogs share the 4-anilidopiperidine core structure, but with various chemical modifications on its five variable regions (**Figure 5-1A**, R_1-R_5).[222–224] Screening of fentanyl and its analogs in seized substances is currently performed using chemical spot tests [225,226] or lateral-flow immunoassays.[227–229] Chemical spot tests use reagents that react with specific chemical functional groups on the drug target to generate a colored product. These tests are rapid and inexpensive but generally unreliable, as they also tend to respond to interferent molecules that share the same functional groups.[319–321] Lateral-flow immunoassays are

much more specific and usually only respond to the intended target with high sensitivity. However, these are based on antibodies with limited cross-reactivity, and which therefore only respond to a handful of analogs.[227–229] There is thus a need for better bioreceptors that can recognize the broad family of fentanyl analogs while also specifically discriminating against interferent molecules to combat the ever-growing opioid crisis.

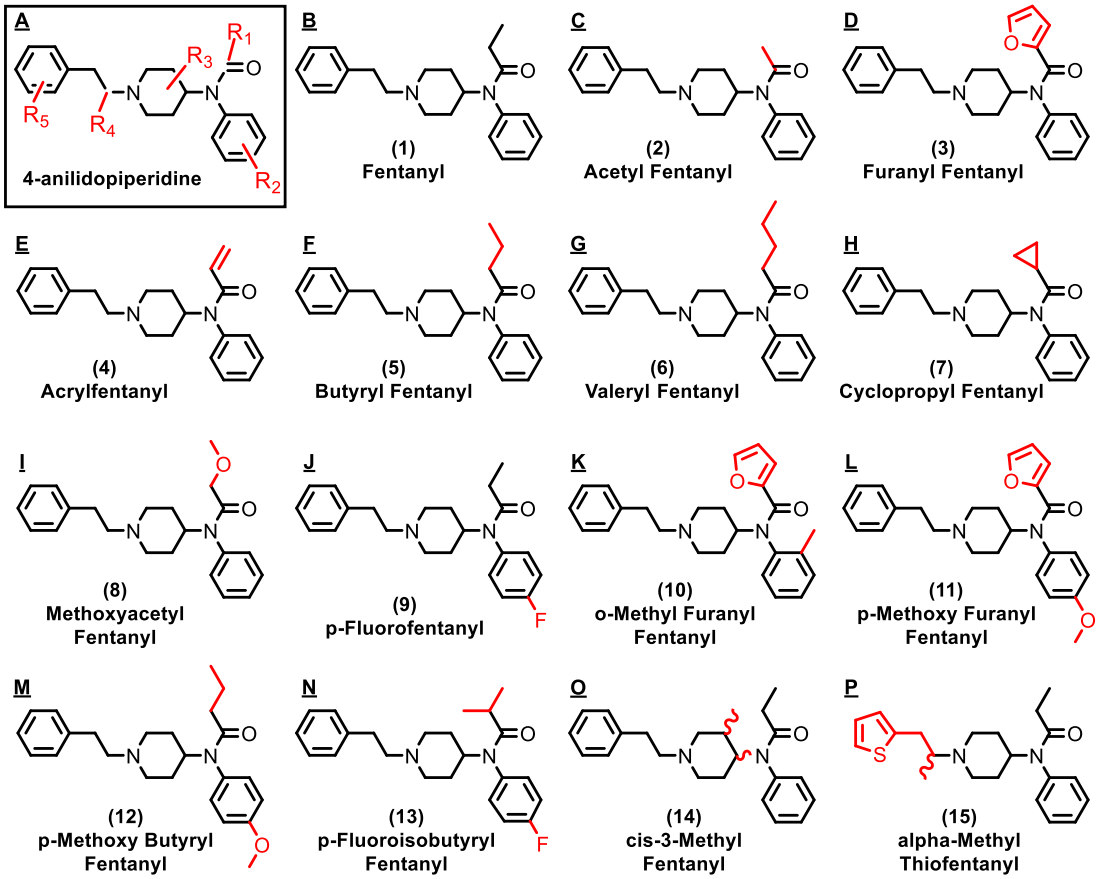

Figure 5-1. The chemical structures of fentanyl and its analogs. (**A**) 4-anilidopiperidine core structure, (**B**) fentanyl (**1**), (**C**) acetyl fentanyl (**2**), (**D**) furanyl fentanyl (**3**), (**E**) acrylfentanyl (**4**), (**F**) butyryl fentanyl (**5**), (**G**) valeryl fentanyl (**6**), (**H**) cyclopropyl fentanyl (**7**), (**I**) methoxyacetyl fentanyl (**8**), (**J**) p-fluorofentanyl (**9**), (**K**) o-methyl furanyl fentanyl (**10**), (**L**) p-methoxy furanyl fentanyl (**11**), (**M**) p-methoxy butyryl fentanyl (**12**), (**N**) p-fluoroisobutyryl fentanyl (**13**), (**Q**) cis-3-methyl fentanyl (**14**), and (**P**) alpha-methyl thiofentanyl (**15**). The substituent sites are marked in red.

To isolate an aptamer that is cross-reactive to fentanyl and its analogs, we selected fentanyl, acetyl fentanyl, and furanyl fentanyl as the selection targets (**Figure 5-1B–D**). These molecules are among the most commonly encountered members[194] in the fentanyl family and possess various modifications at the R_1 site. We began by performing three separate SELEX experiments against these targets with detailed conditions listed in **Tables 5-2, 5-3, and 5-4**. Each library molecule comprises a 73-nucleotide (nt) stem-loop containing a 30-nt random region flanked by two primer binding sites containing a constant 8-base pair stem (**Table 5-1**). Each selection began with an initial pool size of 1,000 pmol that was gradually reduced to 200 pmol over the selection process. The concentration of the selection target and counter-target were steadily reduced and increased, respectively, to apply selection pressure to enrich high-affinity and -specificity aptamers. We observed complete enrichment of the fentanyl pool after 11 rounds of selection (**Figure 5-2A**) and characterized the affinity and specificity of the pool using a gel elution assay. The final pool demonstrated a fentanyl binding affinity of 17 µM, with ~100% cross-reactivity to 25 µM acetyl fentanyl and 74% cross-reactivity to 25 µM furanyl fentanyl (**Figure 5-2B & C**). Moreover, the pool demonstrated excellent specificity against 16 of the counter-targets at 250 µM (<5% cross-reactivity). However, cross-reactivities >12% were observed for lorazepam, noscapine, and papaverine (**Figure 5-2C**), indicating that more effort must be put into counter-selection to remove nonspecific aptamers that bind these counter-targets. Therefore, we employed counter-selection against lorazepam, noscapine, and papaverine during earlier rounds (round 5 onward) for selection against acetyl fentanyl. The acetyl fentanyl-binding pool was fully enriched after 10 rounds (**Figure 5-3A**) and demonstrated a binding affinity of 15 µM with high cross-reactivity to 25 µM fentanyl and furanyl

fentanyl (**Figure 5-3B**). We also observed reduced cross-reactivity to lorazepam, noscapine, and papaverine (**Figure 5-3C**), indicating that even earlier counter-selection may improve the pool's specificity. We therefore employed counter-selection against lorazepam, noscapine, and papaverine starting in round 3 for furanyl fentanyl SELEX. The furanyl fentanyl-binding pool was fully enriched after 10 rounds (**Figure 5-4A**) and demonstrated a binding affinity of 9 μM with high cross-reactivity against 25 μM fentanyl and furanyl fentanyl (**Figure 5-4B**). Although the furanyl fentanyl pool had the earliest employed counter-selection against lorazepam, noscapine, and papaverine, we still observed cross-reactivity (**Figure 5-4C**). This is presumably due to the moderate binding affinity these ligands have against DNA.[322,323]

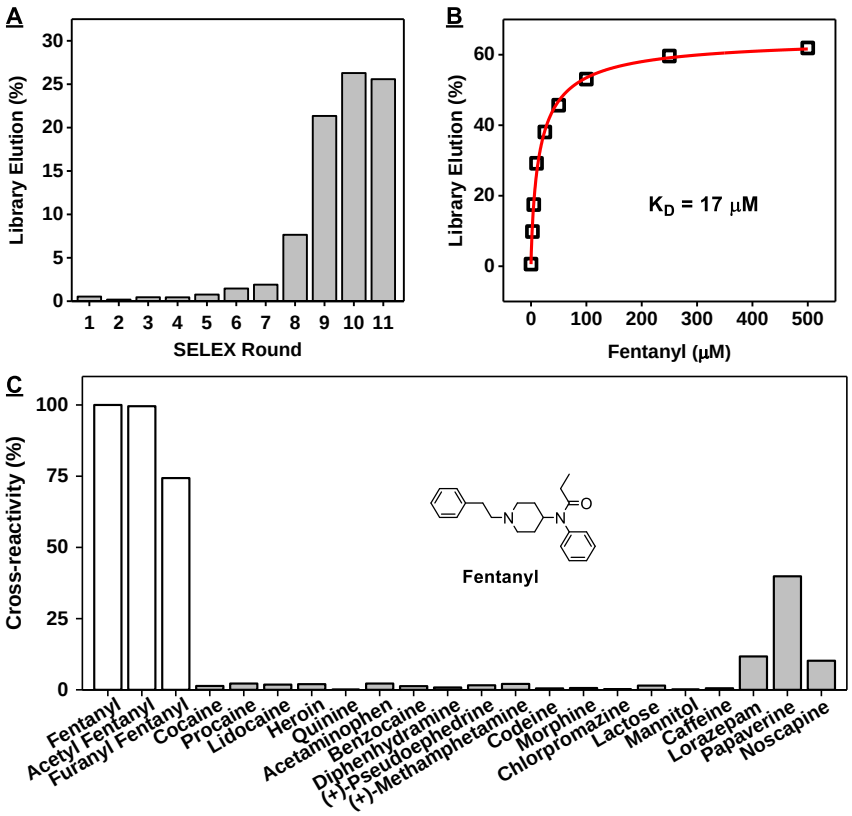

Figure 5-2. Isolation of fentanyl-binding aptamers via library-immobilized SELEX. (**A**) Percent of pools eluted by the target in each selection round. (**B**) Determination of binding

affinity of the round 11 fentanyl pool using a gel elution assay. Percent of pool eluted by fentanyl was plotted against fentanyl concentration (0, 2.5, 5, 10, 25, 50, 100, 250, 500 µM). (**C**) Cross-reactivity of the round 11 fentanyl pool against 25 µM fentanyl, acetyl fentanyl, or furanyl fentanyl, or 250 µM of various counter-targets. Cross-reactivity is calculated relative to the pool eluted by 25 µM fentanyl.

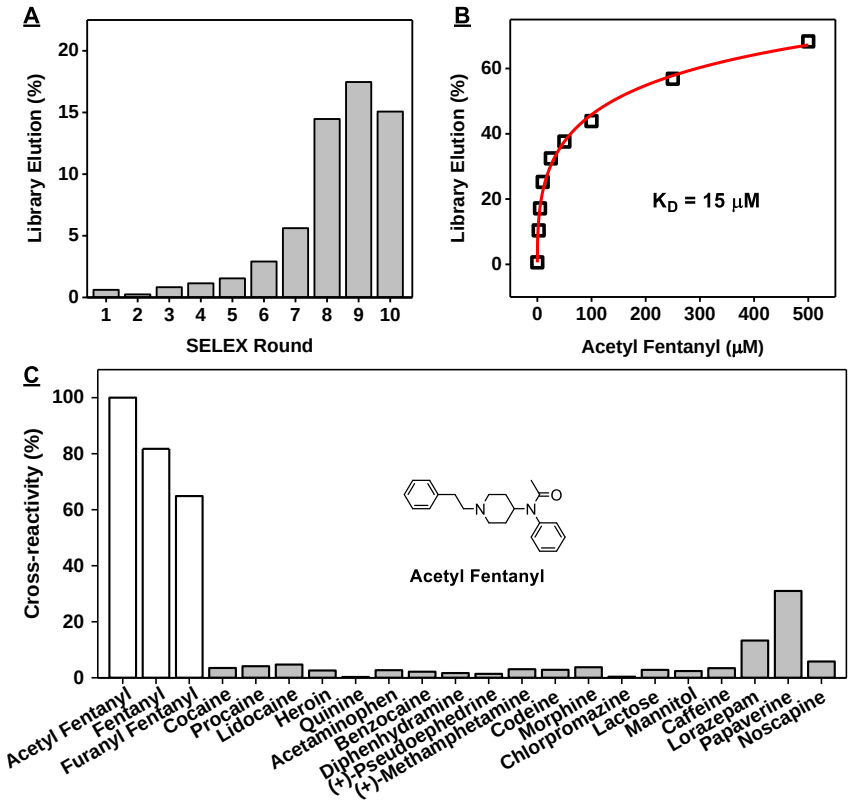

Figure 5-3. Isolation of acetyl fentanyl-binding aptamers via library-immobilized SELEX. (**A**) Percent of pools eluted by the target in each selection round. (**B**) Determination of binding affinity of the round 10 acetyl fentanyl pool using a gel elution assay. Percent of pool eluted by acetyl fentanyl was plotted against acetyl fentanyl concentration (0, 2.5, 5, 10, 25, 50, 100, 250, 500 µM). **C**) Cross-reactivity of the round 10 acetyl fentanyl pool against 25 µM of various counter-targets. Cross-reactivity is calculated relative to the pool eluted by 25 µM acetyl fentanyl.

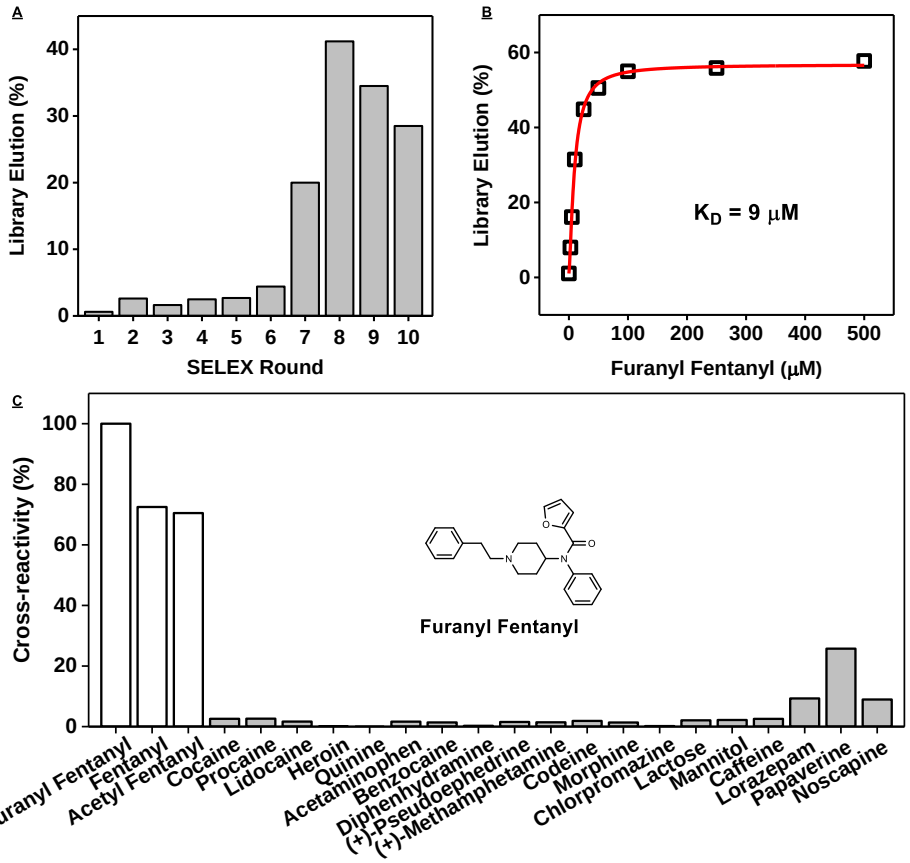

Figure 5-4. Isolation of furanyl fentanyl-binding aptamers via library-immobilized SELEX. (**A**) Percent of pools eluted by the target in each selection round. (**B**) Determination of binding affinity of the round 10 furanyl fentanyl pool using a gel elution assay. Percent of pool eluted by furanyl fentanyl was plotted against furanyl fentanyl concentration (0, 2.5, 5, 10, 25, 50, 100, 250, 500 μM). **C**) Determination of the cross-reactivity of the round 10 furanyl fentanyl pool against 25 μM furanyl fentanyl, fentanyl, or acetyl fentanyl, or 250 μM of various counter-targets. Cross-reactivity is calculated relative to the pool eluted by 25 μM furanyl fentanyl.

5.3.2 High-throughput sequencing (HTS) of enriched pools.

We subjected the final pool from each selection and an earlier pool to HTS to obtain the relative population in the final round and enrichment-fold of each sequence during selection. Rounds 9 and 11 from the fentanyl pool, rounds 8 and 10 from the acetyl fentanyl pool, and rounds 7 and 10 from the furanyl fentanyl pool were sequenced, with a total of

435,632, 521,281, 381,252, 492,320, 410,943, and 1,425,919 reads for each pool, respectively. Cutadapt[316] software was then used to remove the primer regions, after which the population and enrichment-fold for each unique sequence were calculated using the FASTAptamer[317] software. The population of each sequence during both selection rounds is plotted in **Figure 5-5**, with each black circle in **Figures 5-5A, C, & E** representing a unique sequence. The dashed blue line illustrates the position of sequences that had no change in population between rounds and can be used to gauge the growth of other sequences between rounds. Sequences above the blue line had positive enrichment (increase in abundance), while sequences below had negative enrichment (decrease in abundance). For each SELEX experiment, several sequences were observed with negative or positive enrichment, indicating that dynamic changes were still occurring during selection. We employed two selection criteria to identify promising aptamer candidates: aptamers with a final abundance $\geq$3.5%, and aptamers with a final abundance $\geq$1% as well as enrichment-fold $\geq$2 (**Figure 5-5B, D, & F**). Thirty-three sequences fit these criteria, five of which appeared for more than one selection target. Specifically, F2, F6, F21, and F28 appeared in the final fentanyl and furanyl fentanyl pools, and F27 appeared in the final acetyl fentanyl and furanyl fentanyl pools. The other 28 aptamer candidates were chosen for synthesis and subsequent testing (**Table 5-1**).

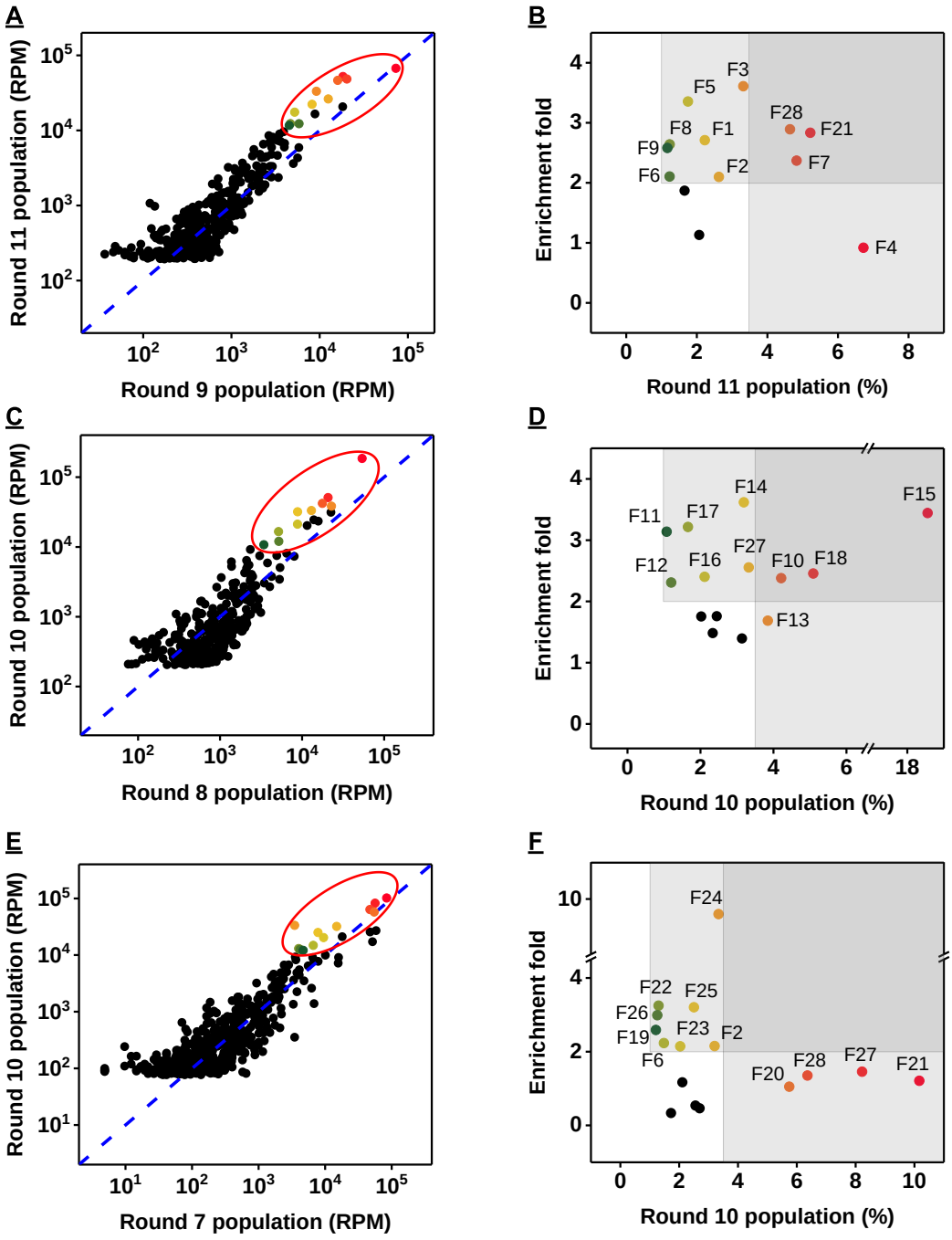

Figure 5-5. HTS analysis of enriched pools. Analysis of sequence abundance between (**A**) round 9 and 11 fentanyl pools, (**C**) round 8 and 10 acetyl fentanyl pools, and (**E**) round 7 and 10 furanyl fentanyl pools. Enrichment-fold of sequences present at >1% of (**B**) round 11 fentanyl pool, (**D**) round 10 acetyl fentanyl pool, and (**F**) round 10 furanyl fentanyl pool. Shaded grey rectangles indicate sequences with ≥3.5% abundance or with ≥1% abundance and ≥2-fold enrichment-fold. Sequences selected for further characterization are shown by colored dots.

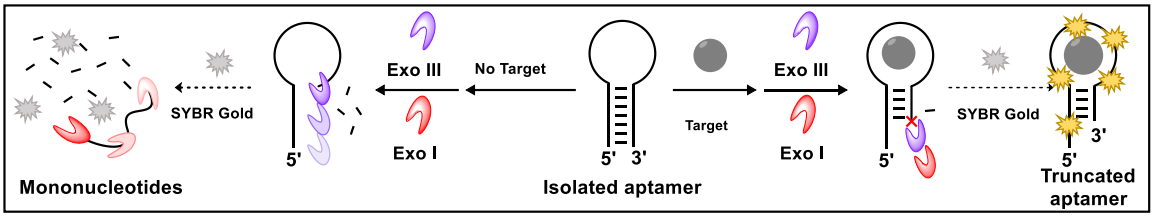

Figure 5-6. Schematic of our exonuclease digestion assay for distinguishing ligand-bound and non-bound aptamers.

5.3.3. Rapid screening of 28 aptamer candidates for their target-binding affinity.

The exonuclease fluorescence assay utilizes Exo III, a 3'-to-5' double-strand exonuclease, and Exo I, a 3'-to-5' single-strand exonuclease, to selectively digest unbound aptamers into mononucleotides (**Figure 5-6**, left) while halting digestion a few bases before the binding domain of ligand-bound aptamers (**Figure 5-6**, right). Digestion is monitored using the DNA-binding dye SYBR Gold, which selectively binds intact oligonucleotides and emits strong fluorescence while having no affinity for mononucleotides (**Figure 5-6**). Using this assay, we screened the target-binding affinity of our 28 aptamer candidates. We anticipated that aptamers with strong ligand affinity will resist digestion and be retained over the entire time-course. In contrast, non-binding or weakly bound aptamers will have produced minimal fluorescence after being rapidly digested into mononucleotides. We first digested each aptamer in the absence or presence of 100 µM of their respective selection target. Several samples were collected over the digestion time-course, and the reaction was stopped by adding a quench solution composed of EDTA, formamide, and SYBR Gold. The fluorescence intensity was plotted against reaction time to construct a time-course of digestion for each aptamer in the presence and absence of their respective selection target (**Figures 5-7, 5-8, and 5-9**). Several parameters can describe the degree of enzyme inhibition, including first-order reaction rate, reaction half-life, and area-under-the-curve

(AUC).[89] To minimize the error associated with fitting slow reaction kinetics with exponential rate equations, we performed all analyses of enzymatic inhibition using the AUC parameter. The AUC value was normalized based on each aptamer's digestion rate using the following equation to determine the 'resistance value': $R_{value} = (AUC_{target}/AUC_{blank})-1$. A large R_{value} indicates potent ligand-induced enzyme inhibition, whereas an R_{value} of 0 indicates no inhibition. We observed 11 aptamers with R_{value} >0.8 (F4, F6, F9, F14, F15, F16, F17, F18, F25, F27, and F28), nine with $0.8 > R_{value} > 0.4$ (F5, F7, F8, F12, F13, F20, F23, F24, and F26), and eight with $R_{value} < 0.4$ (F1, F2, F3, F10, F11, F19, F21, and F22) (**Figure 5-10**). Based on these results, we anticipated that aptamer sequences with large R_{values} (> 0.8) would also have the highest affinity, while those with low R_{values} (< 0.4) would have little to no ligand-binding affinity.

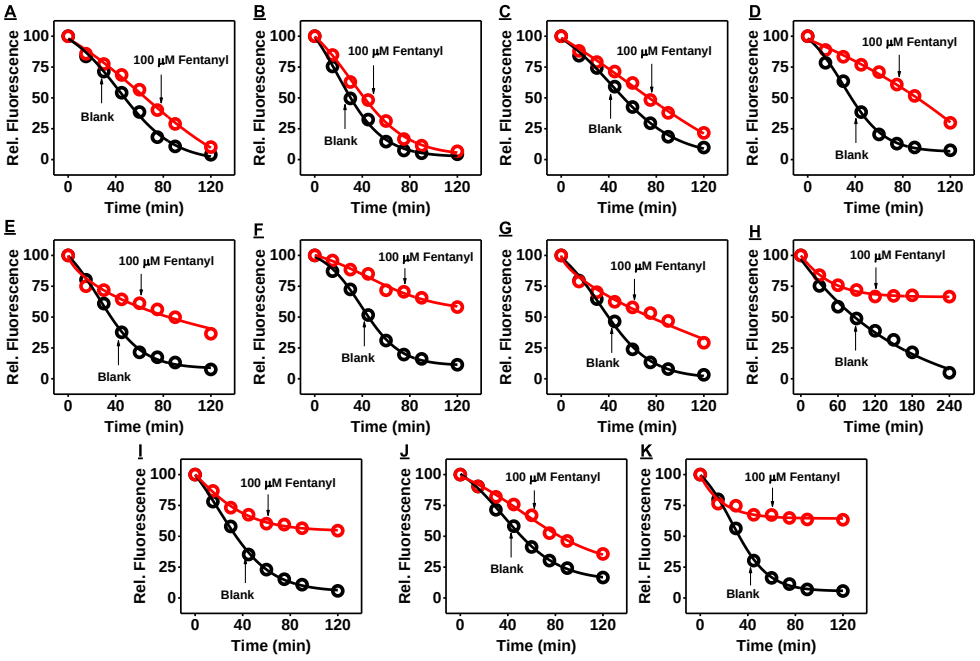

Figure 5-7. Fentanyl binding affinity of 11 aptamer candidates. Time-course digestion of (**A**) F1, (**B**) F2, (**C**) F3, (**D**) F4, (**E**) F5, (**F**) F6, (**G**) F7, (**H**) F8, (**I**) F9, (**J**) F21, and (**K**) F28 in the absence and presence of 100 µM fentanyl.

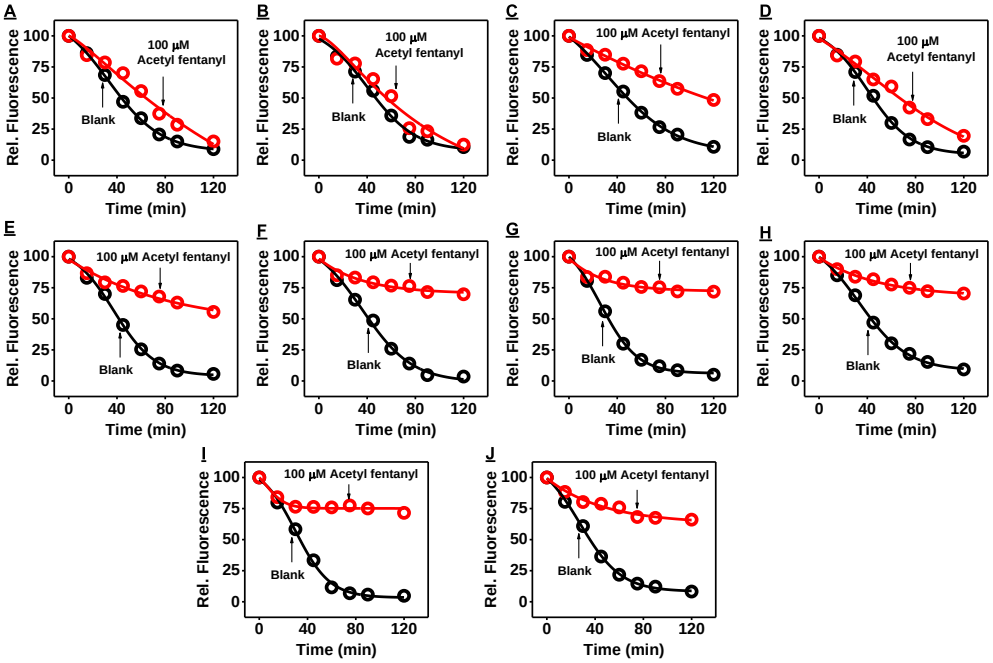

Figure 5-8. Acetyl fentanyl binding affinity of 10 aptamer candidates. Time-course digestion of (**A**) F10, (**B**) F11, (**C**) F12, (**D**) F13, (**E**) F14, (**F**) F15, (**G**) F16, (**H**) F17, (**I**) F18, and (**J**) F27 in the absence and presence of 100 µM acetyl fentanyl.

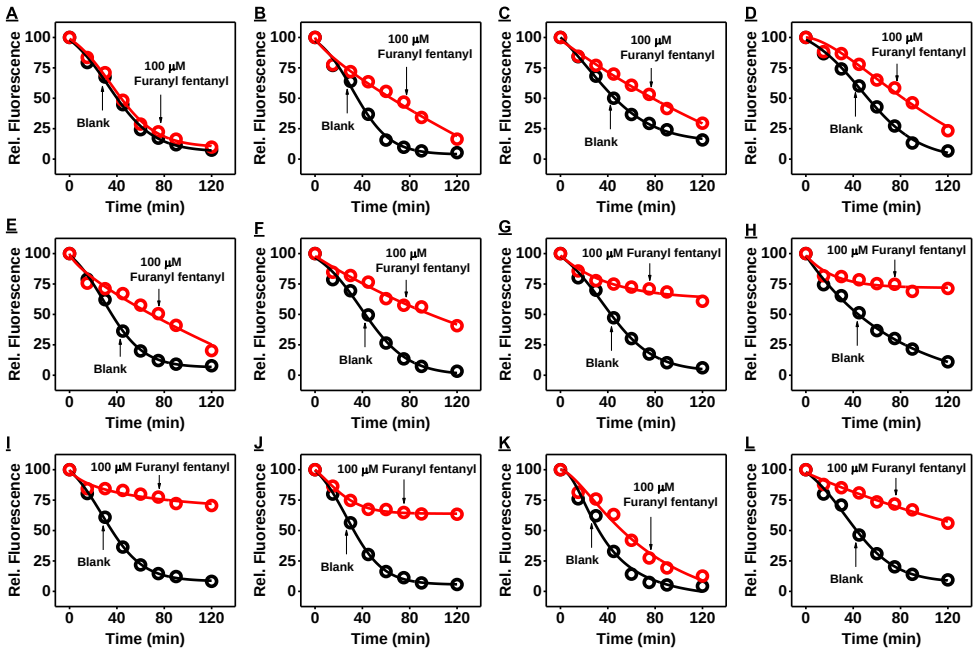

Figure 5-9. Furanyl fentanyl binding affinity of 12 aptamer candidates. Time-course digestion of (**A**) F19, (**B**) F20, (**C**) F21, (**D**) F22, (**E**) F23, (**F**) F24, (**G**) F25, (**H**) F26, (**I**) F27, (**J**) F28, (**K**) F2, and (**L**) F6 in the absence and presence of 100 µM furanyl fentanyl.

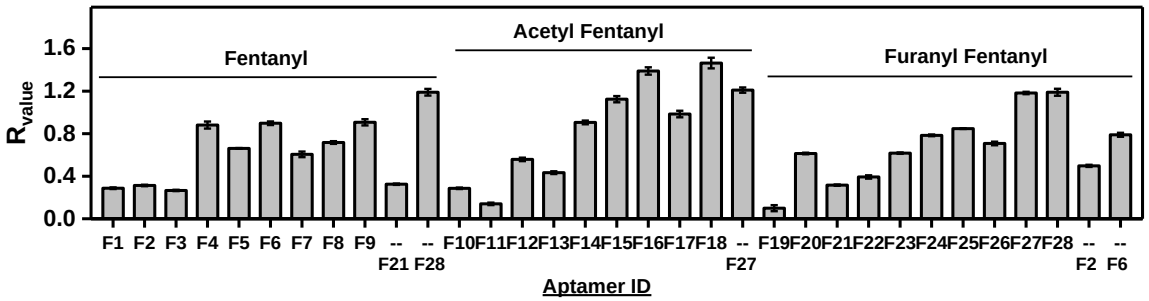

Figure 5-10. R_{value} for aptamer candidates in the presence of 100 μM of their respective selection targets.

Based on this dataset, we set out to find the correlation between an aptamer's R_{value} and K_D. We determined each aptamer candidate's K_D for its selection target using ITC (**Figures 5-11, 5-12, 5-13, 5-14, 5-15, 5-16, and 5-17**) and the strand-displacement fluorescence assay (**Figure 5-18**). Two aptamers had an exceptionally weak binding affinity (K_D > 25 μM), and 25 aptamers had K_D ranging between 10–1,000 nM (**Table 5-5**). One aptamer (F27) demonstrated an exceptionally low K_D for furanyl fentanyl of 4 ± 1 nM (**Figure 5-17**). We suspected that this measurement may have a significant error, given the large c-value of 1,750. However, we confirmed F27's K_D using the strand-displacement method, obtaining similar values of 12.4 ± 1 nM and 7.5 ± 0.4 for acetyl fentanyl and furanyl fentanyl, respectively (**Figure 5-18**).

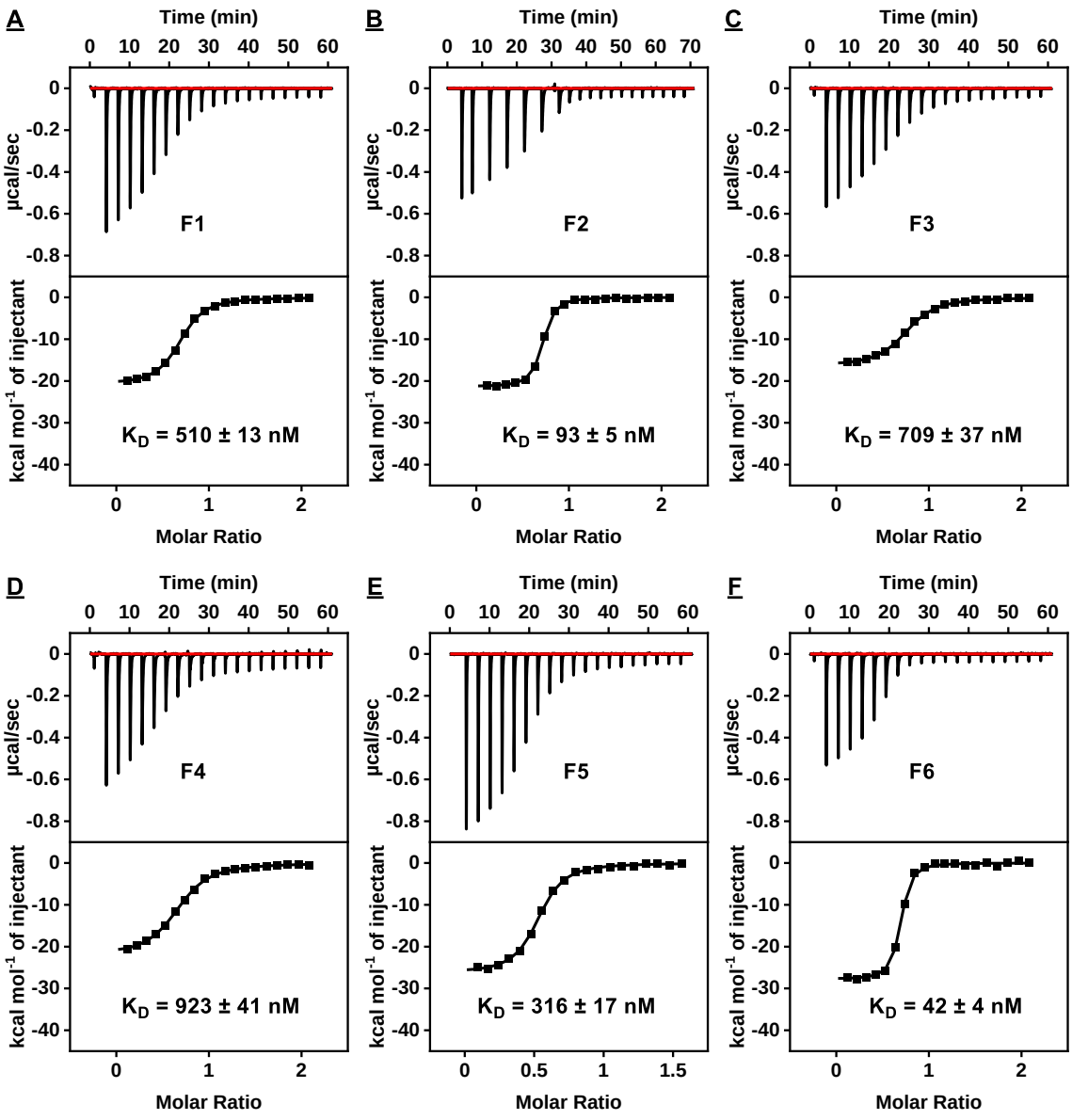

Figure 5-11. Characterization of fentanyl binding affinity of six aptamer candidates using ITC. The top panels display the heat generated from each titration of fentanyl into (**A**) F1, (**B**) F2, (**C**) F3, (**D**) F4, (**E**) F5, and (**F**) F6. The bottom panels show the integrated heat of each titration after correcting for the heat of dilution of the titrant.

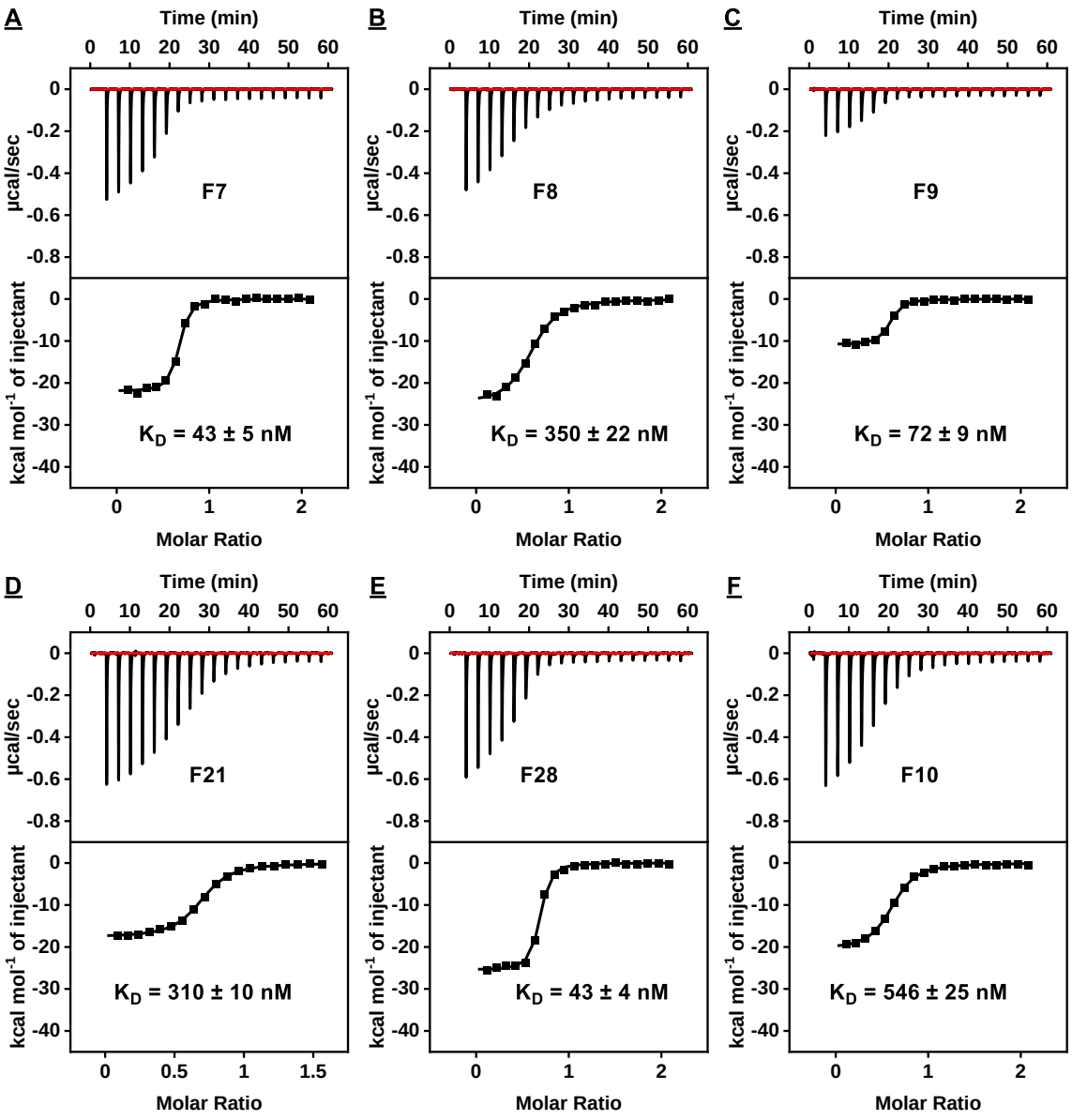

Figure 5-12. Characterization of fentanyl- and acetyl fentanyl-binding affinity of six aptamer candidates using ITC. The top panels display the heat generated from each titration of fentanyl into (**A**) F7, (**B**) F8, (**C**) F9, (**D**) F21, and (**E**) F28, or acetyl fentanyl into (**F**) F10. The bottom panels show the integrated heat of each titration after correcting for the heat of dilution of the titrant.

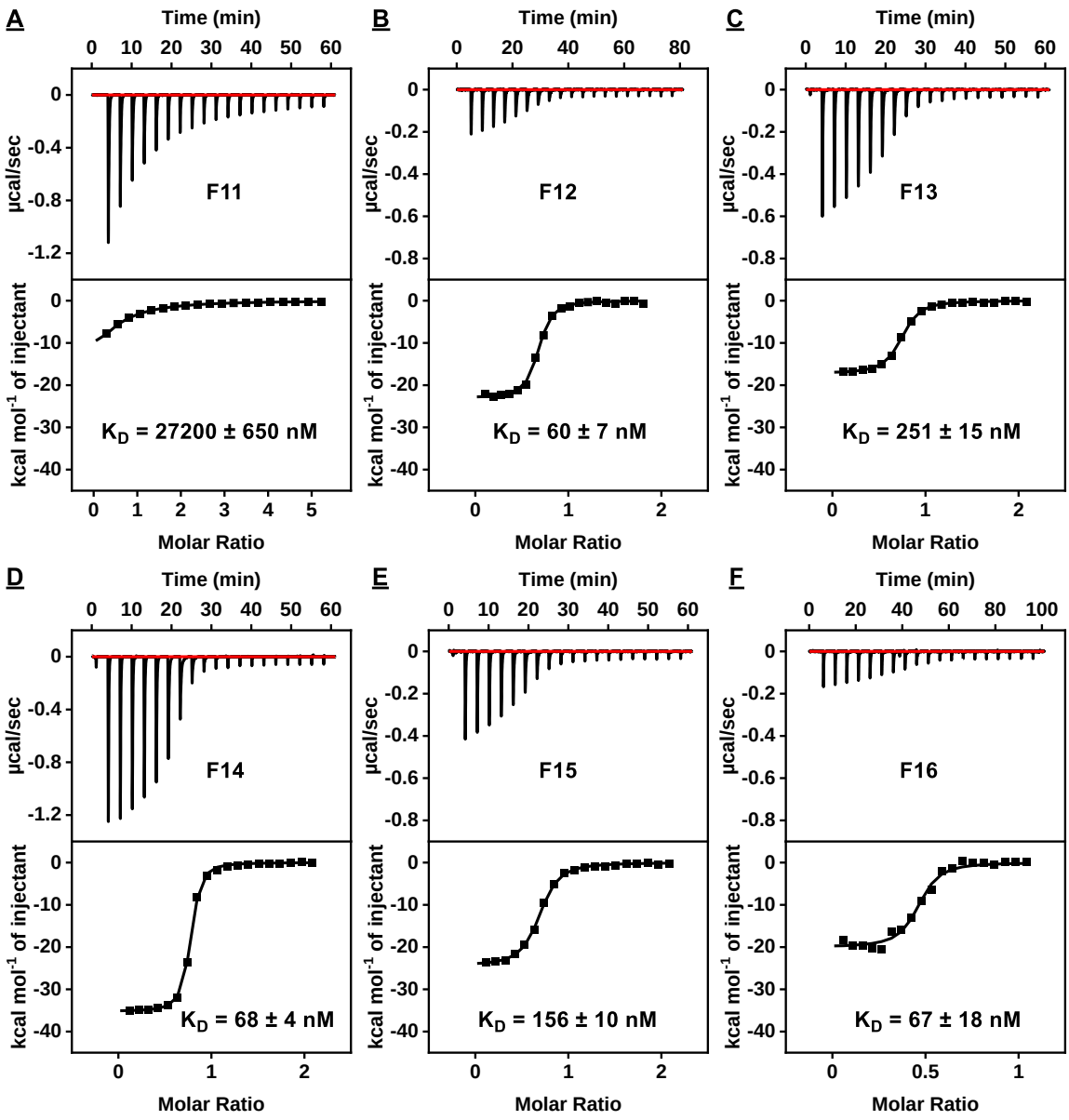

Figure 5-13. Characterization of acetyl fentanyl binding affinity of six aptamer candidates using ITC. The top panels display the heat generated from each titration of acetyl fentanyl into (**A**) F11, (**B**) F12, (**C**) F13, (**D**) F14, (**E**) F15, and (**F**) F16. The bottom panels show the integrated heat of each titration after correcting for the heat of dilution of the titrant.

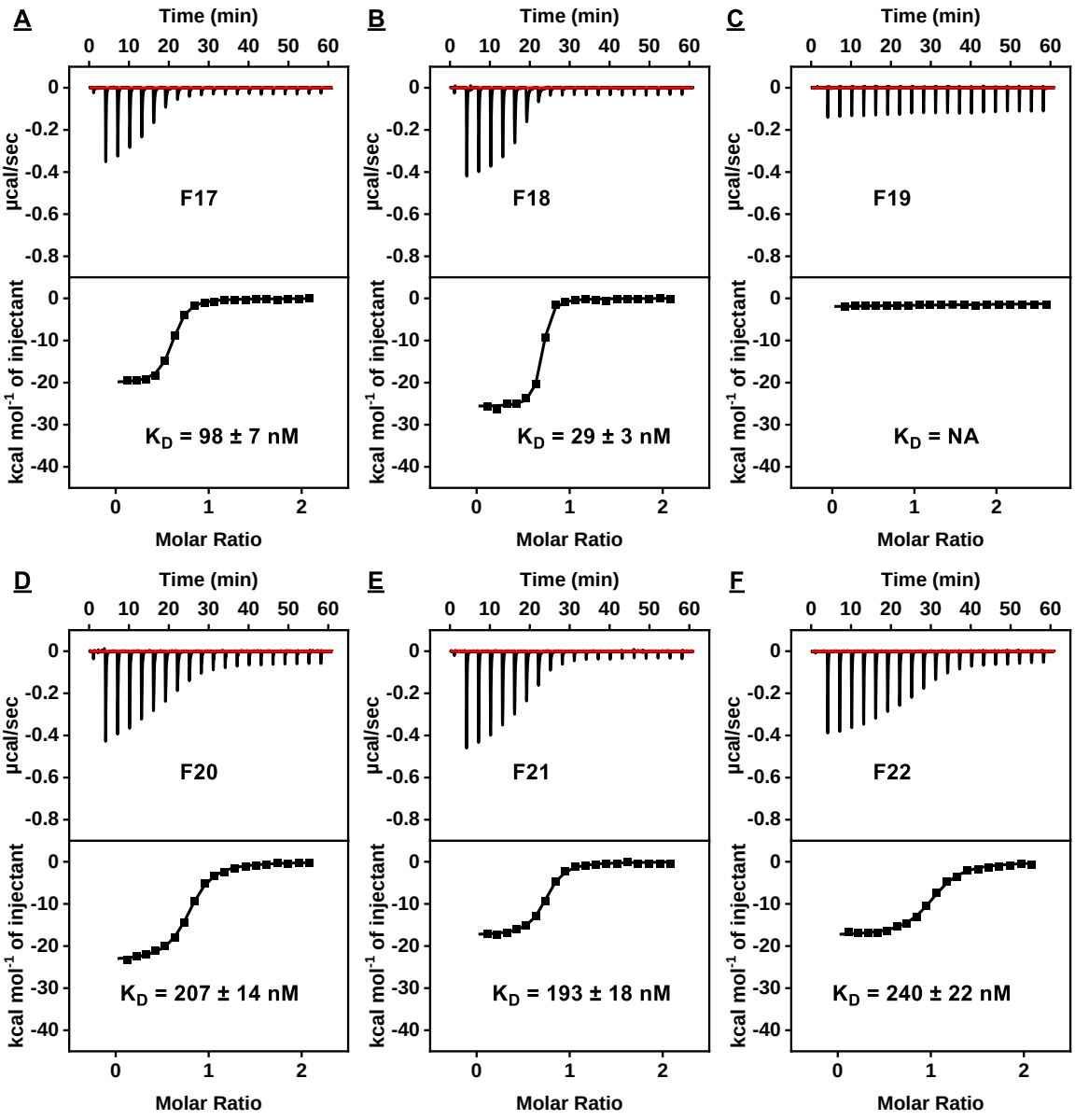

Figure 5-14. Characterization of acetyl fentanyl- and furanyl fentanyl-binding affinity of six aptamer candidates using ITC. The top panels display the heat generated from each titration of acetyl fentanyl into (**A**) F17 and (**B**) F18, or furanyl fentanyl into (**C**) F19, (**D**) F20, (**E**) F21, and (**F**) F22. The bottom panels show the integrated heat of each titration after correcting for the heat of dilution of the titrant.

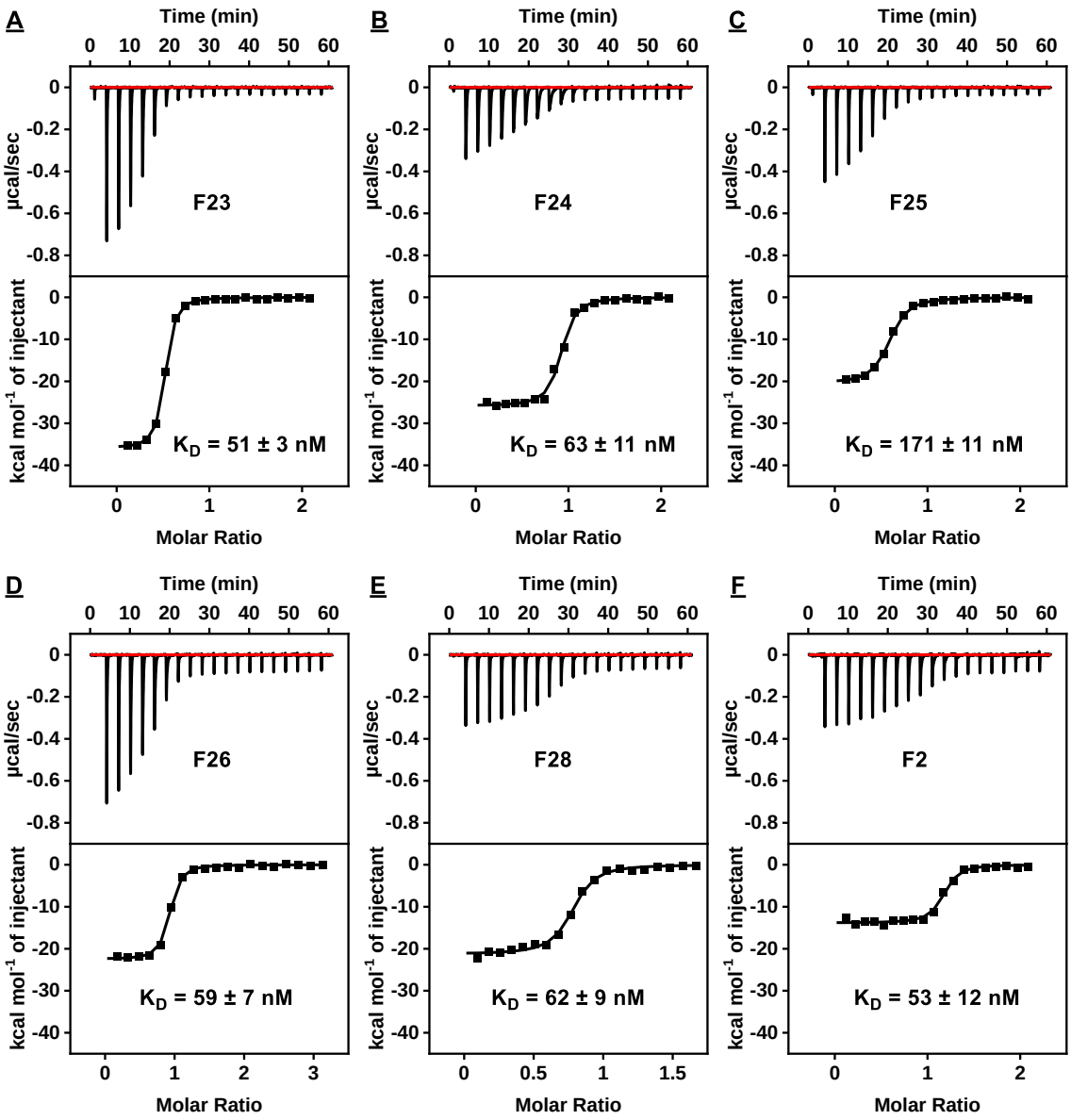

Figure 5-15. Characterization of furanyl fentanyl binding affinity of six aptamer candidates using ITC. The top panels display the heat generated from each titration of furanyl fentanyl into (**A**) F23, (**B**) F24, (**C**) F25, (**D**) F26, (**E**) F28, and (**F**) F2. The bottom panels show the integrated heat of each titration after correcting for the heat of dilution of the titrant.

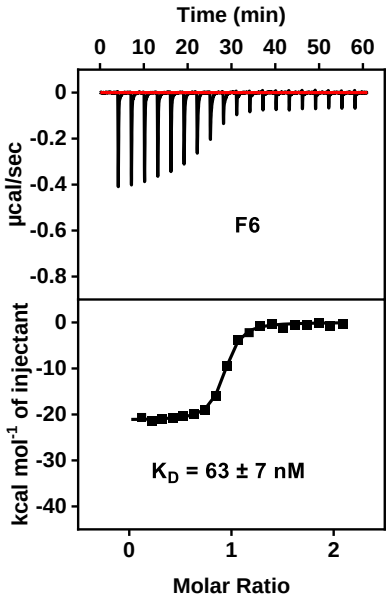

Figure 5-16. Characterization of furanyl fentanyl binding affinity of aptamer candidate F6 using ITC. The top panels display the heat generated from each titration of furanyl fentanyl into F6. The bottom panels show the integrated heat of each titration after correcting for the heat of dilution of the titrant.

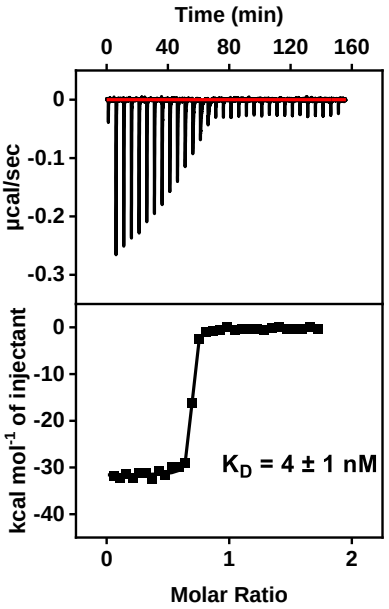

Figure 5-17. Characterization of furanyl fentanyl binding affinity of F27 using ITC. The top panel displays the heat generated from each titration of furanyl fentanyl into F27. The bottom panel shows the integrated heat of each titration after correcting for the heat of dilution of the titrant.

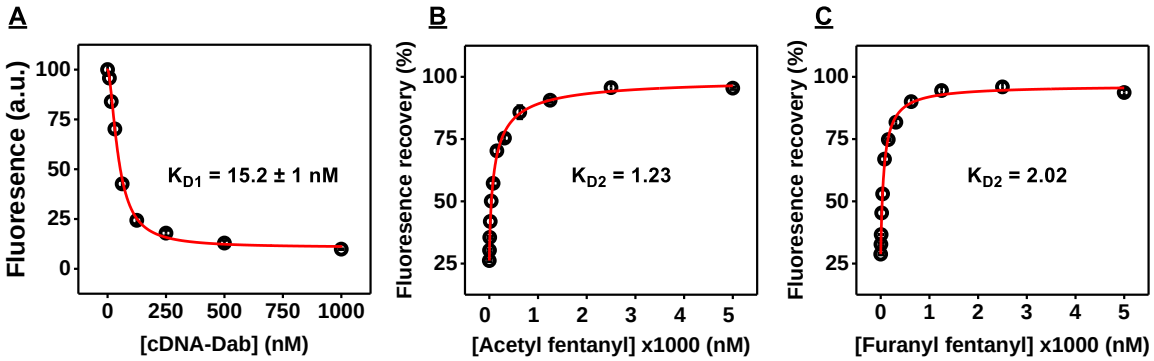

Figure 5-18. Determination of F27's furanyl fentanyl and acetyl fentanyl binding affinity using a fluorescence strand-displacement assay. (**A**) K_{D1} was determined by mixing 50 nM F27-FAM with 0, 8, 16, 31, 62.5, 125, 250, 500, or 1,000 nM cDNA-Dab and measuring the fluorescence quenching at 520 nm. K_{D2} was determined from the fluorescence recovery at 520 nm of 50 nM F27-FAM/125 nM cDNA-Dab complexes upon the addition of varying concentrations of (**B**) furanyl fentanyl or (**C**) acetyl fentanyl. Target concentrations used were 0, 5, 10, 20, 39, 78, 156, 312.5, 625, 1,250, 2,500, and 5,000 nM.

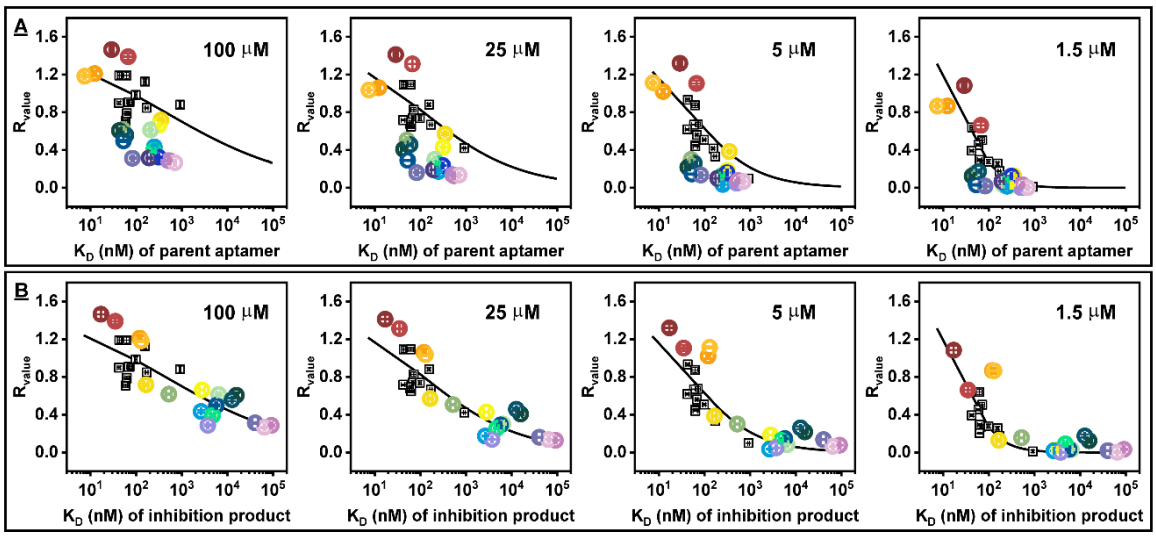

Figure 5-19. Correlation between target-binding-induced exonuclease inhibition and aptamer affinity. (**A**) Schematic of our exonuclease digestion assay for distinguishing ligand-bound and non-bound aptamers. (**B**) Relationship between parent aptamer K_D and R_{value} of each aptamer in the presence of 100, 25, 5, or 1.5 µM of their respective selection targets. (**C**) Relationship between the K_D of the major digestion products of the outliers from **B** (colored) or parent aptamers (black) and the R_{value} of each aptamer in the presence of 100, 25, 5, or 1.5 µM of their respective selection targets. K_D values were determined by ITC or the strand displacement assay.

Most aptamers demonstrated sub-micromolar affinity. Therefore, 100 µM ligand may be too high of a concentration to differentiate minute differences in binding affinity. We then performed digestion of each aptamer using lower target concentrations of their respective targets (1.5, 5, or 25 µM) (**Figures 5-20, 5-21, and 5-22**), calculated their R_{value}, and constructed plots of each aptamer's K_D versus R_{value} at each tested ligand concentration (**Figure 5-19A**). In general, high-affinity aptamers retained a high R_{value} at lower target concentrations relative to weaker affinity aptamers. For example, F28 (K_D = 43 ± 0.9 nM for furanyl fentanyl) demonstrated an R_{value} of 0.93 at a target concentration of 5 µM, while F15 (K_D = 156 ± 10 nM) and F4 (K_D = 923 ± 41 nM) required 25 µM and 100 µM target, respectively, to achieve a similar R_{value} (**Figure 5-19A**). However, there were several instances where aptamers possessed similar K_Ds but vastly different R_{values} at the same target concentration. For example, at a target concentration of 100 µM, F16 (K_D = 67 ± 18 nM) and F2 (K_D = 53 ± 12 nM) had vastly different R_{values} of 1.39 and 0.49, respectively (**Figure 5-19A**).

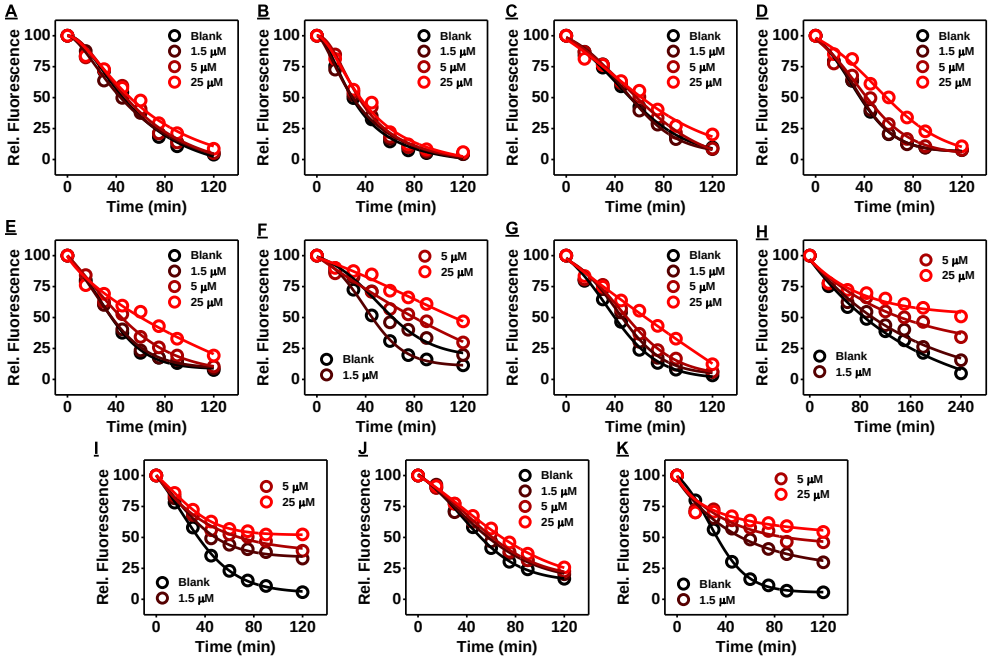

Figure 5-20. Determining enzyme inhibition at low concentrations of fentanyl. Time-course digestion of (**A**) F1, (**B**) F2, (**C**) F3, (**D**) F4, (**E**) F5, (**F**) F6, (**G**) F7, (**H**) F8, (**I**) F9, (**J**) F21, and (**K**) F28 in the absence and presence of 1.5, 5, and 25 µM fentanyl.

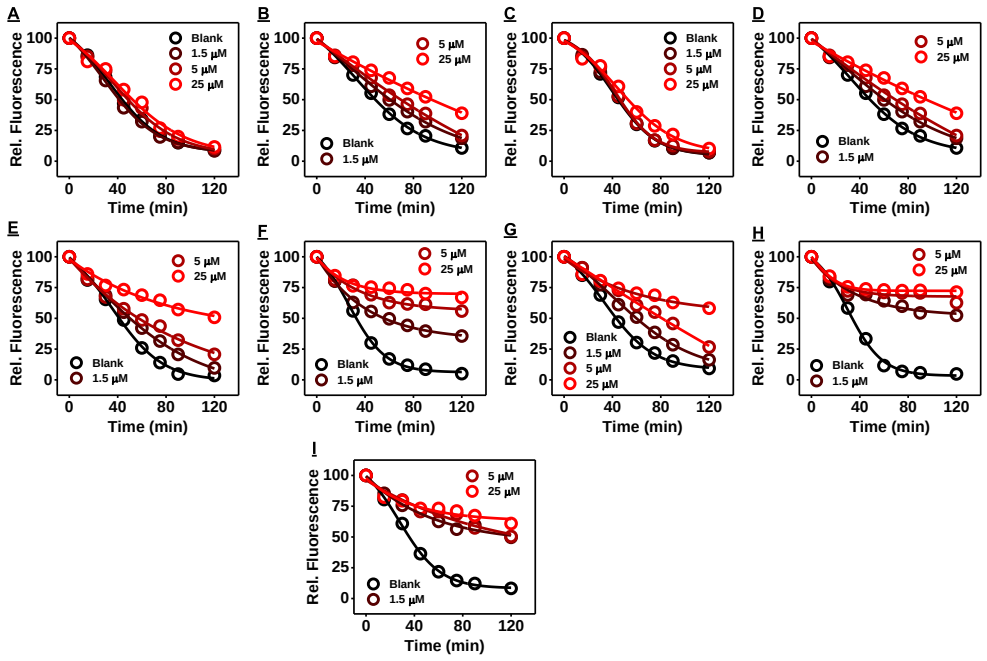

Figure 5-21. Determining enzyme inhibition at low concentrations of acetyl fentanyl. Time-course digestion of (**A**) F10, (**B**) F12, (**C**) F13, (**D**) F14, (**E**) F15, (**F**) F16, (**G**) F17, (**H**) F18, and (**I**) F27 in the absence and presence of 1.5, 5, and 25 µM acetyl fentanyl.

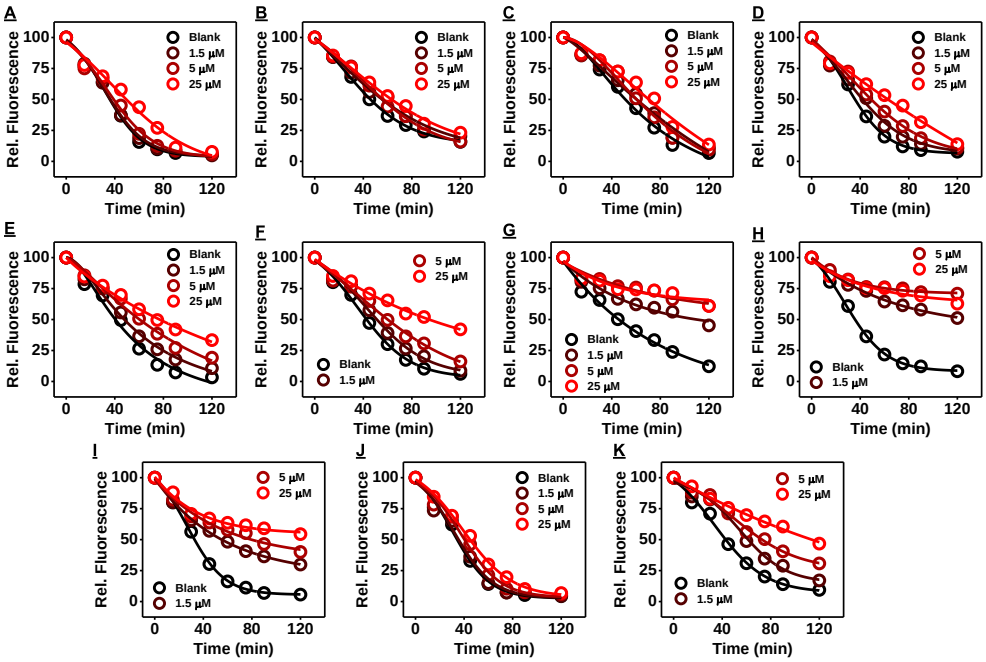

Figure 5-22. Determining enzyme inhibition at low concentrations of furanyl fentanyl. Time-course digestion of (**A**) F20, (**B**) F21, (**C**) F22, (**D**) F23, (**E**) F24, (**F**) F25, (**G**) F26, (**H**) F27, (**I**) F28, (**J**) F2, and (**K**) F6 in the absence and presence of 1.5, 5, and 25 µM furanyl fentanyl.

Previous work has shown that digestion of aptamers with an Exo III and Exo I mixture yields inhibition products whose 3'-ends are truncated ~3–4 bases before the target-binding domain.[291,292,315] We hypothesized that for some aptamers, their truncated products may have vastly different binding affinities relative to their parent aptamer, resulting in the lack of a clear relationship between R_{value} and K_D observed in **Figure 5-19A**. To confirm this, we selected 16 parent aptamers (F1, F2, F3, F5, F7, F8, F10, F12, F13, F16, F18, F20, F21, F22, F23, and F27; 19 aptamer-ligand pairs) **(Figure 5-19A**, colored**)** and ran their digestion time-course on a denaturing polyacrylamide gel with a customized DNA ladder to identify the major inhibition products (**Figures 5-23, 5-24, 5-**

25, 5-26, 5-27, and 5-28). We observed considerable variation in the number of base-pairs adjacent to the target-binding domain that were retained in the major inhibition product following digestion. For example, F3 had only 2 bp, whereas F16 retained 5 bp (**Figures 5-23, 5-24, 5-25, 5-26, 5-27, and 5-28**). Sequences that experience greater truncation may also lose more target-binding affinity. We chemically synthesized each inhibition product and measured its K_D using ITC (**Figures 5-29, 5-30, 5-31, and 5-32**). Thirteen inhibition products had lower K_D relative to their parent aptamers (**Table 5-6**), while three had ~2-fold improved binding affinity (**Table 5-6**). We therefore constructed a new K_D-R_{value} plot to see if the K_D of the major inhibition product is a better predictor of the R_{value} (**Figure 5-19B**, colored). We indeed observed a more significant correlation between K_D and R_{value}, obtaining R^2 values of 0.90, 0.88, 0.83, and 0.79 for 1.5, 5, 25, and 100 µM target, respectively when fitting with a Langmuir equation (**Figure 5-33**).

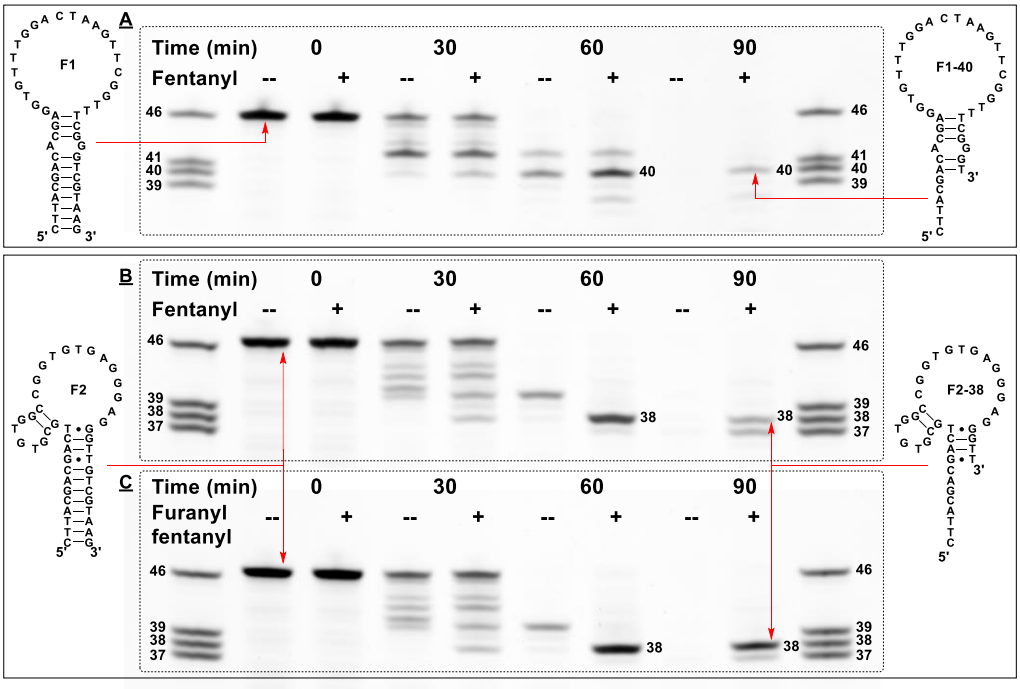

Figure 5-23. Identification of the major inhibition product for three aptamer-ligand pairs. PAGE analysis of a time-course digestion of (**A**) F1 with fentanyl, (**B**) F2 with fentanyl,

and (**C**) F2 with furanyl fentanyl. Predicted secondary structures of parent aptamers (left) and major digestion products (right) are shown at the sides.

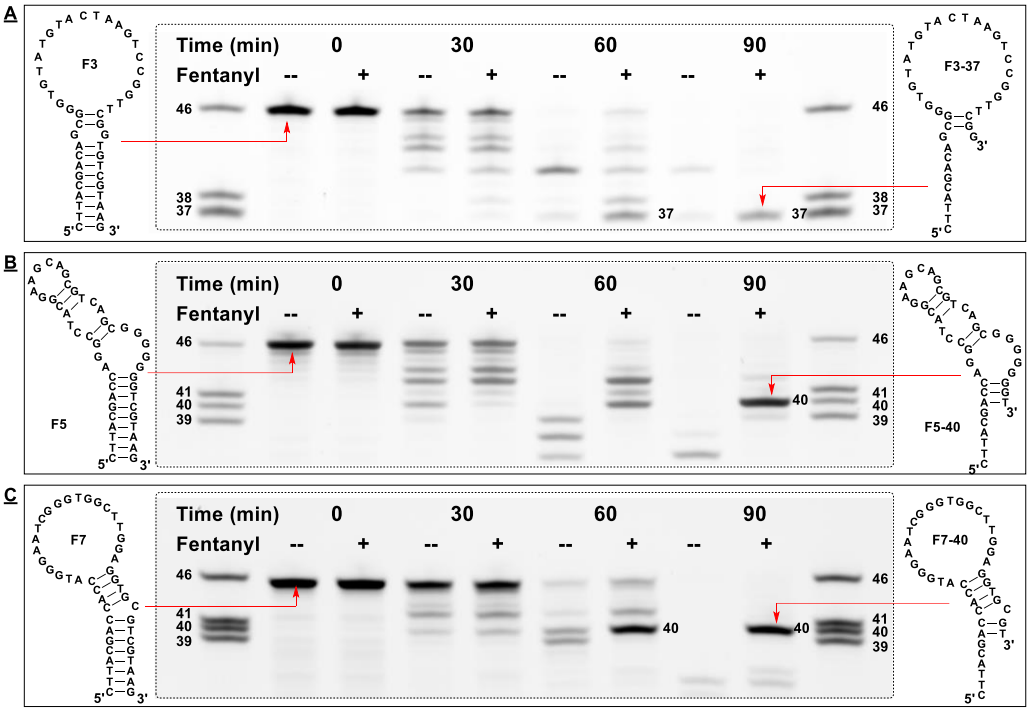

Figure 5-24. Identification of the major inhibition product for three aptamer-ligand pairs. PAGE analysis of a time-course digestion of (**A**) F3 with fentanyl, (**B**) F5 with fentanyl, and (**C**) F7 with fentanyl. Predicted secondary structures of parent aptamers (left) and major digestion products (right) are shown at the sides.

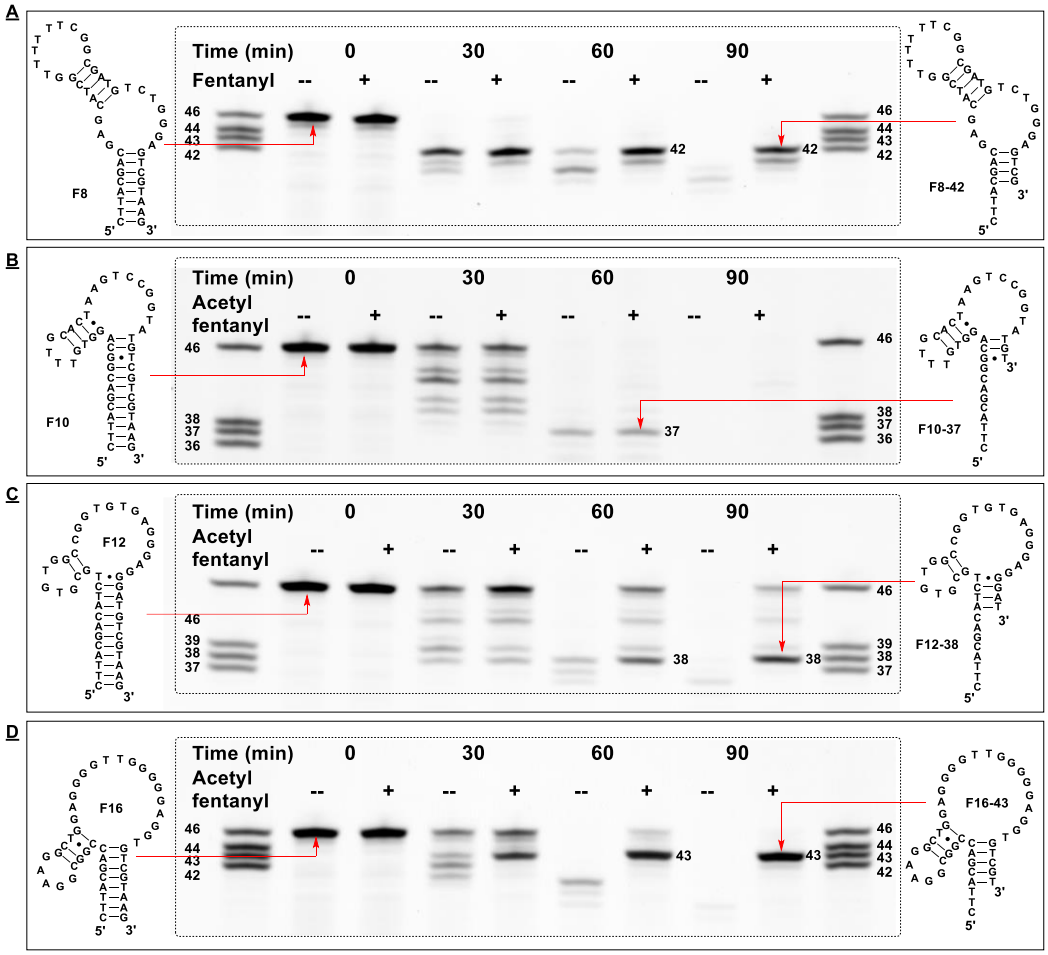

Figure 5-25. Identification of the major inhibition product for three aptamer-ligand pairs. PAGE analysis of a time-course digestion of (**A**) F8 with fentanyl, (**B**) F10 with acetyl fentanyl, (**C**) F12 with acetyl fentanyl, and (**D**) F16 with acetyl fentanyl. Predicted secondary structures of parent aptamers (left) and major digestion products (right) are shown at the sides.

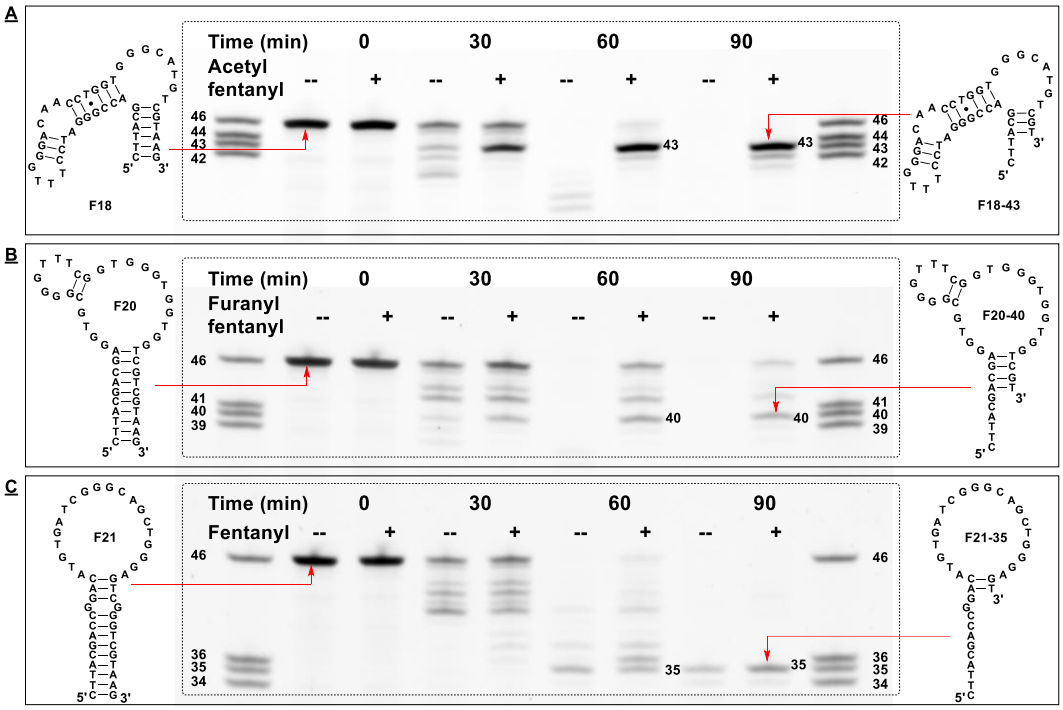

Figure 5-26. Identification of the major inhibition product for three aptamer-ligand pairs. PAGE analysis of a time-course digestion of (**A**) F18 with acetyl fentanyl, (**B**) F20 with furanyl fentanyl, and (**C**) F21 with fentanyl. Predicted secondary structures of parent aptamers (left) and major digestion products (right) are shown at the sides.

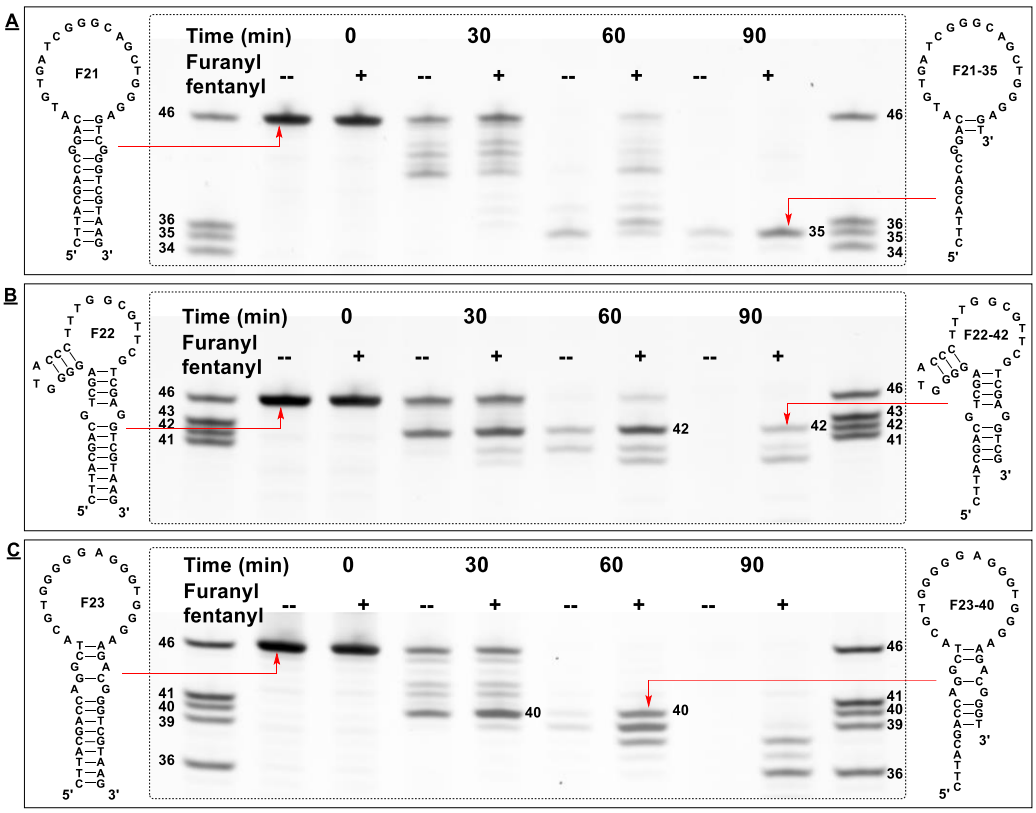

Figure 5-27. Identification of the major inhibition product for three aptamer-ligand pairs. PAGE analysis of a time-course digestion of (**A**) F21 with furanyl fentanyl, (**B**) F22 with furanyl fentanyl, and (**C**) F23 with furanyl fentanyl. Predicted secondary structures of parent aptamers (left) and major digestion products (right) are shown at the sides.

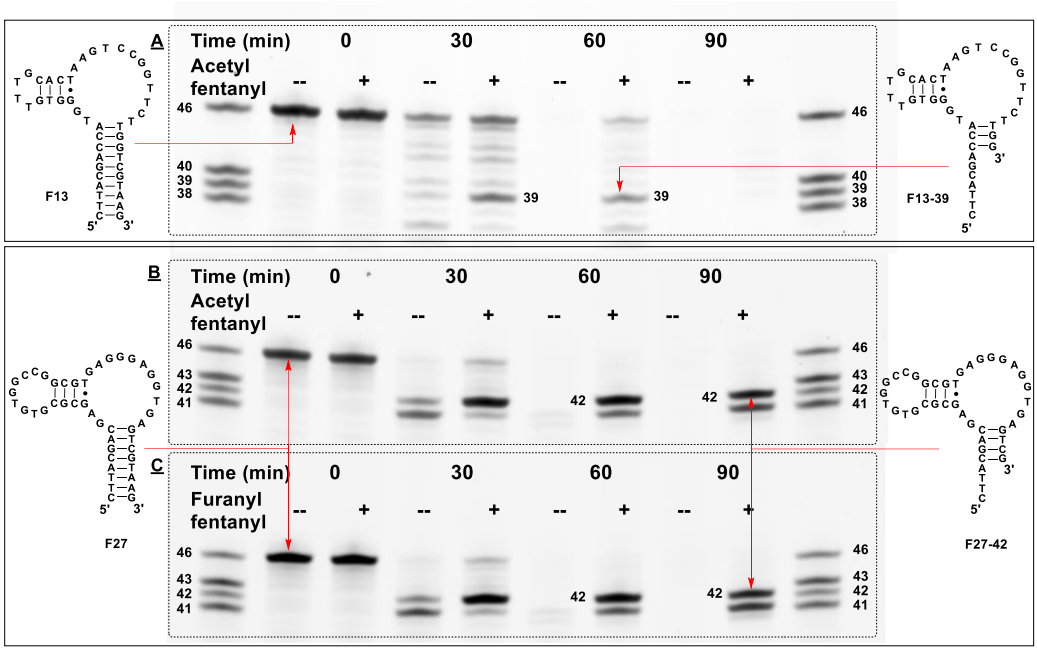

Figure 5-28. Identification of the major inhibition product for three aptamer-ligand pairs. PAGE analysis of a time-course digestion of (**A**) F13 with acetyl fentanyl and (**B**) F27 with acetyl fentanyl and (**C**) furanyl fentanyl. Predicted secondary structures of parent aptamers (left) and major digestion products (right) are shown at the sides.

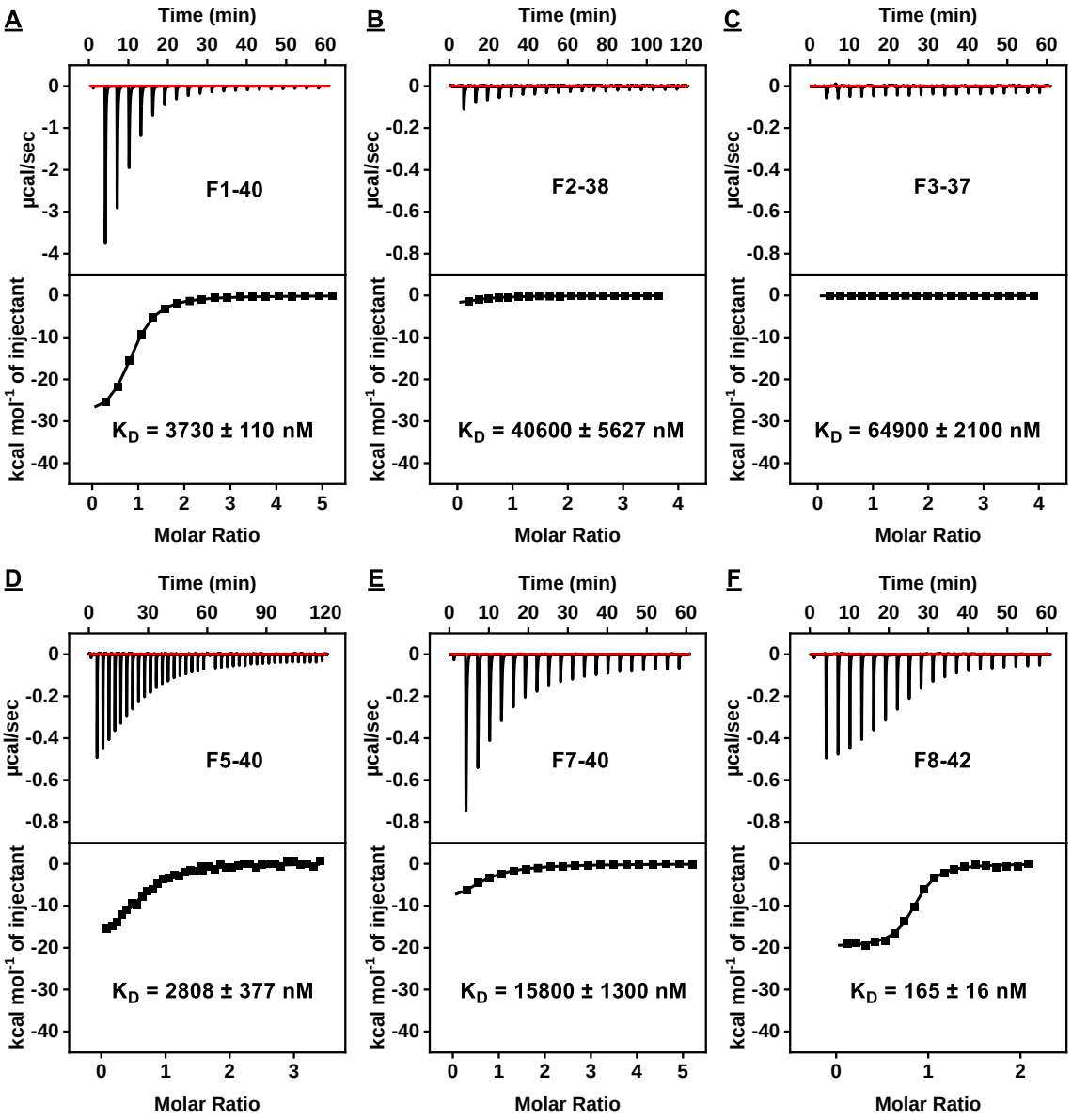

Figure 5-29. Characterization of fentanyl binding affinity of six major inhibition products using ITC. The top panels display the heat generated from each titration of fentanyl into (**A**) F1-40, (**B**) F2-38, (**C**) F3-37, (**D**) F5-40, (**E**) F7-40, and (**F**) F8-42. The bottom panels show the integrated heat of each titration after correcting for the heat of dilution of the titrant.

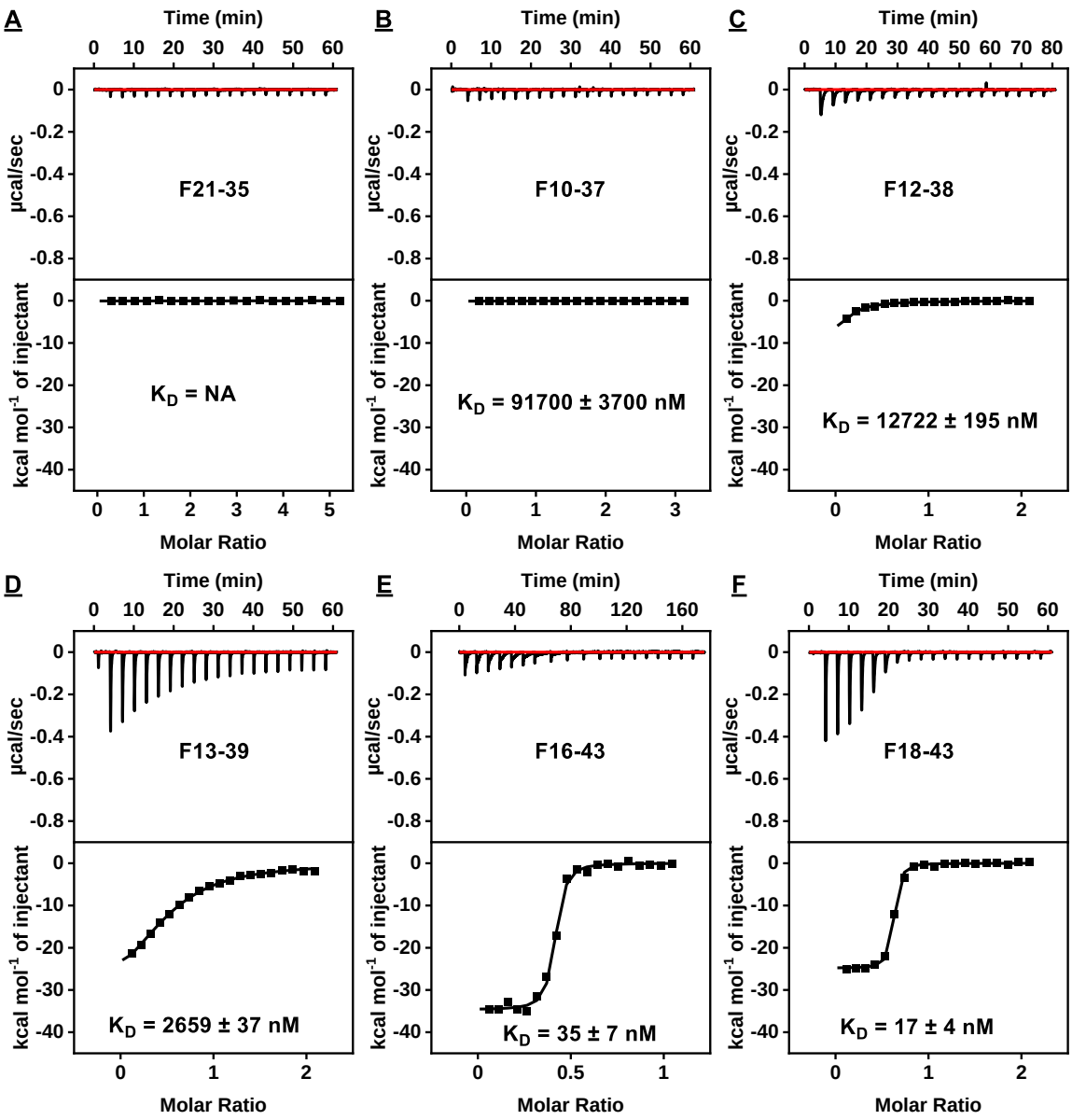

Figure 5-30. Characterization of fentanyl binding affinity of six major inhibition products using ITC. The top panels display the heat generated from the titration of fentanyl into (**A**) F21-35, or acetyl fentanyl into (**B**) F10-37, (**C**) F12-38, (**D**) F13-39, (**E**) F16-43, and (**F**) F18-43. The bottom panels show the integrated heat of each titration after correcting for the heat of dilution of the titrant.

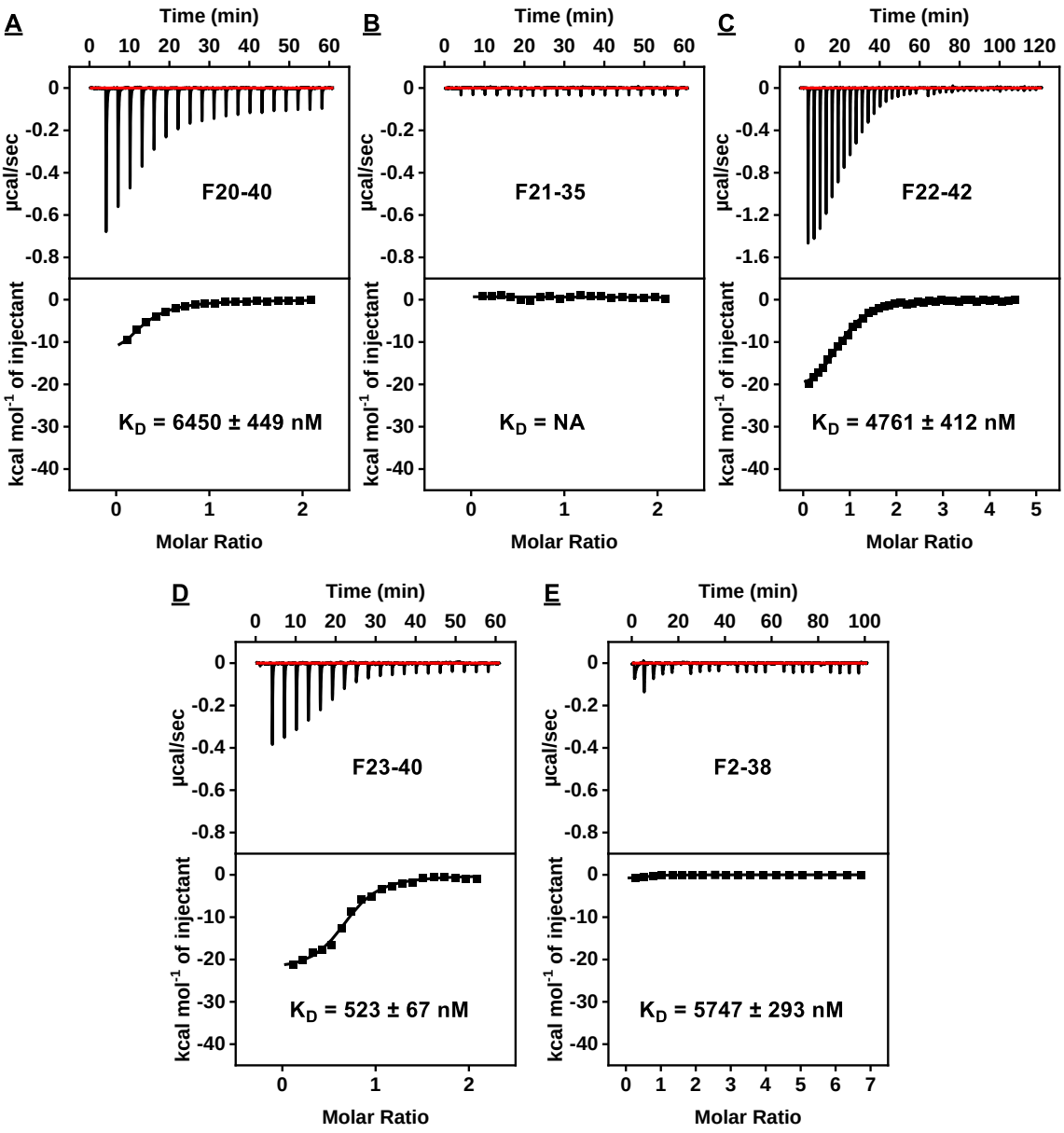

Figure 5-31. Characterization of fentanyl binding affinity of six major inhibition products using ITC. The top panels display the heat generated from each titration of furanyl fentanyl into (**A**) F20-40, (**B**) F21-35, (**C**) F22-42, (**D**) F23-40, and (**E**) F2-38. The bottom panels show the integrated heat of each titration after correcting for the heat of dilution of the titrant.

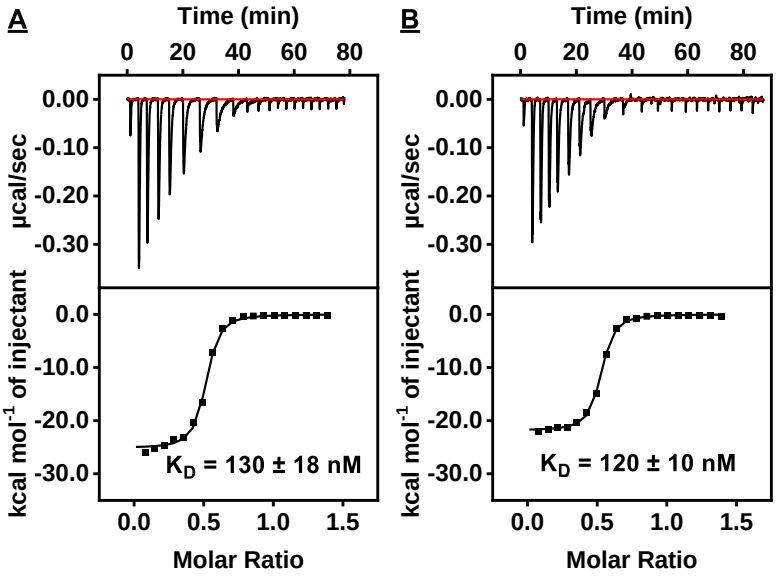

Figure 5-32. Characterization of selection target binding affinity of F27-42 using ITC. The top panels display the heat generated from each titration of furanyl fentanyl (**A**) or acetyl fentanyl (**B**) into F27-42. The bottom panels show the integrated heat of each titration after correcting for the heat of dilution of the titrant.

$$R_{value} = 1.6 - \frac{1.6}{\left(\frac{E_{1/2}}{K_D}\right)^{n} - 1}$$

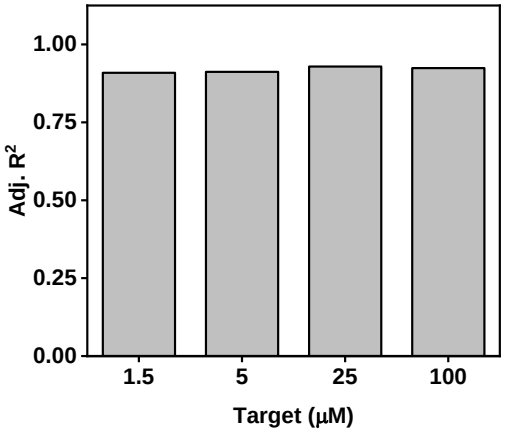

Figure 5-33. The equation used for fitting and adjusted R^2 values obtained during the fitting of parent aptamer/major digestion product K_D against the R_{value} at 1.5, 5, 25, and 100 µM selection target concentrations. $E_{1/2}$ represents the K_D at which half-maximal inhibition is observed, and n represents the steepness of the target response.

5.3.4 High-throughput screening of aptamer specificity.

Given that fentanyl is often mixed with various interferents that make up only 0.1–1% of the substance by weight,[324] the final aptamer must be highly target-specific. We therefore screened the affinity of our aptamer candidates for the counter-targets employed during SELEX, which included a number of different common interferents. These included six controlled substances (cocaine, codeine, heroin, lorazepam, morphine, and (+)-methamphetamine ((+)-METH) and 13 adulterants and cutting agents (acetaminophen (APAP), benzocaine, chlorpromazine (CPZ), diphenhydramine (DPH), lidocaine, noscapine procaine, papaverine, quinine, caffeine, lactose, mannitol, (+)-pseudoephedrine ((+)-PSE)) (**Figure 5-34**). We chose 17 aptamer candidates with R_{values} > 0.4 in the presence of 100 µM of their respective selection target and digested them in the presence of 100 µM of interferents (**Figure 5-35 and 5-36**). Although F7, F12, and F20 demonstrated an R_{value} >0.4, these sequences were neglected from screening as the major inhibition product had poor binding affinity for its selection target (**Figure 5-30C and 5-31A**, K_D > 5 µM).

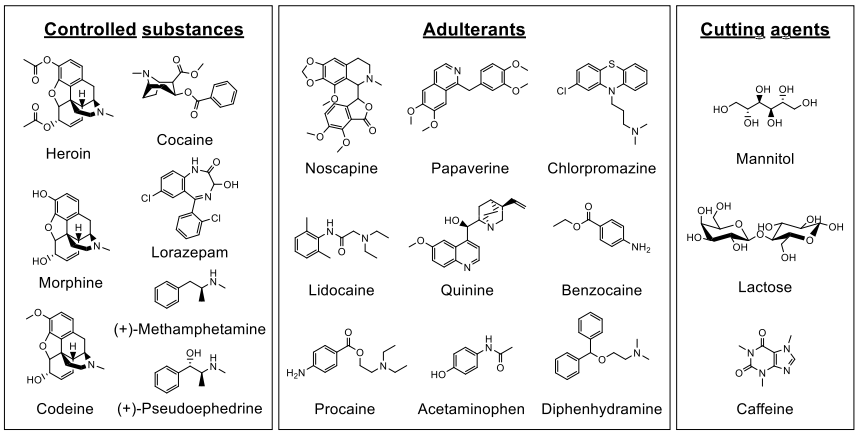

Figure 5-34. The chemical structure of 19 interferent molecules employed for the aptamer specificity test, which included controlled substances, adulterants, and cutting agents.

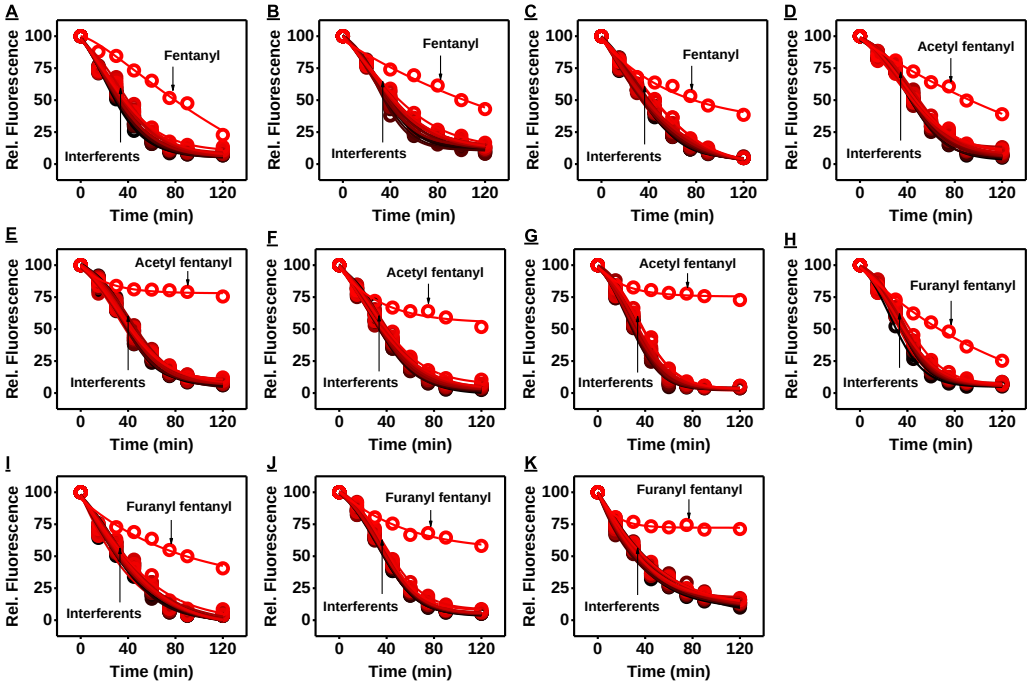

Figure 5-35. Screening the specificity of 11 aptamer candidates using our exonuclease digestion assay. Time-course digestion of (**A**) F4, (**B**) F5, (**C**) F6, (**D**) F13, (**E**) F14, (**F**) F17, (**G**) F18, (**H**) F23, (**I**) F24, (**J**) F25, and (**K**) F27. Aptamers were digested in the absence and presence of 100 µM cocaine, lidocaine, procaine, heroin, quinine, codeine, morphine, chlorpromazine, lactose, mannitol, caffeine, (+)-methamphetamine, (+)-pseudoephedrine, benzocaine, diphenhydramine, acetaminophen, papaverine, noscapine, lorazepam, or their selection target.

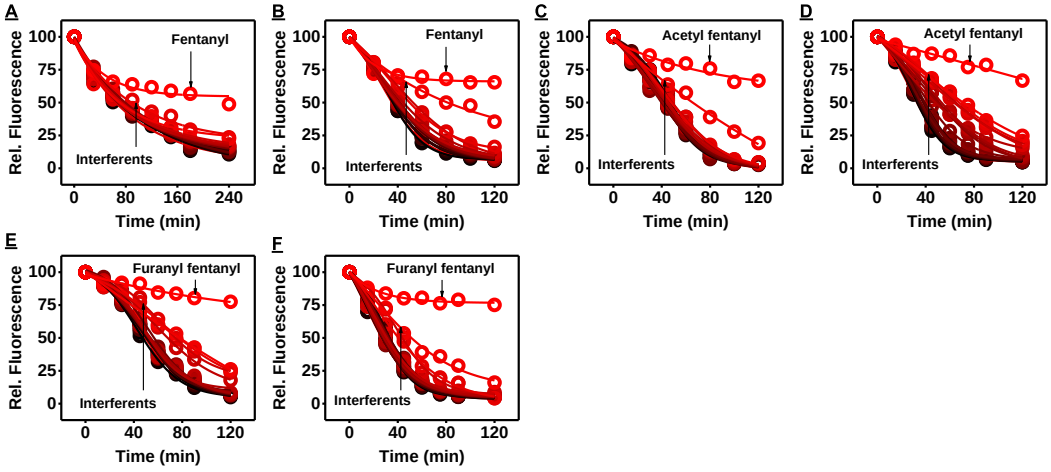

Figure 5-36. Screening the specificity of six aptamer candidates using our exonuclease digestion assay. Time-course digestion of (**A**) F8, (**B**) F9, (**C**) F15, (**D**) F16, (**E**) F26, and (**F**) F28. Aptamers were digested in the absence and presence of 100 µM cocaine, lidocaine, procaine, heroin, quinine, codeine, morphine, chlorpromazine, lactose, mannitol, caffeine,

(+)-methamphetamine, (+)-pseudoephedrine, benzocaine, diphenhydramine, acetaminophen, papaverine, noscapine, lorazepam, or their selection target.

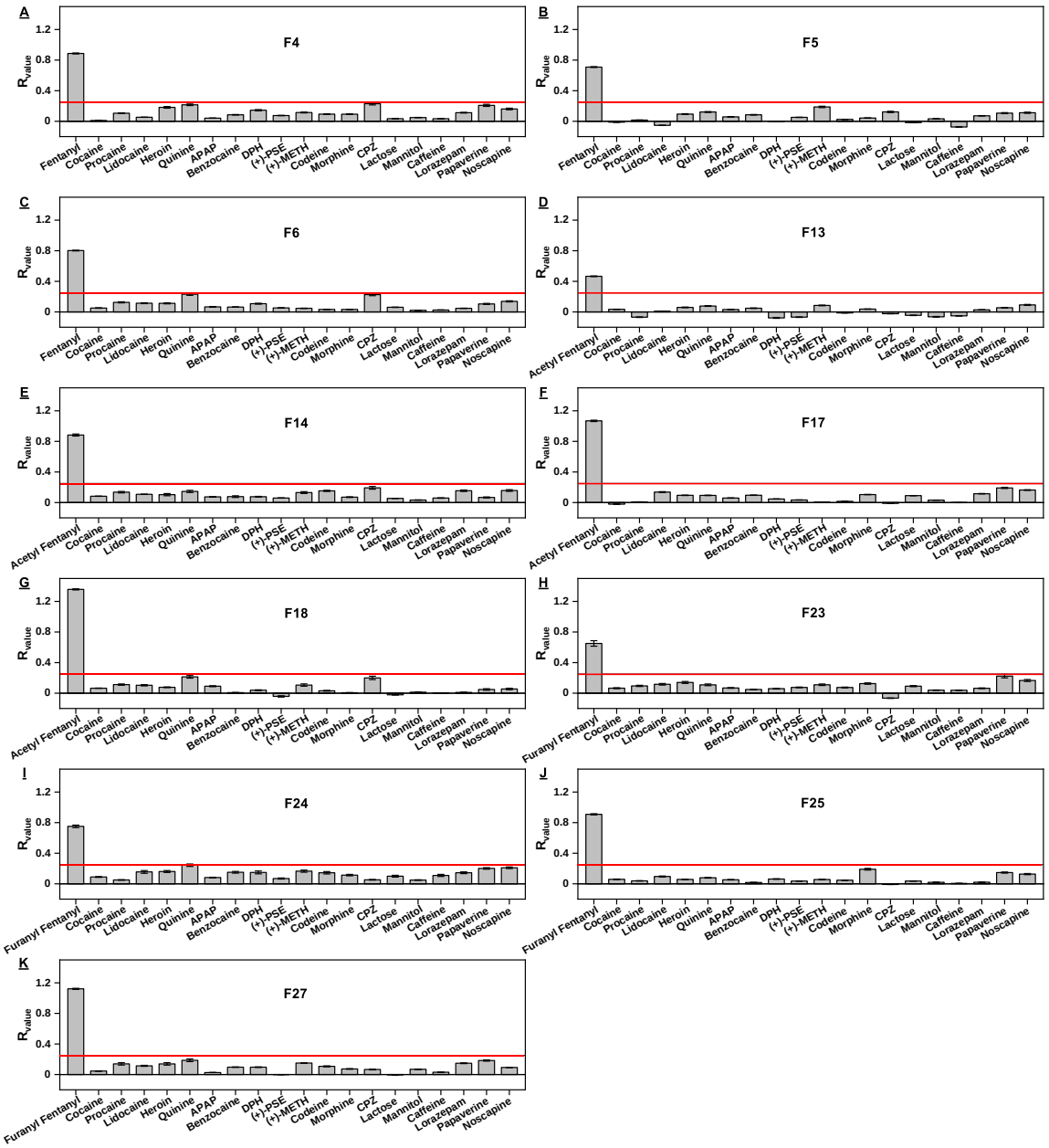

Figure 5-37. Specificity of 11 aptamer candidates. R_{value}s were obtained from time-course digestion of (**A**) F4, (**B**) F5, (**C**) F6, (**D**) F13, (**E**) F14, (**F**) F17, (**G**) F18, (**H**) F23, (**I**) F24, (**J**) F25, and (**K**) F27 in the absence and presence of 100 µM cocaine, procaine, lidocaine, heroin, quinine, acetaminophen (APAP), benzocaine, diphenhydramine (DPH), (+)-pseudoephedrine ((+)-PSE), (+)-methamphetamine ((+)-METH), codeine, morphine, chlorpromazine (CPZ), lactose, mannitol, caffeine, lorazepam, papaverine, noscapine, or

their selection target. The red line indicates a R_{value} of 0.25, which is predicted to be equivalent to an extremely weak K_D of ~100 µM.

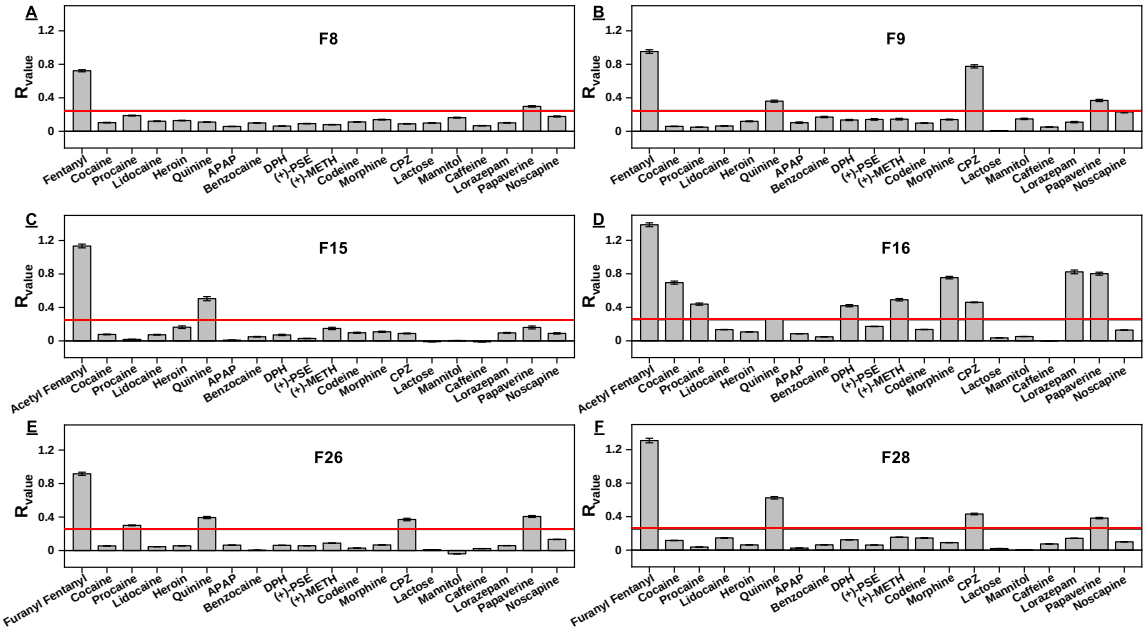

Figure 5-38. Specificity of six aptamer candidates. R_{value}s of (**A**) F8, (**B**) F9, (**C**) F15, (**D**) F16, (**E**) F26, and (**F**) F28 were obtained by exonuclease digestion with 100 µM of various interferents or their selection target. The red line indicates a resistance value of 0.25, which is predicted to be equivalent to an extremely weak K_D of ~100 µM

Based on our previously derived fit parameters (**Figure 5-33**), we used a threshold R_{value} of 0.25, which translates to a very high K_D of ~100 µM as the cut-off for a highly specific aptamer. Eleven aptamers (F4, F5, F6, F13, F14, F17, F18, F23, F24, F25, and F27) demonstrated excellent specificity against the 19 tested interferent molecules (**Figure 5-37**). The remaining six (F8, F9, F15, F16, F26, and F28) demonstrated cross-reactivity to at least one interferent (**Figure 5-38**). To confirm that inhibition from these interferents is indeed due to specific aptamer binding, we characterized the accuracy of the exonuclease assay using the strand-displacement fluorescence assay to test the specificity of F4, F13,

and F27 using an optimized aptamer/cDNA ratio (**Figure 5-39**). As expected, the specificity from both assays correlated well (**Figure 5-40**).

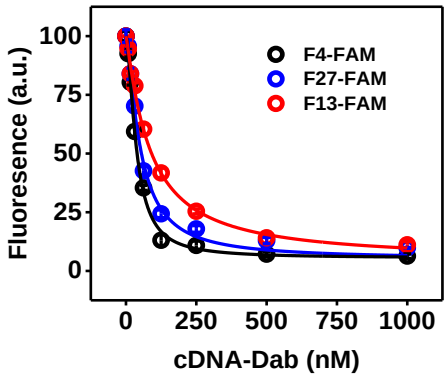

Figure 5-39. Optimization of cDNA-Dab-induced quenching of F4-FAM (black), F27-FAM (brown), and F13-FAM (red). 50 nM fluorophore modified aptamer was incubated with 0, 8, 16, 31, 62.5, 125, 250, 500, or 1,000 nM cDNA-Dab.

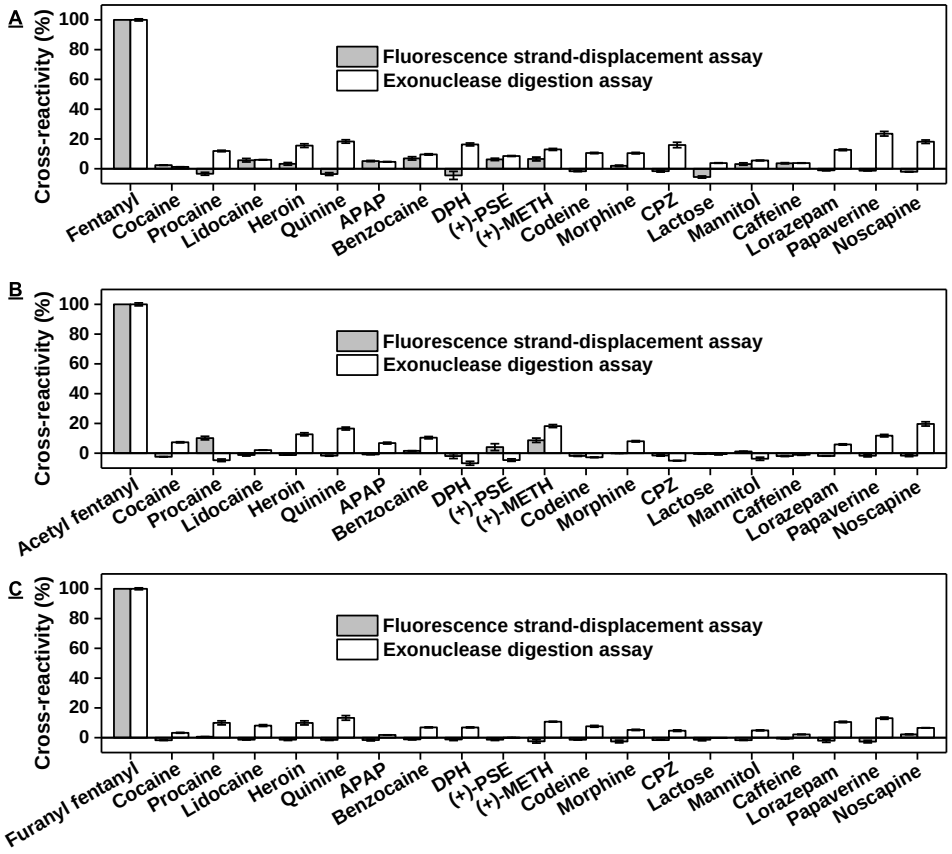

Figure 5-40. Comparison of aptamer specificity determined using fluorescence-strand displacement assay and exonuclease digestion assay. Cross-reactivity of (**A**) F4, (**B**) F13,

and (**C**) F27 against 100 µM of various interferents or their selection target. Cross-reactivity was calculated relative to signal generated by each aptamer's selection target.

5.3.5. High-throughput screening of aptamer cross-reactivity to fentanyl analogs.

Several fentanyl family members have been reported in seized substances, and any aptamer-based sensor for detecting fentanyl and its analogs must therefore be highly cross-reactive. We screened our 11 aptamer candidates using the exonuclease fluorescence assay in the presence of 100 µM fentanyl (**1**) or its analogs: acetyl fentanyl (**2**), furanyl fentanyl (**3**), acrylfentanyl (**4**), butyryl fentanyl (**5**), valeryl fentanyl (**6**), cyclopropyl fentanyl (**7**), methoxyacetyl fentanyl (**8**), p-fluorofentanyl (**9**), o-methyl furanyl fentanyl (**10**), p-methoxy furanyl fentanyl (**11**), p-methoxy butyryl fentanyl (**12**), p-fluoroisobutyryl fentanyl (**13**), cis-3-methyl fentanyl (**14**), alpha-methyl thiofentanyl (**15**) (**Figure 5-41**). Based on our fitted parameters (**Figure 5-33**), an R_{value} of 0.4, which corresponds to a predicted K_D of ~15 µM, was used as a cutoff for appropriate binding affinity to the ligand. Six aptamers F4, F5, F13, F17, F18, and F25) were very tolerant of large bulky groups at the R_1 position but were less tolerant of modifications to the R_3 and R_4 positions (**Figures 5-42A, B, D, F, G, & J**). On the other hand, F14 only retained high affinity to analogs with small R_1 groups such as fentanyl, acetyl fentanyl, and acryl fentanyl (**Figure 5-42E**). Notably, F14 originated from the acetyl fentanyl pool, with a small R_1 functional group. Similarly, F23 and F24, which originated from the furanyl fentanyl pool, primarily cross-reacted to analogs that possess the furanyl group at their R_1 position (**Figures 5-42H & I**). Ultimately, F6 was the most cross-reactive, binding all analogs with an $R_{value} > 0.4$ (**Figure 5-42C**), followed by F27, which recognized all analogs except p-fluoroisobutyryl fentanyl (**Figure 5-42K**). We further confirmed the results of the exonuclease assay by testing the

cross-reactivity of F13 and F27 to fentanyl and its analogs using the strand-displacement fluorescence assay. We observed the same overall trend between both assays, but with some difference in magnitude. This is presumably due to the difference in binding affinity between the parent aptamer used for the strand-displacement assay and the major inhibition product (**Figure 5-43A & B**). When we tested the major inhibition product of F27 (F27-42) using the strand-displacement fluorescence assay using its optimized aptamer/cDNA ratio (**Figure 5-44**), we observed a similar binding profile to the parent aptamer, indicating that truncation does not alter its binding profile (**Figure 5-43C**). These results demonstrate that the exonuclease assay can effectively screen aptamer cross-reactivity.

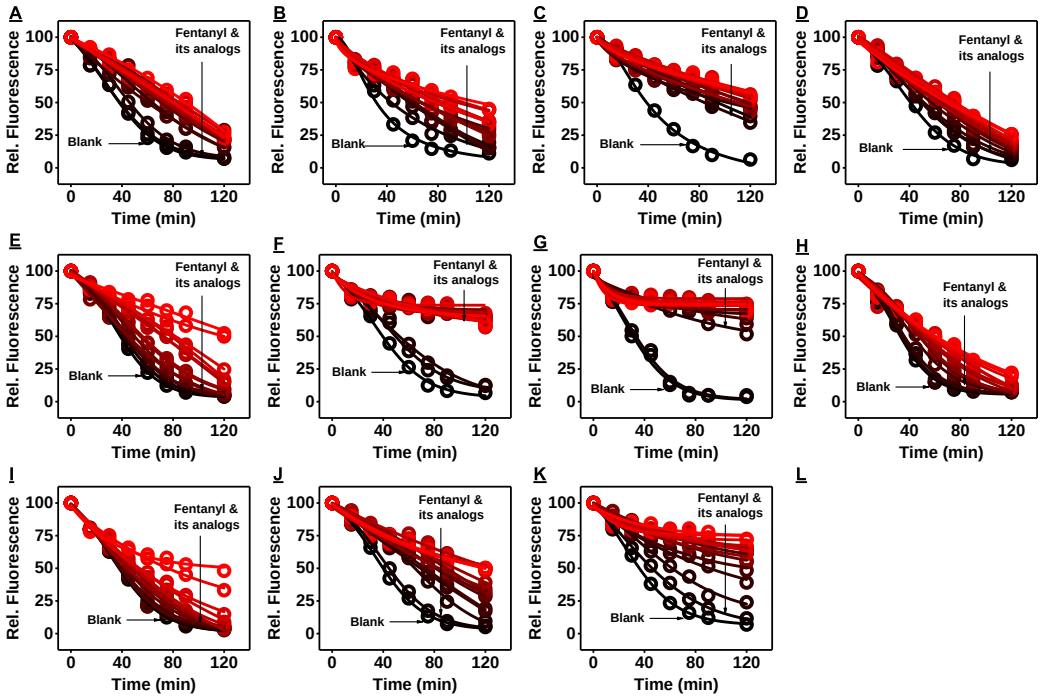

Figure 5-41. Screening the cross-reactivity of 11 aptamer candidates using our exonuclease digestion assay. Time-course digestion of (**A**) F4, (**B**) F5, (**C**) F6, (**D**) F13, (**E**) F14, (**F**) F17, (**G**) F18, (**H**) F23, (**I**) F24, (**J**) F25, and (**K**) F27. Aptamers were digested in the absence and presence of 100 µM fentanyl and 14 of its analogues.

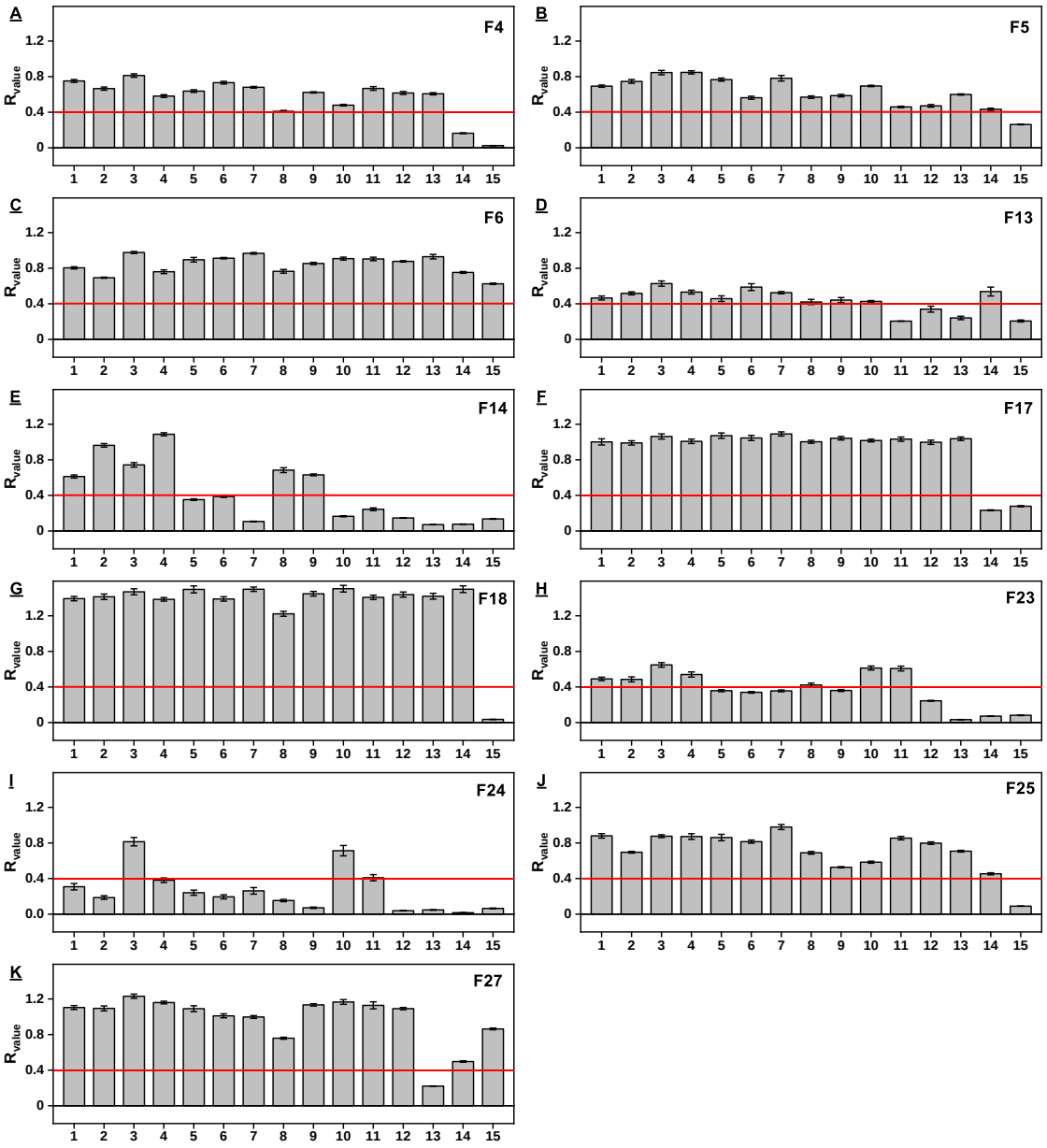

Figure 5-42. Screening the cross-reactivity of 11 aptamer candidates to fentanyl and its analogs using our exonuclease digestion assay. R_{value} obtained from time-course digestion of (**A**) F4, (**B**) F5, (**C**) F6, (**D**) F13, (**E**) F14, (**F**) F17, (**G**) F18, (**H**) F23, (**I**) F24, (**J**) F25, and (**L**) F27 in the absence and presence of 100 μM fentanyl (1) and 14 of its analogs: acetyl fentanyl (2), furanyl fentanyl (3), acrylfentanyl (4), butyryl fentanyl (5), valeryl fentanyl (6), cyclopropyl fentanyl (7), methoxyacetyl fentanyl (8), p-fluorofentanyl (9), o-methyl furanyl fentanyl (10), p-methoxy furanyl fentanyl (11), p-methoxy butyryl fentanyl (12), p-fluoroisobutyryl fentanyl (13), cis-3-methyl fentanyl (14), alpha-methyl thiofentanyl (15). The red line indicates a R_{value} of 0.4, which is predicted to be equivalent to a K_D of ~15 μM.

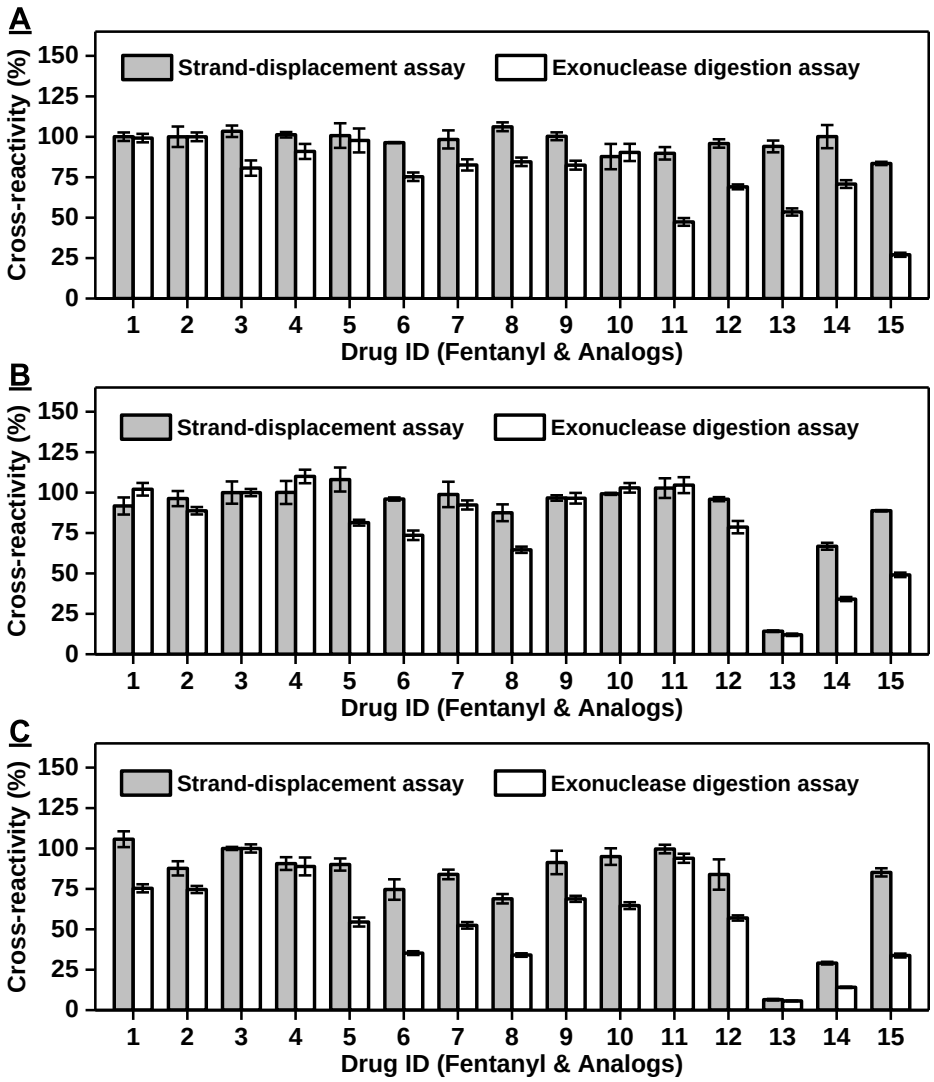

Figure 5-43. Comparison of aptamer cross-reactivity determined using a fluorescence strand-displacement assay and exonuclease digestion assay. Cross-reactivity of (**A**) F13, (**B**) F27 and (**C**) F27-42 to 100 µM fentanyl (1) and 14 of its analogs for the fluorescence strand-displacement assay and enzyme digestion assay, respectively. Cross-reactivity was relative to the signal produced by acetyl fentanyl for F13 or furanyl fentanyl for F27.

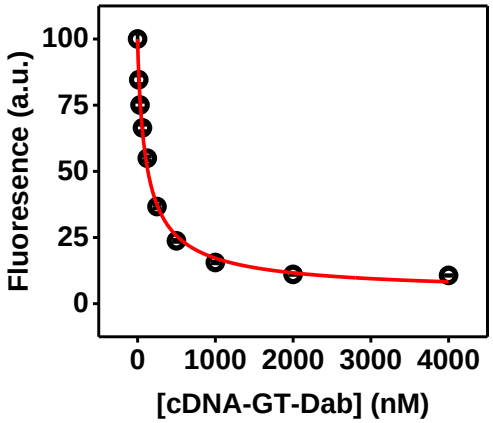

Figure 5-44. Determination of F27-42-FAM's optimal aptamer/cDNA ratio. 50 nM F27-42-FAM was mixed with 0, 16, 31, 62.5, 125, 250, 500, 1,000, 2,000, and 4,000 nM cDNA containing a single G–T mismatch (cDNA-GT-Dab). The fluorescence quenching monitored at 520 nm.

5.3.6. Development of E-AB sensors with customized analytical performance.

We have previously shown that the major inhibition products generated by this exonuclease assay possess structure-switching functionality, which is an essential property for constructing many aptamer-based sensors, including E-AB sensors. In order to demonstrate that our exonuclease digestion assay can streamline sensor production, we used two of our final aptamer candidates to construct a pair of E-AB sensors intended to different purposes in tackling the opioid epidemic. The first is for highly sensitive and specific detection of fentanyl in human saliva. The second is for presumptive testing of fentanyl and its analogs in seized substances. Based on our screening results, aptamer digestion products F27-42 and F13-39 were the top-performing candidates. F27-42 demonstrated a high R_{value} in the presence of 100 μM fentanyl, indicating a predicted K_D of 35 nM—which correlated well with ITC results (**Figure 5-45A**, K_D = 47± 6 nM)—with minimal cross-reactivity to fentanyl analogs or interferents, making it suitable for detecting

low concentrations of fentanyl in biological matrices. In contrast, F13-39 demonstrated high cross-reactivity to fentanyl and its analogs (R_{value} between 0.2 and 0.62), with sufficient affinity for detecting fentanyl in seized substances (**Figure 5-45B**, K_D = 5.55 ± 0.29 μM based on ITC).

We first confirmed the structure-switching functionality of these major inhibition products using CD spectroscopy. Each aptamer demonstrated a large change in intensity upon target addition. F13-39 had a large increase from 260–290 nm with a minor decrease at 245 nm, indicating a transition from single-stranded to B-form double-stranded DNA (**Figure 5-46A**). In contrast, F27-42 demonstrated an increase at 210 nm, an increase at 260 nm, and a decrease at 280, indicating a transition from single-stranded to double-stranded G-C rich Z-form DNA (**Figure 5-46B**). To facilitate E-AB sensing using these aptamers, we chemically synthesized variants of F27-42 and F13-39 (termed F27-38-MB and F13-32-MB) with the 5' overhang truncated and labeled with a 5'-thiol group and 3'-methylene blue redox tag.

We first optimized sensors constructed using F27-38-MB. We used our recently developed target-assisted immobilization strategy[318] to modify F27-38-MB onto gold electrodes. The surface-bound aptamer is predicted to remain unfolded in the absence of the target and produce minimal current, as the methylene blue redox tag is orientated away from the electrode surface (**Figure 5-47A**). Upon binding to the target, the aptamer undergoes a large target-induced conformational change, bringing methylene blue close to the surface and resulting in a large increase in current. We optimized the surface coverage and measurement frequency of F27-38-MB, and determined peak performance at 2.0 pmole/cm^2 and 400 Hz, respectively (**Figure 5-48**). We then constructed a calibration

curve of fentanyl in 50% human saliva using these conditions. We achieved a measurable detection limit of 30 nM (**Figure 5-47B**) which partially overlaps with the range of fentanyl observed in the saliva of intoxicated individuals.[325–327] We then performed the same optimization procedure for sensors constructed with F13-32-MB and obtained optimal surface coverage and measurement frequencies of 3.3 pmole/cm^2 and 200 Hz, respectively (**Figure 5-49**). We then tested the cross-reactivity of this sensor to 5 µM fentanyl or its analogs, obtaining ≥ 25% cross-reactivity for every target (**Figure 5-47C & 5-50**). Moreover, the sensor could also detect fentanyl in binary mixtures in which fentanyl (5 µM) was present at a far lower concentration than various interferents (500 µM or 200 µM for papaverine, noscapine, or lorazepam) (**Figure 5-47D & 5-51**) making it well-suited for detection of fentanyl in seized substances, which typically contain 0.1–1% fentanyl by weight.

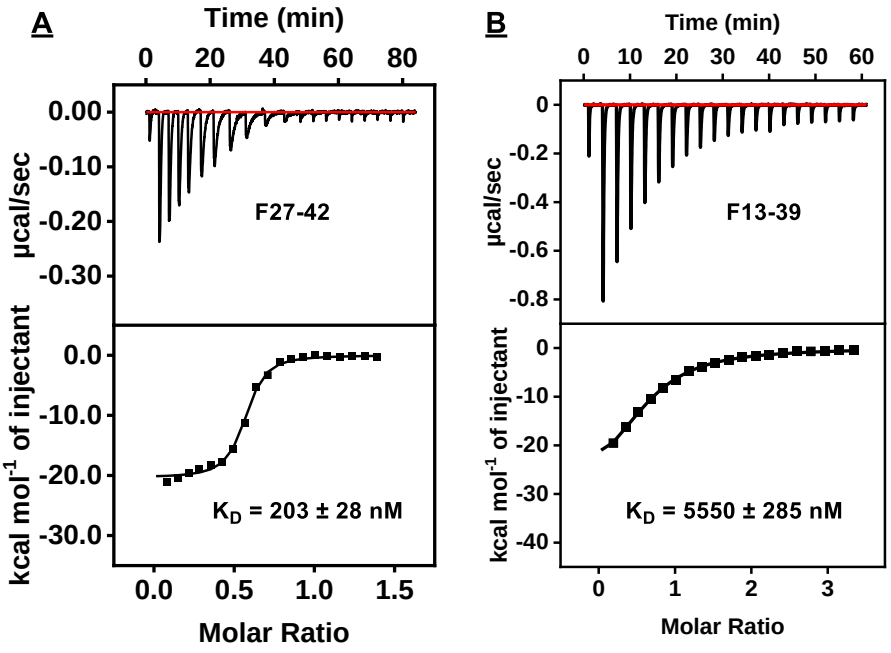

Figure 5-45. Characterization of fentanyl-binding affinity for F27-42 and F13-39 using ITC. Top panels display the heat generated from each titration of fentanyl into (**A**) F27-42

and (**B**) F13-39. Bottom panels show the integrated heat of each titration after correcting for the heat of dilution of the titrant.

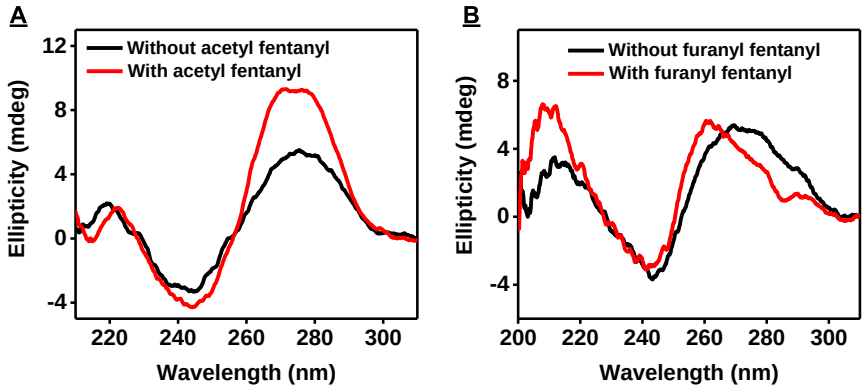

Figure 5-46. Confirmation of structure-switching functionality of major exonuclease digestion products. (**A**) F13-39 and (**B**) F27-42 were analyzed by CD spectroscopy in the absence (black) and presence (red) of 10 µM acetyl fentanyl or furanyl fentanyl, respectively.

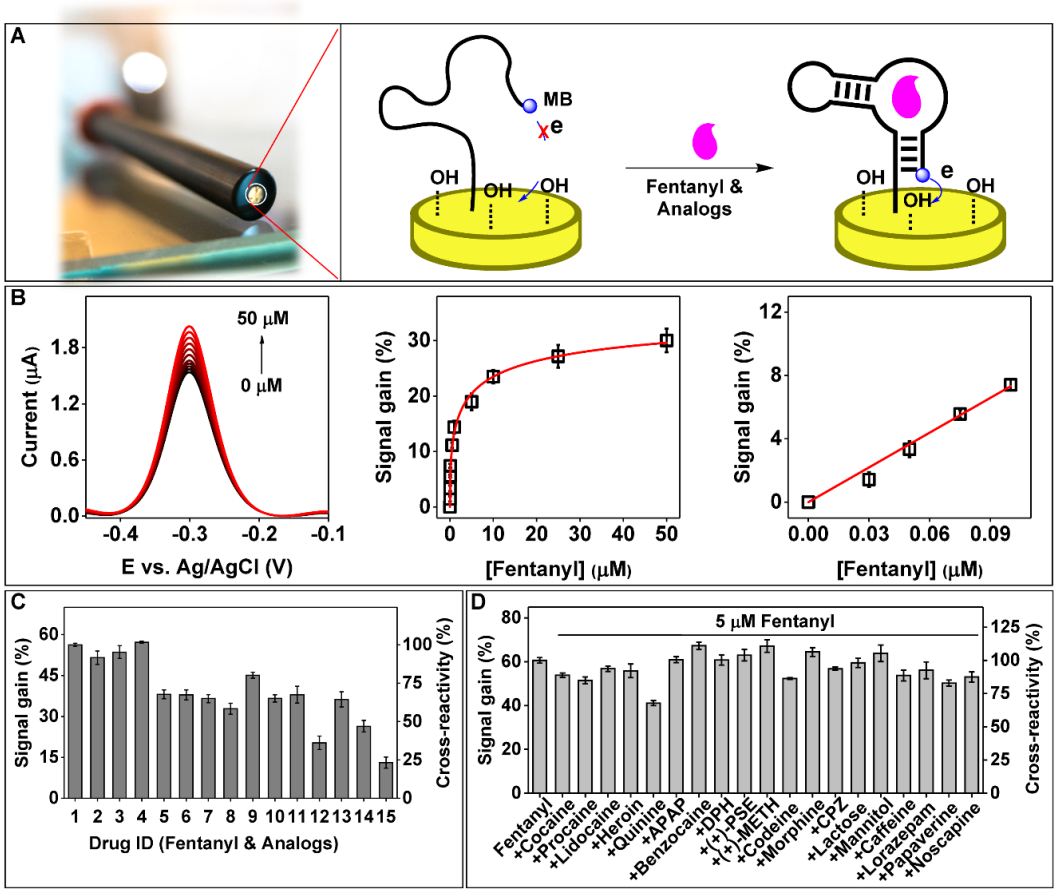

Figure 5-47. Analytical performance of E-AB sensor for detection of fentanyl or its analogs. (**A**) Working principle of the E-AB sensor. (**B**) SWV voltammogram (left),

calibration curve (middle), and linear range (right) for an F27-38-MB-based E-AB sensor in the presence of 0–50 µM fentanyl in 50% saliva. (**C**) Performance of the F13-32-MB-based E-AB sensor, including signal gain in the presence of fentanyl (1) and its analogs (2-15), and cross-reactivity to different binary mixtures containing 1:100 molar ratios of fentanyl and various interferents commonly found in seized substances (1:40 for lorazepam, papaverine, and noscapine).

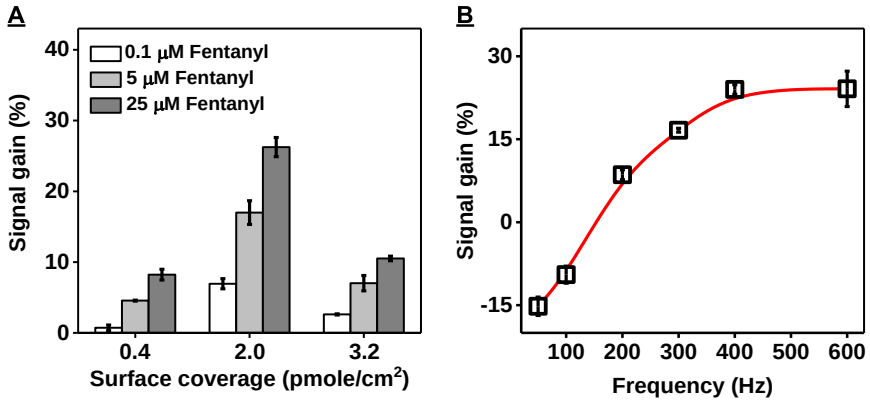

Figure 5-48. Optimization of analytical performance for E-AB sensors constructed with F27-38-MB. (**A**) Optimization of surface coverage for detecting 0.1, 5, and 25 µM fentanyl. (**B**) Performance under different frequencies for detection of 5 µM fentanyl.

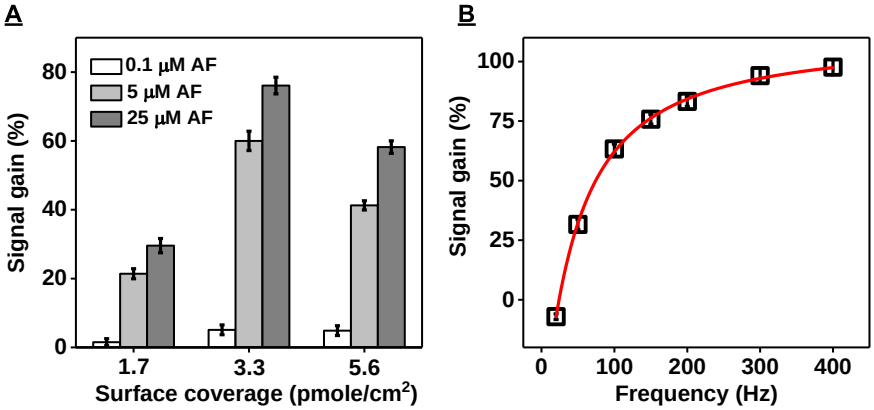

Figure 5-49. Optimization of analytical performance for E-AB sensors constructed with F13-32-MB. (A) Optimization of surface coverage for detecting 50, 100, and 150 µM acetyl fentanyl. (B) Performance under different frequencies for detection of 50 µM acetyl fentanyl.

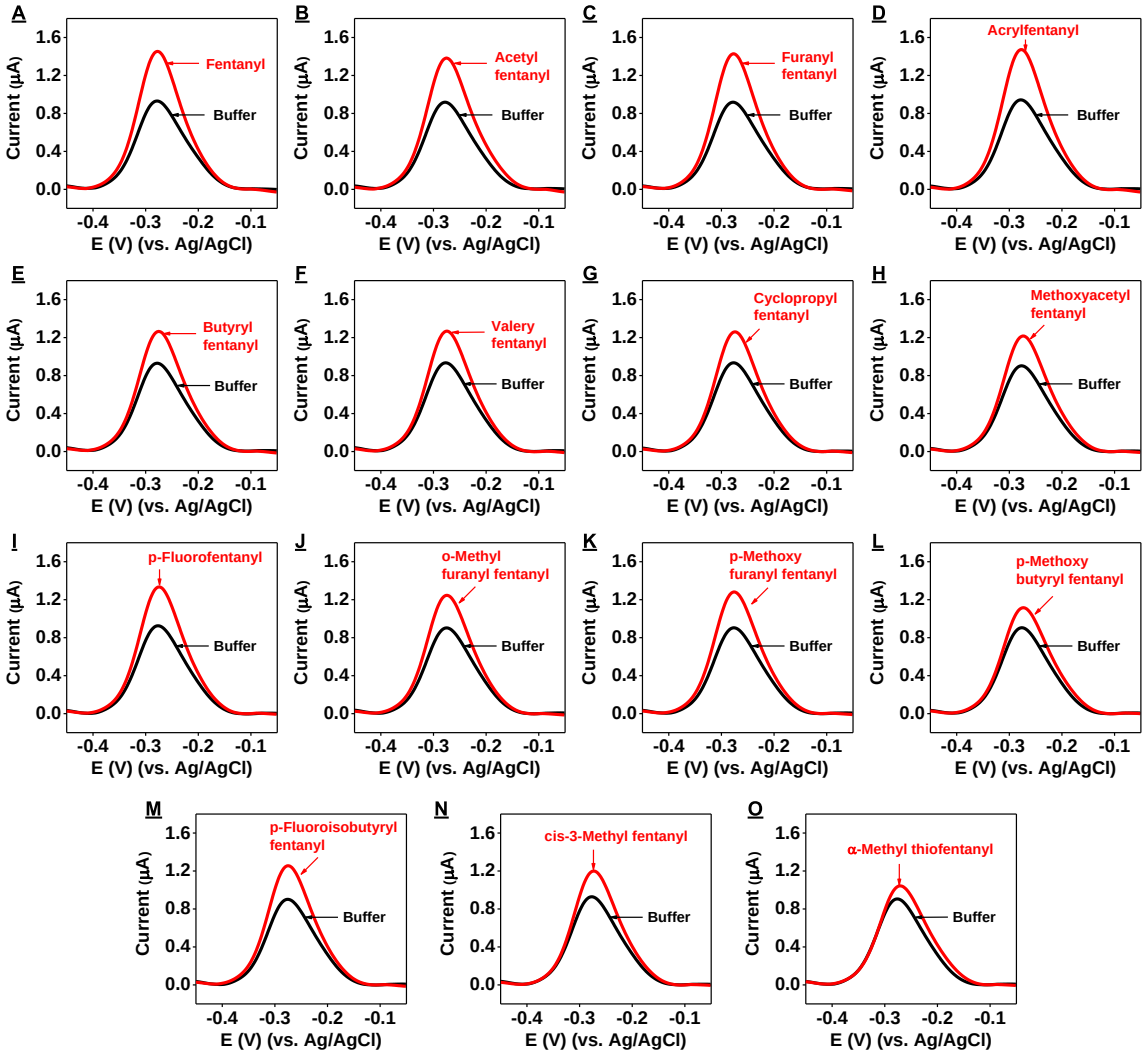

Figure 5-50. SWV response of E-AB sensor constructed with F13-32-MB to 5 μM fentanyl or its analogs.

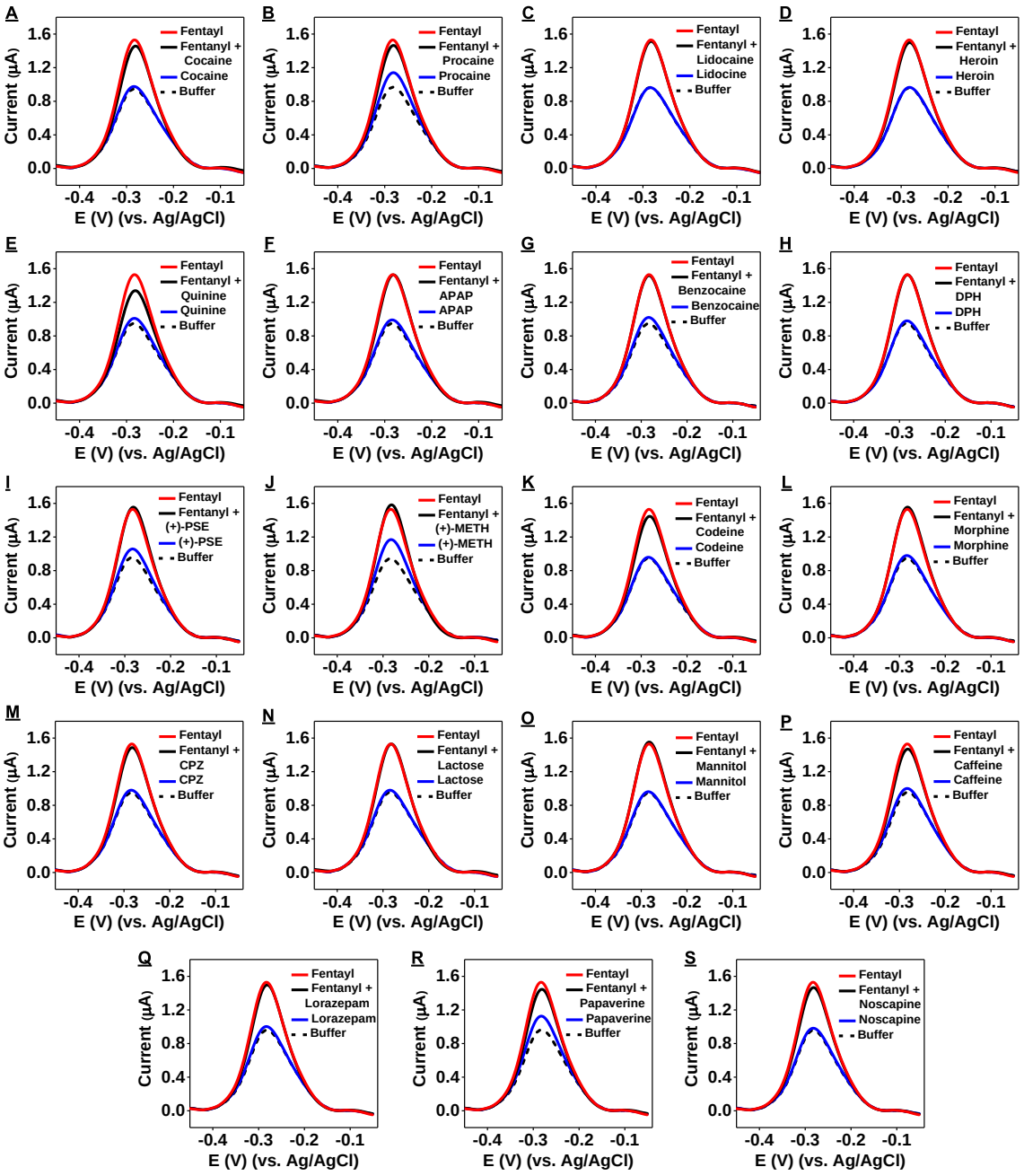

Figure 5-51. SWV response of E-AB sensor constructed with F13-32-MB in binary mixtures containing 1:100 molar ratios of fentanyl (final concentration of 5 μM) and various interferents commonly found in seized substances (the final concentration of papaverine, noscapine, and lorazepam was 200 μM and other interferents were used as a final concentration of 500 μM).

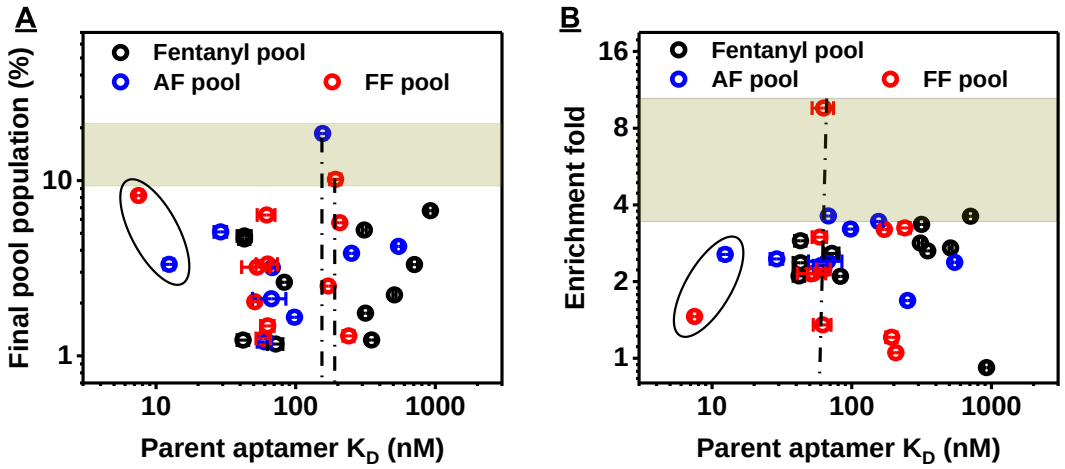

Figure 5-52. Correlation between parent aptamer binding affinity and performance based on (**A**) abundance in the final pool and (**B**) enrichment between early and final rounds. The aptamers with the highest affinity are circled.

5.4 Conclusion

The need for high-throughput aptamer characterization methods is a roadblock in the pipeline of aptamer-based sensor development. We have addressed this issue by demonstrating the performance of our exonuclease digestion assay for the rapid screening of aptamer binding affinity and specificity. Using a testbed of 28 aptamer candidates obtained from three independent SELEX experiments against fentanyl, acetyl fentanyl, and furanyl fentanyl, we validated our exonuclease digestion results for a total of 655 aptamer-ligand pairs against two gold-standard techniques: ITC and the strand-displacement fluorescence assay. Based on these results, we identified a quantitative relationship between ligand-induced enzymatic inhibition (R_{value}) and the binding affinity of the major exonuclease digestion product. This assay does not require prior knowledge of an aptamer's secondary structure, and can be generally applied regardless of its sequence. Moreover, the information generated directly reflects the binding parameters of the major exonuclease digestion products from the assay—and since these have been demonstrated

to possess structure-switching functionality, this is directly relevant to the subsequent development of sensors based on those aptamer digestion products. In this work, we were able to identify two aptamer candidates for the construction of E-AB sensors that can be applied to tackle two aspects of the opioid epidemic. The first was an E-AB sensor for sensitive and rapid detection of fentanyl in human saliva, indicating recent intoxication. The second is focused on cross-reactive detection of fentanyl and its analogs in seized substances, and was capable of discriminating fentanyl compounds even when present in 1:100 binary mixtures with interferents.

Interestingly, we did not observe any relationship between the affinity of an aptamer and its abundance in the final SELEX pool or round-to-round enrichment-fold as determined by HTS. Even aptamers with a relatively high abundance (>1%) and high enrichment-fold (>2-fold) had little to no binding affinity, and such selection criteria would in fact have eliminated the two highest-affinity aptamers that we identified (**Figure 5-52**). This further emphasizes the need to characterize large numbers of aptamer candidates upon completion of SELEX, as sequencing metrics alone are unreliable predictors of an aptamer's performance. This is presumably due at least in part to biases that arise during SELEX, such as low partitioning efficiency during separation, PCR amplification bias, and biases associated with the sequencing technique itself. We envision the possibility of further improving our assay's throughput by making use of DNA microarrays that can accommodate up to ~6×10^6 unique sequences. This would potentially allow monitoring of exonuclease digestion for pools composed of thousands of sequences. Our assay is also sufficiently simple that it could be performed with an automated liquid-handling system and plate reader to enable rapid and continuous testing of massive numbers of aptamer

candidates. Finally, the assay could be further improved by the development of dyes that can report on the digestion process in real-time, eliminating the need for sample collection.

CHAPTER 6: Rapid Development of an E-AB Sensor for Detection of THC

6.1. Introduction.

Cannabis sativa is a flowering herb cultivated as a source of industrial fiber, seed oil, medicine, and for recreational purposes.[233–235] This plant is commonly referred to as hemp when describing strains with non-psychoactive properties, or as marijuana for strains that do possess such effects. This plant produces a variety of cannabinoid compounds, including tetrahydrocannabinol acid (THC-A) and Δ^9-tetrahydrocannabinol (THC).[230,231] THC-A is believed to serve as a chemical protectant against harmful UV-B radiation, and although it is not psychoactive itself, exposure to UV light or heat results in decarboxylation of THC-A into THC, which is the primary psychoactive compound of marijuana.[230,231,328] THC binds to cannabinoid receptors in the brain, resulting in a variety of behavioral and cognitive effects.[329] Marijuana is the most widely abused illicit drug in the United States, with approximately 8.9% of the United States population being marijuana users.[193,194] Acute effects of marijuana use include euphoria, anxiety, impeded short-term memory, increased heart rate, increased appetite, and reduced motor skills.[330] The potency of a given strain depends on its THC and THC-A concentration. As of the 1970 Controlled Substances Act, all forms of *C. sativa* have until recently been illegal under federal law, regardless of their THC content. However, with the recent passing of the Hemp Farming Act of 2018,[232] *C. sativa* plants have been formally differentiated into two distinct categories. Hemp, which is now legal, is the non-psychoactive species of cannabis, with fibers and seeds that can be turned into various commercial and industrial products including rope, textiles, clothing, shoes, food, paper, bioplastics, insulation, and biofuels.[233–235] In contrast, marijuana remains illegal under federal law. These two subtypes

of *C. sativa* are morphologically identical and can only be discriminated based on chemical analysis of their THC levels following decarboxylation.[236] Cannabis with THC levels below 0.3% by dry weight is classified as hemp, whereas plants with higher THC levels are defined as marijuana.[232] With the widespread use of marijuana and the explosion of legalized hemp products, there is a demand for forensic tools that can differentiate between these two cannabis subtypes and thereby aid the criminal justice system in enforcing laws related to the possession, trafficking, and production of marijuana.

Chemical analysis of marijuana begins by drying the seized plant material, followed by homogenization and extraction of its cannabinoids using an organic solvent.[236] Confirmatory THC testing is typically commonly done using mass spectroscopy techniques such as gas or liquid chromatography/mass spectrometry or spectroscopic methods such as Raman or infrared spectroscopy.[236] These techniques allow for specific identification and quantification of THC levels in plant material; however, they require time-consuming sample pretreatment, costly and sophisticated instrumentation, and skilled operators. Due to limited resources, confirmatory testing cannot be employed for every sample submitted to a forensic facility. Consequently, presumptive tests are performed to screen out drug-negative samples as a prelude to confirmatory testing.[236]

Like confirmatory testing, presumptive tests are designed to detect the psychoactive ingredient THC in marijuana extracts. Colorimetric testing is typically the most straightforward and quickest method, and most colorimetric tests are sufficiently sensitive to detect microgram quantities of THC. The most widely-used colorimetric test for THC is the Duquenois-Levine test.[237,238] This test entails performing a chemical reaction with the aromatic ring of THC to yield a highly-conjugated purple-colored product in the presence

of aldehyde, hydrochloric acid, and vanillin. The reagents needed for this test, which can be performed by technicians without extensive training, are inexpensive and readily available, and the resulting colorimetric readout is detectable by naked eye. However, these reagents are also broadly cross-reactive to other compounds that possess aromatic rings, and the Duquenois-Levine test has been shown to produce false-positive results when testing a variety of non-cannabis plant and vegetable extracts.[237,238] Moreover, subjective interpretation of colorimetric results by individual operators makes it challenging to quantify THC for the differentiation of hemp from marijuana. This means that many samples that may not possess illegal levels of THC will be sent for confirmatory testing, further stretching the already limited resources of forensic labs across the United States.

We have previously isolated a THC-binding aptamer via Systematic Evolution of Ligands by Exponential Enrichment (SELEX).[58] The isolated aptamer exhibits high affinity for THC, with excellent specificity against other structurally-similar cannabinoids. However, the aptamer does not have structure-switching functionality, which is a critical component for many aptamer-based sensors.[113] Incorporating such signal reporting capabilities typically entails a lengthy trial-and-error process, but we have utilized our exonuclease-truncation strategy[291,315] to efficiently generate a THC-binding aptamer with structure-switching functionality. The truncated aptamer was then directly employed into an E-AB sensor for the rapid and quantitative screening of THC in seized cannabis. This platform will provide an alternative to colorimetric spot tests for presumptive testing, eliminating false-positive results due to the presence of non-THC aromatic compounds in plant extracts. Moreover, the sensor response is reported digitally, providing a clear and quantitative result for the differentiation of hemp and marijuana. This will be an important

step in detecting marijuana, and this approach also offers a general platform for achieving presumptive testing of other illicit substances.

6.2. Experimental section.

6.2.1. Reagents.

Exonuclease III (Exo III; *E. coli*) (100 U/μL) and Exonuclease I (Exo I; *E. coli*) (20 U/μL) were purchased from New England Biolabs. THC, cannabigerolic acid (CBG-A), cannabigerol (CBG), cannabidiolic acid (CBD-A), cannabidiol (CBD), THC-A, XLR-11, UR-144, heroin HCl, pentylone HCl, α-pyrrolidinopentiophenone HCl, fentanyl HCl, and clonazepam were purchased from Cayman Chemicals. Cocaine HCL, amphetamine hemisulfate, (+)-methamphetamine HCl, procaine HCl, acetaminophen, ibuprofen, nicotine, caffeine, and all other chemicals were purchased from Sigma-Aldrich unless otherwise specified. Nunc 384-well black plates were purchased from Thermo Fisher Scientific. Unmodified oligonucleotides were purchased with desalting purification from Integrated DNA Technologies. Unmodified oligonucleotides were dissolved in deionized (DI) water, and their concentrations were measured using a NanoDrop 2000 spectrophotometer. 5'-thiolated- and 3'-methylene blue-modified aptamers were purchased with dual HPLC purification from LGC Biosearch Technologies and dissolved in 1× TE buffer (10 mM Tris-HCl with 1 mM EDTA, pH 8.0). The DNA sequences employed in this work are shown in **Table 6-1**. DI water with a conductivity of 18.2 MΩ×cm was obtained from a Milli-Q EQ 7000 ultrapure water filtration system.

Table 6-1. DNA sequences used in chapter 6.

Sequences ID	Sequence (5'–3')
TA-47	CTTACGACCCAGGGGGGTGGACAGGCGGGGGTTAGGGGGGTCGTAAG
TA-39	CGACCCAGGGGGGTGGACAGGCGGGGGTTAGGGGGGTCG
TA-35	ACCCAGGGGGGTGGACAGGCGGGGGTTAGGGGGGT
TA-mut1	AACCAGGGGGGTGGACAGGCGGGGGTTAGGGGGTT
TA-mut2	ACACAGGGGGGTGGACAGGCGGGGGTTAGGGGTGT
TA-mut1-MB	/ThiolC6/AACCAGGGGGGTGGACAGGCGGGGGTTAGGGGGTT/MB/
TA-39-MB	/ThiolC6/CGACCCAGGGGGGTGGACAGGCGGGGGTTAGGGGGGTCG/MB/

/ThiolC6/ represents thiol group with six-carbon spacer, /MB/ represents methylene blue redox tag

6.2.2. Aptamer digestion experiments.

Aptamer digestion experiments were performed as previously described.[291,292,315] Specifically, a 1 µL solution of aptamer (final concentration 1 µM) was added to a 31.5 µL Tris–HCl solution (pH 7.4) and heated to 95 °C for 10 min and immediately cooled on ice. The solution was then diluted to a volume of 42.5 µL with salts and BSA (final concentration: 10 mM Tris–HCl, 20 mM NaCl, 0.5 mM MgCl2, 5% (v/v) DMSO, 0.1 mg/mL BSA, pH 7.4). Next, 2.5 µL of 100% DMSO or THC dissolved in 100% DMSO, was added to the reaction mixture and incubated in a thermal cycler (C1000 Touch, Bio-Rad) at 25 °C for 30 min. Finally, 5 µL of exonuclease mixture (final concentrations: 0.025 U/µL Exo III and 0.05 U/µL Exo I) or Exo I alone (final concentration: 0.05 U/µL Exo I) was added to begin the reaction. We collected 5 µL samples of the reaction mixture and adding these to 10 µL of formamide loading buffer (75% formamide, 10% glycerol, 0.125% SDS, 10 mM EDTA, and 0.15% (w/v) xylene cyanol).

6.2.3. Polyacrylamide gel electrophoresis (PAGE) analysis of digestion products.

3 µL of each collected sample was loaded into the wells of a 15% denaturing PAGE gel. Separation was carried out at 6 V/cm for 30 mins followed by 25 V/cm for 3.5 hr in 0.5× TBE running buffer. The gel was then stained with 125 mL of 1× SYBR Gold solution

for 25 min and imaged using a ChemiDoc MP Image system (Bio-Rad). Digestion products of TA-47 were characterized using a DNA ladder customized for each sequence.

6.2.4. Confirmation of structure-switching functionality using circular dichroism (CD) spectroscopy.

CD experiments were performed at room temperature using a Jasco J-815 CD spectrometer. TA-39, TA-35, TA-mut1, and TA-mut2 were diluted to a final concentration of 1.5 µM in 255 µL Tris–HCl buffer, heated to 95 °C for 10 mins, and immediately cooled on ice for 5 min, after which 30 µL of salt solution was added (Final concentration: 10 mM Tris–HCl, pH 7.4, 20 mM NaCl, 0.5 mM $MgCl_2$). Then 15 µL of 100% DMSO or THC dissolved in 100% DMSO (final concentration: 2 µM) was added. The solution was transferred to a 1-cm quartz cuvette (Hellma Analytics), and the spectra were measured using the following parameters: scan range of 210 to 310 nm, scan speed of 50 nm/min, sensitivity of 5 mdeg, response time of 4 s, bandwidth of 1 nm, and accumulation of 5 scans. The reference spectra of buffer or THC prepared in buffer were subtracted from spectra collected with the aptamer in the absence or presence of THC, respectively.

6.2.5. Fabrication of electrochemical aptamer-based (E-AB) sensors.

Aptamer-immobilized electrodes were fabricated as follows. 2-mm diameter gold disk electrodes (CH Instruments) were polished with 1-µm diamond slurry (Buehler) followed by 0.05-µm alumina suspension. Bound particulates were removed by sonicating electrodes in 70% ethanol solution for 5 mins and then in DI water for another 5 min. Electrochemical cleaning was then performed following a previously published protocol.[294] The electrode surface area was calculated based on the charge produced by the reduction of surface gold oxide in 0.05 M H_2SO_4, and a conversion factor of 390 ± 10

$\mu C/cm^{-2}$.[295] Two different aptamer reduction procedures were performed. In one, 2 µL of 200 µM thiolated methylene blue-modified aptamer was mixed with 8 µL of 100 mM tris(2-carboxyethyl)phosphine (TCEP) at room temperature for 2 h to reduce disulfide bonds. The alternative reduction procedure involved mixing 2 µL of 200 µM thiolated MB-modified aptamer with 40 µL of buffer (10 mM Tris–HCl, pH 7.4), after which the solution was heated to 95 °C for 10 mins and immediately cooled on ice for 5 min. Finally, 8 µL of 100 mM TCEP was added to the aptamer solution and incubated at room temperature for 2 h to reduce disulfide bonds. The reduced aptamer solution was then diluted with buffer and salts (final concentration: 10 mM Tris–HCl, pH 7.4, 20 mM NaCl, 0.5 mM $MgCl_2$). The final DNA concentration varied between experiments. Electrochemically cleaned electrodes were dried with nitrogen and incubated overnight in 250 µL of thiolated aptamer solution at room temperature. The electrodes were then backfilled with 1 mM 6-mercapto-1-hexanol (MCH), 1 mM 1-hexanethiol (HEX), 1 mM mercaptohexanoic acid (MHA), or 1 mM 2-[2-[2-[2-mercaptoethoxy]ethoxy]ethoxy (PEG), prepared in immobilization buffer (final concentration: 10 mM Tris–HCl, pH 7.4, 20 mM NaCl, 0.5 mM $MgCl_2$) for 2 h at room temperature. The electrodes were stored in 10 mM Tris buffer (pH 7.4) for at least 1 hr before use. Following target detection, the electrode surface coverage was determined as previously reported.[296]

6.2.6. Electrochemical measurements and optimization of E-AB sensor performance.

All electrochemical measurements were performed using a CHI760D electrochemical workstation with a three-electrode system containing an Ag/AgCl reference electrode (3 M KCl) (CHI), a platinum wire counter electrode (CHI), and an aptamer-modified gold working electrode. The surface coverage of each aptamer was

independently optimized. Specifically, E-AB sensors were constructed with various concentrations of the thiolated aptamer. The calibration curve of THC response was determined for each electrode using square-wave voltammetry (SWV) with frequencies ranging from 10–1,000 Hz. The signal gain was calculated using the equation: $(I - I_0)/I_0 \times 100\%$, where I and I_0 are the peak current in the presence and absence of THC, respectively.

6.2.7. Isothermal titration calorimetry (ITC).

All ITC experiments were performed in binding buffer with a MicroCal ITC200 instrument (Malvern) at 23 °C. For each experiment, 300 µL of aptamer or aptamer mutant (final concentrations: 20 µM) in Tris–HCl buffer (pH 7.4, without salts) was heated at 95 °C for 10 min and immediately cooled on ice. Salts and DMSO were subsequently added to match selection buffer conditions before loading into the sample cell. The syringe was loaded with 150 µM THC in selection buffer. Other experimental details are provided in **Table 6-2**. Typically, each titration consisted of an initial purge injection of 0.4 µL and 19 successive injections of 2 µL. The spacing was changed as necessary for each aptamer or aptamer mutant. For TA-34, TA-mut1, and TA-mut2, additional injections were performed in the same manner to achieve saturation. The raw data were first corrected for the dilution heat of THC and then analyzed with the MicroCal analysis kit integrated into the Origin 7 software and fitted to a single-site binding model.

Table 6-2. Aptamer ID, dissociation constant (K_D), and ITC experiment conditions.

Aptamer ID	[THC] (µM)	[Aptamer] (µM)	K_D (nM)
TA-39	150	20	41 ± 10
TA-34	150	20	6289 ± 1510
TA-mut1	150	20	961 ± 235
TA-mut2	150	20	990 ± 139

6.3. Results and Discussion.

6.3.1. Engineering structure-switching THC-binding aptamers.

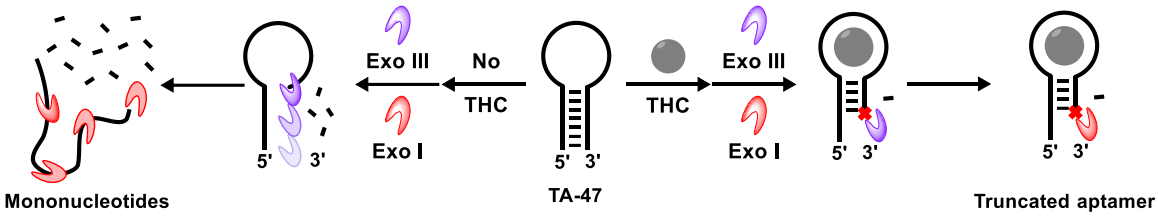

Figure 6-1. Working principle of the exonuclease-assisted truncation strategy. (Left) In the absence of THC, Exo III and Exo I will progressively digest the aptamer into mononucleotides. (Right) In the presence of THC, digestion is halted prior to the target-binding domain, yielding a truncated aptamer that has structure-switching functionality.

We have previously isolated a THC-binding aptamer, termed TA-47, which possesses a hairpin structure with a blunt-ended stem.[58] TA-47 binds THC with an exceptional binding affinity of 40 nM but is ill-suited for aptamer-based sensing because the aptamer exists in a fully-folded form and the binding of THC does not produce a conformational change that could be transduced into a measurable signal. To rapidly engineer TA-47 into a structure-switching aptamer, we utilized an exonuclease-assisted truncation method developed in our laboratory (**Figure 6-1**).[291,315] This truncation strategy uses Exo III, which exhibits 3'-to-5' exonuclease activity on double-stranded DNA, and Exo I, which demonstrates 3'-to-5' exonuclease activity on single-stranded DNA. In the absence of target, Exo III and Exo I completely digest the double- and single-stranded portions of the aptamer (**Figure 6-1**, left). In the presence of THC, however, the progressive digestion of the aptamer from its 3'-end will be halted a few nucleotides short of the target-binding domain (**Figure 6-1**, right), yielding a major digestion product that typically exhibits target-binding-induced structure-switching properties.[291,315]

We performed digestion of TA-47 in the presence and absence of 100 μM THC in binding buffer (10 mM Tris–HCl, pH 7.4, 20 mM NaCl, 0.5 mM $MgCl_2$, and 5% DMSO) and identified 43- and 41-nt inhibition products via PAGE (**Figure 6-2A**). To confirm whether the observed products possessed structure-switching functionality, we chemically synthesized the 43- and 41-nt products with their 5-overhangs removed (**Figure 6-2B**), yielding blunt ended constructs TA-39 and TA-35, respectively. We then measured their CD spectra in the absence and presence of THC (**Figure 6-2C & D**). In the absence of THC, we observed positive peaks at 210, 260, and 290 nm and a negative peak at 240 nm for both sequences. These spectra suggest that the center loop adopts a parallel G-quadruplex structure.[300,301] Upon adding THC, we observed a change shift at 210 and 285 nm towards negative CD, which indicates that the truncated stem is folding into a Z-form type G–C rich duplex.[300,301] These results confirmed that both digestion products are structure-switching aptamers. We observed that TA-35 underwent a smaller change upon addition of THC, and this appears to be a consequence of reduced binding affinity due to its shorter stem. We measured the binding affinity of TA-39 and TA-35 using ITC, yielding dissociation constants (K_D) of 41 ± 10 nM and 6,289 ± 1,510 nM, respectively (**Figure 6-3A & B**).

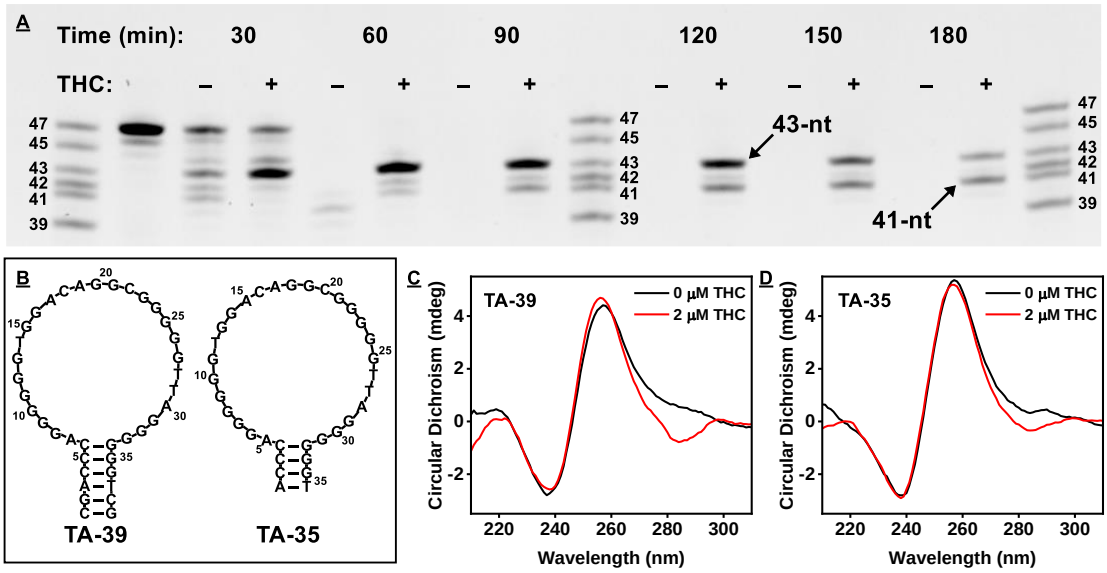

Figure 6-2. Engineering a TA-47-derived structure-switching aptamer using an exonuclease-assisted truncation strategy. (**A**) PAGE analysis of TA-47 digestion products. (**B**) Major digestion products of TA-47. CD spectroscopy measurements of (**C**) TA-39 and (**D**) TA-35 in the absence and presence of 2 μM THC.

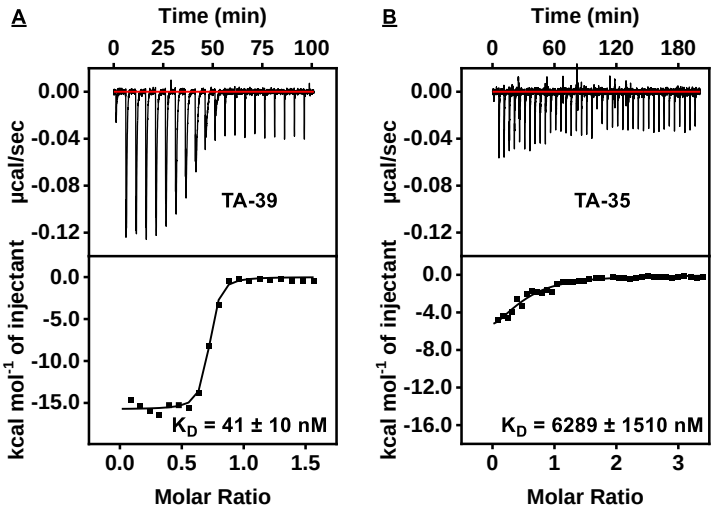

Figure 6-3. Characterization of TA-39 and TA-35 THC binding affinity using ITC. The top panels display the heat generated from each titration of THC into (**A**) TA-39 and (**B**) TA-35. The bottom panels show the integrated heat of each titration after correcting for the heat of dilution of the titrant.

Although TA-35 exhibits poor affinity, we hypothesized that it could prove useful for aptamer-based sensing, given that its shorter stem would be expected to be more thermodynamically unstable, leading to lower background. The loop of TA-35 is highly G-rich (~60% nucleotide composition), and its poor affinity may be the product of misfolding in its C-rich stem. To remedy this issue, we synthesized two TA-35 mutants, TA-mut1 and TA-mut2, that possess double-site mutations in their stem, converting C–G base-pairs into A–T base-pairs (**Figure 6-4A**). To determine the relative binding strength of each mutant compared to TA-35, we first digested each aptamer in the absence and presence of 100 μM THC using Exo I alone (**Figure 6-4B–D**). Since Exo I only digests single-stranded DNA, the digestion speed in the absence of target will indicate the degree of unfolding, with fully unfolded aptamers digesting rapidly while folded or partially-folded aptamers digest more slowly. In parallel, the degree of inhibition in the presence of 100 μM THC will demonstrate the degree of target-induced folding. In the absence of target, TA-35 had the fastest digestion speed, being completely digested within 90 mins (**Figure 6-4E**, black), followed by TA-mut1, which took 120 mins (**Figure 6-4F**, black), and TA-mut2, which took 180 mins (**Figure 6-4G**, black). TA-35 also had the weakest inhibition in the presence of 100 μM THC (**Figure 6-4G**, red), whereas both TA-mut1 and TA-mut2 demonstrating similar degrees of inhibition, with > 65% of the input DNA intact after 180 mins (**Figure 6-4F, G**, red).

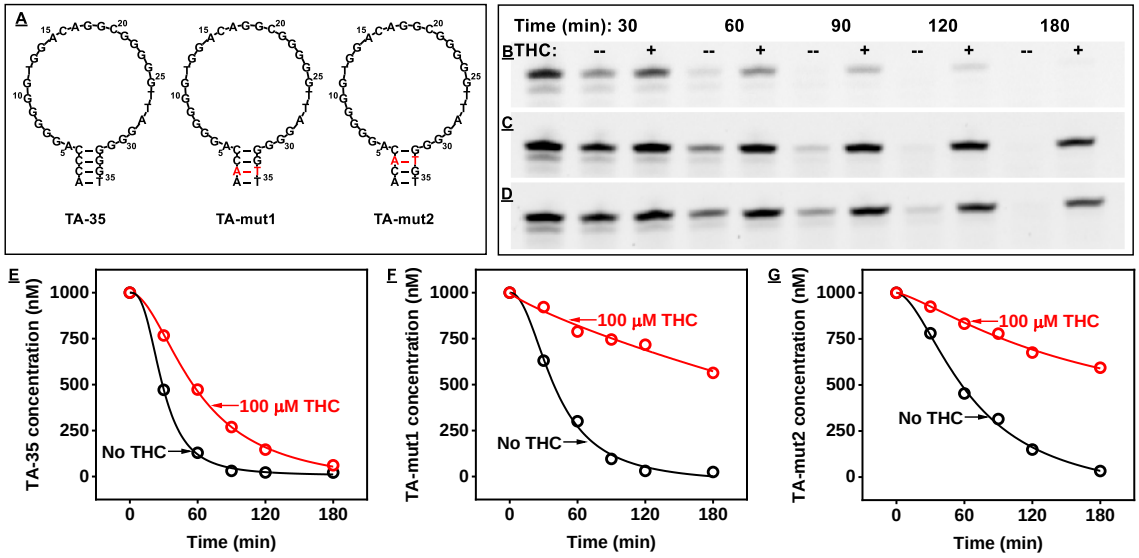

Figure 6-4. Engineering high-affinity mutants of TA-35. (**A**) Sequence and structure of TA-35 mutants. PAGE analysis of (**B**) TA-35, (**C**) TA-mut1, and (**D**) TA-mut2 Exo I inhibition in the presence and absence of 100 µM THC. Concentration of (**E**) TA-35, (**F**) TA-mut1, and (**G**) TA-mut2 over a 3 hr time-course of Exo I digestion in the absence and presence of 100 µM THC.

We confirmed the structure-switching properties of each mutant using CD and observed a similar spectrum as TA-35 (**Figure 6-5A & B**). In the absence of THC, positive peaks were observed at 210, 260, and 290 nm, with a negative peak at 240 nm. Upon addition of THC, the peak at 290 nm became more negative, confirming that these mutants are structure-switching aptamers. Finally, we tested the binding affinities of TA-mut1 and TA-mut2 using ITC, obtaining K_D values of 961 ± 235 and 990 ± 139 nM, respectively (**Figure 6-5C & D**). Both TA-mut1 and TA-mut2 demonstrated improved binding affinity relative to TA-35; however, based on the more rapid digestion of TA-mut1 by Exo I, it may undergo more efficient structure-switching relative to TA-mut2. Based on our results, we selected TA-39 and TA-mut1 to construct an E-AB sensor for detecting THC in plant material.

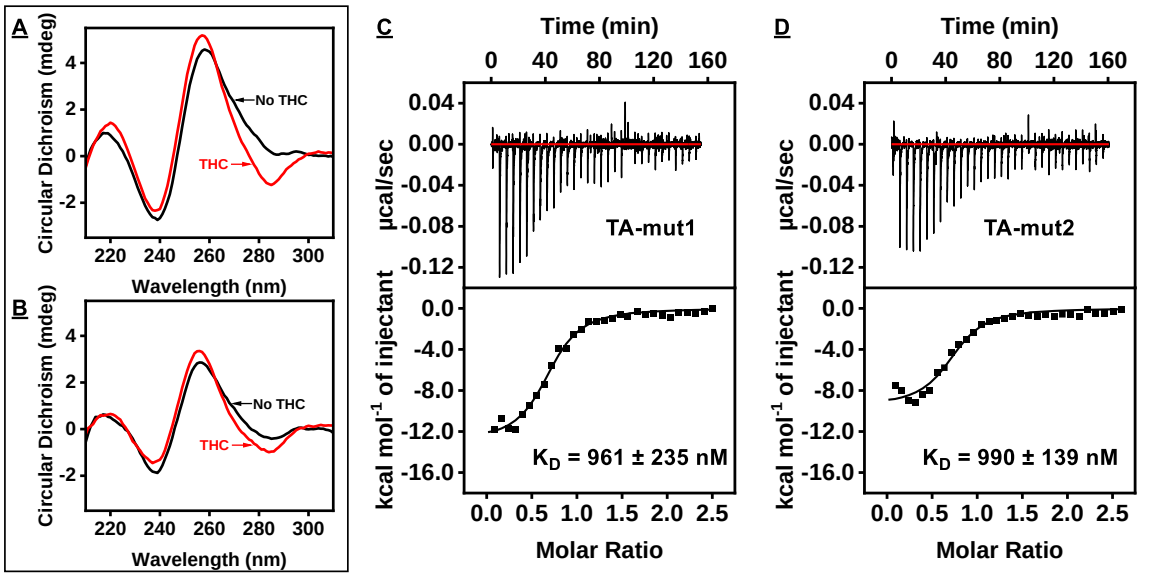

Figure 6-5. Characterization of TA-mut1 and TA-mut2 structure-switching functionality and THC binding affinity. CD spectroscopy measurements of (**A**) TA-mut1 and (**B**) TA-mut2 in the absence and presence of 2 µM THC. ITC determination of K_D for (**C**) TA-mut1 and (**D**) TA-mut2. The top panels display the heat generated from each titration of THC into the aptamer. The bottom panels show the integrated heat of each titration after correcting for the heat of dilution of the titrant.

6.3.2. Construction of E-AB sensors using a hydrophobic monolayer.

To perform rapid, sensitive, and specific THC detection in cannabis extract, we incorporated our structure-switching THC-binding aptamers into an E-AB sensor, a platform that has previously demonstrated sensitive and specific detection of small-molecule targets in complex samples.[116,117,281] E-AB sensor detection is based on a target-binding-induced change in the conformation of an electrode-bound, redox-modified aptamer, which alters electron transfer efficiency between the redox reporter and the electrode surface. E-AB sensing is rapid—on the order of seconds—and highly target-specific due to the utilization of surface-immobilized aptamers that were selected for their ability to achieve sensitive and specific THC binding. This is important, because cannabis extracts contain diverse mixtures of endogenous compounds, and it has been reported that

some of these are structurally-similar molecules that can interfere with and produce false positives in THC testing platforms such as chemical spot tests or portable Raman spectroscopy. E-AB sensors also offer a number of other critical advantages for sensing in plant extracts. For example, they are insensitive to matrix properties such as turbidity or color, and common endogenous plant compounds do not produce an electrochemical signal under the employed voltage (-0.2 V vs. SCE), resulting in minimal background.

We synthesized TA-mut1 and TA-39 with a 5' thiol-C6 group and a 3' methylene blue redox tag (**Figure 6-6A**)—termed TA-mut1-MB and TA-39-MB, respectively—and immobilized these constructs onto a clean gold electrode surface via thiol–gold chemistry and backfilled. In the absence of THC, the unfolded aptamer lifts the redox tag away from the electrode surface, minimizing electron transfer and producing a minimal background current (**Figure 6-6B**). THC binding induces a conformational change in the aptamer, bringing the methylene blue tag close to the electrode surface (**Figure 6-6C**) and resulting in increased electron transfer and a large current increase.

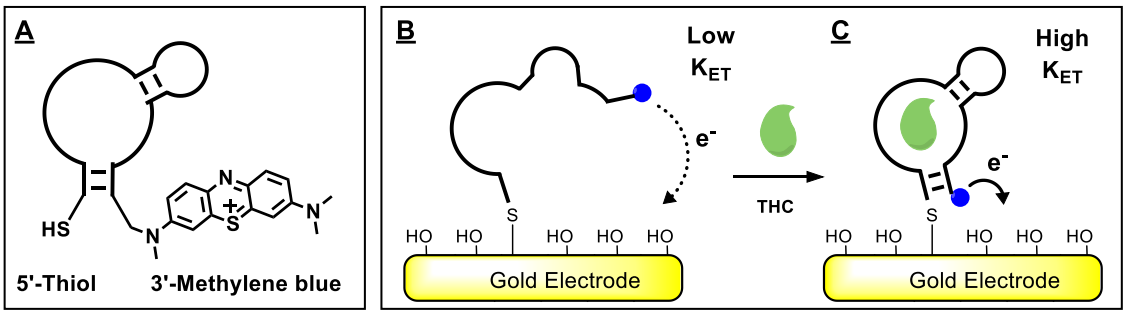

Figure 6-6. Fabrication of an E-AB sensor for THC detection. (**A**) TA-mut1 and TA-39 were chemically synthesized with a 5'-thiol and 3'-methylene blue redox tag. (**B**) In the absence of THC, the aptamer exists in a single-stranded state, orienting the methylene blue redox tag away from the electrode surface, resulting in minimal current. (**C**) In the presence of THC, the aptamer folds into a double-stranded conformation, bringing the redox tag close to the electrode surface and increasing the current.

We first constructed E-AB sensors using TA-mut1-MB following a previously reported protocol.[294] TA-mut1-MB was prepared by incubating with TCEP to reduce the disulfide bond, and the freshly-reduced aptamer solution (50, 100, 150, 200, 250, or 300 nM) was incubated overnight with a clean gold electrode. The modified electrodes were backfilled with HEX rather than MCH, as we believed this would favor the approach of hydrophobic THC molecules to the electrode surface for aptamer binding. We first optimized each sensor's SWV measurement frequency to detect 25 µM THC (**Figure 6-7A**). Under these measurement conditions (50 nM DNA, 15 Hz), we obtained a signal gain of 76% for 25 µM THC using electrodes modified with 50 nM TA-mut1-MB. Using this aptamer concentration with the optimized measurement conditions, the sensor achieved a linear range from 500–5,000 nM with a detection limit of 500 nM THC (**Figure 6-7B & C**).

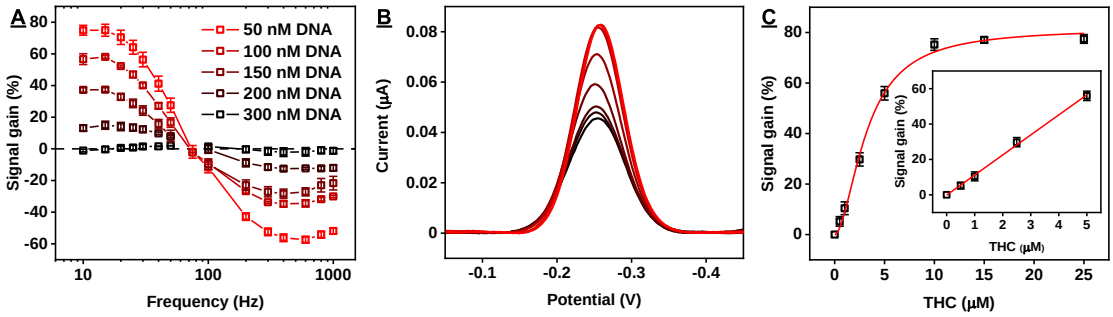

Figure 6-7. Detection of THC using a TA-mut1-MB-based E-AB sensor. (**A**) Optimization of SWV measurement frequency and DNA immobilization concentration with a HEX backfill. Gain was determined based on signal generated in the absence or presence of 25 µM THC. (**B**) SWV and (**C**) signal gain from a calibration curve of THC in binding buffer. Inset shows the linear range of the sensor.

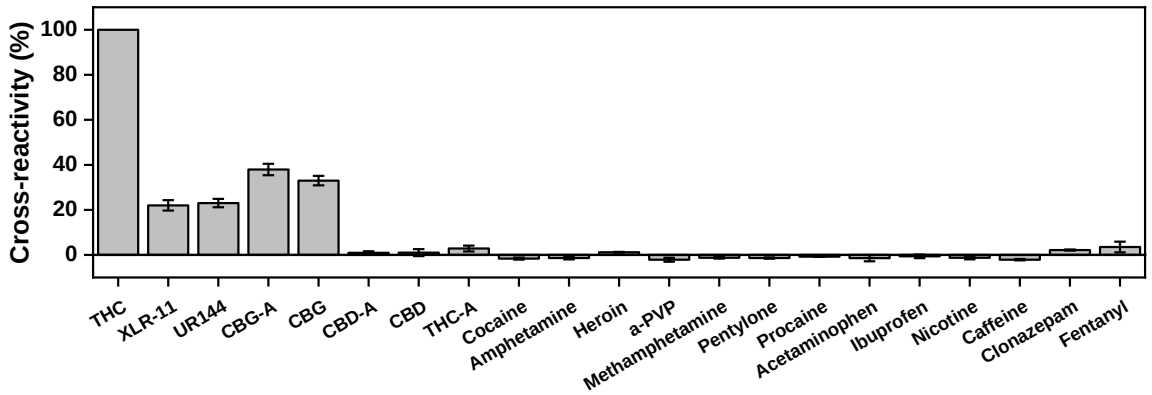

Figure 6-8. Specificity of TA-mut1-MB-based E-AB sensors. Sensors were screened against 10 µM THC, XLR-11, UR144, cannabigerolic acid (CBG-A), cannabigerol (CBG), cannabidiolic acid (CBD-A), cannabidiol (CBD), or tetrahydrocannabinolic acid (THC-A); 250 µM cocaine, amphetamine, heroin, α-PVP, (+)-methamphetamine, pentylone, procaine, acetaminophen, ibuprofen, nicotine, caffeine, or fentanyl; or 100 µM clonazepam. Cross-reactivity was calculated relative to 10 µM THC.

We then tested the specificity of the E-AB sensor against interferent compounds commonly encountered in seized substances, including other controlled substances (XLR-11, UR144, cocaine, amphetamine, heroin, α-PVP, (+)-methamphetamine, pentylone, clonazepam, and fentanyl), adulterants (procaine, acetaminophen, ibuprofen, nicotine, and caffeine), or natural cannabinoids (CBG, CBG-A, CBD, CBD-A, and THC-A). We observed little to no cross-reactivity from 16 out of 20 interferents (**Figure 6-8**). However, XLR-11, UR-144, CBG, and CBG-A demonstrated significant cross-reactivity (20–40%). This is problematic, as CBG and CBG-A can be present at high concentrations in marijuana extract samples. We have previously confirmed the specificity of the THC-binding parent aptamer using a dye-displacement assay, and observed no cross-reactivity to these molecules. Therefore, the signal seen here was most likely due to non-specific adsorption of these interferents onto the hydrophobic monolayer, which interferes with electron transfer between methylene blue and the electrode surface.

6.3.3. THC detection using E-AB sensors backfilled with hydrophilic monolayers.

Since the hydrophobic HEX monolayer was unfavorable for E-AB sensing, we selected three hydrophilic monolayers for further testing: MCH, MHA, and PEG. We began by optimizing our E-AB sensors using TA-39-MB, with the same workflow described above. With the MCH monolayer, the E-AB sensor modified using 150 nM TA-39-MB resulted in the greatest signal gain (41%) when detecting 10 µM THC with a measurement frequency of 1000 Hz (**Figure 6-9A**). We also obtained a maximal signal gain of 78% using 50 nM TA-39-MB backfilled with MHA with an 800 Hz measurement frequency, and a signal gain of 65% using 150 nM TA-39-MB backfilled with PEG with a 600 Hz measurement frequency (**Figure 6-9B & C**).

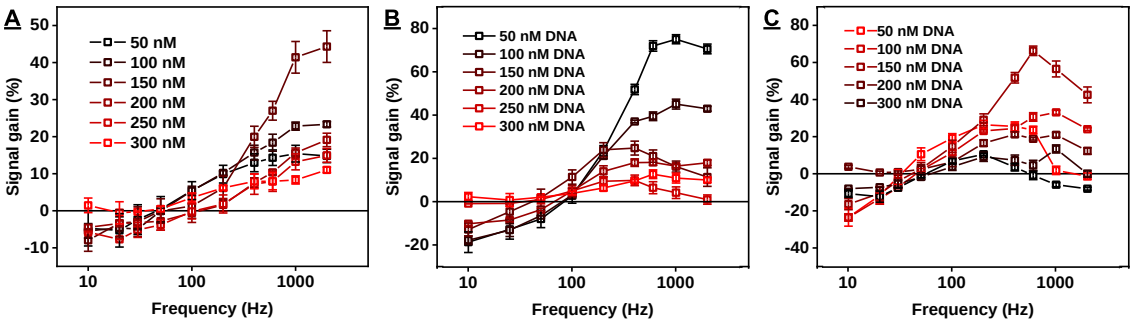

Figure 6-9. Detection of THC using TA-39-MB-based E-AB sensors backfilled with hydrophilic monolayers. Optimization of SWV measurement frequency and DNA immobilization concentration of sensors backfilled with (**A**) MCH, (**B**) MHA, or (**C**) PEG. Gain was measured based on signal generated in the absence and presence of 10 µM THC.

We then constructed calibration curves for detecting THC using the optimal conditions in binding buffer, 50% serum, and 50% saliva spiked with various concentrations of THC. Using the MCH monolayer, we observed significantly reduced signal gain in 50% saliva and 50% serum relative to buffer (**Figure 6-10A**). This is presumably due to the non-specific adsorption of matrix proteins onto the electrode surface.

The MHA monolayer yielded better sensing performance in 50% saliva relative to 50% serum (**Figure 6-10B**). In contrast, the PEG monolayer displayed roughly equivalent performance in both complex matrices (**Figure 6-10C**), and this is consistent with previous literature reporting the antifouling properties of PEG monolayers.[331–333]

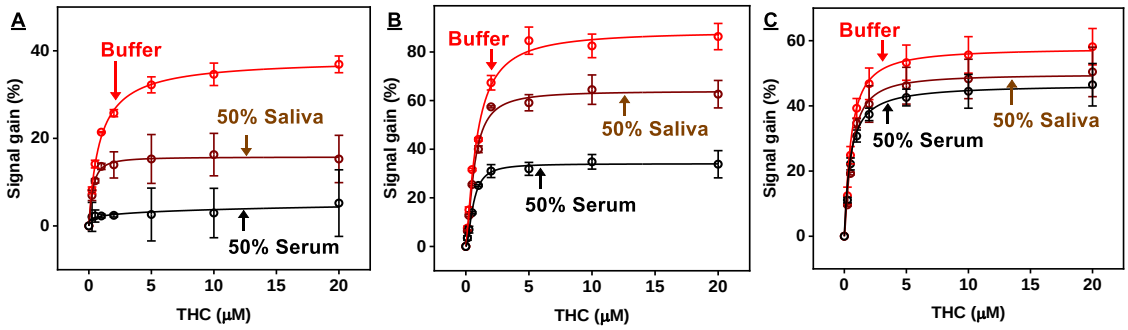

Figure 6-10. Performance of different E-AB hydrophilic monolayers in complex matrices. Calibration curves were constructed using (**A**) MCH-, (**B**) MHA-, and (**C**) PEG-backfilled electrodes based on detection in binding buffer, 50% saliva, or 50% serum. Signal gain was calculated using the following equation: $(I_{THC}-I_{Blank})/I_{Blank}\times100$, where I_{THC} is the peak current in the presence of THC, and I_{Blank} is the peak current in the absence of THC.

We observed that MHA-backfilled electrodes produce the highest signal gain for THC detection in buffer, but we faced challenges in the reproducible fabrication of such electrodes. Specifically, we observed that the optimal frequency for peak SWV measurement varied between 600–1,000 Hz across different electrodes (**Figure 6-11A**), indicating that the surface monolayer was not consistently uniform. We made two changes to the electrode immobilization procedure to overcome this issue. First, before aptamer immobilization, we heat-treated TA-39-MB at 95 °C for 10 mins, followed by snap cooling on ice for 1 min. We believed that this step would help denature aptamer aggregates present in the solution, allowing for more uniform immobilization onto the electrode surface. Second, during the backfilling step, we employed a high ionic strength solution (10 mM Tris–HCl, pH 7.4, 1 M NaCl, 1 mM $MgCl_2$) to shield the repulsion between surface-bound

MHA molecules, allowing them to pack more tightly. These measures resulted in a more reproducible frequency for peak SWV measurement at 600 Hz (**Figure 6-11B**). To confirm the actual signal gain from specific target binding, we attempted to regenerate the E-AB sensor by incubating the electrode in 6 M guanidinium HCl for 5 mins, followed by a DI water rinse for 1 min. However, we observed 20% signal gain even after extensive washing (**Figure 6-11C**), indicating the presence of defect that allow THC adsorption onto the sensor surface.

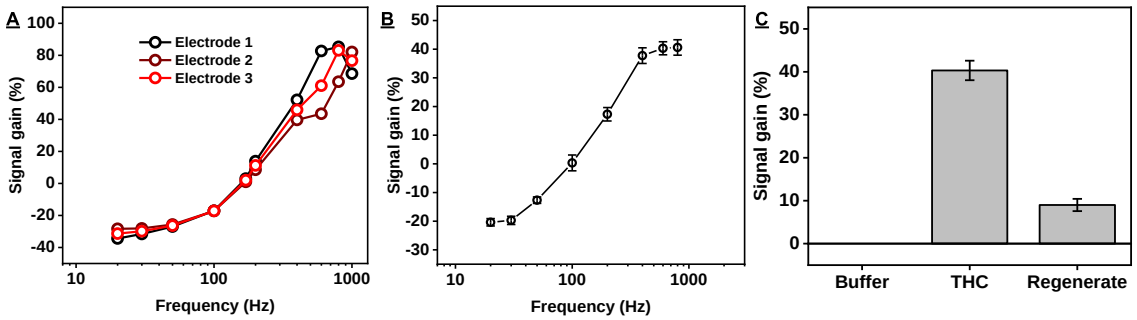

Figure 6-11. Testing E-AB sensors constructed with MHA monolayers. (**A**) Poor reproducibility of measurement frequency for peak SWV could be improved by (**B**) using a modified procedure with high ionic strength conditions. (**C**) Incomplete regeneration of MHA-backfilled E-AB sensors after incubating electrodes in 6 M guanidinium HCl for 5 mins, then washing with DI water for 1 min.

This poor regeneration may indicate that some THC molecules were nonspecifically adsorbed onto the MHA monolayer and could not be washed away. To confirm this, we measured the resistance of the electrode surface in the absence and presence of 25 µM THC using electrochemical impedance spectroscopy (EIS). EIS is a sensitive technique for determining the adsorption of molecules onto electrode surfaces. We performed measurements for electrodes backfilled with HEX (**Figure 6-12A**), MHA (**Figure 6-12B**), and PEG (**Figure 6-12C**). We observed a significant increase in electrochemical resistance for the HEX monolayer, indicating that a large quantity of THC

had adsorbed onto the hydrophobic backfiller. In contrast, electrodes backfilled with MHA had a moderate change in resistance, indicating lower levels of THC adsorption. PEG showed only a slight decrease in resistance, indicating that it adsorbs the least THC among the tested monolayers. These results confirmed that MHA alone is not a suitable backfill, where the repulsion between negatively-charged MHA molecules ultimately leads to small defects in the monolayer that can adsorb hydrophobic molecules and result in false-positive results.

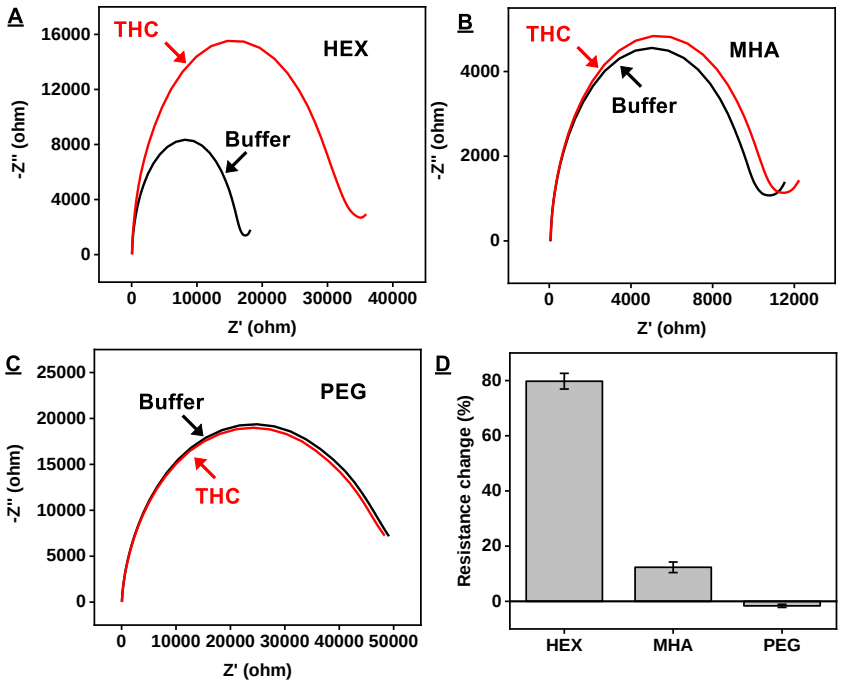

Figure 6-12. Determination of THC adsorption onto electrode surfaces modified with various backfillers. Electrochemical resistance measurements for electrodes backfilled with (**A**) HEX, (**B**) MHA, and (**C**) PEG in the absence and presence of 25 µM THC in binding buffer. (**D**) Summary of resistance change measurements due to THC adsorption.

Finally, we constructed a full calibration curve for THC using TA-39-MB-modified electrodes backfilled with PEG (**Figure 6-13A**). The electrode was then exposed to increasing concentrations of THC; upon reaching saturation, we regenerated it by

performing the guanidinium treatment described earlier. Based on the calibration curve, we achieved a detection limit of 100 nM in binding buffer (**Figure 6-13B**). The sensor remained challenging to regenerate, requiring two guanidinium treatments (**Figure 6-13A**). Moreover, the addition of saturating concentrations of THC initially only produced a half-maximal signal gain, and required exposure to a new THC solution to approach maximal signal gain. Both these behaviors are uncommon for E-AB sensors, which can generally be regenerated by rinsing with DI water without guanidinium treatment. This may indicate that THC is still nonspecifically adsorbing onto the monolayer surface. Moreover, using the same target preparation, regenerated E-AB sensors can reach maximal signal gain over several cycles. This may indicate that the current preparation procedure for THC is not stable and requires higher concentrations of organic solvent to prevent precipitation or aggregation of THC.

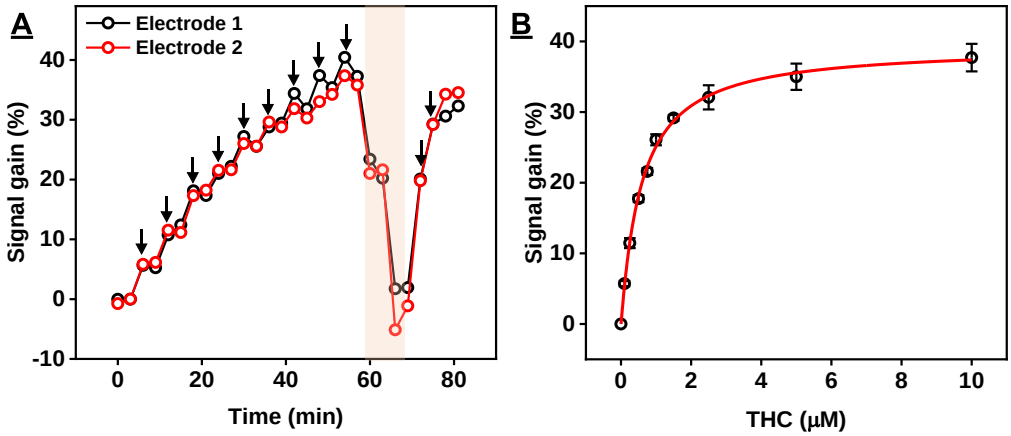

Figure 6-13. Detection of THC using electrodes immobilized with TA-39-MB and backfilled with PEG. (**A**) Time-course of THC detection. Arrows indicate spiking of THC into the binding buffer. The two regeneration steps areis highlighted in orange with the final concentration of THC being 10 µM. (**B**) Calibration curve constructed from data obtained with two electrodes.

6.3.4. Detection of THC spiked into marijuana placebo extract.

Finally, we tested the performance of the E-AB sensor in marijuana placebo extract. The extraction was performed by placing 50 mg homogenized marijuana placebo plant material suspended in 1 mL MeOH in an ultrasonic bath for 15 mins, followed by removal of the plant material using a 0.45 µM filter. We prepared various dilutions of this extract in binding buffer containing MeOH instead of DMSO. We observed that a minimum dilution of 200-fold was needed, as lower dilutions resulted in precipitation of the extract. Additionally, the extract produced a large background signal regardless of the dilution performed (**Figure 6-14A**). This background signal may be due to adsorption of fatty acids, esters, or other hydrophobic molecules extracted from the plant. To remedy this, we performed measurements of various placebo extracts in the presence of 0.01% Triton X-100, Tween-20, or SDS to aid in solubilizing hydrophobic molecules and thereby preventing their adsorption onto the electrode surface. We observed that measurements performed in the presence of 0.01% SDS resulted in minimal background signal from the placebo extract (**Figure 6-14A**). Thus, we constructed a calibration curve for THC spiked into 1,000-fold diluted extracts containing 0.01% SDS (**Figure 6-14B**), and observed a linear range of 50–800 nM with a measurable detection limit of 50 nM.

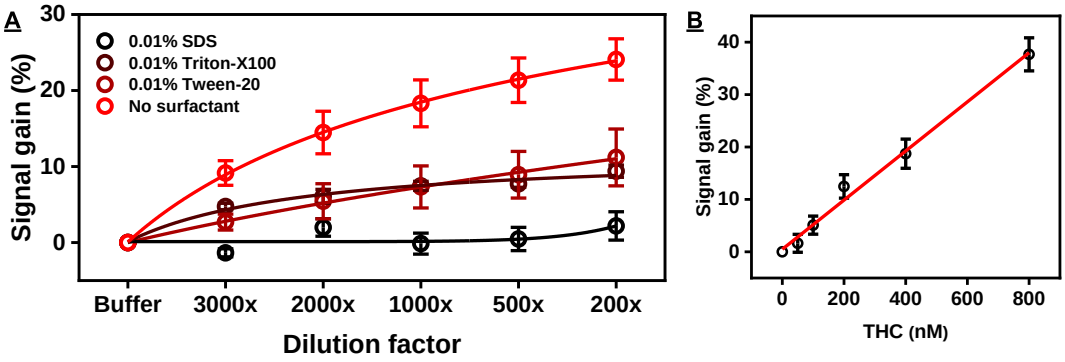

Figure 6-14. Detection of THC spiked into marijuana placebo extracts in MeOH in the presence of various surfactants. (**A**) Background signal observed over different dilution factors in the absence and presence of various surfactants. (**B**) Detection of spiked THC in 1,000-fold diluted marijuana placebo MeOH extract containing 0.01% SDS.

6.4. Conclusion.

This work utilized an exonuclease-assisted truncation strategy to rapidly engineer two THC-binding aptamers with structure-switching functionality. We engineered two additional aptamer mutants from one of these digestion products, measured the binding affinity of each truncated aptamer using ITC, and confirmed their structure-switching functionality using CD spectroscopy. Two of these aptamer candidates, TA-39 and TA-mut1, were employed to construct E-AB sensors to detect THC. We observed that hydrophobic monolayers are prone to absorbing hydrophobic molecules, which modulates the electron transfer rate of methylene blue to the electrode surface, resulting in false-positive signals. We therefore tested three different hydrophilic monolayers, MCH, MHA, and PEG. Although MCH is the most widely used monolayer for most E-AB sensors, we could not achieve satisfactory THC detection in complex matrices such as 50% saliva or 50% serum, and MHA and PEG demonstrated better performance. In particular, PEG exhibited consistent performance in both matrices and was not affected by the charge of the protein. Further testing revealed that some of the signal generated by E-AB sensors

constructed with MHA monolayers resulted from non-specific THC adsorption, which is presumably due to defects in the monolayer resulting from electrostatic repulsion between MHA molecules. We attempted to remedy this by using higher ionic strength conditions during the MHA backfilling step, but still observed a persistent ~20% background signal linked to THC adsorption. EIS measurements further confirmed these results, and revealed that PEG-backfilled electrodes had the lowest adsorption of THC among the tested monolayers. We therefore used E-AB sensors backfilled with PEG to detect THC spiked into marijuana placebo extract, achieving a detection limit of 50 nM. However, these sensors still have two unusual behaviors relative to other E-AB sensors. First, regeneration of these sensors was not achievable using DI water alone, and instead required harsh treatment with guanidinium. This is problematic, as this may indicate adsorption of THC that cannot be washed away. Moreover, saturating concentrations of THC after regeneration did not produce a maximal signal; instead, the sensor had to be reintroduced to a fresh solution of THC to reach maximal signal gain. This may indicate that the current preparation procedure for THC is not stable, and should be supplemented with higher concentrations of organic solvents or other molecules that prevent precipitation or aggregation. Based on these preliminary results, we plan to study other monolayers to identify those that are best at resisting adsorption by such low-solubility molecules. Moreover, we will explore other preparation methods of THC to ensure that it remains soluble during testing to obtain robust results.

CHAPTER 7: Summary and Future Work

7.1. Summary

Aptamers offer a variety of advantages over antibodies that make them promising alternative biorecognition elements for a variety of sensing applications such as clinical diagnostics, environmental monitoring, and food analysis. These include the customizability of the SELEX procedure, which allows for isolation of high-affinity aptamers that are tailored to function under various buffer conditions, ionic strengths, or organic co-solvents with desirable cross-reactivity and specificity. However, the aptamer selection process still faces several barriers that can stall the fabrication of aptamer-based sensors. SELEX yields hundreds or even thousands of candidates that must be carefully characterized to identify the optimal aptamer for particular application. This is especially challenging for small-molecule-binding aptamers, for which there is currently no high-throughput strategy for characterizing aptamer binding properties. Once the best aptamer has been identified, signal-reporting functionality must be introduced for sensor fabrication. This is a lengthy trial-and-error process requiring aptamer truncation or splitting to yield thermally destabilized aptamers that are unfolded at room temperature but fold in the presence of its target.

In Chapter 3, we showed that the binding of small-molecule targets to their respective aptamers can inhibit exonuclease digestion, and used this phenomenon to develop a simple exonuclease-based fluorescence assay for multiplexed target detection. In this assay, Exo III and Exo I progressively digest unbound aptamers into mononucleotides in a sequence-independent manner. Target-bound aptamers resist exonuclease digestion, resulting in partially-digested oligonucleotide products that can act as a readout for target detection by

using a variety of DNA detection strategies. Using the DNA-binding dye SYBR Gold, this assay provides a rapid and label-free detection strategy for small-molecule targets, even in complex matrices. Using DIS- and cocaine-binding aptamers as a demonstration, we obtained detection limits of 500 and 100 nM in 50% urine and 10% saliva, respectively, mirroring its performance in buffer. Alternatively, the use of sequence-specific molecular beacons allowed for simultaneous, multiplexed detection of cocaine and ATP in a single sample volume. Although the assay is not well suited for on-site detection in its current format, exonuclease-based fluorescence assays could offer a label-free and generalizable detection strategy for small-molecule targets in a laboratory testing environment.

In Chapter 4, we generalized this exonuclease-based fluorescence assay for characterizing the binding properties of small-molecule-binding aptamers and isolated aptamer candidates for a particular application in a high-throughput manner. Using a panel of mutants derived from the ochratoxin A-binding aptamer, we found a correlation between an aptamer's affinity for a ligand and the kinetics of aptamer digestion. Based on these findings, we tested our assay with 13 aptamer mutants derived from an ATP-binding aptamer and screened their affinities for ATP, ADP, AMP, and adenosine. We were able to identify two aptamers that preferentially bind adenosine over the other analogs. Additionally, the digestion products from these aptamers exhibited structure-switching functionality, and could be directly incorporated into folding-based sensing platforms. We demonstrated this by fabricating E-AB sensors using both structure-switching aptamers, enabling detection of adenosine at concentrations as low as 1 μM in 50% serum.

Based on these results, we further explored the relationship between aptamer-ligand binding affinity and the degree of enzymatic inhibition in Chapter 5. We performed three

independent SELEX experiments against fentanyl, acetyl fentanyl, and furanyl fentanyl, assessed the target-binding affinity of each aptamer against its respective target using our exonuclease-based fluorescence assay, and correlated the results with the gold-standard method ITC. We found a quantitative relationship between the degree of enzyme inhibition and the binding affinity of the structure-switching digestion product. We further screened aptamer candidates against fentanyl and 15 of its analogs as well as 19 interferent molecules, and validated the results using a strand-displacement fluorescence assay. Our screening process spanned a total of 655 aptamer-ligand pairs. As a demonstration, two of the structure-switching aptamers were incorporated into an E-AB sensor to fulfill different purposes; one was used to achieve sensitive detection of fentanyl in 50% saliva, whereas the second was used for highly cross-reactive detection of fentanyl and its analogs in seized substances.

Finally, as a further demonstration of the exonuclease-based fluorescence assay's capacity for identifying structure-switching aptamers for use in aptamer sensors, in Chapter 6, we digested a THC-binding aptamer and confirmed the structure-switching functionality of its digestion product. This digestion product was then incorporated into an E-AB sensor for detection of THC in plant extracts. After optimizing the measurement frequency and surface coverage of the E-AB sensor, we achieved a detection limit of 50 nM THC in 1,000-fold diluted placebo marijuana MeOH extract.

7.2. Future work

The work showcased in this dissertation highlights the strengths of the exonuclease-based fluorescence assay for aptamer characterization, engineering, and sensor development. Successful application of this assay has been demonstrated for a wide variety

of aptamers with different secondary structures and sequences, which is of importance when working with recently-isolated and completely uncharacterized aptamers. Moreover, the exonucleases employed in this assay demonstrated robust performance over a variety of buffer conditions, ionic strengths, and temperatures, further expanding this assay's potential utility. Although the screening of aptamer candidates and mutants in this work was performed with manual pipetting, the same task could easily be automated with a liquid-handling system to enable high-throughput screening of aptamer candidates. Based on the quantitative relationship established between each aptamer's structure-switching digestion product and the observed enzymatic inhibition, we have shown that we can predict the performance of folding-based sensors derived from that aptamer and thereby streamline the development of such sensors in a high-throughput and label-free manner.

REFERENCES

(1) Peltomaa, R.; Glahn-Martínez, B.; Benito-Peña, E.; Moreno-Bondi, M. C. Optical Biosensors for Label-Free Detection of Small Molecules. *Sensors* **2018**, *18*: 4126.

(2) Patel, S.; Nanda, R.; Sahoo, S.; Mohapatra, E. Biosensors in Health Care: The Milestones Achieved in Their Development towards Lab-on-Chip-Analysis. *Biochem. Res. Int.* **2016**, *2016*: 3130469.

(3) Nguyen, V.-T.; Kwon, Y. S.; Gu, M. B. Aptamer-Based Environmental Biosensors for Small Molecule Contaminants. *Curr. Opin. Biotechnol.* **2017**, *45*, 15–23.

(4) Bhalla, N.; Jolly, P.; Formisano, N.; Estrela, P. Introduction to Biosensors. *Essays Biochem.* **2016**, *60*, 1–8.

(5) Ham, B. M.; MaHam, A. *Analytical Chemistry: A Chemist and Laboratory Technician's Toolkit*; Wiley, **2015**.

(6) Metkar, S. K.; Girigoswami, K. Diagnostic Biosensors in Medicine – A Review. *Biocatal. Agric. Biotechnol.* **2019**, *17*, 271–283.

(7) Lee, T. M.-H. Over-the-Counter Biosensors: Past, Present, and Future. *Sensors* **2008**, *8*, 5535–5559.

(8) Conroy, P. J.; Hearty, S.; Leonard, P.; O'Kennedy, R. J. Antibody Production, Design and Use for Biosensor-Based Applications. *Semin. Cell Dev. Biol.* **2009**, *20*, 10–26.

(9) Rocchitta, G.; Spanu, A.; Babudieri, S.; Latte, G.; Madeddu, G.; Galleri, G.; Nuvoli, S.; Bagella, P.; Demartis, M. I.; Fiore, V.; Manetti, R.; Serra, P. A. Enzyme Biosensors for Biomedical Applications: Strategies for Safeguarding Analytical Performances in Biological Fluids. *Sensors* **2016**, *16*: 780.

(10) Gheorghiu, M. A Short Review on Cell-Based Biosensing: Challenges and Breakthroughs in Biomedical Analysis. *J. Biomed. Res.* **2021**, *35*, 255–263.

(11) Iliuk, A. B.; Hu, L.; Tao, W. A. Aptamer in Bioanalytical Applications. *Anal. Chem.* **2011**, *83*, 4440–4452.

(12) Howes, P. D.; Chandrawati, R.; Stevens, M. M. Colloidal Nanoparticles as Advanced Biological Sensors. *Science* **2014**, *346*: 1247390.

(13) Pohanka, M. The Piezoelectric Biosensors: Principles and Applications, a Review. *Int. J. Electrochem. Sci.* **2017**, *12*, 496–506.

(14) Ronkainen, N. J.; Halsall, H. B.; Heineman, W. R. Electrochemical Biosensors. *Chem. Soc. Rev.* **2010**, *39*, 1747–1763.

(15) Zhang, L.; Gu, C.; Ma, H.; Zhu, L.; Wen, J.; Xu, H.; Liu, H.; Li, L. Portable Glucose Meter: Trends in Techniques and Its Potential Application in Analysis. *Anal. Bioanal. Chem.* **2019**, *411*, 21–36.

(16) Yoo, E.-H.; Lee, S.-Y. Glucose Biosensors: An Overview of Use in Clinical Practice. *Sensors* **2010**, *10*, 4558–4576.

(17) Bahadir, E. B.; Sezgintürk, M. K. Applications of Commercial Biosensors in Clinical, Food, Environmental, and Biothreat/Biowarfare Analyses. *Anal. Biochem.* **2015**, *478*, 107–120.

(18) Orgel, L. E. Prebiotic Chemistry and the Origin of the RNA World. *Crit. Rev. Biochem. Mol. Biol.* **2010**, *39*, 99–123.

(19) Serganov, A.; Nudler, E. A Decade of Riboswitches. *Cell* **2013**, *152*, 17–24.

(20) Rinn, J. L.; Chang, H. Y. Genome Regulation by Long Noncoding RNAs. *Annu. Rev. Biochem.* **2012**, *81*, 145–166.

(21) Cech, T. R.; Steitz, J. A. The Noncoding RNA Revolution—Trashing Old Rules to Forge New Ones. *Cell* **2014**, *157*, 77–94.

(22) Tucker, B. J.; Breaker, R. R. Riboswitches as Versatile Gene Control Elements. *Curr. Opin. Struct. Biol.* **2005**, *15*, 342–348.

(23) Ellington, A. D.; Szostak, J. W. *In Vitro* Selection of RNA Molecules That Bind Specific Ligands. *Nature* **1990**, *346*, 818–822.

(24) Tuerk, C.; Gold, L. Systematic Evolution of Ligands by Exponential Enrichment: RNA Ligands to Bacteriophage T4 DNA Polymerase. *Science* **1990**, *249*, 505–510.

(25) Sanger, F.; Nicklen, S.; Coulson, A. R. DNA Sequencing with Chain-Terminating Inhibitors. *Proc. Natl. Acad. Sci. U. S. A.* **1977**, *74*, 5467.

(26) Oh, S. S.; Plakos, K.; Xiao, Y.; Eisenstein, M.; Soh, H. T. *In Vitro* Selection of Shape-Changing DNA Nanostructures Capable of Binding-Induced Cargo Release. *ACS Nano* **2013**, *7*, 9675–9683.

(27) Yang, K. A.; Barbu, M.; Halim, M.; Pallavi, P.; Kim, B.; Kolpashchikov, D. M.; Pecic, S.; Taylor, S.; Worgall, T. S.; Stojanovic, M. N. Recognition and Sensing of Low-Epitope Targets via Ternary Complexes with Oligonucleotides and Synthetic Receptors. *Nat. Chem.* **2014**, *6*, 1003–1008.

(28) Yang, K. A.; Pei, R.; Stefanovic, D.; Stojanovic, M. N. Optimizing Cross-Reactivity with Evolutionary Search for Sensors. *J. Am. Chem. Soc.* **2012**, *134*, 1642–1647.

(29) Jenison, R. D.; Gill, S. C.; Pardi, A.; Polisky, B. High-Resolution Molecular Discrimination by RNA. *Science* **1994**, *263*, 1425–1429.

(30) Qian, J.; Lou, X.; Zhang, Y.; Xiao, Y.; Tom Soh, H. Generation of Highly Specific Aptamers via Micromagnetic Selection. *Anal. Chem.* **2009**, *81*, 5490–5495.

(31) Lou, X.; Qian, J.; Xiao, Y.; Viel, L.; Gerdon, A. E.; Lagally, E. T.; Atzberger, P.; Tarasow, T. M.; Heeger, A. J.; Soh, H. T. Micromagnetic Selection of Aptamers in Microfluidic Channels. *Proc. Natl. Acad. Sci. U. S. A.* **2009**, *106*, 2989–2994.

(32) Dunn, M. R.; Jimenez, R. M.; Chaput, J. C. Analysis of Aptamer Discovery and Technology. *Nat. Rev. Chem.* **2017**, *1*: 0076.

(33) Jayasena, S. D. Aptamers: An Emerging Class of Molecules That Rival Antibodies in Diagnostics. *Clin. Chem.* **1999**, *45*, 1628–1650.

(34) Liu, J. K. H. The History of Monoclonal Antibody Development – Progress, Remaining Challenges and Future Innovations. *Ann. Med. Surg.* **2014**, *3*, 113–116.

(35) Ruscito, A.; DeRosa, M. C. Small-Molecule Binding Aptamers: Selection Strategies, Characterization, and Applications. *Front. Chem.* **2016**, *4*: 14.

(36) Yu, H.; Alkhamis, O.; Canoura, J.; Liu, Y.; Xiao, Y. Advances and Challenges in Small-Molecule DNA Aptamer Isolation, Characterization, and Sensor Development. *Angew. Chem., Int. Ed.* **2021**, *60*, 16800–16823.

(37) Yang, K. A.; Pei, R.; Stojanovic, M. N. *In Vitro* Selection and Amplification Protocols for Isolation of Aptameric Sensors for Small Molecules. *Methods* **2016**, *106*, 58–65.

(38) Wang, Y.; Killian, J.; Hamasaki, K.; Rando, R. R. RNA Molecules That Specifically and Stoichiometrically Bind Aminoglycoside Antibiotics with High Affinities. *Biochemistry* **1996**, *35*, 12338–12346.

(39) Mann, D.; Reinemann, C.; Stoltenburg, R.; Strehlitz, B. *In Vitro* Selection of DNA Aptamers Binding Ethanolamine. *Biochem. Biophys. Res. Commun.* **2005**, *338*, 1928–1934.

(40) Famulok, M. Molecular Recognition of Amino Acids by RNA-Aptamers: An L-Citrulline Binding RNA Motif and Its Evolution into an L-Arginine Binder. *J. Am. Chem. Soc.* **1994**, *116*, 1698–1706.

(41) Lauhon, C. T.; Szostak, J. W. RNA Aptamers That Bind Flavin and Nicotinamide Redox. *J. Am. Chem. Soc* **1995**, *117*, 1246–1257.

(42) Walker, J. M.; Gaastra, W. *Methods in Molecular Biology*; Springer, **2012**.

(43) Ozer, A.; Pagano, J. M.; Lis, J. T. New Technologies Provide Quantum Changes in the Scale, Speed, and Success of SELEX Methods and Aptamer Characterization. *Mol. Ther. --Nucleic Acids* **2014**, *3*, e183.

(44) Cao, F.; Lu, X.; Hu, X.; Zhang, Y.; Zeng, L.; Chen, L.; Sun, M. *In Vitro* Selection of DNA Aptamers Binding Pesticide Fluoroacetamide. *Biosci., Biotechnol., Biochem.* **2016**, *80*, 823–832.

(45) McKeague, M.; Bradley, C. R.; de Girolamo, A.; Visconti, A.; David Miller, J.; DeRosa, M. C. Screening and Initial Binding Assessment of Fumonisin B1 Aptamers. *Int. J. Mol. Sci.* **2010**, *11*, 4864–4881.

(46) Kim, Y. S.; Hyun, C. J.; Kim, I. A.; Gu, M. B. Isolation and Characterization of Enantioselective DNA Aptamers for Ibuprofen. *Bioorg. Med. Chem.* **2010**, *18*, 3467–3473.

(47) Hermanson, G. T. *Bioconjugate Techniques*, 3rd ed.; Elsevier, 2013.

(48) Rosenthal, M.; Pfeiffer, F.; Mayer, G. A Receptor-Guided Design Strategy for Ligand Identification. *Angew. Chem., Int. Ed.* **2019**, *58*, 10752–10755.

(49) Jauset-Rubio, M.; Luz Botero, M.; Skouridou, V.; Betu, lsen; Svobodova, M.; Bashammakh, A. S.; El-Shahawi, M. S.; Alyoubi, A. O.; O'Sullivan, C. K. One-Pot SELEX: Identification of Specific Aptamers against Diverse Steroid Targets in One Selection. *ACS Omega* **2019**, *4*, 20188–20196.

(50) McKeague, M.; DeRosa, M. C. Challenges and Opportunities for Small Molecule Aptamer Development. *J. Nucleic Acids* **2012**, *2012*: 748913.

(51) Ding, Y.; Liu, X.; Huang, P.-J. J.; Liu, J. Homogeneous Assays for Aptamer-Based Ethanolamine Sensing: No Indication of Target Binding. *Analyst* **2022**, *147*, 1348–1356.

(52) Lyu, C.; Khan, I. M.; Wang, Z. Capture-SELEX for Aptamer Selection: A Short Review. *Talanta* **2021**, *229*: 122274.

(53) Hofmann, K.; Titus, G.; Montibeller, J. A.; Finn, F. M. Avidin Binding of Carboxyl-Substituted Biotin and Analogues. *Biochemistry* **1982**, *21*, 978–984.

(54) Nutiu, R.; Li, Y. *In Vitro* Selection of Structure-Switching Signaling Aptamers. *Angew. Chem., Int. Ed.* **2005**, *44*, 1061–1065.

(55) Munzar, J. D.; Ng, A.; Juncker, D. Comprehensive Profiling of the Ligand Binding Landscapes of Duplexed Aptamer Families Reveals Widespread Induced Fit. *Nat. Commun.* **2018**, *9*, 343.

(56) Yang, K. A.; Chun, H.; Zhang, Y.; Pecic, S.; Nakatsuka, N.; Andrews, A. M.; Worgall, T. S.; Stojanovic, M. N. High-Affinity Nucleic-Acid-Based Receptors for Steroids. *ACS Chem. Biol.* **2017**, *12*, 3103–3112.

(57) Nakatsuka, N.; Yang, K.-A.; Abendroth, J. M.; Cheung, K. M.; Xu, X.; Yang, H.; Zhao, C.; Zhu, B.; Rim, Y. S.; Yang, Y.; Weiss, P. S.; Stojanović, M. N.; Andrews, A. M. Aptamer–Field-Effect Transistors Overcome Debye Length Limitations for Small-Molecule Sensing. *Science* **2018**, *362*, 319–324.

(58) Xiao, Y.; Yu, H.; Luo, Y.; Alkhamis, O.; Canoura, J.; Yu, B. Isolation of Natural DNA Aptamers for Challenging Small-Molecule Targets, Cannabinoids. *Anal. Chem.* **2021**, *93*, 3172–3180.

(59) Mendonsa, S. D.; Bowser, M. T. *In Vitro* Selection of High-Affinity DNA Ligands for Human IgE Using Capillary Electrophoresis. *Anal. Chem.* **2004**, *76*, 5387–5392.

(60) Mosing, R. K.; Mendonsa, S. D.; Bowser, M. T. Capillary Electrophoresis-SELEX Selection of Aptamers with Affinity for HIV-1 Reverse Transcriptase. *Anal. Chem.* **2005**, *77*, 6107–6112.

(61) Yang, J.; Bowser, M. T. Capillary Electrophoresis-SELEX Selection of Catalytic DNA Aptamers for a Small-Molecule Porphyrin Target. *Anal. Chem.* **2013**, *85*, 1525–1530.

(62) Chen, X.; Huang, Y.; Duan, N.; Wu, S.; Xia, Y.; Ma, X.; Zhu, C.; Jiang, Y.; Wang, Z. Screening and Identification of DNA Aptamers against T-2 Toxin Assisted by Graphene Oxide. *J. Agric. Food Chem.* **2014**, *62*, 10368–10374.

(63) Park, J. W.; Tatavarty, R.; Kim, D. W.; Jung, H. T.; Gu, M. B. Immobilization-Free Screening of Aptamers Assisted by Graphene Oxide. *Chem. Commun.* **2012**, *48*, 2071–2073.

(64) Wu, M.; Kempaiah, R.; Huang, P. J. J.; Maheshwari, V.; Liu, J. Adsorption and Desorption of DNA on Graphene Oxide Studied by Fluorescently Labeled Oligonucleotides. *Langmuir* **2011**, *27*, 2731–2738.

(65) Gu, H.; Duan, N.; Wu, S.; Hao, L.; Xia, Y.; Ma, X.; Wang, Z. Graphene Oxide-Assisted Non-Immobilized SELEX of Okdaic Acid Aptamer and the Analytical Application of Aptasensor. *Sci. Rep.* **2016**, *6*: 21665.

(66) Nguyen, V. T.; Kwon, Y. S.; Kim, J. H.; Gu, M. B. Multiple GO-SELEX for Efficient Screening of Flexible Aptamers. *Chem. Commun.* **2014**, *50*, 10513–10516.

(67) Sanford, A. A.; Rangel, A. E.; Feagin, T. A.; Lowery, R. G.; Argueta-Gonzalez, H. S.; Heemstra, J. M. RE-SELEX: Restriction Enzyme-Based Evolution of Structure-Switching Aptamer Biosensors. *Chem. Sci.* **2021**, *12*, 11692–11702.

(68) Polisky, B.; Greene, P.; Garfin, D. E.; McCarthy, B. J.; Goodman, H. M.; Boyer, H. W. Specificity of Substrate Recognition by the EcoRI Restriction Endonuclease. *Proc. Natl. Acad. Sci. U. S. A.* **1975**, *72*, 3310–3314.

(69) Cho, M.; Xiao, Y.; Nie, J.; Stewart, R.; Csordas, A. T.; Oh, S. S.; Thomson, J. A.; Soh, H. T. Quantitative Selection of DNA Aptamers through Microfluidic Selection and High-Throughput Sequencing. *Proc. Natl. Acad. Sci. U. S. A.* **2010**, *107*, 15373–15378.

(70) Schütze, T.; Wilhelm, B.; Greiner, N.; Braun, H.; Peter, F.; Mörl, M.; Erdmann, V. A.; Lehrach, H.; Konthur, Z.; Menger, M.; Arndt, P. F.; Glökler, J. Probing the SELEX Process with Next-Generation Sequencing. *PLoS One* **2011**, *6*: e29604.

(71) Polz, M. F.; Cavanaugh, C. M. Bias in Template-to-Product Ratios in Multitemplate PCR. *Appl. Environ. Microbiol.* **1998**, *64*, 3724–3730.

(72) Kanagawa, T. Bias and Artifacts in Multitemplate Polymerase Chain Reactions (PCR). *J. Biosci. Bioeng.* **2003**, *96*, 317–323.

(73) Klug, S. J.; Famulok, M. All You Wanted to Know about SELEX. *Mol. Biol. Rep.* **1994**, *20*, 97–107.

(74) Berens, C.; Thain, A.; Schroeder, R. A Tetracycline-Binding RNA Aptamer. *Bioorg. Med. Chem.* **2001**, *9*, 2549–2556.

(75) Reuss, A. J.; Vogel, M.; Weigand, J. E.; Suess, B.; Wachtveitl, J. Tetracycline Determines the Conformation of Its Aptamer at Physiological Magnesium Concentrations. *Biophys. J.* **2014**, *107*, 2962–2971.

(76) Shtatland, T.; Gill, S. C.; Javornik, B. E.; Johansson, H. E.; Singer, B. S.; Uhlenbeck, O. C.; Zichi, D. A.; Gold, L. Interactions of *Escherichia Coli* RNA with Bacteriophage MS2 Coat Protein: Genomic SELEX. *Nucleic Acids Res.* **2000**, *28*: e93.

(77) Cowan, J. A.; Ohyama, T.; Wang, D.; Natarajan, K. Recognition of a Cognate RNA Aptamer by Neomycin B: Quantitative Evaluation of Hydrogen Bonding and Electrostatic Interactions. *Nucleic Acids Res.* **2000**, *28*, 2935–2942.

(78) Ladbury', J. E.; Chowdhrv2, B. Z. Sensing the Heat: The Application of Isothermal Titration Calorimetry to Thermodynamic Studies of Biomolecular Interactions. *Chem. Biol.* **1996**, *3*, 791–801.

(79) Slavkovic, S.; Johnson, P. E. Isothermal Titration Calorimetry Studies of Aptamer-Small Molecule Interactions: Practicalities and Pitfalls. *Aptamer* **2018**, *2*, 45–51.

(80) Baaske, P.; Wienken, C. J.; Reineck, P.; Duhr, S.; Braun, D. Optical Thermophoresis for Quantifying the Buffer Dependence of Aptamer Binding. *Angew. Chem., Int. Ed.* **2010**, *49*, 2238–2241.

(81) Duhr, S.; Braun, D. Why Molecules Move along a Temperature Gradient. *Proc. Natl. Acad. Sci. U. S. A.* **2006**, *103*, 19678–19682.

(82) Braun, D.; Libchaber, A. Trapping of DNA by Thermophoretic Depletion and Convection. *Phys. Rev. Lett.* **2002**, *89*: 188103.

(83) Entzian, C.; Schubert, T. Studying Small Molecule–Aptamer Interactions Using MicroScale Thermophoresis (MST). *Methods* **2016**, *97*, 27–34.

(84) Rangel, A. E.; Chen, Z.; Ayele, T. M.; Heemstra, J. M. *In Vitro* Selection of an XNA Aptamer Capable of Small-Molecule Recognition. *Nucleic Acids Res.* **2018**, *46*, 8057–8068.

(85) Chang, A. L.; McKeague, M.; Smolke, C. D. Facile Characterization of Aptamer Kinetic and Equilibrium Binding Properties Using Surface Plasmon Resonance. *Methods Enzymol.* **2014**, *549*, 451–466.

(86) Chang, A. L.; McKeague, M.; Liang, J. C.; Smolke, C. D. Kinetic and Equilibrium Binding Characterization of Aptamers to Small Molecules Using a Label-Free, Sensitive, and Scalable Platform. *Anal. Chem.* **2014**, *86*, 3273–3278.

(87) Win, M. N.; Klein, J. S.; Smolke, C. D. Codeine-Binding RNA Aptamers and Rapid Determination of Their Binding Constants Using a Direct Coupling Surface Plasmon Resonance Assay. *Nucleic Acids Res.* **2006**, *34*, 5670–5682.

(88) Hu, J.; Easley, C. J. A Simple and Rapid Approach for Measurement of Dissociation Constants of DNA Aptamers against Proteins and Small Molecules via Automated Microchip Electrophoresis. *Analyst* **2011**, *136*, 3461–3468.

(89) Alkhamis, O.; Yang, W.; Farhana, R.; Yu, H.; Xiao, Y. Label-Free Profiling of DNA Aptamer-Small Molecule Binding Using T5 Exonuclease. *Nucleic Acids Res.* **2020**, *48*: e120.

(90) Travascio, P.; Li, Y.; Sen, D. DNA-Enhanced Peroxidase Activity of a DNA Aptamer-Hemin Complex. *Chem. Biol.* **1998**, *5*, 505–517.

(91) Lauhon, C. T.; Szostak, J. W. RNA Aptamers That Bind Flavin and Nicotinamide Redox. *J. Am. Chem. Soc* **1995**, *117*, 1246–1257.

(92) Shoara, A. A.; Slavkovic, S.; Donaldson, L. W.; Johnson, P. E. Analysis of the Interaction between the Cocaine-Binding Aptamer and Its Ligands Using Fluorescence Spectroscopy. *Can. J. Chem.* **2017**, *95*, 1253–1260.

(93) Samokhvalov, A. v.; Safenkova, I. v.; Zherdev, A. v.; Dzantiev, B. B. The Registration of Aptamer–Ligand (Ochratoxin A) Interactions Based on Ligand Fluorescence Changes. *Biochem. Biophys. Res. Commun.* **2018**, *505*, 536–541.

(94) Paige, J. S.; Wu, K. Y.; Jaffrey, S. R. RNA Mimics of Green Fluorescent Protein. *Science* **2011**, *333*, 642–646.

(95) Tan, X.; Constantin, T. P.; Sloane, K. L.; Waggoner, A. S.; Bruchez, M. P.; Armitage, B. A. Fluoromodules Consisting of a Promiscuous RNA Aptamer and Red or Blue Fluorogenic Cyanine Dyes: Selection, Characterization, and Bioimaging. *J. Am. Chem. Soc.* **2017**, *139*, 9001–9009.

(96) Sassanfar, M.; Szostak, J. W. An RNA Motif That Binds ATP. *Nature* **1993**, *364*, 550–553.

(97) Tao, J.; Frankel, A. D. Arginine-Binding RNAs Resembling TAR Identified by *In Vitro* Selection. *Biochemistry* **1996**, *35*, 2229–2238.

(98) Huizenga, D. E.; Szostak, J. W. A DNA Aptamer That Binds Adenosine and ATP. *Biochemistry* **1995**, *34*, 656–665.

(99) Thiel, W. H.; Bair, T.; Wyatt Thiel, K.; Dassie, J. P.; Rockey, W. M.; Howell, C. A.; Liu, X. Y.; Dupuy, A. J.; Huang, L.; Owczarzy, R.; Behlke, M. A.; McNamara, J. O.; Giangrande, P. H. Nucleotide Bias Observed with a Short SELEX RNA Aptamer Library. *Nucleic Acid Ther.* **2011**, *21*, 253–263.

(100) Takahashi, M.; Wu, X.; Ho, M.; Chomchan, P.; Rossi, J. J.; Burnett, J. C.; Zhou, J. High Throughput Sequencing Analysis of RNA Libraries Reveals the Influences of Initial Library and PCR Methods on SELEX Efficiency. *Sci. Rep.* **2016**, *6*: 33697.

(101) Levay, A.; Brenneman, R.; Hoinka, J.; Sant, D.; Cardone, M.; Trinchieri, G.; Przytycka, T. M.; Berezhnoy, A. Identifying High-Affinity Aptamer Ligands with Defined Cross-Reactivity Using High-Throughput Guided Systematic Evolution of Ligands by Exponential Enrichment. *Nucleic Acids Res.* **2015**, *43*: e82.

(102) Bartel, D. P.; Zapp, M. L.; Green, M. R.; Szostak, J. W. HIV-1 Rev Regulation Involves Recognition of Non-Watson-Crick Base Pairs in Viral RNA. *Cell* **1991**, *67*, 529–536.

(103) Neves, M. A. D.; Reinstein, O.; Saad, M.; Johnson, P. E. Defining the Secondary Structural Requirements of a Cocaine-Binding Aptamer by a Thermodynamic and Mutation Study. *Biophys. Chem.* **2010**, *153*, 9–16.

(104) Autour, A.; Westhof, E.; Ryckelynck, M. iSpinach: A Fluorogenic RNA Aptamer Optimized for *In Vitro* Applications. *Nucleic Acids Res.* **2016**, *44*, 2491–2500.

(105) Jimenez, J. I.; Xulvi-Brunet, R.; Campbell, G. W.; Turk-Macleod, R.; Chen, I. A. Comprehensive Experimental Fitness Landscape and Evolutionary Network for Small RNA. *Proc. Nat. Acad. Sci. U. S. A.* **2013**, *110*, 14984–14989.

(106) Knight, R.; Yarus, M. Analyzing Partially Randomized Nucleic Acid Pools: Straight Dope on Doping. *Nucleic Acids Res.* **2003**, *31*: e30.

(107) Nonaka, Y.; Yoshida, W.; Abe, K.; Ferri, S.; Schulze, H.; Bachmann, T. T.; Ikebukuro, K. Affinity Improvement of a VEGF Aptamer by in Silico Maturation for a Sensitive VEGF-Detection System. *Anal. Chem.* **2013**, *85*, 1132–1137.

(108) Roncancio, D.; Yu, H.; Xu, X.; Wu, S.; Liu, R.; Debord, J.; Lou, X.; Xiao, Y. A Label-Free Aptamer-Fluorophore Assembly for Rapid and Specific Detection of Cocaine in Biofluids. *Anal. Chem.* **2014**, *86*, 11100–11106.

(109) Zhang, Z.; Oni, O.; Liu, J. New Insights into a Classic Aptamer: Binding Sites, Cooperativity and More Sensitive Adenosine Detection. *Nucleic Acids Res.* **2017**, *45*, 7593–7601.

(110) Xu, G.; Zhao, J.; Liu, N.; Yang, M.; Zhao, Q.; Li, C.; Liu, M. Structure-Guided Post-SELEX Optimization of an Ochratoxin A Aptamer. *Nucleic Acids Res.* **2019**, *47*, 5963–5972.

(111) Biniuri, Y.; Albada, B.; Willner, I. Probing ATP/ATP-Aptamer or ATP-Aptamer Mutant Complexes by Microscale Thermophoresis and Molecular Dynamics Simulations: Discovery of an ATP-Aptamer Sequence of Superior Binding Properties. *J. Phys. Chem. B* **2018**, *122*, 9102–9109.

(112) Zheng, X.; Hu, B.; Gao, S. X.; Liu, D. J.; Sun, M. J.; Jiao, B. H.; Wang, L. H. A Saxitoxin-Binding Aptamer with Higher Affinity and Inhibitory Activity Optimized by Rational Site-Directed Mutagenesis and Truncation. *Toxicon* **2015**, *101*, 41–47.

(113) Han, K.; Liang, Z.; Zhou, N. Design Strategies for Aptamer-Based Biosensors. *Sensors* **2010**, *10*, 4541–4557.

(114) Stojanovic, M. N.; de Prada, P.; Landry, D. W. Aptamer-Based Folding Fluorescent Sensor for Cocaine. *J. Am. Chem. Soc.* **2001**, *123*, 4928–4931.

(115) Zhao, W.; Chiuman, W.; Lam, J. C. F.; McManus, S. A.; Chen, W.; Cui, Y.; Pelton, R.; Brook, M. A.; Li, Y. DNA Aptamer Folding on Gold Nanoparticles: From Colloid Chemistry to Biosensors. *J. Am. Chem. Soc.* **2008**, *130*, 3610–3618.

(116) Xiao, Y.; Lubin, A. A.; Heeger, A. J.; Plaxco, K. W. Label-Free Electronic Detection of Thrombin in Blood Serum by Using an Aptamer-Based Sensor. *Angew. Chem., Int. Ed.* **2005**, *117*, 5592–5595.

(117) Baker, B. R.; Lai, R. Y.; Wood, M. S.; Doctor, E. H.; Heeger, A. J.; Plaxco, K. W. An Electronic, Aptamer-Based Small-Molecule Sensor for the Rapid, Label-Free Detection of Cocaine in Adulterated Samples and Biological Fluids. *J. Am. Chem. Soc.* **2006**, *128*, 3138–3139.

(118) Ozaki, H.; Nishihira, A.; Wakabayashi, M.; Kuwahara, M.; Sawai, H. Biomolecular Sensor Based on Fluorescence-Labeled Aptamer. *Bioorg. Med. Chem. Lett.* **2006**, *16*, 4381–4384.

(119) Urata, H.; Nomura, K.; Wada, S. ichi; Akagi, M. Fluorescent-Labeled Single-Strand ATP Aptamer DNA: Chemo- and Enantio-Selectivity in Sensing Adenosine. *Biochem. Biophys. Res. Commun.* **2007**, *360*, 459–463.

(120) Ferguson, B. S.; Hoggarth, D. A.; Maliniak, D.; Ploense, K.; White, R. J.; Woodward, N.; Hsieh, K.; Bonham, A. J.; Eisenstein, M.; Kippin, T. E.; Plaxco, K. W.; Soh, H. T. Real-Time, Aptamer-Based Tracking of Circulating Therapeutic Agents in Living Animals. *Sci. Transl. Med.* **2013**, *5*: 213ra165.

(121) Li, H.; Somerson, J.; Xia, F.; Plaxco, K. W. Electrochemical DNA-Based Sensors for Molecular Quality Control: Continuous, Real-Time Melamine Detection in Flowing Whole Milk. *Anal. Chem.* **2018**, *90*, 10641–10645.

(122) Somerson, J.; Plaxco, K. W. Electrochemical Aptamer-Based Sensors for Rapid Point-of-Use Monitoring of the Mycotoxin Ochratoxin A Directly in a Food Stream. *Molecules* **2018**, *23*: 912.

(123) Santos-Cancel, M.; Simpson, L. W.; Leach, J. B.; White, R. J. Direct, Real-Time Detection of Adenosine Triphosphate Release from Astrocytes in Three-Dimensional Culture Using an Integrated Electrochemical Aptamer-Based Sensor. *ACS Chem. Neurosci.* **2019**, *10*, 2070–2079.

(124) Neves, M. A. D.; Reinstein, O.; Johnson, P. E. Defining a Stem Length-Dependent Binding Mechanism for the Cocaine-Binding Aptamer. A Combined NMR and Calorimetry Study. *Biochemistry* **2010**, *49*, 8478–8487.

(125) White, R. J.; Rowe, A. A.; Plaxco, K. W. Re-Engineering Aptamers to Support Reagentless, Self-Reporting Electrochemical Sensors. *Analyst* **2010**, *135*, 589–594.

(126) Chen, A.; Yan, M.; Yang, S. Split Aptamers and Their Applications in Sandwich Aptasensors. *TrAC- Trends Anal. Chem.* **2016**, *80*, 581–593.

(127) Stojanovic, M. N.; de Prada, P.; Landry, D. W. Fluorescent Sensors Based on Aptamer Self-Assembly. *J. Am. Chem. Soc.* **2000**, *122*, 11547–11548.

(128) Zou, R.; Lou, X.; Ou, H.; Zhang, Y.; Wang, W.; Yuan, M.; Guan, M.; Luo, Z.; Liu, Y. Highly Specific Triple-Fragment Aptamer for Optical Detection of Cocaine. *RSC Adv.* **2012**, *2*, 4636–4638.

(129) Freeman, R.; Sharon, E.; Ran, T. V.; Willner, I. Supramolecular Cocaine-Aptamer Complexes Activate Biocatalytic Cascades. *J. Am. Chem. Soc.* **2009**, *131*, 5028–5029.

(130) Zhao, T.; Liu, R.; Ding, X.; Zhao, J.; Yu, H.; Wang, L.; Xu, Q.; Wang, X.; Lou, X.; He, M.; Xiao, Y. Nanoprobe-Enhanced, Split Aptamer-Based Electrochemical Sandwich Assay for Ultrasensitive Detection of Small Molecules. *Anal. Chem.* **2015**, *87*, 7712–7719.

(131) Kent, A. D.; Spiropulos, N. G.; Heemstra, J. M. General Approach for Engineering Small-Molecule-Binding DNA Split Aptamers. *Anal. Chem.* **2013**, *85*, 9916–9923.

(132) Bing, T.; Zheng, W.; Zhang, X.; Shen, L.; Liu, X.; Wang, F.; Cui, J.; Cao, Z.; Shangguan, D. Triplex-Quadruplex Structural Scaffold: A New Binding Structure of Aptamer. *Sci. Rep.* **2017**, *7*, 15467.

(133) Zuo, X.; Xiao, Y.; Plaxco, K. W. High Specificity, Electrochemical Sandwich Assays Based on Single Aptamer Sequences and Suitable for the Direct Detection of Small-Molecule Targets in Blood and Other Complex Matrices. *J. Am. Chem. Soc.* **2009**, *131*, 6944–6945.

(134) Sharma, A. K.; Kent, A. D.; Heemstra, J. M. Enzyme-Linked Small-Molecule Detection Using Split Aptamer Ligation. *Anal. Chem.* **2012**, *84*, 6104–6109.

(135) Sharma, A. K.; Heemstra, J. M. Small-Molecule-Dependent Split Aptamer Ligation. *J. Am. Chem. Soc.* **2011**, *133*, 12426–12429.

(136) Yu, H.; Canoura, J.; Guntupalli, B.; Lou, X.; Xiao, Y. A Cooperative-Binding Split Aptamer Assay for Rapid, Specific and Ultra-Sensitive Fluorescence Detection of Cocaine in Saliva. *Chem. Sci.* **2016**, *8*, 131–141.

(137) Weiss, J. N. The Hill Equation Revisited: Uses and Misuses. *FASEB J.* **1997**, *11*, 835–841.

(138) Yu, H.; Canoura, J.; Guntupalli, B.; Alkhamis, O.; Xiao, Y. Sensitive Detection of Small-Molecule Targets Using Cooperative Binding Split Aptamers and Enzyme-Assisted Target Recycling. *Anal. Chem.* **2018**, *90*, 1748–1758.

(139) Liang, P.; Canoura, J.; Yu, H.; Alkhamis, O.; Xiao, Y. Dithiothreitol-Regulated Coverage of Oligonucleotide-Modified Gold Nanoparticles to Achieve Optimized Biosensor Performance. *ACS Appl. Mat. Interfaces* **2018**, *10*, 4233–4242.

(140) Luo, Y.; Yu, H.; Alkhamis, O.; Liu, Y.; Lou, X.; Yu, B.; Xiao, Y. Label-Free, Visual Detection of Small Molecules Using Highly Target-Responsive Multimodule Split Aptamer Constructs. *Anal. Chem.* **2019**, *91*, 7199–7207.

(141) Dai, Y.; Furst, A.; Liu, C. C. Strand Displacement Strategies for Biosensor Applications. *Trends Biotechnol.* **2019**, *37*, 1367–1382.

(142) Nutiu, R.; Li, Y. Structure-Switching Signaling Aptamers. *J. Am. Chem. Soc.* **2003**, *125*, 4771–4778.

(143) Tang, Z.; Mallikaratchy, P.; Yang, R.; Kim, Y.; Zhu, Z.; Wang, H.; Tan, W. Aptamer Switch Probe Based on Intramolecular Displacement. *J. Am. Chem. Soc.* **2008**, *130*, 11268–11269.

(144) Thompson, I. A. P.; Zheng, L.; Eisenstein, M.; Soh, H. T. Rational Design of Aptamer Switches with Programmable PH Response. *Nat. Commun.* **2020**, *11*: 2946.

(145) Day, H. A.; Pavlou, P.; Waller, Z. A. E. I-Motif DNA: Structure, Stability and Targeting with Ligands. *Bioorg. Med. Chem.* **2014**, *22*, 4407–4418.

(146) Stojanovic, M. N.; Landry, D. W. Aptamer-Based Colorimetric Probe for Cocaine. *J. Am. Chem. Soc.* **2002**, *124*, 9678–9679.

(147) Alkhamis, O.; Canoura, J.; Bukhryakov, K. v.; Tarifa, A.; DeCaprio, A. P.; Xiao, Y. DNA Aptamer–Cyanine Complexes as Generic Colorimetric Small-Molecule Sensors. *Angew. Chem., Int. Ed.* **2022**, *61*: e202112305.

(148) Ji, D.; Wang, H.; Ge, J.; Zhang, L.; Li, J.; Bai, D.; Chen, J.; Li, Z. Label-Free and Rapid Detection of ATP Based on Structure Switching of Aptamers. *Anal. Biochem.* **2017**, *526*, 22–28.

(149) Pei, R.; Stojanovic, M. N. Study of Thiazole Orange in Aptamer-Based Dye-Displacement Assays. *Anal. Bioanal. Chem.* **2008**, *390*, 1093–1099.

(150) Sun, H.; Xiang, J.; Gai, W.; Shang, Q.; Li, Q.; Guan, A.; Yang, Q.; Liu, Y.; Tang, Y.; Xu, G. Visual Detection of Potassium by a Cyanine Dye Supramolecular Aggregate Responsive to G-Quadruplex Motif Transition. *Analyst* **2012**, *137*, 5713–5715.

(151) Shoorideh, K.; Chui, C. O. On the Origin of Enhanced Sensitivity in Nanoscale FET-Based Biosensors. *Proc. Natl. Acad. Sci. U. S. A.* **2014**, *111*, 5111–5116.

(152) Vacic, A.; Criscione, J. M.; Rajan, N. K.; Stern, E.; Fahmy, T. M.; Reed, M. A. Determination of Molecular Configuration by Debye Length Modulation. *J. Am. Chem. Soc.* **2011**, *133*, 13886–13889.

(153) Kim, J.; Rim, Y. S.; Chen, H.; Cao, H. H.; Nakatsuka, N.; Hinton, H. L.; Zhao, C.; Andrews, A. M.; Yang, Y.; Weiss, P. S. Fabrication of High-Performance Ultrathin In_2O_3 Film Field-Effect Transistors and Biosensors Using Chemical Lift-off Lithography. *ACS Nano* **2015**, *9*, 4572–4582.

(154) Cheung, K. M.; Yang, K. A.; Nakatsuka, N.; Zhao, C.; Ye, M.; Jung, M. E.; Yang, H.; Weiss, P. S.; Stojanović, M. N.; Andrews, A. M. Phenylalanine Monitoring via Aptamer-Field-Effect Transistor Sensors. *ACS Sens.* **2019**, *4*, 3308–3317.

(155) Wang, B.; Zhao, C.; Wang, Z.; Yang, K. A.; Cheng, X.; Liu, W.; Yu, W.; Lin, S.; Zhao, Y.; Cheung, K. M.; Lin, H.; Hojaiji, H.; Weiss, P. S.; Stojanović, M. N.; Tomiyama, A. J.; Andrews, A. M.; Emaminejad, S. Wearable Aptamer-Field-Effect Transistor Sensing System for Noninvasive Cortisol Monitoring. *Sci. Adv.* **2022**, *8*: eabk0967.

(156) Sayers, J. R.; Eckstein, F. Properties of Overexpressed Phage T5 D15 Exonuclease. Similarities with Escherichia Coli DNA Polymerase I 5‘-3‘ Exonuclease. *J. Biol. Chem.* **1990**, *265*, 18311–18317.

(157) Sayers, J. R.; Eckstein, F. A Single-Strand Specific Endonuclease Activity Copurifies with Overexpressed T5 D15 Exonuclease. *Nucleic Acids Res.* **1991**, *19*, 4127–4132.

(158) AlMalki, F. A.; Flemming, C. S.; Zhang, J.; Feng, M.; Sedelnikova, S. E.; Ceska, T.; Rafferty, J. B.; Sayers, J. R.; Artymiuk, P. J. Direct Observation of DNA Threading in Flap Endonuclease Complexes. *Nat. Struct. Mol. Biol.* **2016**, *23*, 640–646.

(159) Lehman, I. R.; Nussbaum, A. L. The Deoxyribonucleases of Escherichia Coli: V. ON THE SPECIFICITY OF EXONUCLEASE I (PHOSPHODIESTERASE). *J. Biol. Chem.* **1964**, *239*, 2628–2636.

(160) Yu, H.; Yang, W.; Alkhamis, O.; Canoura, J.; Yang, K. A.; Xiao, Y. *In Vitro* Isolation of Small-Molecule-Binding Aptamers with Intrinsic Dye-Displacement Functionality. *Nucleic Acids Res.* **2018**, *46*: e43.

(161) Richardson, C. C.; Kornberg, A. A Deoxyribonucleic Acid Phosphatase-Exonuclease from *Escherichia Coli* I. PURIFICATION OF THE ENZYME AND CHARACTERIZATION OF THE PHOSPHATASE ACTIVITY. *J. Biol. Chem.* **1964**, *239*, 242–250.

(162) Kerr, C.; Sadowski, P. D. Gene 6 Exonuclease of Bacteriophage T7: I. PURIFICATION AND PROPERTIES OF THE ENZYME. *J. Biol. Chem.* **1972**, *247*, 305–310.

(163) Kunitz, M. Crystalline Desoxyribonuclease I. Isolation and General Properties Spectrophotometric Method for the Measurement of Desoxyribonuclease Activity. *J. Gen. Phys.* **1950**, *33*, 349–362.

(164) Galas, D. J.; Schmitz, A. DNAse Footprinting: A Simple Method for the Detection of Protein-DNA Binding Specificity. *Nucleic Acids Res.* **1978**, *5*, 3157–3170.

(165) Dyke, M. W. van; Dervan, P. B. Methidiumpropyl-EDTA-Fe(II) and DNase I Footprinting Report Different Small Molecule Binding Site Sizes on DNA. *Nucleic Acids Res.* **1983**, *11*, 5555–5567.

(166) Tian, L.; Sayer, J. M.; Kroth, H.; Kalena, G.; Jerina, D. M.; Shuman, S. Benzo[a]Pyrene-DG Adduct Interference Illuminates the Interface of Vaccinia Topoisomerase with the DNA Minor Groove. *J. Biol. Chem.* **2003**, *278*, 9905–9911.

(167) Yakovleva, L.; Handy, C. J.; Yagi, H.; Sayer, J. M.; Jerina, D. M.; Shuman, S. Intercalating Polycyclic Aromatic Hydrocarbon-DNA Adducts Poison DNA Religation by Vaccinia Topoisomerase and Act as Roadblocks to Digestion by Exonuclease III. *Biochemistry* **2006**, *45*, 7644–7653.

(168) Ekambareswara Rao, K.; William Lown, J. DNA Sequence Selectivities in the Covalent Bonding of Antibiotic Saframycins Mxl, Mx3, A, and S Deduced from MPE*Fe(II) Footprinting and Exonuclease III Stop Assays. *Biochemistry* **1992**, *31*, 12076–12082.

(169) Albert, F. G.; Eckdahl, T. T.; Fitzgerald, D. J.; Anderson, J. N. Heterogeneity in the Actions of Drugs That Bind in the DNA Minor Groove. *Biochemistry* **1999**, *38*, 10135–10146.

(170) Wang, Z.; Yu, H.; Canoura, J.; Liu, Y.; Alkhamis, O.; Fu, F.; Xiao, Y. Introducing Structure-Switching Functionality into Small-Molecule-Binding Aptamers via Nuclease-Directed Truncation. *Nucleic Acids Res.* **2018**, *46*: e81.

(171) Qing, T.; He, D.; He, X.; Wang, K.; Xu, F.; Wen, L.; Shangguan, J.; Mao, Z.; Lei, Y. Nucleic Acid Tool Enzymes-Aided Signal Amplification Strategy for Biochemical Analysis: Status and Challenges. *Anal. Bioanal. Chem.* **2015**, *408*, 2793–2811.

(172) Shlyahovsky, B.; Li, D.; Weizmann, Y.; Nowarski, R.; Kotler, M.; Willner, I. Spotlighting of Cocaine by an Autonomous Aptamer-Based Machine. *J. Am. Chem. Soc.* **2007**, *129*, 3814–3815.

(173) Heiter, D. F.; Lunnen, K. D.; Wilson, G. G. Site-Specific DNA-Nicking Mutants of the Heterodimeric Restriction Endonuclease R.BbvCI. *J. Mol. Biol.* **2005**, *348*, 631–640.

(174) Jacobsen, H.; Klenow, H.; Overoaard-Hansen, K. The N-Terminal Amino-Acid Sequences of DNA Polymerase I from *Escherichia Coli* and of the Large and the Small Fragments Obtained by a Limited Proteolysis. *Eur. J. Biochem.* **1974**, *45*, 623–627.

(175) Wang, F.; Freage, L.; Orbach, R.; Willner, I. Autonomous Replication of Nucleic Acids by Polymerization/Nicking Enzyme/DNAzyme Cascades for the Amplified Detection of DNA and the Aptamer-Cocaine Complex. *Anal. Chem.* **2013**, *85*, 8196–8203.

(176) Leung, K. H.; He, B.; Yang, C.; Leung, C. H.; Wang, H. M. D.; Ma, D. L. Development of an Aptamer-Based Sensing Platform for Metal Ions, Proteins, and Small Molecules through Terminal Deoxynucleotidyl Transferase Induced G-Quadruplex Formation. *ACS Appl. Mater. Interfaces* **2015**, *7*, 24046–24052.

(177) Roychoudhury, R.; Jay, E.; Wu, R. Terminal Labeling and Addition of Homopolymer Tracts to Duplex DNA Fragments by Terminal Deoxynucleotidyl Transferase. *Nucleic Acids Res.* **1976**, *3*, 863–877.

(178) Zheng, D.; Zou, R.; Lou, X. Label-Free Fluorescent Detection of Ions, Proteins, and Small Molecules Using Structure-Switching Aptamers, SYBR Gold, and Exonuclease I. *Anal. Chem.* **2012**, *84*, 3554–3560.

(179) Zuo, X.; Xia, F.; Xiao, Y.; Plaxco, K. W. Sensitive and Selective Amplified Fluorescence DNA Detection Based on Exonuclease III-Aided Target Recycling. *J. Am. Chem. Soc.* **2010**, *132*, 1816–1818.

(180) Gerasimova, Y. v.; Kolpashchikov, D. M. Enzyme-Assisted Target Recycling (EATR) for Nucleic Acid Detection. *Chem. Soc. Rev.* **2014**, *43*, 6405–6438.

(181) Lu, C. H.; Li, J.; Lin, M. H.; Wang, Y. W.; Yang, H. H.; Chen, X.; Chen, G. N. Amplified Aptamer-Based Assay through Catalytic Recycling of the Analyte. *Angew. Chem., Int. Ed.* **2010**, *49*, 8454–8457.

(182) Liu, X.; Freeman, R.; Willner, I.; Liu, X.; Freeman, R.; Willner, I. Amplified Fluorescence Aptamer-Based Sensors Using Exonuclease III for the Regeneration of the Analyte. *Chem. – Eur. J.* **2012**, *18*, 2207–2211.

(183) Patil, A. J.; Vickery, J. L.; Scott, T. B.; Mann, S. Aqueous Stabilization and Self-Assembly of Graphene Sheets into Layered Bio-Nanocomposites Using DNA. *Adv. Mater.* **2009**, *21*, 3159–3164.

(184) Wang, H. B.; Wu, S.; Chu, X.; Yu, R. Q. A Sensitive Fluorescence Strategy for Telomerase Detection in Cancer Cells Based on T7 Exonuclease-Assisted Target Recycling Amplification. *Chem. Commun.* **2012**, *48*, 5916–5918.

(185) Biebricher, A. S.; Heller, I.; Roijmans, R. F. H.; Hoekstra, T. P.; Peterman, E. J. G.; Wuite, G. J. L. The Impact of DNA Intercalators on DNA and DNA-Processing Enzymes Elucidated through Force-Dependent Binding Kinetics. *Nat. Commun.* **2015**, *6*: 7304.

(186) Prough, R. A.; Clark, B. J.; Klinge, C. M. Novel Mechanisms for DHEA Action. *J. Mol. Endocrinol.* **2016**, *56*, R139–R155.

(187) Kroboth, P. D.; Salek, F. S.; Pittenger, A. L.; Fabian, T. J.; Frye, R. F. DHEA and DHEA-S: A Review. *J. Clin. Pharmacol.* **1999**, *39*, 327–348.

(188) Schiffer, L.; Barnard, L.; Baranowski, E. S.; Gilligan, L. C.; Taylor, A. E.; Arlt, W.; Shackleton, C. H. L.; Storbeck, K. H. Human Steroid Biosynthesis, Metabolism and Excretion Are Differentially Reflected by Serum and Urine Steroid Metabolomes: A Comprehensive Review. *J. Steroid Biochem. Mol. Biol.* **2019**, *194*, 105439.

(189) Sonka, J.; Fassati, M.; Fassati, P.; Gregorová, I.; Picek, K. Serum Lipids and Dehydroepiandrosterone Excretion in Normal Subjects. *J. Lipid Res.* **1968**, *9*, 769–772.

(190) Arlt, W.; Biehl, M.; Taylor, A. E.; Hahner, S.; Libé, R.; Hughes, B. A.; Schneider, P.; Smith, D. J.; Stiekema, H.; Krone, N.; Porfiri, E.; Opocher, G.; Bertherat, J.; Mantero, F.; Allolio, B.; Terzolo, M.; Nightingale, P.; Shackleton, C. H. L.; Bertagna, X.; Fassnacht, M.; Stewart, P. M. Urine Steroid Metabolomics as a Biomarker Tool for Detecting Malignancy in Adrenal Tumors. *J. Clin. Endocrinol. Metab.* **2011**, *96*, 3775–3784.

(191) Fragachan, F.; Millbtte, B.; Genest, A. J. Further Evidence of Altered Adrenocortical Function in Hypertension. Dehydroepiandrosterone Excretion Rate. *Can. J. Biochem.* **1968**, *46*, 1031–1038.

(192) Plowman, T. The Identification of Coca (*Erythroxylum Species*): 1860–1910. *Bot. J. Linn. Soc.* **1982**, *84*, 329–353.

(193) Drug Enforcement Administration. 2020 National Drug Threat Assessment (NDTA). DEA-DCT-DIR-008-21. **2020**.

(194) U. S. Drug Enforcement Administration, Diversion Control Division. (**2021**). National Forensic Laboratory Information System: NFLIS Drug 2020 Annual Report. Springfield, VA: U. S. Drug Enforcement Administration.

(195) Jr., J. V. P.; Magnusson, P.; LeQuang, J. A. K.; Breve, F.; Varrassi, G. Cocaine and Cardiotoxicity: A Literature Review. *Cureus* **2021**, *13*: e14594.

(196) Velapoldi, R. A.; Wicks, S. A. The Use of Chemical Spot Tests Kits for the Presumptive Identification of Narcotics and Drugs of Abuse. *J. Forensic Sci.* **1974**, *19*, 636–656.

(197) Oguri, K.; Wada, S.; Eto, S.; Yamada, H. Specificity and Mechanism of the Color Reaction of Cocaine with Cobaltous Thiocyanate. *Jpn. J. Toxicol. Eviron. Health* **1995**, *41*, 274–279.

(198) United Nations Office on Drugs and Crime. Recommended Methods for the Identification and Analysis of Cocaine in Seized Materials. ST/NAR/7/Rev.1. **2012**.

(199) Andexer, J. N.; Richter, M. Emerging Enzymes for ATP Regeneration in Biocatalytic Processes. *ChemBioChem* **2015**, *16*, 380–386.

(200) Marsh, E. N. G.; Patterson, D. P.; Li, L. Adenosyl Radical: Reagent and Catalyst in Enzyme Reactions. *ChemBioChem* **2010**, *11*, 604–621.

(201) Linden, J.; Koch-Nolte, F.; Dahl, G. Purine Release, Metabolism, and Signaling in the Inflammatory Response. *Annu. Rev. Immunol.* **2019**, *37*, 325–347.

(202) Traut, T. W. Physiological Concentrations of Purines and Pyrimidines. *Mol. Cell. Biochem.* **1994**, *140*, 1–22.

(203) Layland, J.; Carrick, D.; Lee, M.; Oldroyd, K.; Berry, C. Adenosine: Physiology, Pharmacology, and Clinical Applications. *JACC: Cardiovas. Interv.* **2014**, *7*, 581–591.

(204) Eltzschig, H. K.; Warner, D. S.; Warner, M. A. Adenosine: An Old Drug Newly Discovered. *Anesthesiology* **2009**, *111*, 904–915.

(205) Sommerschild, H. T.; Kirkebøen, K. A. Adenosine and Cardioprotection during Ischaemia and Reperfusion – an Overview. *Acta Anaesthesiol. Scand.* **2000**, *44*, 1038–1055.

(206) Li, Y.; Wang, W.; Parker, W.; Clancy, J. P. Adenosine Regulation of Cystic Fibrosis Transmembrane Conductance Regulator through Prostenoids in Airway Epithelia. *Am. J. Res. Cell Mol. Biol.* **2006**, *34*, 600–608.

(207) Fisher, O.; Benson, R. A.; Imray, C. H. The Clinical Application of Purine Nucleosides as Biomarkers of Tissue Ischemia and Hypoxia in Humans *In Vivo*. *Biomark. Med.* **2019**, *13*, 953–965.

(208) Latini, S.; Pedata, F. Adenosine in the Central Nervous System: Release Mechanisms and Extracellular Concentrations. *J. Neurochem.* **2001**, *79*, 463–484.

(209) van der Merwe, K. J.; Steyn, P. S.; Fourie, L.; Scott, D. B.; Theron, J. J. Ochratoxin A, a Toxic Metabolite Produced by *Aspergillus Ochraceus* Wilh. *Nature* **1965**, *205*, 1112–1113.

(210) Scudamore, K. A.; Banks, J.; Macdonald, S. J. Fate of Ochratoxin A in the Processing of Whole Wheat Grains during Milling and Bread Production. *Food Addit. Contam.* **2003**, *20*, 1153–1163.

(211) de Cerain, A. L.; González-Peñas, E.; Jiménez, A. M.; Bello, J. Contribution to the Study of Ochratoxin A in Spanish Wines. *Food Addit. Contam.* **2002**, *19*, 1058–1064.

(212) Tsubouchi, H.; Yamamoto, K.; Hisada, K.; Sakabe, Y.; Udagawa, S. ichi. Effect of Roasting on Ochratoxin A Level in Green Coffee Beans Inoculated with Aspergillus Ochraceus. *Mycopathologia* **1987**, *97*, 111–115.

(213) Pfohl-Leszkowicz, A.; Manderville, R. A. Ochratoxin A: An Overview on Toxicity and Carcinogenicity in Animals and Humans. *Mol. Nutr. Food Res.* **2007**, *51*, 61–99.

(214) Niemiec, J.; Borzemska, W.; Goliński, P.; Karpińska, E.; Szeleszczuk, P.; Celeda, T. The Effect of Ochratoxin A on Egg Quality, Development of Embryos and the Level of toxin in Eggs and Tissues of Hens and Chicks. *J. Anim. Feed Sci.* **1994**, *3*, 309–316.

(215) Battacone, G.; Nudda, A.; Pulina, G. Effects of Ochratoxin A on Livestock Production. *Toxins* **2010**, *2*, 1796–1824.

(216) Armenian, P.; Vo, K. T.; Barr-Walker, J.; Lynch, K. L. Fentanyl, Fentanyl Analogs and Novel Synthetic Opioids: A Comprehensive Review. *Neuropharmacology* **2018**, *134*, 121–132.

(217) Suzuki, J.; El-Haddad, S. A Review: Fentanyl and Non-Pharmaceutical Fentanyls. *Drug Alcohol Depend.* **2017**, *171*, 107–116.

(218) United Nations Office on Drugs and Crime. Fentanyl and Its Analogues-50 Years On. **2017**.

(219) U.S. Drug Enforcement Administration, Diversion Control Division. (2017). NFLIS Brief: Fentanyl and Fentanyl-Related Substances Reported in NFLIS, 2015–2016. Springfield, VA: U.S. Drug Enforcement Administration.

(220) U. S. Drug Enforcement Administration, Diversion Control Division. Tracking Fentanyl and Fentanyl-Related Substances Reported in NFLIS-Drug by State, 2016–2017. **2019**.

(221) U. S. Drug Enforcement Administration, Diversion Control Division. Tracking Fentanyl and Fentanyl-Related Compounds Reported in NFLIS-Drug by State: 2018–2019. **2020**.

(222) Skulska, A.; Ka£a, M.; Parczewski, A. Fentanyl and its Analogues in the Forensic Laboratory. Medical and Analytical Problems. *Problems of Forensic Sciences* **2004**, *59*, 127–142.

(223) Bi-Yi, C.; Wen-Qiao, J.; Jie, C.; Xin-Jian, C.; You-Cheng, Z.; Zhi-Qiang, C. Analgesic Activity and Selectivity of Isothiocyanate Derivatives of Fentanyl Analogs for Opioid Receptors. *Life Sci.* **1999**, *65*, 1589–1595.

(224) Valter, Karel.; Arrizabalaga, Philippe. *Designer Drugs Directory*; Elsevier, **1998**.

(225) Marinetti, L. J.; Ehlers, B. J. A Series of Forensic Toxicology and Drug Seizure Cases Involving Illicit Fentanyl Alone and in Combination with Heroin, Cocaine or Heroin and Cocaine. *J. Anal. Toxicol.* **2014**, *38*, 592–598.

(226) *NIK Fentanyl Test Pack - Lynn Peavey Company*. https://lynnpeavey.com/product/nik-fentanyl-test-pack/ (accessed May 13, 2022).

(227) Wharton, R. E.; Casbohm, J.; Hoffmaster, R.; Brewer, B. N.; Finn, M. G.; Johnson, R. C. Detection of 30 Fentanyl Analogs by Commercial Immunoassay Kits. *J. Anal. Toxicol.* **2021**, *45*, 111–116.

(228) Schackmuth, M.; Kerrigan, S. Immunoassay-Based Detection of Fentanyl Analogs in Forensic Toxicology. *Forensic Toxicol.* **2019**, *37*, 231–237.

(229) Helander, A.; Stojanovic, K.; Villén, T.; Beck, O. Detectability of Fentanyl and Designer Fentanyls in Urine by 3 Commercial Fentanyl Immunoassays. *Drug Test. Anal.* **2018**, *10*, 1297–1304.

(230) Mechoulam, R.; Shani, A.; Edery, H.; Grunfeld, Y. Chemical Basis of Hashish Activity. *Science* **1970**, *169*, 611–612.

(231) Baker, P. B.; Taylor, B. J.; Gough, T. A. The Tetrahydrocannabinol and Tetrahydrocannabinolic Acid Content of Cannabis Products. *J. Pharm. Pharmacol.* **1981**, *33*, 369–372.

(232) Agriculture Improvement Act of 2018. Public Law 115-334. **2018**.

(233) United States Department of Agriculture. Industrial Hemp in the United States: Status and Market Potential. **2000**.

(234) Rehman, M. S. U.; Rashid, N.; Saif, A.; Mahmood, T.; Han, J. I. Potential of Bioenergy Production from Industrial Hemp (*Cannabis Sativa*): Pakistan Perspective. *Renewable Sustainable Energy Rev.* **2013**, *18*, 154–164.

(235) Fike, J. Industrial Hemp: Renewed Opportunities for an Ancient Crop. *Crit. Rev. Plant Sci.* **2017**, *35*, 406–424.

(236) United Nations Office on Drugs and Crime. Recommended Methods for the Identification and Analysis of Cannabis and Cannabis Products. ST/NAR/40/REV.1. **2022**.

(237) Rubiano, C.; Firmin, J. S.; Coticone, S. R. The Effect of Benzene Ring Substituents on the Mechanism of Duquenois Levine (DL) Test for Cannabinoid Detection. *J. Chem. Pharm. Res.* **2014**, *6*, 1261–1264.

(238) Kovar, K.-A.; Laudszun, M. Chemistry and Reaction Mechanisms of Rapid Tests for Drugs of Abuse and Precursors Chemicals. *United Nations Scientific and Technical Notes SCITEC/6*, **1989**.

(239) Puapaiboon, U.; Jai-nhuknan, J.; Cowan, J. A. Characterization of a Multi-Functional Metal-Mediated Nuclease by MALDI-TOF Mass Spectrometry. *Nucleic Acids Res.* **2001**, *29*, 3652–3656.

(240) Mol, C. D.; Kuo, C.-F.; Thayer, M. M.; Cunningham, R. P.; Tainer, J. A. Structure and Function of the Multifunctional DNA-Repair Enzyme Exonuclease III. *Nature* **1995**, *374*, 381–386.

(241) Richardson, C. C.; Kornberg, A. A Deoxyribonucleic Acid Phosphatase-Exonuclease from *Escherichia Coli*: II. CHARACTERIZATION OF THE EXONUCLEASE ACTIVITY. *J. Biol. Chem.* **1964**, *239*, 251–258.

(242) Henikoff, S. Unidirectional Digestion with Exonuclease III Creates Targeted Breakpoints for DNA Sequencing. *Gene* **1984**, *28*, 351–359.

(243) Lovett, S. T. The DNA Exonucleases of Escherichia Coli . *EcoSal Plus* **2011**, *4*: ecosalplus.4.4.7.

(244) Hoheisel, J. D. On the Activities of Escherichia Coli Exonuclease III. *Anal. Biochem.* **1993**, *209*, 238–246.

(245) Brody, R. S. Nucleotide Positions Responsible for the Processivity of the Reaction of Exonuclease I with Oligodeoxyribonucleotides. *Biochemistry* **1991**, *30*, 7072–7080.

(246) Thomas, K. R.; Olivera, B. M. Processivity of DNA Exonucleases. *J. Biol. Chem.* **1978**, *253*, 424–429.

(247) Korada, S. K. C.; Johns, T. D.; Smith, C. E.; Jones, N. D.; McCabe, K. A.; Bell, C. E. Crystal Structures of Escherichia Coli Exonuclease I in Complex with Single-Stranded DNA Provide Insights into the Mechanism of Processive Digestion. *Nucleic Acids Res.* **2013**, *41*, 5887–5897.

(248) Sandigursky, M.; Franklin, W. A. *Escherichia Coli* Single-Stranded DNA Binding Protein Stimulates the DNA Deoxyribophosphodiesterase Activity of Exonuclease I. *Nucleic Acids Res.* **1994**, *22*, 247–250.

(249) Fei, L.; Tian, S. S.; Moysey, R.; Misca, M.; Barker, J. J.; Smith, M. A.; McEwan, P. A.; Pilka, E. S.; Crawley, L.; Evans, T.; Sun, D. Structural and Biochemical Studies of a Moderately Thermophilic Exonuclease I from *Methylocaldum Szegediense*. *PLoS ONE* **2015**, *10*: e0117470.

(250) Sutton, B. J.; Gould, H. J. The Human IgE Network. *Nature* **1993**, *366*, 421–428.

(251) Gounni, A. S.; Lamkhioued, B.; Ochial, K.; Tanaka, Y.; Delaporte, E.; Capron, A.; Kinet, J. P.; Capron, M. High-Affinity IgE Receptor on Eosinophils Is Involved in Defence against Parasites. *Nature* **1994**, *367*, 183–186.

(252) Rosenwasser, L. J. Mechanisms of IgE Inflammation. *Curr. Allergy Asthama Rep.* **2011**, *11*, 178–183.

(253) Wolberg, A. S. Thrombin Generation and Fibrin Clot Structure. *Blood Rev.* **2007**, *21*, 131–142.

(254) Monroe, D. M.; Hoffman, M.; Roberts, H. R. Platelets and Thrombin Generation. *Arterioscler., Thromb., Vasc. Biol.* **2002**, *22*, 1381–1389.

(255) Kaplan, K. L. Direct Thrombin Inhibitors. *Expert Opin. Pharmacother.* **2005**, *4*, 653–666.

(256) Fitzgerald, G. A. The Human Pharmacology of Thrombin Inhibition. *Coron. Artery Dis.* **1996**, *7*, 911–918.

(257) Hayat, A.; Marty, J. L. Aptamer Based Electrochemical Sensors for Emerging Environmental Pollutants. *Front. Chem.* **2014**, *2*: 41.

(258) Zhang, J.; Smaga, L. P.; Satyavolu, N. S. R.; Chan, J.; Lu, Y. DNA Aptamer-Based Activatable Probes for Photoacoustic Imaging in Living Mice. *J. Am. Chem. Soc.* **2017**, *139*, 17225–17228.

(259) Liang, H.; Chen, S.; Li, P.; Wang, L.; Le, J.; Li, J.; Yang, H. H.; Tan, W. Nongenetic Approach for Imaging Protein Dimerization by Aptamer Recognition and Proximity-Induced DNA Assembly. *J. Am. Chem. Soc.* **2018**, *140*, 4186–4190.

(260) Sun, H.; Zhu, X.; Lu, P. Y.; Rosato, R. R.; Tan, W.; Zu, Y. Oligonucleotide Aptamers: New Tools for Targeted Cancer Therapy. *Mol. Ther. --Nucleic Acids* **2014**, *3*: e182.

(261) Nimjee, S. M.; Rusconi, C. P.; Sullenger, B. A. Aptamers: An Emerging Class of Therapeutics. *Annu. Rev. Med.* **2005**, *56*, 555–583.

(262) Pfeiffer, F.; Mayer, G. Selection and Biosensor Application of Aptamers for Small Molecules. *Front. Chem.* **2016**, *4*: 25.

(263) Liu, J.; Lu, Y. Fast Colorimetric Sensing of Adenosine and Cocaine Based on a General Sensor Design Involving Aptamers and Nanoparticles. *Angew. Chem., Int. Ed.* **2005**, *45*, 90–94.

(264) Freeman, R.; Girsh, J.; Fang-Ju Jou, A.; Ho, J. A. A.; Hug, T.; Dernedde, J.; Willner, I. Optical Aptasensors for the Analysis of the Vascular Endothelial Growth Factor (VEGF). *Anal. Chem.* **2012**, *84*, 6192–6198.

(265) Nutiu, R.; Li, Y.; Nutiu,] R; Li, Y. A DNA–Protein Nanoengine for "On-Demand" Release and Precise Delivery of Molecules. *Angew. Chem., Int. Ed.* **2005**, *44*, 5464–5467.

(266) Armstrong, R. E.; Strouse, G. F. Rationally Manipulating Aptamer Binding Affinities in a Stem-Loop Molecular Beacon. *Bioconjugate Chem.* **2014**, *25*, 1769–1776.

(267) Ricci, F.; Vallée-Bélisle, A.; Porchetta, A.; Plaxco, K. W. Rational Design of Allosteric Inhibitors and Activators Using the Population-Shift Model: *In Vitro* Validation and Application to an Artificial Biosensor. *J. Am. Chem. Soc.* **2012**, *134*, 15177–15180.

(268) Tuma, R. S.; Beaudet, M. P.; Jin, X.; Jones, L. J.; Cheung, C. Y.; Yue, S.; Singer, V. L. Characterization of SYBR Gold Nucleic Acid Gel Stain: A Dye Optimized for Use with 300-nm Ultraviolet Transilluminators. *Anal.Biochem.* **1999**, *268*, 278–288.

(269) Kirsanov, K. I.; Lesovaya, E. A.; Yakubovskaya, M. G.; Belitsky, G. A. SYBR Gold and SYBR Green II Are Not Mutagenic in the Ames Test. *Mutat. Res.* **2010**, *699*, 1–4.

(270) Cosa, G.; Focsaneanu, K.-S.; McLean, J. R. N.; McNamee, J. P.; Scaiano, J. C. Photophysical Properties of Fluorescent DNA-Dyes Bound to Single- and Double-Stranded DNA in Aqueous Buffered Solution. *Photochem. Photobiol.* **2001**, *73*, 585–599.

(271) Long, G. L.; Winefordner, J. D. Limit of Detection: A Closer Look at the IUPAC Definition. *Anal. Chem.* **1983**, *55*, 712A-724A.

(272) Dahlquist, F. W. The Meaning of Scatchard and Hill Plots. *Methods Enzymol.* **1978**, *48*, 270–299.

(273) Ling, M. M.; Ricks, C.; Lea, P. Multiplexing Molecular Diagnostics and Immunoassays Using Emerging Microarray Technologies. *Expert Rev. Mol. Diagn.* **2014**, *7*, 87–98.

(274) Cirino, N. M.; Musser, K. A.; Egan, C. Multiplex Diagnostic Platforms for Detection of Biothreat Agents. *Expert Rev. Mol. Diagn.* **2014**, *4*, 841–857.

(275) Elshal, M. F.; McCoy, J. P. Multiplex Bead Array Assays: Performance Evaluation and Comparison of Sensitivity to ELISA. *Methods* **2006**, *38*, 317–323.

(276) Li, J. J.; Chu, Y.; Lee, B. Y. H.; Xie, X. S. Enzymatic Signal Amplification of Molecular Beacons for Sensitive DNA Detection. *Nucleic Acids Res.* **2008**, *36*: e36.

(277) di Giusto, D. A.; Wlassoff, W. A.; Gooding, J. J.; Messerle, B. A.; King, G. C. Proximity Extension of Circular DNA Aptamers with Real-Time Protein Detection. *Nucleic Acids Res.* **2005**, *33*: e64.

(278) Lizardi, P. M.; Huang, X.; Zhu, Z.; Bray-Ward, P.; Thomas, D. C.; Ward, D. C. Mutation Detection and Single-Molecule Counting Using Isothermal Rolling-Circle Amplification. *Nat. Genet.* **1998**, *19*, 225–232.

(279) Liu, X.; Freeman, R.; Golub, E.; Willner, I. Chemiluminescence and Chemiluminescence Resonance Energy Transfer (CRET) Aptamer Sensors Using Catalytic Hemin/G-Quadruplexes. *ACS Nano* **2011**, *5*, 7648–7655.

(280) Xing, H.; Zhang, C. L.; Ruan, G.; Zhang, J.; Hwang, K.; Lu, Y. Multimodal Detection of a Small Molecule Target Using Stimuli-Responsive Liposome Triggered by Aptamer-Enzyme Conjugate. *Anal. Chem.* **2016**, *88*, 1506–1510.

(281) Swensen, J. S.; Xiao, Y.; Ferguson, B. S.; Lubin, A. A.; Lai, R. Y.; Heeger, A. J.; Plaxco, K. W.; Soh, H. T. Continuous, Real-Time Monitoring of Cocaine in Undiluted Blood Serum via a Microfluidic, Electrochemical Aptamer-Based Sensor. *J. Am. Chem. Soc.* **2009**, *131*, 4262–4266.

(282) McKeague, M.; McConnell, E. M.; Cruz-Toledo, J.; Bernard, E. D.; Pach, A.; Mastronardi, E.; Zhang, X.; Beking, M.; Francis, T.; Giamberardino, A.; Cabecinha, A.; Ruscito, A.; Aranda-Rodriguez, R.; Dumontier, M.; DeRosa, M. C. Analysis of *In Vitro* Aptamer Selection Parameters. *J. Mol. Evol.* **2015**, *81*, 150–161.

(283) Stoltenburg, R.; Reinemann, C.; Strehlitz, B. SELEX–A (R)evolutionary Method to Generate High-Affinity Nucleic Acid Ligands. *Biomol. Eng.* **2007**, *24*, 381–403.

(284) Vorobyeva, M. A.; Davydova, A. S.; Vorobjev, P. E.; Pyshnyi, D. V.; Venyaminova, A. G. Key Aspects of Nucleic Acid Library Design for *In Vitro* Selection. *Int. J. Mol. Sci.* **2018**, *19*: 470.

(285) Hendrix, M.; Priestley, E. S.; Joyce, G. F.; Wong, C. H. Direct Observation of Aminoglycoside - RNA Interactions by Surface Plasmon Resonance. *J. Am. Chem. Soc.* **1997**, *119*, 3641–3648.

(286) Torres, F. E.; Recht, M. I.; Coyle, J. E.; Bruce, R. H.; Williams, G. Higher Throughput Calorimetry: Opportunities, Approaches and Challenges. *Curr. Opin. Struct. Biol.* **2010**, *20*, 598–605.

(287) Torres, F. E.; Kuhn, P.; de Bruyker, D.; Bell, A. G.; Wolkin, M. V.; Peeters, E.; Williamson, J. R.; Anderson, G. B.; Schmitz, G. P.; Recht, M. I.; Schweizer, S.; Scott, L. G.; Ho, J. H.; Elrod, S. A.; Schultz, P. G.; Lerner, R. A.; Bruce, R. H. Enthalpy Arrays. *Proc. Natl. Acad. Sci. U. S. A.* **2004**, *101*, 9517–9522.

(288) Katilius, E.; Flores, C.; Woodbury, N. W. Exploring the Sequence Space of a DNA Aptamer Using Microarrays. *Nucleic Acids Res.* **2007**, *35*, 7626–7635.

(289) Platt, M.; Rowe, W.; Knowles, J.; Day, P. J.; Kell, D. B. Analysis of Aptamer Sequence Activity Relationships. *Integr. Biol.* **2009**, *1*, 116–122.

(290) Ketterer, S.; Fuchs, D.; Weber, W.; Meier, M. Systematic Reconstruction of Binding and Stability Landscapes of the Fluorogenic Aptamer Spinach. *Nucleic Acids Res.* **2015**, *43*, 9564–9572.

(291) Liu, Y.; Yu, H.; Alkhamis, O.; Moliver, J.; Xiao, Y. Tuning Biosensor Cross-Reactivity Using Aptamer Mixtures. *Anal. Chem.* **2020**, *92*, 5041–5047.

(292) Canoura, J.; Wang, Z.; Yu, H.; Alkhamis, O.; Fu, F.; Xiao, Y. No Structure-Switching Required: A Generalizable Exonuclease-Mediated Aptamer-Based Assay for Small-Molecule Detection. *J. Am. Chem. Soc.* **2018**, *140*, 9961–9971.

(293) Fasman, G. D. *Circular Dichroism and the Conformational Analysis of Biomolecules*; Plenum Press, **1996**.

(294) Xiao, Y.; Lai, R. Y.; Plaxco, K. W. Preparation of Electrode-Immobilized, Redox-Modified Oligonucleotides for Electrochemical DNA and Aptamer-Based Sensing. *Nat. Protoc.* **2007**, *2*, 2875–2880.

(295) Trasatti, S.; Petrii, O. A. Real Surface Area Measurements in Electrochemistry. *J. Electroanal. Chem.* **1992**, *327*, 353–376.

(296) Herne, T. M.; Tarlov, M. J. Characterization of DNA Probes Immobilized on Gold Surfaces. *J. Am. Chem. Soc.* **1997**, *119*, 8916–8920.

(297) Cruz-Aguado, J. A.; Penner, G. Determination of Ochratoxin A with a DNA Aptamer. *J. Agric. Food Chem.* **2008**, *56*, 10456–10461.

(298) Petrucci, R. H.; Herring, F. G.; Madura, J. D.; Bissonnette, C. General Chemistry: Principles and Modern Applications. 11th ed.; Pearson, **2017**, 37.

(299) Lin, C. H.; Patel, D. J. Structural Basis of DNA Folding and Recognition in an AMP-DNA Aptamer Complex: Distinct Architectures but Common Recognition Motifs for DNA and RNA Aptamers Complexed to AMP. *Chem. Biol.* **1997**, *4*, 817–832.

(300) Kypr, J.; Kejnovská, I.; Renčiuk, D.; Vorlíčková, M. Circular Dichroism and Conformational Polymorphism of DNA. *Nucleic Acids Res.* **2009**, *37*, 1713–1725.

(301) del Villar-Guerra, R.; Trent, J. O.; Chaires, J. B. G-Quadruplex Secondary Structure Obtained from Circular Dichroism Spectroscopy. *Angew. Chem., Int. Ed.* **2018**, *57*, 7171–7175.

(302) Schoukroun-Barnes, L. R.; Glaser, E. P.; White, R. J. Heterogeneous Electrochemical Aptamer-Based Sensor Surfaces for Controlled Sensor Response. *Langmuir* **2015**, *31*, 6563–6569.

(303) Porchetta, A.; Vallée-Bélisle, A.; Plaxco, K. W.; Ricci, F. Using Distal-Site Mutations and Allosteric Inhibition to Tune, Extend, and Narrow the Useful Dynamic Range of Aptamer-Based Sensors. *J. Am. Chem. Soc.* **2012**, *134*, 20601–20604.

(304) Drabovich, A. P.; Okhonin, V.; Berezovski, M.; Krylov, S. N. Smart Aptamers Facilitate Multi-Probe Affinity Analysis of Proteins with Ultra-Wide Dynamic Range of Measured Concentrations. *J. Am. Chem. Soc.* **2007**, *129*, 7260–7261.

(305) Hanssen, B. L.; Siraj, S.; Wong, D. K. Y. Recent Strategies to Minimise Fouling in Electrochemical Detection Systems. *Rev. Anal. Chem.* **2016**, *35*, 1–28.

(306) Tasset, D. M.; Kubik, M. F.; Steiner, W. Oligonucleotide Inhibitors of Human Thrombin That Bind Distinct Epitopes. *J. Mol. Biol.* **1997**, *272*, 688–698.

(307) Bock, L. C.; Griffin, L. C.; Latham, J. A.; Vermaas, E. H.; Toole, J. J. Selection of Single-Stranded DNA Molecules That Bind and Inhibit Human Thrombin. *Nature* **1992**, *355*, 564–566.

(308) Mani, R. J.; Dye, R. G.; Snider, T. A.; Wang, S.; Clinkenbeard, K. D. Bi-Cell Surface Plasmon Resonance Detection of Aptamer Mediated Thrombin Capture in Serum. *Biosens. Bioelectron.* **2011**, *26*, 4832–4836.

(309) Kinet, D.; Tasset, T. W.; Wiegand, P. B.; Williams, S. C.; Dreskin, M. H.; Jouvin, J. P. High-Affinity Oligonucleotide Ligands to Human IgE Inhibit Binding to Fc Epsilon Receptor I. *J. Immunol.* **1996**, *157*, 221–230.

(310) Li, Y.; Liu, B.; Huang, Z.; Liu, J. Engineering Base-Excised Aptamers for Highly Specific Recognition of Adenosine. *Chem. Sci.* **2020**, *11*, 2735–2743.

(311) Hoinka, J.; Zotenko, E.; Friedman, A.; Sauna, Z. E.; Przytycka, T. M. Identification of Sequence–Structure RNA Binding Motifs for SELEX-Derived Aptamers. *Bioinformatics* **2012**, *28*, i215–i223.

(312) Bailey, T. L.; Elkan, C. Fitting a Mixture Model by Expectation Maximization to Discover Motifs in Biopolymers. *Proc. Int. Conf. Intell. Syst. Mol. Biol.* **1994**, *2*, 28–36.

(313) Tombelli, S.; Mascini, M. Aptamers Biosensors for Pharmaceutical Compounds. *Comb. Chem. High Throughput Screening* **2012**, *13*, 641–649.

(314) Cho, M.; Oh, S. S.; Nie, J.; Stewart, R.; Eisenstein, M.; Chambers, J.; Marth, J. D.; Walker, F.; Thomson, J. A.; Soh, H. T. Quantitative Selection and Parallel Characterization of Aptamers. *Proc. Natl. Acad. Sci. U. S. A.* **2013**, *110*, 18460–18465.

(315) Canoura, J.; Yu, H.; Alkhamis, O.; Roncancio, D.; Farhana, R.; Xiao, Y. Accelerating Post-SELEX Aptamer Engineering Using Exonuclease Digestion. *J. Am. Chem. Soc.* **2021**, *143*, 805–816.

(316) Martin, M. Cutadapt Removes Adapter Sequences from High-Throughput Sequencing Reads. *EMBnet J.* **2011**, *17*, 10–12.

(317) Alam, K. K.; Chang, J. L.; Burke, D. H. FASTAptamer: A Bioinformatic Toolkit for High-Throughput Sequence Analysis of Combinatorial Selections. *Mol. Ther. -- Nucleic Acids* **2015**, *4*: e230

(318) Liu, Y.; Canoura, J.; Alkhamis, O.; Xiao, Y. Immobilization Strategies for Enhancing Sensitivity of Electrochemical Aptamer-Based Sensors. *ACS Appl. Mater. Interfaces* **2021**, *13*, 9491–9499.

(319) O'Neal, C. L.; Crouch, D. J.; Fatah, A. A. Validation of Twelve Chemical Spot Tests for the Detection of Drugs of Abuse. *Forensic Sci. Int.* **2000**, *109*, 189–201.

(320) Velapoldi, R. A.; Wicks, S. A. The Use of Chemical Spot Tests Kits for the Presumptive Identification of Narcotics and Drugs of Abuse. *J. Forensic Sci.* **1974**, *19*, 636–656.

(321) Elkins, K. M.; Weghorst, A. C.; Quinn, A. A.; Acharya, S. Colour Quantitation for Chemical Spot Tests for a Controlled Substances Presumptive Test Database. *Drug Test. Anal.* **2017**, *9*, 306–310.

(322) Maurya, N.; Alzahrani, K. A.; Patel, R. Probing the Intercalation of Noscapine from Sodium Dodecyl Sulfate Micelles to Calf Thymus Deoxyribose Nucleic Acid: A Mechanistic Approach. *ACS Omega* **2019**, *4*, 15829–15841.

(323) Masotti, L.; Avitabile, M.; Barcellona, M. L.; von Berger, J.; Manca, N.; Turano, A. Interaction of Papaverine with Covalently Closed DNA. *Microbiologica* **1985**, *8*, 263–268.

(324) U. S. Department of Justice Drug Enforcement Agency. Fentanyl Signature Profiling Program Report, **2019**.

(325) Heltsley, R.; DePriest, A.; Black, D. L.; Robert, T.; Marshall, L.; Meadors, V. M.; Caplan, Y. H.; Cone, E. J. Oral Fluid Drug Testing of Chronic Pain Patients. I. Positive Prevalence Rates of Licit and Illicit Drugs. *J. Anal. Toxicol.* **2011**, *35*, 529–540.

(326) Heltsley, R.; DePriest, A.; Black, D. L.; Crouch, D. J.; Robert, T.; Marshall, L.; Meadors, V. M.; Caplan, Y. H.; Cone, E. J. Oral Fluid Drug Testing of Chronic Pain Patients. II. Comparison of Paired Oral Fluid and Urine Specimens. *J. Anal. Toxicol.* **2012**, *36*, 75–80.

(327) Desrosiers, N. A.; Huestis, M. A. Oral Fluid Drug Testing: Analytical Approaches, Issues and Interpretation of Results. *J. Anal. Toxicol.* **2019**, *43*, 415–443.

(328) Lydon, J.; Teramura, A. H.; Coffman, C. B. UV-B Radiation Effects on Photosynthesis, Growth and Cannabinoid Production of Two *Cannabis Sativa* Chemotypes. *Photochem. Photobiol.* **1987**, *46*, 201–206.

(329) Pertwee, R. G. The Diverse CB1 and CB2 Receptor Pharmacology of Three Plant Cannabinoids: Δ9-Tetrahydrocannabinol, Cannabidiol and Δ^9-Tetrahydrocannabivarin. *Br. J. Pharmacol.* **2008**, *153*, 199–215.

(330) Ameri, A. The Effects of Cannabinoids on the Brain. *Prog. Neurobiol.* **1999**, *58*, 315–348.

(331) Amiji, M.; Park, K. Surface Modification of Polymeric Biomaterials with Poly(Ethylene Oxide), Albumin, and Heparin for Reduced Thrombogenicity. *J. Biomater. Sci. Polym. Ed. 7* **2012**, *4*, 217–234.

(332) Prime, K. L.; Whitesides, G. M. Self-Assembled Organic Monolayers: Model Systems for Studying Adsorption of Proteins at Surfaces. *Science* **1991**, *252*, 1164–1167.

(333) Bearinger, J. P.; Terrettaz, S.; Michel, R.; Tirelli, N.; Vogel, H.; Textor, M.; Hubbell, J. A. Chemisorbed Poly(Propylene Sulphide)-Based Copolymers Resist Biomolecular Interactions. *Nat. Mater.* **2003**, *2*, 259–264.

VITA

JUAN CANOURA

EDUCATION

2011–2016	B.S., Chemistry Florida International University Miami, FL
2016–2018	Ronald E. McNair Graduate Fellowship Florida International University Miami, FL
2018–2020	Research Assistant Florida International University Miami, FL
2020–2021	NIJ Graduate Research Fellow Florida International University Miami, FL
2021–2021	Dissertation Year Fellowship Award Florida International University Miami, FL
2022	Provost Degree Completion Tuition Fellowship Florida International University Miami, FL

SELECTED PUBLICATIONS AND PRESENTATIONS

Liu, Y., Canoura, J., Alkhamis, O. & Xiao, Y. Immobilization strategies for enhancing sensitivity of electrochemical aptamer-based sensors. *ACS Appl. Mater. Interfaces* 2021, *13*, 9491–9499.

Canoura, J., Yu, H., Alkhamis, O., Roncancio, D., Farhana, R. Xiao, Y. Accelerating post-SELEX aptamer engineering using exonuclease digestion. *J. Am. Chem. Soc.* 2021, *143*,

805–816.

Yu, H., Alkhamis, O., Canoura, J., Liu, Y. & Xiao, Y. Advances and challenges in small-molecule DNA aptamer isolation, characterization, and sensor development. *Angew. Chem., Int. Ed.* 2021, *60*, 2–26.

Alkhamis, O., Canoura, J., Yu, H., Liu, Y. & Xiao, Y. Innovative engineering and sensing strategies for aptamer-based small-molecule detection. *TrAC, Trends Anal. Chem.* 2019, *121*, 115699.

Yang, W., Yu, H., Alkhamis, O., Liu, Y., Canoura, J., Fu, F. & Xiao, Y. *In vitro* isolation of class-specific oligonucleotide-based small-molecule receptors. *Nucleic Acids Res.* 2019, *47*, e71.

Canoura, J., Wang, Z., Yu, H., Alkhamis, O., Fu, F. & Xiao, Y. No structure-switching required: A generalizable exonuclease-mediated aptamer-based assay for small-molecule detection. *J. Am. Chem. Soc.* 2018, *140*, 9961–9971.

Yu, H., Canoura, J., Guntupalli, B., Alkhamis, O. & Xiao, Y. Sensitive detection of small-molecule targets using cooperative binding split aptamers and enzyme-assisted target recycling. *Anal. Chem.* 2018, *90*, 1748–1758.

Yu, H., Canoura, J., Guntupalli, B., Lou, X. & Xiao, Y. A cooperative-binding split aptamer assay for rapid, specific and ultra-sensitive fluorescence detection of cocaine in saliva. *Chem. Sci.* 2017, *8*, 131–141.

Canoura, J., Liu, Y. & Xiao, Y. (2021) Electrochemical aptamer-based sensor platform for detection of fentanyl and its analogs. Oral presentation, Crossing Forensic Borders Global Webinar Series, April 14.

Canoura, J., Farhana, R., Roncancio, R. & Xiao, Y. (2020) Screening of aptamer mutants for enhanced target specificity using a dual exonuclease digestion assay. Oral presentation, Pittcon Conference & Expo, Chicago, IL, March 1–5.

Canoura, J., Wang, Z. W., Yu, H. X., Alkhamis, O., Fu, F. F. & Xiao, Y. (2019) No Structure-Switching Required: A Generalizable Exonuclease-Mediated Aptamer-Based Assay for Small-Molecule Detection. Oral presentation, Pittcon Conference & Expo, Philadelphia, PA, March 17–21.